



**University of
Nottingham**
UK | CHINA | MALAYSIA

High-Performance Machine Design for Propulsion and On-Board Integrated Battery Charger for a Heavy-Duty Commercial Electric Vehicle

Hatim Alwadie

Thesis submitted to the University of
Nottingham for the degree of Doctor of
Philosophy

August 2023

Abstract

The adoption of four-wheel electric vehicles (EVs) in the automotive market has helped to alleviate the climate change issue. One of the most prominent but least explored areas is the electrification of trucks/lorries. Electrification of trucks has a vital role in achieving a cleaner environment as they consume more fuel than four-wheel passenger cars. Inherently having massive torque and power requirements along with huge field weakening range (four-five times base speed) makes this application extremely challenging and difficult to consider.

This thesis provides a thorough literature review on different machine topologies to identify the superior machine topology that suits the application. Permanent magnet assisted synchronous reluctance (PMA-SynREL) machines present a promising prospective to satisfy the application requirements. Structurally, PMA-SynREL machines are extremely pushed and needs multi-physics understanding. An 8-pole 48-slot machine is designed as an initial design to understand the multi-physics of the machine. Further, an investigation into the slot-pole effect on the motors performance and weight is covered. Finite element analysis (FEA) and optimization are performed to produce an ideal design with high electromagnetic performance, thermal limits within the required limitation and a mechanically safe rotor at high speed.

EVs use grid power to charge the battery, the traction motor is not normally engaged in the charging mode. The secondary goal of this thesis is to incorporate the traction motor in the charging circuit. This thesis presents a successful attempt to reconfigure the motor windings and exploit the motor inherent magnets. A 90-kW 36-slot 6-pole surface mount permanent magnet (SMPM) motor designed at the University of Nottingham (UoN) is used to practically reconfigure the motor windings and test a series of layouts to prove the simulation results. The layouts conducted in the laboratory present how the electromechanical device (traction motor) can be used as an inductor. The knowledge acquired from the experimental validation, shows how many switches are required to reconfigure the traction motor windings. The rotor behaviour is analysed for all layouts and a vibration meter is used in the experimental validation to capture the radial vibration.

Acknowledgments

I am thankful and grateful to all of those who have helped me throughout completing this difficult journey.

I would like to especially thank my supervisors Dr Gaurang Vakil, Dr Adam Walker and Professor Chris Gerada for the help, guidance and encouragement they provided. I would like to thank my internal assessor Dr Tom Cox for his valuable annual feedback.

Sincere thanks and appreciation to all my colleagues in the Power Electronics, Machines and Control (PEMC) Research Group who worked closely with me for their help and cooperation. Many thanks to all the technicians for making the experimental work achievable.

Also, presenting gratitude and thanks to all the members of the PEMC Research Group for making the office and lab an enjoyable environment to work in.

Finally, many thanks to my family and friends for their continuous encouragement and support throughout the PhD journey.

Abbreviations

AC	Alternating Current
AFM	Axial Flux Machine
APF	Active Power Filter
BLAC	Brushless Alternating Current
BLDC	Brushless Direct current
CW	Concentrated Windings
DC	Direct Current
DSPM	Double saliency Permanent Magnet
DW	Distributed Windings
EMF	Electromotive Force
EMI	Electromagnetic Interference
EV	Electric Vehicle
FCEV	Fuel Cell Electric Vehicle
FEA	Finite Element Analysis
FFT	Fast Fourier Transform
FRM	Flux Reversal Machine
FSCW	Fractional Slot Concentric Windings
FSPM	Flux Switching Permanent Magnet
GHG	Greenhouse Gas
GVWR	Gross Vehicle Weight Rating
GM	General Motors
HEV	Hybrid Electric Vehicle
ICE	Internal Combustion Engine
IEA	International Energy Agency
IM	Induction Machine
IPM	Interior Permanent Magnet
Li-ion	Lithium-ion
LDEV	Light Duty Electric Vehicle
MHDV	Medium Heavy-Duty Vehicle
MMF	Magneto Motive Force
NdFeB	Neodymium Iron Boron

NiMH	Nickel Metal Hydride
Pb-Acid	Lead-Acid
PEMC	Power Electronic Machine Control
BEV	Battery Electric Vehicle
PFC	Power Factor Correction
PHEV	Plug-in Hybrid Electric Vehicle
PM	Permanent Magnet
PMa-SynREL	Permanent Magnet assisted Synchronous Reluctance
PMSM	Permanent magnet synchronous machine
REL	Reluctance
RFM	Radial Flux Machines
RFPM	Radial Flux Permanent magnet
RMS	Root Mean Square
RPM	Revolution Per Minute
SmCo	Samarium Cobalt
SMPM	Surface Mount Permanent Magnet
SPP	Slot per Pole per Phase
SRM	Switched Reluctance Machine
SynREL	Synchronous reluctance
TFM	Transverse Flux Machine
UCs	Ultra-capacitors
UK	United Kingdom
WFSM	Wound Field Synchronous Machine

List of Symbols

A	Electric loading (A/m)
a	Parallel paths
B	Flux density (T)
B_t	Tooth flux density (T)
B_{bi}	Back-iron flux density (T)
B_{peak}	Air gap peak flux density (T)
D	Stator bore diameter (mm)
D_{bi}	Diameter at back iron (mm)
D_{so}	Stator outer diameter (mm)
E_{MAX}	Maximum RMS phase voltage (volt)
E_{ph}	RMS electromotive force per phase (volt)
F	Force (N)
f	Frequency (Hz)
I_s	Stator current (A)
i_{ds}	D-axis current (A)
i_{qs}	Q-axis current (A)
i	Electric current (A)
J	Current density (A/mm^2)
k_h	Hysteresis loss constant
k_c	Lamination factor
k_e	Eddy current constant
k_{fill}	Fill factor
k_w	Winding factor
$L_{\ell s}$	Stator leakage inductance (H)
L_{ds}	D-axis self-inductance (H)
L_{qs}	Q-axis self-inductance (H)
L_{md}	D-axis magnetizing inductance (H)
L_{mq}	Q-axis magnetizing inductance (H)
L	Wire length (mm)
L_{stack}	Stack length (mm)
m	Number of phases

n	Turns per coil
N_{ph}	Turns per phase
P	Pole Pairs
P_{cu}	Copper losses (Watt)
P_{in}	Input power (Watt)
P_{out}	Output power (Watt)
q	Number of slots per pole per phase
Q	Number of slots
r	Stator Bore radius (mm)
R_{DC}	Direct current resistance (Ω)
S_{slot}	Slot area (mm^2)
S_{cu-all}	Copper area (mm^2)
t	Material thickness (mm)
T_e	Electromagnetic torque (Nm)
v_{ds}	D-axis voltage (V)
v_{qs}	Q-axis voltage (V)
ω_r	Angular velocity (rad/s)
w_{tooth}	Tooth width (mm)
w_{yoke}	Yoke width (mm)
λ_{PM}	Permanent magnet flux linkage (Wb)
λ_{ds}	D-axis flux linkage (Wb-t)
λ_{qs}	Q-axis flux Linkage (Wb-t)
λ_s	Stator flux linkage (Wb-t)
λ_{slot}	Slot pitch
λ_p	Pole pitch
ϕ	Flux per pole (Wb)
α	Hysteresis loss constant (flux density)
β	Hysteresis loss constant (frequency)
γ	Phase advance angle ($^\circ$)
θ	Torque angle ($^\circ$)
φ	Phase angle ($^\circ$)

Table of Contents

Abstract.....	I
Acknowledgments.....	II
Abbreviations.....	III
List of Symbols.....	V
List of Figures.....	XII
List of Tables.....	XVII
Chapter 1. Introduction.....	1
1.1 Project description.....	2
1.2 Thesis aims and objectives.....	3
1.3 Thesis outline.....	5
1.4 Novelty of the thesis.....	7
Chapter 2. Overview of Electric Vehicles.....	8
2.1 Background and driving factors for vehicles electrification technology.....	8
2.2 Configurations of EVs.....	10
2.2.1 Battery electric vehicles (BEVs).....	11
2.2.2 Fuel cell electric vehicles (FCEVs).....	11
2.2.3 Hybrid electric vehicles (HEVs).....	11
2.2.3.1 Series hybrid.....	12
2.2.3.2 Parallel hybrid.....	12
2.2.3.3 Series-Parallel hybrid.....	12
2.2.3.4 Complex hybrid.....	13
2.2.4 Plug-in hybrid electric vehicles (PHEVs).....	13
2.3 Energy storage and battery charging capabilities.....	14
2.4 EV Charging.....	15
2.5 Electric machines requirements in EVs.....	17

2.6 Key differences between electric MHDVs and light-duty electric vehicles (LDEVs) in their design and operational capacities	18
2.7 Examples of traction machines equipped in heavy-duty vehicles	19
2.8 Heavy-duty power/torque profile.....	20
2.9 Summary	21
Chapter 3. Overview on Machine Topologies and On-board Traction Machine Integrated Battery Chargers	23
3.1 Introduction.....	23
3.1.1 DC machines.....	24
3.1.2 Induction machines (IMs).....	25
3.1.3 Switched reluctance machines (SRMs)	26
3.1.4 Wound field synchronous machine (WFSM)	27
3.1.5 Permanent magnet machines (PM machines).....	28
3.1.6 Radial flux permanent magnet (RFPM) machines.....	28
3.1.7 Surface mount permanent magnet (SMPM) machines	28
3.1.8 Interior PM (IPM) machines	30
3.1.9 Radial flux machines with PMs in the stator	31
3.1.10 Synchronous reluctance (SynREL) machines.....	34
3.1.11 Permanent magnet assisted synchronous reluctance (PMA-SynREL) machines ..	35
3.1.12 Axial field machines (AFMs)	36
3.1.13 The transverse flux machines (TFMs).....	37
3.2 Comparison of IPM machines with different motor topologies used in HEVs	38
3.3 Integrated on-board battery charger	41
3.4 Three-phase on-board integrated battery chargers.....	49
3.5 Summary	60
Chapter 4. Preliminary Machine Design.....	61
4.1 Introduction.....	61

4.2 Application specifications and constraints.....	61
4.3 Design methodology	64
4.4 Optimization workflow	67
4.5 PMA-SynREL machine torque production.....	69
4.6 Limitations of electric loading and magnetic loading.....	71
4.7 PMA-SynREL machine equivalent circuit and basic characteristic	73
4.8 Torque quality in PMA-SynREL machines	76
4.9 Design consideration.....	77
4.9.1 Selection of the slot-pole combination	77
4.9.2 Winding configuration	79
4.9.3 Material selection.....	80
4.9.3.1 Stator and rotor lamination	80
4.9.3.2 Permanent magnet material.....	82
4.9.4 Electromagnetic losses and efficiency	83
4.9.5 Cooling options.....	86
4.10 Initial machine design.....	87
4.10.1 Stator sizing	87
4.10.2 Rotor sizing.....	90
4.10.3 Machine dimensions and materials.....	93
4.11 Winding type.....	94
4.12 Electromagnetic results.....	96
4.13 Reluctance torque vs magnetic torque	101
4.14 No-load test.....	101
4.15 Electromagnetic losses and efficiency of the designed machine	103
4.16 Thermal management.....	106
4.17 Demagnetization analysis	108
4.18 Mechanical check.....	110

4.19 Summary	114
Chapter 5. Dual Purpose Traction Machines	115
5.1 Introduction.....	115
5.2 Traction motor characteristics.....	116
5.3 Winding arrangement.....	118
5.4 Traction mode specifications	120
5.5 Traction mode self and mutual inductance	121
5.6 Using the traction machine for dual purpose	121
5.7 Experimental rig setup for SMPM motor inductance and vibration testing	122
5.8 Aligning the rotor position to the d-axis	123
5.9 Simulation and experimental results	125
5.10 Layout comparison.....	137
5.11 Functionality of PMA-SynREL machine as an inductor	141
5.12 Heavy-duty machine as a high current density inductor for a three-phase charging system	144
5.13 Simulation results of the dual 3-phase symmetrical layout	147
5.14 Simulation results of the dual 3-phase asymmetrical layout	151
5.15 Thermal management in charging mode.....	157
5.16 Summary	158
Chapter 6. Optimization of Various Slot-Pole Configurations of PMA-SynREL Machines	160
6.1 Introduction.....	160
6.2 Slot-pole combination.....	160
6.3 PMA-SynREL machine geometry	162
6.4 Input variables in the optimization process	163
6.5 Design Workflow.....	165
6.6 Electromagnetic results.....	167
6.7 Open circuit test.....	168

6.8 PM flux and field weakening 174

6.9 Mechanical integrity 175

6.10 Thermal performance 177

6.11 Summary 178

Chapter 7. Conclusion and Future Work 180

 7.1 Future research directions 182

References 183

Appendix A Technical skills 195

Appendix B Vibration meter results 196

Appendix C SKF vibration meter sensor positioning 199

Appendix D Inductance measurement 200

Appendix E Rig supply and load 201

List of Figures

Figure 1-1 Carbon dioxide emissions in the transportation sector for 2022.....	1
Figure 2-1 Heavy-duty trucks Class 7 and 8[11].....	9
Figure 2-2 Vehicle configuration a) BEV b) HEV c) PHEV and d) FCEV	10
Figure 2-3 HEVs configurations, a) series hybrid b) parallel hybrid c) series parallel hybrid and d) complex hybrid.....	13
Figure 2-4 Schematic of torque-speed characteristic of electric vehicles.....	17
Figure 2-5 Torque/power requirements of a heavy-duty truck from Cummins.....	20
Figure 3-1 Brushed PM DC machine.....	24
Figure 3-2 Induction machine (IM)	25
Figure 3-3 Switched reluctance machine (SRM).....	26
Figure 3-4 Wound field synchronous machine (WFSM)	27
Figure 3-5 Surface mount PM machine	29
Figure 3-6 a) 10-pole 12-slot SMPM machine b) SMPM rotor [56].....	29
Figure 3-7 Interior PM machine	30
Figure 3-8 Evolution of PM rotors in EVs[57].....	30
Figure 3-9 DSPM 4-pole machine[55]	31
Figure 3-10 6-Pole FRM[55]	32
Figure 3-11 FSPM topology[55].....	33
Figure 3-12 SynREL machine topology	34
Figure 3-13 8-pole PMA-synREL machine	35
Figure 3-14 (AFMs) a) single-rotor single-stator (b) double-sided rotor and single-stator and (c) double-sided stator and single-rotor[13]	36
Figure 3-15 TFM topology[79].....	37
Figure 3-16 On-board battery charger	42
Figure 3-17 Integrated on-board battery charger using two IMs windings	43
Figure 3-18 Integrated on-board battery charger by reconfiguring one phase of an IM	44
Figure 3-19 Integrated on-board charger using 4-IMs.....	45
Figure 3-20 Integrated battery charger using a PM motor windings.....	45
Figure 3-21 On-board integrated charger using a SRM windings.....	46
Figure 3-22 Single-phase integrated battery charger using a PM machine winding and an APF	47

Figure 3-23 Integrated on-board charger using (a) 9-phase winding (b) 6-phase windings and (c) 5-phase windings	48
Figure 3-24 Single-phase on-board charger by Hyundai	49
Figure 3-25 Integrated battery charger based on a split-phase machine, red arrows indicate the charging process and the blue arrows the traction mode	50
Figure 3-26 3-phase integrated charger using a 6 phase motor windings.....	51
Figure 3-27 3-Phase integrated charger using an IPM (FSCW)	52
Figure 3-28 Integrated battery charger using a 2*3phase FSCW	53
Figure 3-29 Integrated charger based on a 6-phase machine and a 9-switch converter	54
Figure 3-30 3-phase integrated charger based on a 5-phase motor	54
Figure 3-31 3-phase integrated charger using an asymmetrical 6 phase windings.....	55
Figure 3-32 3-phase integrated battery charger using a 9-phase motors neutral points	56
Figure 3-33 3-phase integrated battery charger based on a split phase motor configuration ..	56
Figure 3-34 Integrated on-board charger using an input filter and machine windings.....	57
Figure 3-35 Fast integrated charger by Renault.....	58
Figure 4-1 Torque/Power vs speed characteristic of required motor from Cummins	62
Figure 4-2 Design methodology process	66
Figure 4-3 Optimization workflow	67
Figure 4-4 PMA-SynREL machine configuration	72
Figure 4-5 Equivalent circuit of a PMA-SynREL machine (a) q-axis and (b) d-axis	73
Figure 4-6 Phasor diagram of PMA-SynREL machine	75
Figure 4-7 Distributed windings represented on the left side and concentrated windings on the right side.....	79
Figure 4-8 High performance electric steel[117].....	81
Figure 4-9 (a) N10 0.1 iron characteristic for the stator and (b) 35HXT780T iron for the rotor	82
Figure 4-10 Double-layer per slot (a) 8 turns/1strand (b) 8 turns/8strands and (c) 8 turns/10 strands	84
Figure 4-11 Rotor sketch of a PMA-SynREL machine	91
Figure 4-12 Geometry model 8-pole 48-slot	93
Figure 4-13 (a) 3-phase distributed windings (b) phase A with 8 parallel paths.....	95
Figure 4-14 Slot with different fill factor	95

Figure 4-15 Electromagnetic output torque for peak and rated operation at base speed and rated torque at maximum speed	97
Figure 4-16 Output Torque /Power vs speed	98
Figure 4-17 Phase voltage across speed and the phase advance angle	98
Figure 4-18 Flux density distribution at (a) Peak torque base speed (b) Continuous torque base speed and (c) Continuous torque max speed.....	100
Figure 4-19 Magnetic Torque and Reluctance Torque share at all operation conditions base speed(5000rpm) and Maximum speed (15000 rpm).....	101
Figure 4-20 Back-EMF Line-Line with speed (rpm).....	102
Figure 4-21 (a) back-EMF Line-Line at 15000rpm (b) FFT of Back-EMF at 15000rpm.....	103
Figure 4-22 Electromagnetic loss (a) copper losses (b) stator iron losses (c) rotor iron losses and (d) PM losses.....	104
Figure 4-23 Power factor of machine at rated power	105
Figure 4-24 Efficiency of machine at rated power	105
Figure 4-25 N42UH demagnetization curves[128].....	108
Figure 4-26 N42UH 150 C magnets at maximum speed, with 90 degree phase advance angle	109
Figure 4-27 Peripheral speed impact on rotor stresses	110
Figure 4-28 Rotor stress with speed variation	111
Figure 4-29 Sharp edges flux barriers and magnets equal to 1049.016 MPa	112
Figure 4-30 Rounded flux barriers and magnets with a stress equal to 718.14 MPa	112
Figure 5-1 6-pole 36-slot SMPM machine	117
Figure 5-2 Phase A with 3 paths open end	118
Figure 5-3 3-Phase inverter drive configuration	119
Figure 5-4 3 by 3 -phase drive configuration	119
Figure 5-5 2 by 3 -phase inverter open end configuration.....	120
Figure 5-6 Self and mutual inductance for Phase (A).....	121
Figure 5-7 Experimental rig setup	122
Figure 5-8 Star connection of the 3-phase motor.....	123
Figure 5-9 6-pole 36-slot SMPM motor connections	124
Figure 5-10 Winding connection Layout (1)	126
Figure 5-11 Flux distribution plot layout (1)	126
Figure 5-12 Layout-1 results.....	128

Figure 5-13 Schematic of layout (2) connections	129
Figure 5-14 Layout-2 results.....	130
Figure 5-15 Schematic of layout (3) connections	131
Figure 5-16 layout_3 results	132
Figure 5-17 layout_4 winding schematic.....	133
Figure 5-18 Layout_4 results	134
Figure 5-19 Layout-5 winding schematic	135
Figure 5-20 Layout_5 results	136
Figure 5-21 SMPM vs PMA-SynREL (machine as an inductor)	143
Figure 5-22 Dual three phase symmetrical winding layout.....	145
Figure 5-23 Phasor diagram (a) Traction mode (b) Charging mode	145
Figure 5-24 8-pole 48-slot PMA-SynREL machine (Dual three phase symmetrical windings)	146
Figure 5-25 Dual 3-phase symmetrical windings (traction and charging) results.....	148
Figure 5-26 Dual 3-phase symmetrical layout (Phase A1 and A2) in series.....	149
Figure 5-27 Results of dual 3-phase symmetrical layout all paths in series per phase.....	150
Figure 5-28 Dual three phase asymmetrical winding layout	151
Figure 5-29 Phasor diagram for asymmetrical layout (a) Traction mode (b) Charging mode	152
Figure 5-30 8-pole 48-slot PMA-SynREL machine (Dual three phase asymmetrical windings)	152
Figure 5-31 Dual 3-phase asymmetrical windings (traction and charging) results	154
Figure 5-32 Dual 3-phase asymmetrical layout (Phase A1 and B2) in series	155
Figure 5-33 Results of dual 3-phase asymmetrical layout all phases paths in series	156
Figure 6-1 PMA-SynREL radial configuration important dimensions.....	162
Figure 6-2 Torque Power characteristic of a heavy-duty vehicle	164
Figure 6-3 Workflow for the optimization process.....	165
Figure 6-4 Back-EMF and FFT for 6-pole and 8-pole	168
Figure 6-5 Back-EMF and its FFT for 10, 12 and 14 poles.....	169
Figure 6-6 Continuous operation efficiency	171
Figure 6-7 Active weight for the optimized machines.....	172
Figure 6-8 PMs weight for different poles.....	173
Figure 6-9 Moment of inertia for the designed machines.....	173

Figure 6-10 PMs flux with the required I_d for all poles	174
Figure 6-11 Reluctance torque and magnetic torque at top speed (15000rpm) continuous current	175
Figure 6-12 Mechanical Stresses of (a) 14p/84s (b) 12p/72s (c) 10p/60s (d) 8p/48s and (e) 6p/36s.....	176
Figure C-1 SMPM machine with SKF meter sensor positioned 90 degrees	199
Figure C-2 Rotor aligned to d-axis	199
Figure D-1 Inductance measurement for phase A SMPM machine	200
Figure E-1 Machine as inductor circuit	201

List of Tables

Table 2-1 Different energy storage systems used in EVs	15
Table 2-2 Classification of EVs chargers	16
Table 2-3 Available electric machines used in heavy-duty vehicles	19
Table 3-1 Comparing parameters of IPM, SRM and IM	38
Table 3-2 Performance comparison at (a) 1500 rpm and (b) 6000 rpm	39
Table 3-3 Comparing machine topologies for automotive applications	40
Table 3-4 Comparison of traction machine integrated battery chargers	59
Table 4-1 Traction machine performance requirements and geometrical constraints	62
Table 4-2 Geometry initial values and optimization range	92
Table 4-3 Radial and axial dimensions of the 8-pole 48-slot	93
Table 4-4 Machine materials and weight	94
Table 4-5 Windings Characteristics of machine windings	94
Table 4-6 Comparison of initial machine design to machine target	99
Table 4-7 Cooling systems and fluid characteristic	107
Table 4-8 Temperature results using Water-Jacket and Water-Jacket + Spray cooling	107
Table 4-9 PMA-SynREL machine physical dimensions and materials	113
Table 5-1 Traction motor physical dimensions	116
Table 5-2 SMPM machine materials	117
Table 5-3 6-pole 36-slot winding characteristics	118
Table 5-4 Traction motor specifications	120
Table 5-5 Inductance comparison between simulation and experiment results layout 1	127
Table 5-6 Inductance comparison between simulation and experiment results layout 2	130
Table 5-7 Inductance comparison between simulation and experiment results layout 3	132
Table 5-8 Inductance comparison between simulation and experiment results layout 4	134
Table 5-9 Inductance comparison between simulation and experiment results layout 5	136
Table 5-10 Comparative evaluation of potential layouts for using the traction machine as an inductor	137
Table 5-11 Geometry comparison SMPM machine vs PMA-SynREL machine	141
Table 5-12 Winding characteristics of SMPM machine vs PMA-SynREL machine	141
Table 5-13 Inductance measurements in traction and charging mode (dual 3-phase symmetrical windings)	147

Table 5-14 Inductance measurements in traction and charging mode (dual 3-phase asymmetrical windings).....	153
Table 5-15 Windings and magnets temperature during charging mode.....	157
Table 6-1 Winding Factor and SPP for different slot-poles	161
Table 6-2 Input variables in the optimization model.....	163
Table 6-3 Constraints set in the optimization model and objective.....	164
Table 6-4 Input currents and winding characteristics	167
Table 6-5 Electromagnetic Optimization results	167
Table 6-6 Physical dimensions of the designed PMA-SynREL machines	172
Table 6-7 Thermal results of the machine most important components.....	177
Table 6-8 Performance and physical comparison of all slot/pole combinations	179

Chapter 1. Introduction

The severity of climate change demands immediate preventative actions to mitigate its significant threats to human civilization and to curb global warming [1]. In response to this matter, governments world-wide have set agreements and legislations to combat this issue such as the Paris agreement, some governments promised to put ambitious actions to achieve net-zero emissions such as the United Kingdom (UK) by 2050[2]. According to the International Energy Agency (IEA), the transport sector accounts for 23% of total emissions in 2022[3]. Figure (1-1) illustrates that within the transport sector, road transport is responsible for 79% of carbon dioxide emissions. This 79% is primarily composed of emissions from different types of vehicles: passenger cars and vans contribute the largest share with 48%, followed by buses at 6% and heavy-medium road freight vehicles accounting for 25%[4].

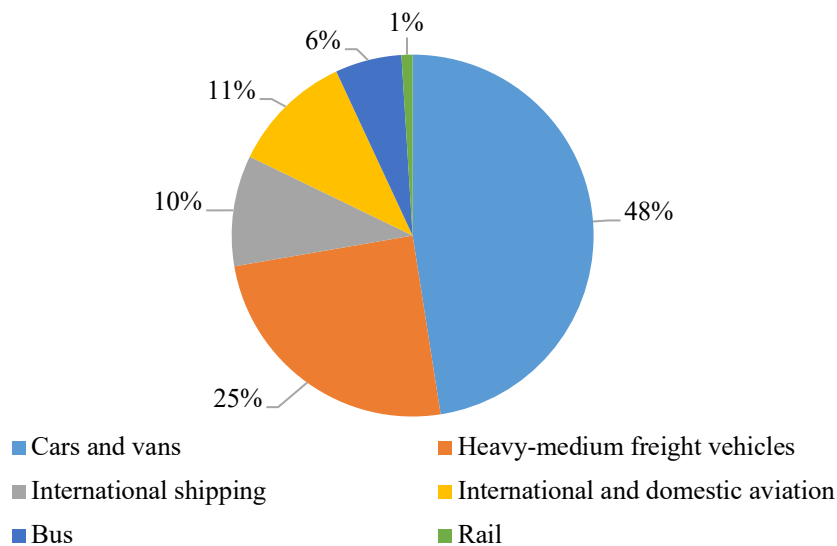


Figure 1-1 Carbon dioxide emissions in the transportation sector for 2022

The transport sector is growing, and high demand of on-road vehicles is expected with the increase in the global population. Therefore, it is of a prime necessity to electrify the on-road vehicles to combat the climate change issue. EVs, are a promising solution to reduce greenhouse gas (GHG) emissions. The electrification of on-road vehicles bring out salient merits when coupled with renewable energy resources[5]. One of the most prominent but least explored areas is the electrification of heavy-duty trucks. The adoption of electric trucks in the automotive market brings out the benefit of cleaner environment as heavy-duty trucks consume more fuel compared to passenger cars per vehicle. The fuel efficiency of heavy-duty trucks is

less than that of passenger cars, owing to their greater size, heavier weight, and more powerful engines[6].

1.1 Project description

This thesis is concerned with the design of a traction motor for a heavy-duty truck. The aim is to produce a traction motor that fits the application requirements. The power and torque requirements for traction motors in heavy-duty trucks are double those in passenger cars, which makes the design challenging. The main focus of this thesis is to design a high-power high-speed electric motor with high efficiency.

In this thesis, a comprehensive literature review on traction machines is carried out to select the best electric motor that can meet the challenging targets for the heavy-duty truck. This leads to PMA-SynREL machines, the torque of this motor is a summation of magnet torque and reluctance torque. Advancements in high-performance electric steels and permanent magnets (PMs) are crucial technologies that lead to the success of electric motor implementation in EVs.

In this thesis Chapter 4 begins with an initial design of an 8-pole 48-slot machine to understand the multi-physics of PMA-SynREL machines. This thesis includes an investigation into various slot-pole combinations for the motor, with a focus on their overall weight. The goal is to select the configuration with the lowest magnet weight among the different slot-pole combinations. A detailed optimization is performed covering all aspects of electromagnetic characteristics, thermal management and mechanical integrity.

The second topic of this thesis is concerned with the use of the traction machine inherent magnets (windings) as an inductor. This thesis details a series of layouts representing how the traction motor can be engaged in the charging mode. The rotors behaviour is analysed in all potential layouts. The complexity of the layouts is judged by the number of switches required to swap between the traction mode and charging mode as well as the amount of inductance.

1.2 Thesis aims and objectives

The aim of this thesis is to contribute to knowledge about the design of a traction machine for a heavy-duty truck. The goal is to achieve high power-to-mass ratio while retaining high torque and efficiency over a wide speed range.

The secondary goal of this thesis is to propose solutions on how the traction motor (windings) can be used as an inductor in the charging mode of the vehicle. The focus is to examine a series of layouts by measuring the inductance of each layout. Moreover, to practically test the potential layouts to check the vibration that might occur for validation.

To achieve these aims, the following objectives were laid down:

- Perform a comprehensive literature review divided into 3 topics, on transport electrification, traction machine topologies and on-board traction machine integrated battery chargers.
 - Review on EVs covering topologies, energy storage for EVs and charging capabilities and highlight the challenges of EVs. Furthermore, to highlight the types of electric machines used currently in EVs.
 - A thorough review on traction machines. The machine technologies are compared to highlight the outstanding electric machine that can fit the application.
 - A review on on-board traction machine integrated battery chargers. This covers previous suggestions to use the electric motor (windings) in the charging mode.
- Understand the multi-physics of the PMA-SynREL traction machine, highlight the important parameters that have a significant influence on the machine's performance.
- Propose a series of methods to reconfigure the motor windings, to be used in the charging circuit. Investigate the rotor behaviour in all potential layouts and highlight radial vibration and the torque produced.

- Investigate the impact of various slot-pole combinations on both the performance and weight of the motor. This investigation involves performing a multi-physics optimization on all machine designs, with the ultimate objective of producing a machine that has a high power-to-mass ratio.

1.3 Thesis outline

The outline of the PhD thesis is organized as follows.

1) Chapter 1- Introduction

This chapter serves as a comprehensive introduction to the thesis, articulating the project's aims and objectives. It underscores the novelty of the thesis and represents the thesis structure.

2) Chapter 2- Overview of electric vehicles

In this chapter a detailed overview of EVs topologies, encompassing aspects of energy storage and traction machine requirements. This overview includes type of chargers in EVs and their charging modes. Examples of some electric motors used in heavy-duty trucks are illustrated.

3) Chapter 3- Overview on machine topologies and on-board traction machine integrated battery chargers

This chapter presents an extensive literature review of traction machines, emphasizing machine topologies that demonstrate superior field weakening capabilities, high power density, high torque density, good power factor and cost-effectiveness. The second focus of this chapter delves into the subject of machine-integrated on-board chargers. It sheds light on both single-phase and three-phase on-board integrated topologies, offering insights into their unique properties and benefits. Furthermore, the chapter explores various strategies for integrating the machine windings into the battery charger circuit showcasing potential designs and their implications.

4) Chapter 4- Preliminary machine design

This chapter looks into the initial design phase of the PMA-SynREL machine, highlighting the crucial design considerations. The main goal of this chapter is to explore the specific 8-pole 48-slot combination. This exploration helps to better understand the multi-physics of the PMA-SynREL machine for heavy-duty applications.

5) Chapter 5- Dual purpose traction machines

This chapter investigates the use of a SMPM machine as an inductor. It provides several options on reconfiguring the motor windings and leveraging the machine inductance. Experimental examination on the proposed layouts is done in this chapter to highlight the vibration that might occur in each layout. The layout showcasing the highest inductance within the SMPM machine

is implemented within the PMa-SynREL machine, previously examined in chapter 4 as a traction machine for a heavy-duty truck. This implementation serves to evaluate its functionality as an inductor.

6) Chapter 6- Optimization of various slot-pole configurations of PMa-SynREL machines

This chapter focuses on optimizing different slot-pole combinations in the PMa-SynREL machine. Five specific configurations: 14-pole 84-slot, 12-pole 72-slot, 10-pole 60-slot, 8-pole 48-slot and 6-pole 36-slot. The main goal of the optimization process is to reduce the active mass of the machine. Finally, the performance of each configuration is analysed to determine the configuration that has the lowest active mass and the topology that has the lowest magnet weight.

7) Chapter 7- Conclusion

This chapter summarize the conclusion of the work and highlight future directions.

1.4 Novelty of the thesis

The thesis presents:

- This thesis explores the design of a high peripheral speed PMa-SynREL machine for a heavy-duty vehicle application. The selection of this machine is primarily due to its wide field weakening range. The research covers all fundamental elements including electromagnetic, mechanical and thermal characteristics of the machine. In addition, the thesis examines the implications of slot-pole count variations on the motor's active mass.
- Novel options for using the traction machine's windings as an inductor, with a focus on implications for the machine, such as torque, rotor oscillations and vibrations. Utilizing the traction machine as an inductor for on-board battery chargers reduces weight, space and cost.

Chapter 2. Overview of Electric Vehicles

This chapter provides a background on EVs, it also highlights the driving factors for the electrification of the transportation sector in medium and heavy-duty vehicles (MHDVs). The EVs architectures are presented in detail showing the advantages and disadvantage of each configuration. Energy storage devices used in EVs are emphasized and the battery charger types are covered. The core technology of EVs is the traction motor that converts electric power to the required mechanical power, the strict requirements that the traction motor must possess are discussed. Finally, examples of electric motors used in heavy-duty trucks are stated.

2.1 Background and driving factors for vehicles electrification technology

EVs have been available since the mid-twentieth century. Its survival began to dwindle with the introduction of internal combustion engine (ICE) vehicles. EVs coexisted with ICE vehicles in urban areas until they succumbed to their ICE counterparts. The energy density of ICE vehicles is higher than that of EVs. The introduction of electric self-starting capability in ICE vehicles, as well as their excellent performance, has accelerated their development and gained widespread acceptance in the automobile market.

Electrification of on-road vehicles is a method of replacing reliance on fossil fuels with electricity to power on-road vehicles. It is a strategy for reducing GHG emissions and improving air quality[7]. Electrifying on-road vehicles accelerates the transition to zero net emissions. Governments such as the UK have declared that no petrol or diesel cars will be sold in 2030[8]. The ultimate scarcity of fossil fuels is one of the driving forces behind vehicle electrification.

Currently, there is a rapid increase in the transition to electric power for on-road vehicles. This includes not only passenger cars, but also specialized vehicles such as construction trucks, rail vehicles, and agricultural vehicles. The primary effort is on propulsion technology, with the goal of developing an EV that is low in emissions, efficient and reliable[9].

In the United States, the primary contributors to rising fuel usage and GHG emissions are MHDVs such as trucks and buses. Electrifying these MHDVs is seen as a vital strategy for reducing GHG emissions and cutting fuel expenses. While hybrid and plug-in hybrid light duty vehicles are finding market success, the commercial EV sector particularly for MHDVs, lags behind and needs more initiatives to boost market penetration. Trucks are categorized based on their gross vehicle weight rating (GVWR) in terms of fuel consumption and emissions[10]. Heavy-duty vehicles are those with a gross vehicle weight above 26,001 lbs, falling under Classes 7 and 8 as shown in Figure (2-1).

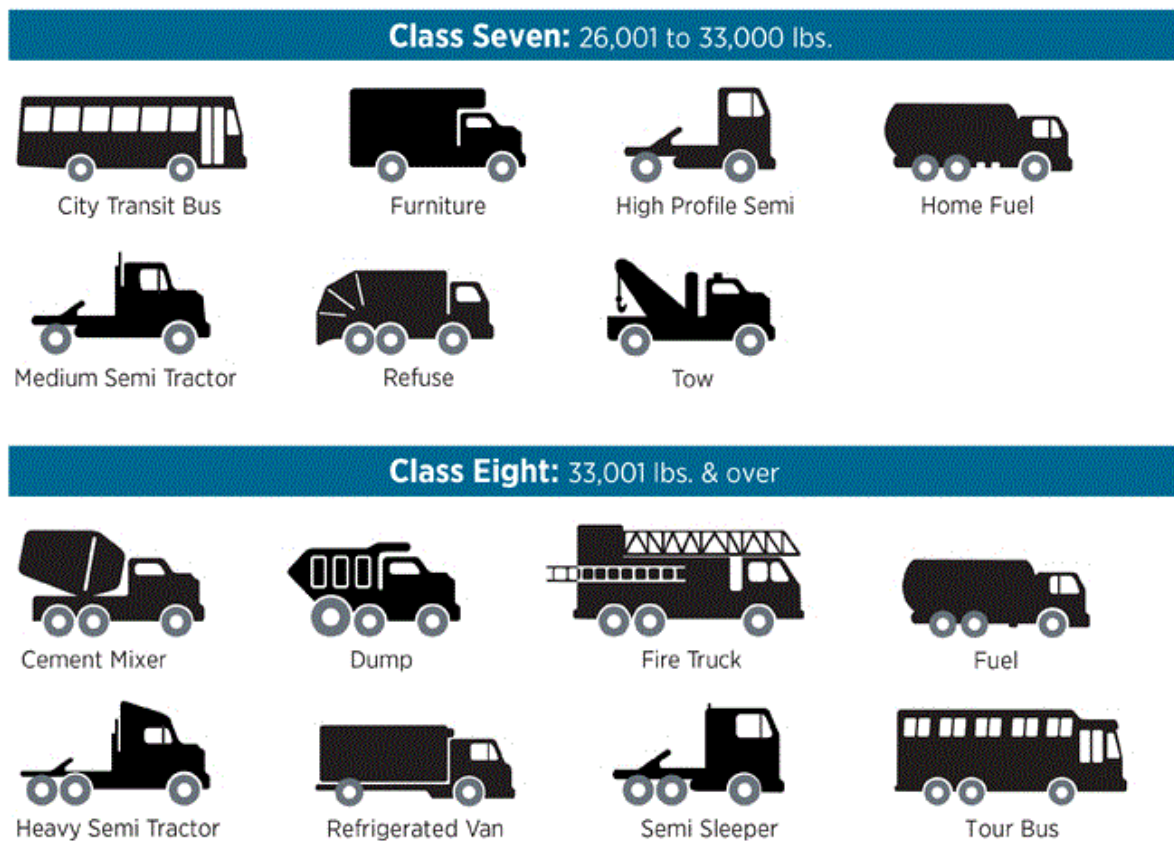


Figure 2-1 Heavy-duty trucks Class 7 and 8[11]

2.2 Configurations of EVs

The core technology of EVs is based on electric motors that propel the vehicle powered by batteries or fuel cells. EVs shown in Figure (2-2) are categorized based on the energy source and the propulsion system as follows:

- a) Battery electric vehicles (BEVs).
- b) Hybrid electric vehicles (HEVs).
- c) Plug-in hybrid electric vehicles (PHEVs).
- d) Fuel cell electric vehicles (FCEVs).

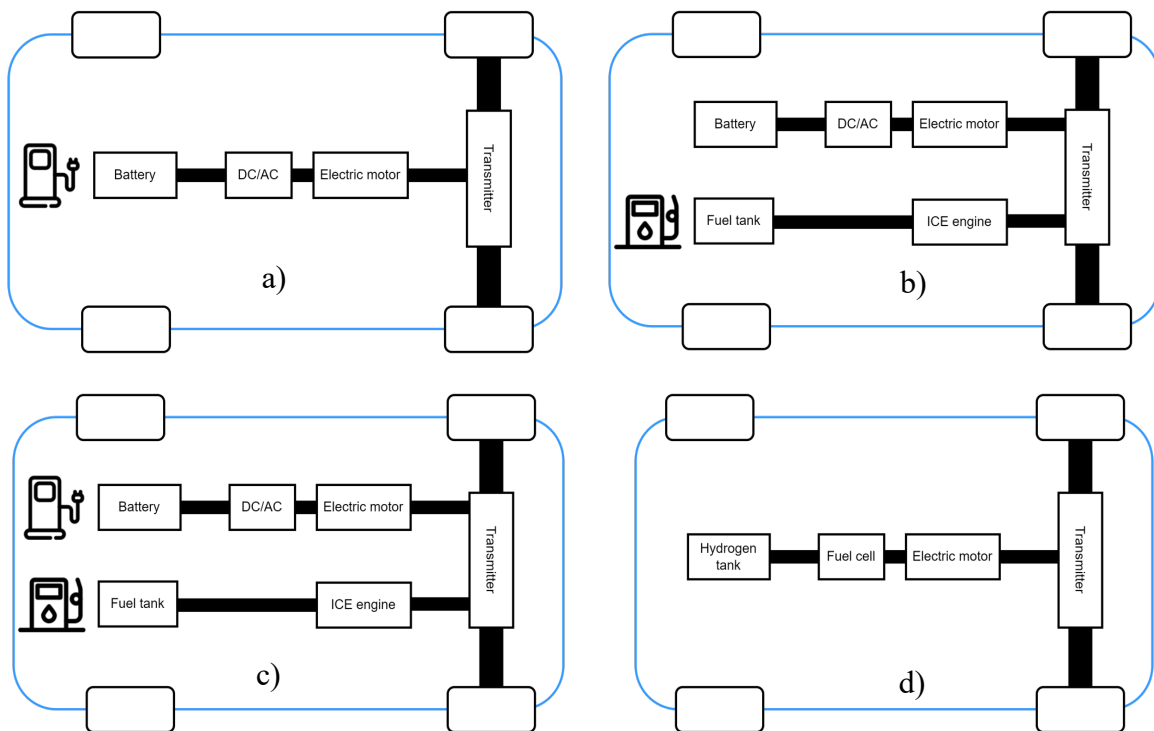


Figure 2-2 Vehicle configuration a) BEV b) HEV c) PHEV and d) FCEV

2.2.1 Battery electric vehicles (BEVs)

Batteries are the energy source in BEVs as shown in Figure (2-2a) and electric motors are the driving component. Moreover, the electric motor in BEVs can operate as a generator when the vehicle is going downhill. A key advantage of BEVs it offers no road emissions. The driving range of BEVs depends on the battery's capacity. Batteries can be charged by grid electricity such as recharging stations and home outlets or by non-grid electricity such as solar panels and on-board regenerative braking system [12]. Due to the dependency on batteries as the sole energy this configuration faces major challenges that needs improvement. These challenges are the battery capacity and charging time it takes to recharge the battery. Furthermore, the lack of charging infrastructure. Therefore, BEVs are less preferable to ICE vehicles which require less time for refuelling and have a longer driving range[13, 14]. An example of BEVs is the BYD-manufactured Class 8 Quantum Rear Loader, an all-electric refuse truck[10].

2.2.2 Fuel cell electric vehicles (FCEVs)

FCEVs shown in Figure (2-2d) configuration is similar to BEVs, it has zero roadside emissions. The fuel cells, which are fuelled with hydrogen, provide power to the electric motor. Water and heat are the only waste products. The driving range of FCEV is similar to ICE vehicles. However, the lack of hydrogen refuelling infrastructure compared to gasoline refuelling station is a major challenge. Furthermore, the cost of fuel cells is expensive. The low power density of fuel cells leads to an increasing weight of the power unit which is a disadvantage in FCEV[15]. An example of a FCEV is the Nikola fuel cell Class 8 truck[10].

2.2.3 Hybrid electric vehicles (HEVs)

To extend the driving range of the BEVs, HEVs shown in Figure (2-2b) have been introduced. This configuration incorporates two energy sources, electric motors and ICE to propel the vehicle. The merit of no road emission in this configuration is lost. Nevertheless, HEVs are less pollutant to ICE vehicles while having the same travel range. Moreover, this configuration has definite merits, one of which is that its driving range has been extended 3 to 4 times that of BEVs[16]. HEVs can be mild hybrids or full hybrids. Mild hybrids employ a small electric drive and energy storage combined with a transmission and internal combustion engine. An example of a mild hybrids is the delivery truck AVID 48 V. Furthermore, a full hybrid example is the parallel hybrid Class 5 Hino diesel-electric[10].

HEVs are classified into four types namely.

- 1) Series hybrid.
- 2) Parallel hybrid.
- 3) Series-parallel hybrid.
- 4) Complex hybrid.

2.2.3.1 *Series hybrid*

In series hybrid configuration, the power flow to the wheels of the vehicle is in series as shown in Figure (2-3a). The ICE is the prime mover of the generator and the produced electricity is supplied to the electric motor which is mechanically connected to the wheels or delivered to the battery. The ICE can operate at its optimal efficiency due to its not mechanically connected to the vehicle's wheels. This topology has a simple architecture and it can operate the motor as generator in the deceleration mode to recover energy through regenerative braking. Furthermore, a complex transmission between the electric motor and vehicles wheels is not required due to the ideal torque-speed characteristic of electric motors and their efficiency over a wide speed range [16-19].

2.2.3.2 *Parallel hybrid*

Parallel hybrid configuration differs from series hybrid configuration, both the ICE and the electric motor provide torque to drive the vehicle as shown in Figure (2-3b) therefore, smaller electric motors and ICEs are used compared to the series configuration. Furthermore, as only one unit is used as either generator or motor, this configuration offers improved compactness, lower energy loss compared to the series hybrid configuration. The traction motor can be used as a generator during regenerative braking and charge the battery. The downside of parallel hybrid configuration is its complex structure and control because the engine and electric motor need to work together and sometimes simultaneously to propel the vehicle [20, 21].

2.2.3.3 *Series-Parallel hybrid*

Series-Parallel hybrid configuration shown in Figure (2-3c) is a combination of both series hybrid and parallel hybrid. Both the ICE and the electric motor are mechanically coupled to the wheels through a power splitter. Furthermore, the ICE operates the generator to charge the battery. Their major advantage lies in their flexibility, allowing them to operate in electric-only mode at low speeds (like a series hybrid) for reduced emissions and increased fuel economy, while also permitting the ICE to directly drive the wheels at higher speeds (like a parallel

hybrid) for improved efficiency. This configuration is complex and costly. However, with the rapid advancement of control and manufacturing technologies this configuration is preferred to modern HEV[21].

2.2.3.4 Complex hybrid

The complex hybrid configuration shown in Figure (2-3d) is like the series-parallel hybrid configuration the key difference is, complex hybrid generator can operate as generator/motor. Therefore, the power flow in the complex hybrid is unidirectional. The drawback of this configuration is the complexity of its design and its cost[22].

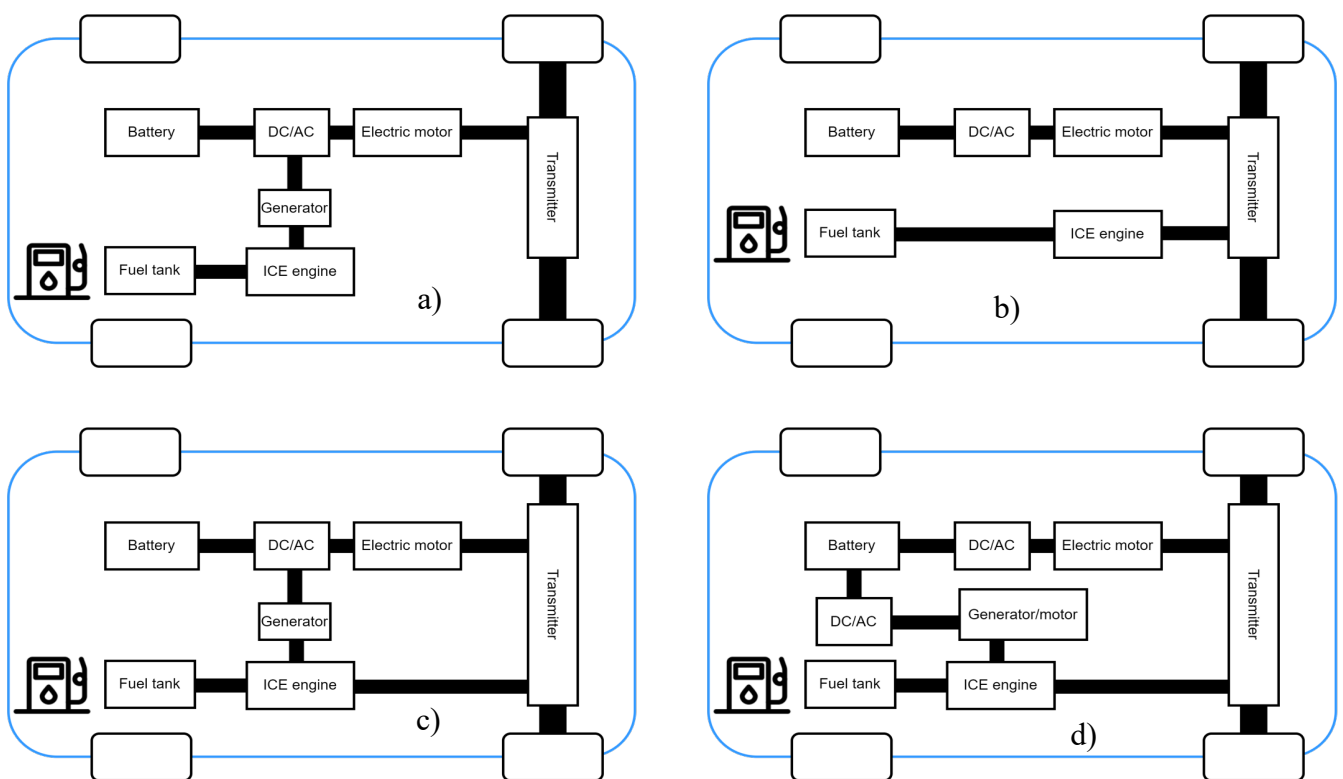


Figure 2-3 HEVs configurations, a) series hybrid b) parallel hybrid c) series parallel hybrid and d) complex hybrid

2.2.4 Plug-in hybrid electric vehicles (PHEVs)

PHEV configuration shown in Figure (2-2c) is an updated version of HEV. It has an advantage of a plug to recharge the battery of the vehicle from the grid. Similar to HEV, PHEV can have series, parallel and series parallel configurations. The key difference between PHEV and HEV is PHEV uses electricity as the main energy source to propel the vehicle and ICE as a secondary energy source. Therefore, this configuration requires large battery packs. However, it has a plus of it can be gasoline independent for daily commuting[23, 24]. An example of this

configuration is employed in electric trucks such as, the medium duty truck Class 6 PowerDrive 6000 and the heavy-duty vehicle Class 8 TransPower ElecTruck[10].

2.3 Energy storage and battery charging capabilities

From the previous section, BEVs and PHEVs can offer zero tailpipe emissions which makes these topologies an attractive solution to address the climate change issue and combat the increase of GHG emissions. However, energy storage plays a crucial role in the successful transition from ICEs to electric MHDVs. Batteries provide the energy required to propel an automobile that weighs two tons and upward. Battery size is expected to increase with vehicle weight as Class 7 and Class 8 are heavy-duty vehicles with weight above 26,001 lbs[10]. Energy storage systems like batteries are an essential component of an EV drive system. The success of EVs is highly dependent on the improvement of energy storage capacity and cost. Moreover, the lifespan of the battery considering the number of charging cycles a battery can retain as well as the thermal losses it generates in the charging mode are appealing factors to EVs manufacturers. The EVs battery consists of hundreds of individual cells connected in a structural frame forming a module, then the modules are connected together creating a unit, packed in a case forming a large rechargeable battery. Therefore, a large number of cells means more weight added to the vehicle, but also a larger capacity and a longer driving range that the vehicle can achieve. The energy capacity of a battery is generally measured in kilowatt-hour (kWh). There are different kinds of energy storage in modern EVs [25-27], such as

- 1) **Lithium-Ion (Li-ion) batteries** are widely used in EVs and in most portable electronics such as laptops and cell phones. This is due to their high energy density that enables it to be manufactured in reduced size. They also have good thermal performance and low discharge. Li-ion batteries are the most used within electric MHDVs[10].
- 2) **Lead-Acid (Pb-Acid) batteries** offer high power, uncostly and are common in conventional vehicles. However, they possess low specific energy, and their lifespan is short.
- 3) **Nickel-Metal Hydride (NiMH) batteries** offer high specific energy and power capabilities. They also have a better lifespan than lead-acid batteries. The main concern with these batteries is the high cost, high self-discharge rates and thermal performance. NiMH batteries are commonly used in many electronic devices and HEVs.

4) **Ultra-Capacitors (UCs)** an energy storage device that stores electricity in a static state instead of storing energy in a form of chemicals like the way batteries work. They have a greater power density compared to batteries which enables them to charge and discharge faster than batteries. UCs can be used as a secondary energy storage device, it can assist the battery by providing additional power.

Table 2-1 Different energy storage systems used in EVs

Energy storage	Power density (W/kg)	Energy density (Wh /kg)
Li-ion Batteries [26]	350-3000	100-275
Pb-Acid Batteries [26]	75-100	30-60
NiMH Batteries [26]	250-100	60-120
UCs [28]	10000	5 (typical)

From Table (2-1) the Li-ion batteries have the highest energy density, which is a merit to design a reduced size battery when compared to other energy storage devices. On the other side UCs have the highest power density which means higher recharge rate but shorter driving range due to the low energy density. The current solution is to combine both the Li-ion batteries with UCs forming a hybrid system. In this hybrid system the UCs assist the battery in fast charging and high power can be delivered in short time[29, 30].

2.4 EV Charging

To boost the adoption of EVs in the automotive market there are challenges that need to be addressed, the availability of charger infrastructure, how fast the vehicles can be charged. EVs chargers are categorized into three types namely, slow chargers, semi-fast chargers and fast chargers as shown in Table (2-2). Slow chargers and semi-fast chargers are on-board chargers; the power conversion from AC to DC takes place within the vehicle. In contrast, fast chargers are off-board and are typically located in commercial areas, serving a function similar to fuel stations for ICE vehicles [31]. The charging time of an EV depends on the following factors:

- 1) The capacity of the battery, the technology used, and the efficiency of the on-board charger.
- 2) The power rating of the charger circuit and the current capacity of the charger cable.

Table 2-2 Classification of EVs chargers

	On-board Chargers		Off-board Chargers
Charger Types[32]	Slow Charger	Fast Charger	Rapid Chargers
Number of Phases	1-Phase	1-3 Phases	DC Source
Location	Home, workplace	Car parks, Supermarkets	Motor way service station
Power Rating (kW)	3	7 or 22	Starts from 43
Charging time	8-10 hours	3-4 hours	30-60 minutes

As seen in Table (2-2), off-board chargers are the rapid chargers. They start from 43 kW and can go up to 150 kW with 90% efficiency. An example of rapid chargers is the eVGO DC Fast charger. Therefore, it is likely that DC fast charger will dominate EV charging for electric MHDVs[10].

There are 4 different charging modes in EVs battery charging[33];

Mode-1, which is a slow charging mode that uses a (home socket, rated at 13 Amps in UK), it utilizes a wire with no control unit. Due to the limitation of the permissible power this mode takes more time to recharge the EV battery.

Mode-2 uses a non-dedicated infrastructure it can use a domestic or industrial socket, the cable in mode-2 unlike mode-1 incorporates an in-cable control and protection device unit. The power rating is limited to 3kW (13Amps) in residential areas and to 7.4kW (32Amps) in industrial areas.

Mode-3 uses a dedicated EV charging circuit, the (smart) charging point has a control, communication and protection functions. The power rating in mode-3 is limited to 3.7kW (16Amps), 7.4 kW (32Amps) and in industrial or public charging the power rating could go higher. High fast charging is achieved in mode-3 due to higher power capabilities compared to mode-1 and mode-2.

Mode-4 provides high power rating around 50kW and could go to much higher power rating depending on the capability of charging point. It uses a DC supply directly connected to the battery, in this mode no on-board charger for power conversion is required, and it is found in

commercial and public areas. The charging point incorporates communication, protection and control functions. This mode is the most suitable charging mode for electric heavy-duty vehicles as it supports high power charging rate.

2.5 Electric machines requirements in EVs

Electric machine technology lies at the heart of an EV drivetrain, serving as the critical link that transforms electrical power into mechanical power via electromagnetic energy. Designing an electric machine suitable for an EV involves tackling extreme requirements. As shown in Figure (2-4), the torque-speed characteristics play a vital role in defining the EV's performance. The advancement in energy storage technology is important, but the performance of the traction motor holds equal significance. To compete with the ICEs used in conventional vehicles, the capabilities of these traction motors must be continuously enhanced and optimized.

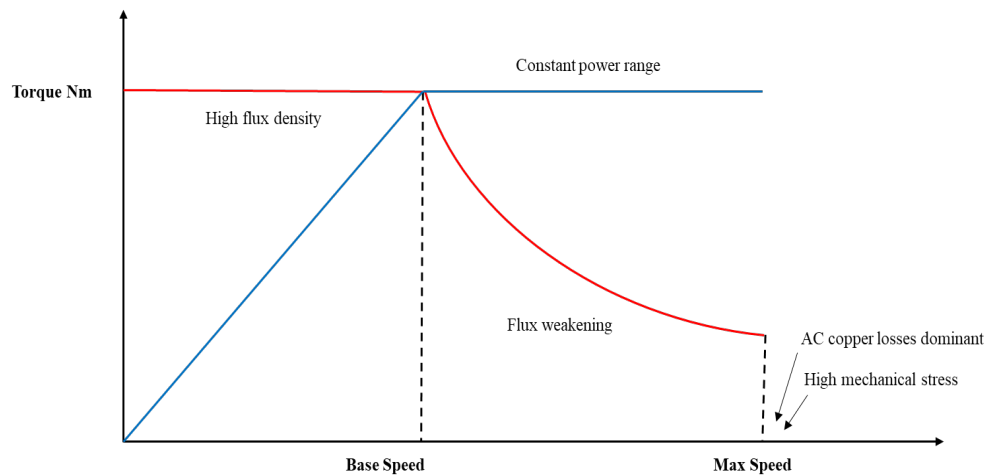


Figure 2-4 Schematic of torque-speed characteristic of electric vehicles

- High torque density and power density over a wide speed range.
- A wide constant power/speed range 3-4 times the base speed.
- The motor must operate as efficiently as possible at all operating regions to extend the span of the battery.
- Reduced torque ripple and audible noise.
- High reliability and good fault tolerance characteristics.
- Overloading capability for short time.
- Reasonable cost.

2.6 Key differences between electric MHDVs and light-duty electric vehicles (LDEVs) in their design and operational capacities

To successfully commercialize electrified MHDVs, innovation must extend beyond adapting light-duty electric vehicle technology which is designed for passenger cars. The significant differences between MHDVs and LDEVs present unique research and development challenges that need addressing to advance the electrification of the commercial vehicle sector. Overcoming these challenges and customizing technology to meet MHDVs specific needs are crucial for their market success. The critical differences between electric MHDVs and LDEVs encompass several key aspects[10]:

1. **Durability of components:** Components in heavy-duty vehicles must be significantly more robust than those in light-duty vehicles. Heavy-duty vehicles are designed to last over 1 million miles with an average operational life of about 14 years. Heavy-duty vehicles operate under challenging conditions, this requires parts that can withstand more intense usage and longer wear and tear.
2. **Power and energy requirements:** Cost-effective freight movement relies on high-powered vehicles that need up to double the horsepower and five times the energy compared to lighter vehicles. MHDVs require more energy for propulsion and braking, ranging from 500 to 5200 Wh/mile, which is significantly higher than the 250 to 400 Wh/mile typical of light-duty vehicles. This is largely due to their larger mass, payload capacity and diverse operational conditions.
3. **Vehicle weight and powertrain strain:** MHDVs can support GVWs of up to 80,000 lb, which places a higher strain on their powertrains compared to light-duty vehicles.
4. **Battery size and range:** MHDVs need larger batteries, currently up to 660 kWh and potentially exceeding 1,200 kWh, to match the range that engine-powered trucks achieve.

5. **Charging infrastructure requirements:** The fast charging requirements for electric MHDVs greatly exceed those for LDEVs, highlighting the need for more robust charging infrastructure capable of delivering over a megawatt to accommodate these vehicle's needs.

2.7 Examples of traction machines equipped in heavy-duty vehicles

Table (2-3) showcases a selection of traction machines available in the market that are used in heavy-duty vehicles with electric traction systems[10, 34]. It clearly shows that the motors equipped are induction machines (IMs) and PM machines. As seen in Table (2-3), high torque (over 1000 Nm) is represented this is attributed to the high vehicle weight in heavy-duty vehicles.

Table 2-3 Available electric machines used in heavy-duty vehicles

Manufacturer	Electric Machine Type	Peak Power (kW)	Peak Torque (Nm)
BYD k11	AC Synchronous Motor	2×180	2×1500
Allison EP 50/40	IM	150	-
BAE Series E	IM	200	5200
BAE Series ER	IM	230	6400
BorgWarner-Remy	PM	300	-
Zytek continental	PM	170	-
Volvo	PM	185	-
Oshkosh	PM	300	

2.8 Heavy-duty power/torque profile

The power/torque requirement of the traction motor for the heavy-duty trucks that will be designed in this thesis, is shown in Figure (2-5), it is provided by Cummins. It is evident that the peak power/torque is more than that of 4-wheel passenger cars. The requirement for high peak torque at base speed, being 526 Nm, necessitates a substantial current leading to an increased thermal load. Furthermore, achieving a maximum speed of 15000 rpm places greater mechanical stress on the system.

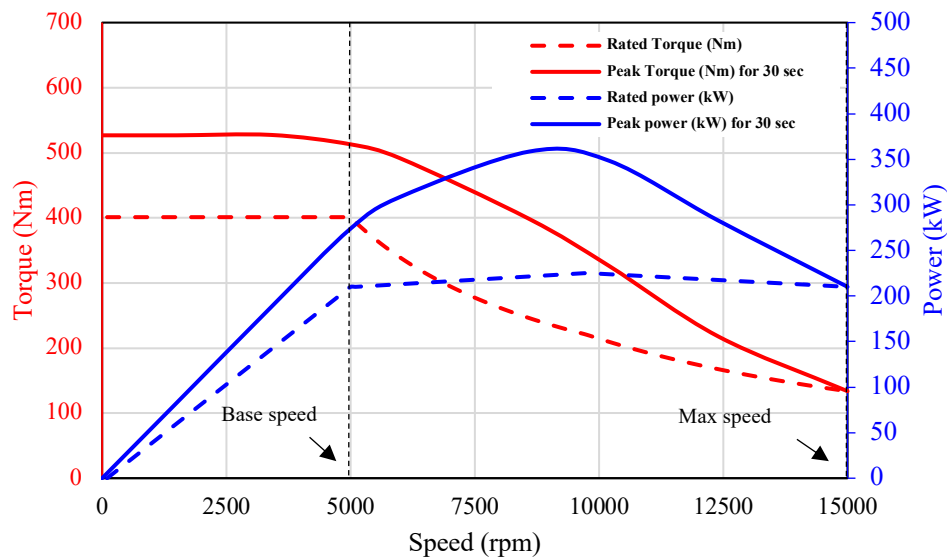


Figure 2-5 Torque/power requirements of a heavy-duty truck from Cummins

2.9 Summary

This chapter provided a comprehensive review on EVs, with a focus on heavy-duty trucks. Vehicles in Class 7 and 8 are heavy-duty vehicles. They have a gross weight (over 26,001 lbs.). The configurations of EVs are presented as follows, BEVs, FCEVs, HEVs and PHEVs.

BEVs and FCEVs have zero tailpipe emissions and are the optimum configuration to alleviate the climate change issue. Nevertheless, there are difficulties related to energy storage. Since BEVs depend solely on batteries for their energy configuration, this reliance imposes a limitation on the driving range of such vehicles, the capacity of the battery dictates the driving range and large battery packs are required to extend the driving range. FCEVs have hydrogen cells as the power unit, the lack of infrastructure of hydrogen refueling stations and the low power density of FCEVs limited the widespread of this configuration. HEVs are a solution to reduce the size of the battery in EVs, in this configuration ICE is used with an electric motor to propel the vehicle and extend the driving range. However, zero tailpipe emissions is sacrificed in this configuration. PHEVs an updated version of HEVs, have a plug to directly charge the battery and they use electricity as the main energy source and gasoline as secondary energy source. PHEVs can be gasoline independent for daily commuting.

Classification of different energy storages in EVs has been underlined, Li-ion batteries are the most used in modern EVs this includes both passenger cars and MHDVs, due to their high energy density. Current solutions to enhance the energy storage in EVs involve combining two energy sources Li-ion batteries with UCs, UCs have a higher power density compared to lithium-ion batteries. EV chargers can be categorized into three types: slow, semi-fast, and fast. Slow and semi-fast chargers are typically located on-board the vehicle, while fast chargers are commonly found at commercial charging stations. Fast chargers, are equipped with a DC source and expected to become the predominant charging system for electric MHDVs.

The core technology of EVs is the traction motor that converts the electric power to the required mechanical output power. The design of electric machines for EVs is associated with strict requirements such as, high power to mass ratio, wide speed range, high efficiency, low torque ripple, fault tolerant characteristic, overload capability and reasonable cost. The performance of the traction machine is important to extend the lifespan of the battery. The traction motor must operate at high efficiency.

Finally, this chapter briefly presents various traction machines used in heavy-duty trucks. It introduces the torque/power profile of the required traction machine provided by Cummins for the heavy-duty truck application, which will be designed in this thesis. The following chapter will provide a thorough review of different electric machines to identify the best traction machine that fits the specific requirements of heavy-duty truck applications.

Chapter 3. Overview on Machine Topologies and On-Board Traction Machine Integrated Battery Chargers

In this chapter, a comprehensive review of traction machine topologies is conducted. The advantages and disadvantages are highlighted. As it has been introduced this thesis is concerned with the design of a traction machine for a heavy-duty truck. Given the strict power and speed requirements for this application, this chapter aims to determine the most suitable topology.

3.1 Introduction

The propulsion system in EVs is a core technology as it converts the power received from the power inverter into desired mechanical power. Traction motors for EVs require a set of specifications as listed in [35], which include high power, wide speed range, high torque, moderate cost, low noise and compact size. Among the different types of electric motors used for electric traction, there are four major types: DC machines, IMs, Synchronous machines, Switched reluctance machines (SRMs). This chapter explores different motor topologies to identify the best topology that suits the heavy-duty truck.

3.1.1 DC machines

DC motors, either series-excited or separately-excited were widely accepted in electric traction due to their simple control, the use of moderate cost choppers and their outstanding performance [35]. Separately-excited DC motors suits the application of EVs due to the decoupled torque and flux providing excellent field weakening [36]. The power density of a brushed DC motor can be improved by replacing the field windings with high energy PMs as shown in Figure (3-1) resulting in high efficiency and power [37]. However, they suffer from torque ripple caused by the commutator which then will limit the motor speed. Its maintenance is highly needed due to wear and tear of the commutator and brushes making them less reliable. Less reliability and high maintenance demand made brushed DC motors no longer attractive for modern electric traction applications [35, 38].

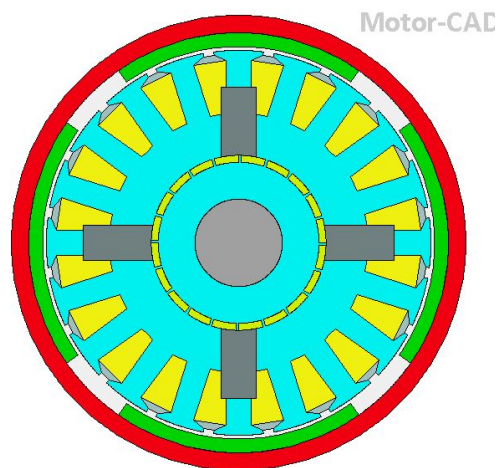


Figure 3-1 Brushed PM DC machine

3.1.2 Induction machines (IMs)

Among all types of electric machines, IMs shown in Figure (3-2) are found in many on-road EVs. A recent example is the Tesla Model S that uses an IM in its drivetrain, the motor is rated at 225kW and has a maximum speed of 15000 rpm[39]. Its rugged construction, moderate cost, low maintenance and high reliability made IMs a good candidate to be used in electric traction [40]. However, due to the non-linearity of the dynamic model of IMs using conventional control strategies such as variable voltage variable frequency are not able to afford the needed performance [38]. Vector control is needed to overcome their nonlinearity hence; a good torque control is achieved by using vector control or direct torque control [41]. A well-designed IM with vector control can reach a flux weakening range 3-5 times the base speed e.g., spindle motor. However, the occurrence of breakdown torque is an obstacle to extend the constant power operation resulting in an oversized motor [42]. The current induced in the rotor of the IM causes copper losses which increase the rotor temperature, it is difficult to cool down a rotating circuit compared to a stationary circuit (windings in stator). Using a copper rotor cage instead of aluminium cage is a method to push the boundaries of IM performance[43]. Nevertheless, IMs are less competitive to PM machines because of their low continuous power/torque density, low power factor and low efficiency at low speed making them less desirable for application requiring high torque density and high-speed range.

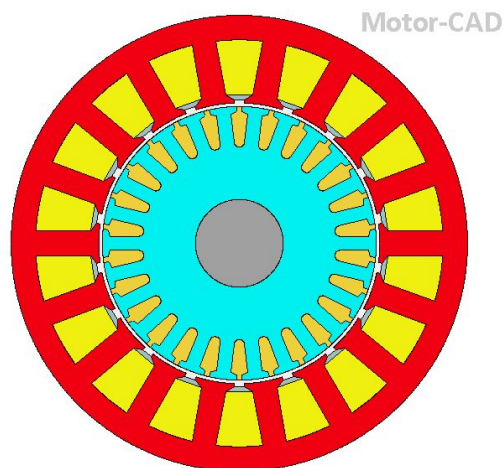


Figure 3-2 Induction machine (IM)

3.1.3 Switched reluctance machines (SRMs)

SRM shown in Figure (3-3) has a potential to be used in the electric traction applications because of its method of operation which is inherently fault tolerant due to low cross-coupling between phases only one phase is energised at a given time. Besides, it has a wide power range making it suitable choice for high-speed applications such as, EV applications. The mechanical construction of SRMs is robust the rotor is simple containing no magnets and copper making the cost low and low maintenance is needed. The windings layout in the stator are concentric with short end windings therefore, SRMs have reduced copper losses and better thermal characteristic.

SRMs struggle with low power factor and torque/power density due to their high inductance. This results in significant reactive power and less efficient performance compared to PM machines and IMs [44]. The control of SRMs is more complex compared to a 3-phase machine due to the electromagnetic behaviour i.e., inductance and flux linkage are highly non-linear because of magnetic saturation. A lot of connections are required to connect the motor with the inverter. Issues such as torque ripple, acoustic noise and core losses needs improvements. Control techniques have been carried out to minimize the torque ripple such as indirect torque and direct torque control. A 40kW SRM is shown in [45] it has high torque density however, the efficiency is low. The Land Rover 110 Defender model represents a successful attempt at using a SRM in a HEV drivetrain. It is powered by a Li-ion battery with a capacity of 27kWh and produces 70kW of mechanical power [46]. SRMs have been used for a few EVs due to its disadvantages that needs to be improved [47, 48].

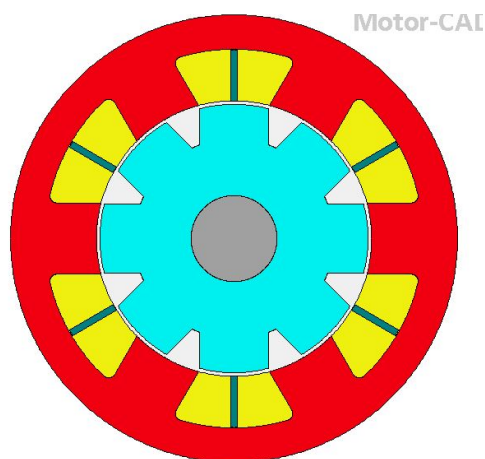


Figure 3-3 Switched reluctance machine (SRM)

3.1.4 Wound field synchronous machine (WFSM)

The WFSM shown in Figure (3-4), exhibits significant advantages such as its rotor is free from PMs thus, it has a low cost. Two electric circuits are employed and excited separately in the stator and rotor. It works on the principle of field synchronizing between the stator and rotor. The rotor being supplied by a separate source gives an advantage of easily controlling the rotors field in the field weakening region. However, the main challenge is the added weight from the rotor field source, brushless exciter and rotating transforming[49]. An example of WFSM is used in the Renault Zeo EV[50]. The extra copper losses in the rotor puts a burden on the thermal aspect. The separate direct current (DC) source and the brush and slip ring system to transfer the excitation current to the rotating field winding makes the design more complex, this is why WFSMs haven't seen a widespread in the EV market. PMs are a solution to replace the field winding as in the following section[51].

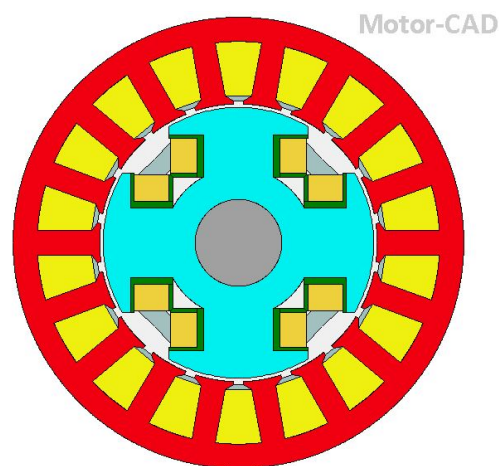


Figure 3-4 Wound field synchronous machine (WFSM)

3.1.5 Permanent magnet machines (PM machines)

The trend in recent years is to use PM machines in the transportation sector due to the advancement in power electronics and new control techniques [52]. PM machines are competitive to other types of machines owing to their attractive features including high torque density, high reliability and excellent performance. The absence of the rotor windings reduces the cooling requirements, the motor is efficient, light weight and runs at low temperature. The main drawback of PM motors is that they have a narrow power range due to the use of high energy PMs which makes it difficult to weaken the air gap flux. However, by implementing the field weakening method by opposing a negative d-axis current by (a certain amount limit to avoid demagnetization of the magnets) to weaken the magnetic flux its speed range can be improved 3-times the base speed. Moreover, PM motors face some problems like demagnetization of PM and its high cost [53]. EV applications require a wide speed range with high output power therefore applying field weakening technique for such applications is essential.

PM brushless drives can be divided into two groups, based on the type of current fed into the stator windings: namely, sinusoidal brushless AC (BLAC) PM machines and trapezoidal brushless DC (BLDC) PM machines. The following section shows PM machine topologies that are viable for traction applications: Radial PM machines.

3.1.6 Radial flux permanent magnet (RFPM) machines

The structure of the RFPM machines comes with high energy PMs into the rotor or attached to its surface. The position of the PMs determines the configuration type therefore, RFPM machines are categorised to surface mount PM (SMPM) machines and interior PM (IPM) machines [38, 52-55];

3.1.7 Surface mount permanent magnet (SMPM) machines

SMPM machines are widely used in industry due to the advantage of their simplicity. SMPM machines have PMs on its rotor laminations as shown in Figure (3-5). Therefore, its magnets directly face the air gap providing high air gap flux density. On the downside, the rotor mechanical integrity is low due to its structure beside that the physical air gap width which contains on both the designed air gap of the machine and PM thickness leading to low phase

inductance and the magnets can be demagnetized due to its exposure to the armature field. The torque produced by SMPM machine is a magnetic torque with no reluctance torque due to the small variation between the direct axis and quadrature axis inductances. The arrangement of this kind of PM machine makes it less attractive for high-speed applications because of the position of the magnets which require a sleeve to maintain the PMs when exposed to high forces.

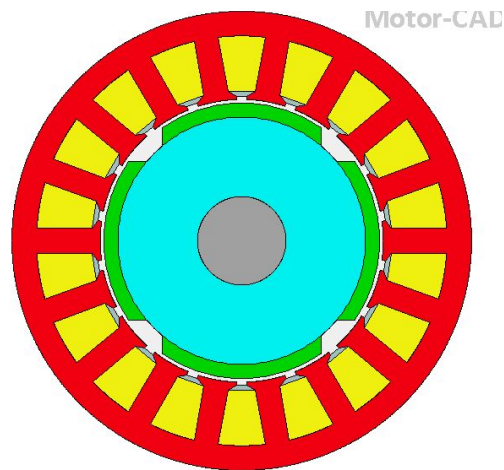


Figure 3-5 Surface mount PM machine

A 10-pole 12-slot double-layer fractional slot concentrated winding (FSCW) shown in Figure (3-6) was designed in [56] to meet the FreedomCAR 2020 targets. It is shown that this topology is able to meet several of the challenging targets. It has been reported that significant improvements in terms of full load power density and efficiency compared to the state of art machines.

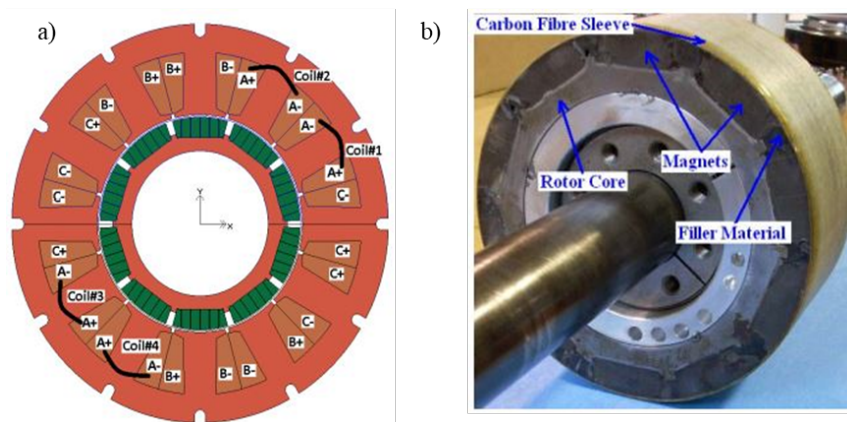


Figure 3-6 a) 10-pole 12-slot SMPM machine b) SMPM rotor [56]

3.1.8 Interior PM (IPM) machines

The PMs are embedded into the rotor laminations in a radial orientation as shown in Figure (3-7). This kind of construction is called interior PM machines. The placement of the PM into the rotor provides a robust mechanical structure that is appropriate for high-speed applications like EVs. IPM machines have the advantages of utilizing the reluctance torque due to the difference between the q-axis and d-axis thus, torque is a combination of reluctance torque and magnetic torque. Furthermore, the variation between the d-axis and q-axis facilitates extending the speed range due to field weakening ability.

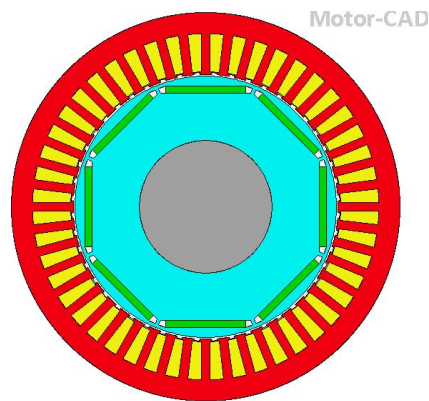


Figure 3-7 Interior PM machine

Different vehicle automakers such as Toyota, Lexus, Nissan, Ford and Chevy Volt have incorporated a PM machine in their drivetrain shown in Figure (3-8). The evolution of the rotor configuration for the famous Toyota Prius is shown in Figure (3-8) [57-60].

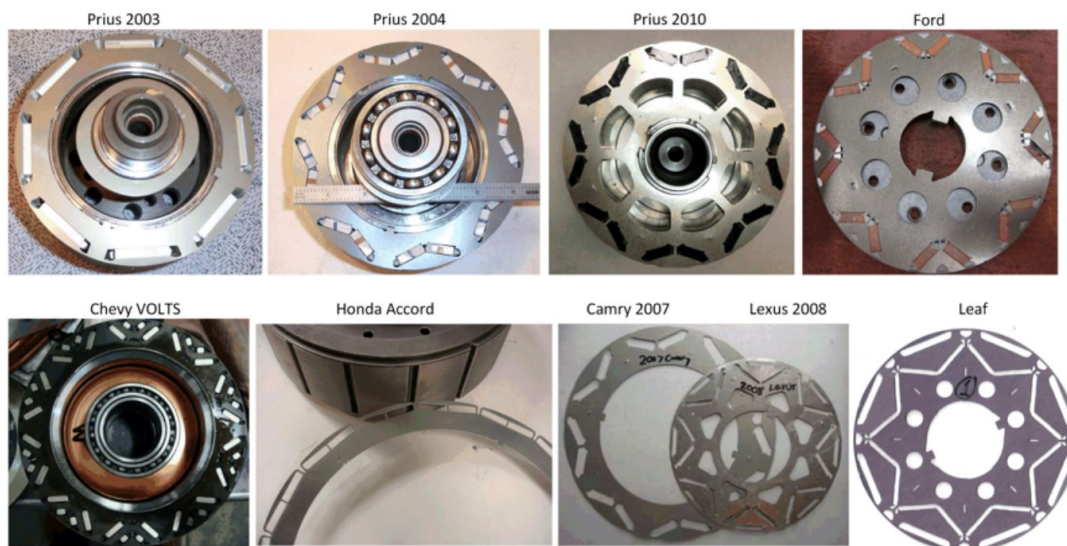


Figure 3-8 Evolution of PM rotors in EVs[57]

3.1.9 Radial flux machines with PMs in the stator

One method of situating PMs involves embedding them into the stator's back iron width. Radial flux machines with PMs embedded into the stator can be divided into three types based on PM placement [55];

- High energy PMs inserted into the lamination of stator back iron width known as doubly salient permanent magnet (DSPM) machines shown in Figure (3-9): in this configuration the three-phase machine requires a magnet for every three teeth and four phase machine requires a magnet for every four teeth. Its rotor is similar to the rotor of SRM, it is mechanically robust and able to operate at elevated speeds. The inserted magnets in the stator core constitute a high reluctance path for the main flux path of armature reaction flux. The importance of the magnets is to sustain the magnetization and demagnetization of the stator flux and to maintain a constant flux density in the air gap. At no-load, no cogging torque is produced this is due to the constant air gap reluctance seen by the inserted magnets with respect to rotor position. DSPM machines gives a trapezoidal back-EMF therefore it is more appropriate for BLDC operation. However, with rotor skewing a sinusoidal back-EMF can be obtained. The torque in DSPM machines is pulsating torque, therefore for applications where torque quality is critical this topology is not a suitable option[61]. In comparison to other PM topologies the DSPM machine has a lower torque density due to its unipolar flux linkage[62].

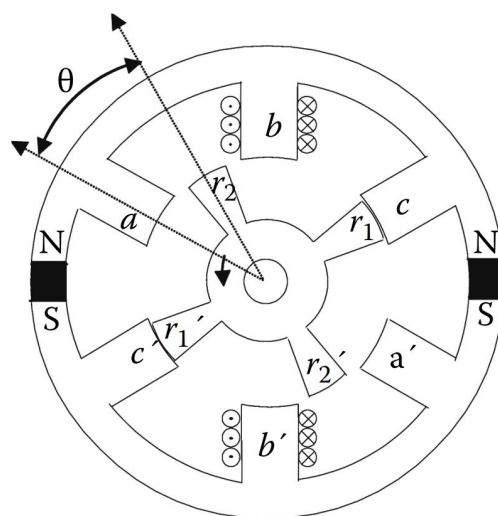


Figure 3-9 DSPM 4-pole machine[55]

- PMs inserted into the lamination of the stator tooth shoes known as flux reversal machines (FRMs) shown in Figure (3-10): in this topology each stator tooth has a pair of PMs with opposite polarity inserted in its shoes. The type of the machine winding is a tooth wound layout. In terms of its operation, when a coil is excited, the field produced by first magnet is reduced while for the adjacent magnet the field is increased causing the rotor to align itself with the strongest magnetic field. The winding inductance is low due to that the permeability of magnets is nearly equal to air, so there is a big reluctance. The flux linkage variation is bipolar, and the back-EMF is trapezoidal. The PMs are vulnerable to high temperature; hence the residual flux density of the magnets will decrease. Additionally, due to the placement of the magnets and half of them are in effective use, the air gap flux density is limited by the PMs field therefore, the torque density is compromised by the magnets [63, 64].

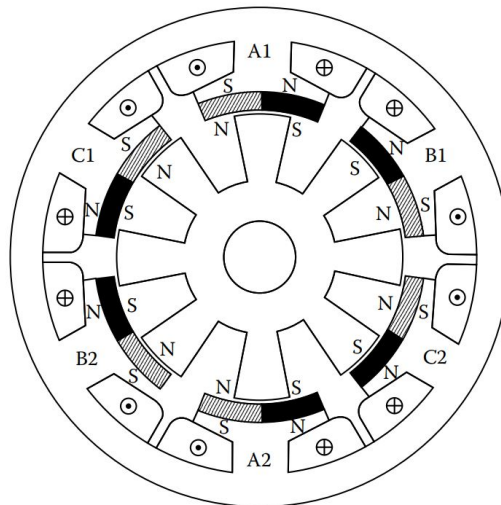


Figure 3-10 6-Pole FRM[55]

- PMs sandwiched in the stator teeth as shown in Figure (3-11) are known as flux switching PM (FSPM) machines, each stator tooth is inserted by a PM, the magnetic direction is reversed from one tooth to the next tooth. The electric loading can be very high due to the influence of the armature reaction that is minimal on the magnets working point. This topology has high torque density compared to DSPM, due to the benefit from high electric loading. FSPMs are suitable for BLAC operation because of its sinusoidal back-EMF and are appropriate for wide speed range because of the ability to achieve high winding inductance [65]. In [62] it is shown that FSPM machines have better merits than the DSPM machines.

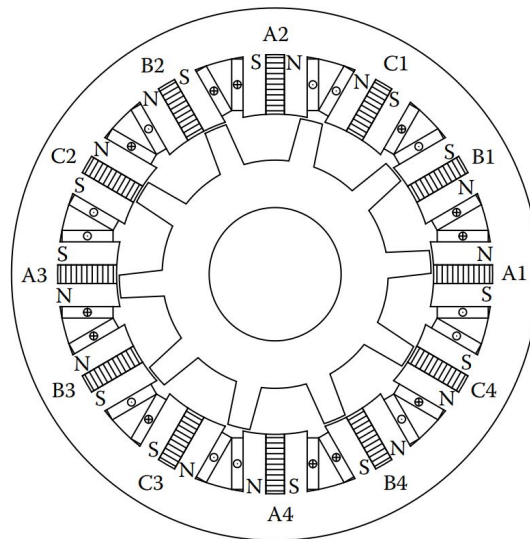


Figure 3-11 FSPM topology[55]

3.1.10 Synchronous reluctance (SynREL) machines

SynREL machines run at synchronous speed and are reluctance-based machines. The stator of SynREL machines is identical to that used in IMs and in synchronous PM machines. The rotor is designed with iron segments called bridge and has no windings as well as its free from PMs as shown in Figure (3-12). SynREL machine is gaining a lot of interest in automotive applications owing to their advantages: Its rotor consists of soft magnetic material with no magnets, the absence of field windings and high energy PMs led to low temperature and operate at high speed. The absence of PM material contributes to reduce its cost. SynREL motors are fault tolerant as the rotor has no flux when the stator winding is not active. It's able to provide the same features that an IM can deliver. The control of SynREL motors is easier than the control of IMs. However, SynREL motors suffer from low power factor, thus large inverters are needed to achieve good power factor, leading to the use of large motor drives.

In [66], a comparison between IM and SynREL machine for a railway application , reveals that IMs exhibit higher torque capabilities , better power factor and higher output power at high speeds. In order for SynREL motor to be highly accepted in automotive applications there are aspects that needs to be improved such as design and control techniques as well as manufacture problems, especially for high-pole count [67-69].

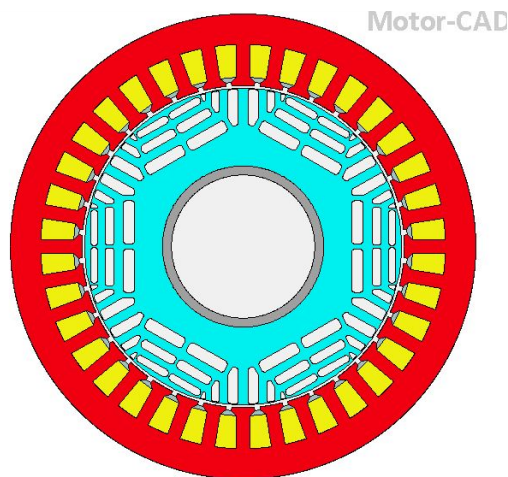


Figure 3-12 SynREL machine topology

3.1.11 Permanent magnet assisted synchronous reluctance (PMA-SynREL) machines

SynREL motors suffer from poor power factor. Several researchers have examined the use of PMs into the rotor flux barriers in order to saturate the iron bridges and improve the power factor which is generally low. The resulting construction is called PMA-SynREL machine shown in Figure (3-13). Small amount of high energy PMs are used compared to that used in IPM machines. By inserting the suitable amount of PMs excellent efficiency can be achieved with reasonable back-EMF. The torque is a combination of reluctance torque and magnetic torque therefore the torque density is improved compared to pure SynREL motors. The type of magnets accommodated in the rotor slots will determine the power/torque density of the PMA-SynREL machine. Generally, neodymium magnets are used this will not only improve power factor but the power/torque density is improved compared to SynREL machines. Cost wise PMA-SynREL machines are less expensive than IPM and SMPM machines due to the utilization of less magnets[70]. High temperature and demagnetization of PMs are major obstacles in IPM machines when the motor is overloaded, however PMA-SynREL motors are free from these problems [71-74].

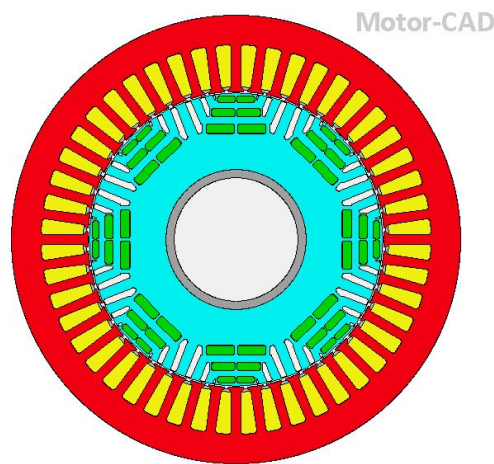


Figure 3-13 8-pole PMA-synREL machine

3.1.12 Axial field machines (AFMs)

Machines that have flux flowing parallel with the direction of the shaft are referred to as AFMs [55]. Applications that have limited space finds AFMs a suitable topology. Radial field machines (RFMs) can be constructed to exhibit an axial field such as SMPM and IPM machines. An example of an AFM was designed in [75], the motor was sized based on the same dimensions of the Toyota Prius machine which has an IPM machine. The results show that an AFM has an output torque twice of its radial machine counterpart. Although this was at half speed. AFMs are in different topologies, namely single-stator with single-rotor, double-sided stator with a rotor, and a double-sided rotor with a stator as shown in Figure (3-14). The radial dimension for an AFM is not changed with the increase in the number of poles, which makes this topology advantageous in applications that require high speed high torque. Axial forces are present between the stator and rotor in the single-stator single-rotor configuration however, this issue is eliminated in the double-stator single-rotor and double-rotor single-stator. In AFMs slotless stator is preferred to slotted stator due to the difficulty of the manufacturing process. The PM quantity in AFMs is large, to produce the air gap flux density required. High torque density is a feature of AFMs however, they suffer from limited constant power range due to small inductance for a wide effective air gap. RFMs are superior in terms of construction to AFMs [53, 76].

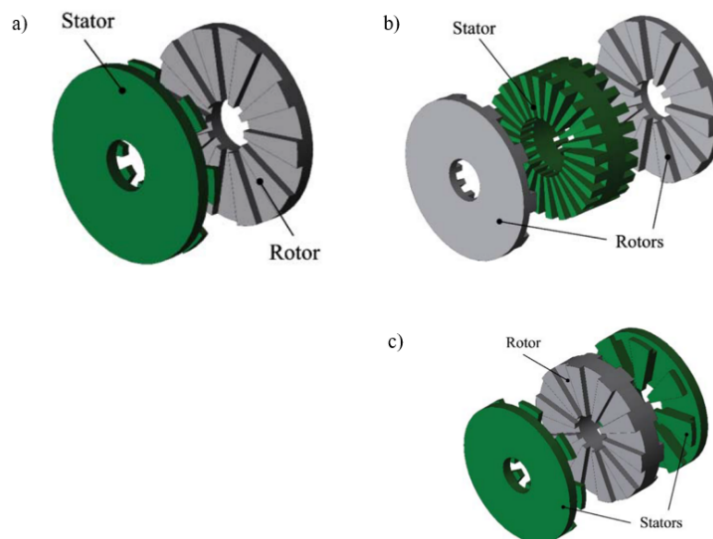


Figure 3-14 (AFMs) a) single-rotor single-stator (b) double-sided rotor and single-stator and (c) double-sided stator and single-rotor[13]

3.1.13 The transverse flux machines (TFMs)

TFM shown in Figure (3-15), has a three-dimension flux path, therefore its structure is complex and costly. Each phase winding is accommodated in an independent module, this increases the fault tolerance of the machine. Due to the ring-shaped coil, it has a reduced length compared to RFMs, thus lower resistive losses. TFMs can have high number of poles that interact with the armature flux yielding high torque density. The electric and magnetic design parameters in this topology are decoupled, hence large coil cross section can be achieved. TFMs in rotation have some magnets not aligned due to its small mechanical pole pitch hence, a reduction in the total magnet flux. Moreover, leakage flux leads to increasing the machine losses. The structure of the TFMs is complicated and the motor has poor power factor due to large inductance, consequently, requires an overrated power converter [53, 77-81].

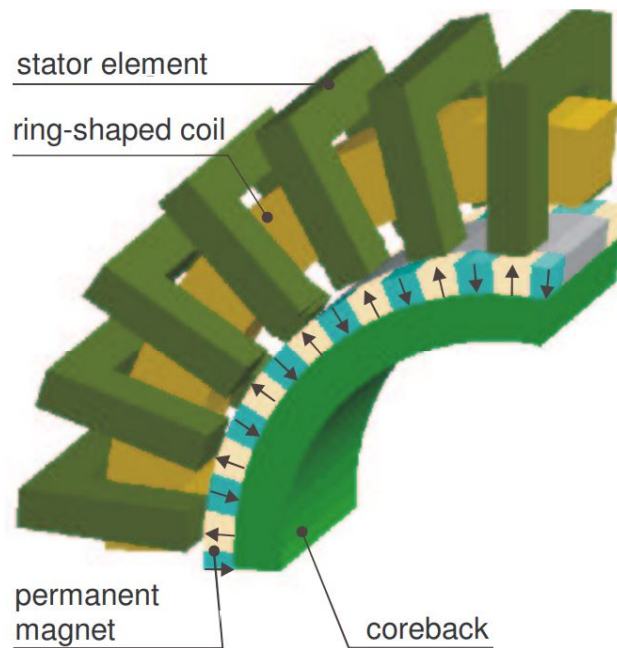


Figure 3-15 TFM topology[79]

A comparison has been carried out between RFMs, AFMs and TFMs. It has been noted that the RFMs are superior in performance and construction[82].

3.2 Comparison of IPM machines with different motor topologies used in HEVs

This section will give a quantitative comparison of an IPM machine with an IM and a SRM based on the results in [83]. Researchers have been motivated to explore and compare different topologies. PM machines are the optimal selection to be implemented in an automotive application due to their superior electromagnetic performance. Table (3-1) highlights the geometry dimensions differences between the topologies. It can be seen from Table (3-1) that the stator outer diameter and the axial length are fixed for a fair comparison. The SRM has the lowest rotor weight due to the absence of copper and magnets from its rotor. On the other side, IM has the highest copper weight. The IPM machine has a higher cost than the SRM and IM due to the use of PMs. On the other side, SRM has the lowest cost due to its rotor that has no copper.

Table 3-1 Comparing parameters of IPM, SRM and IM

Parameter	Unit	IPM	SRM	IM
Stator Outer Diameter	mm	269.0	269.0	269.0
Rotor Outer Diameter	mm	160.5	170.0	180.0
Rotor Inner Diameter	mm	111	111	111
Air gap length	mm	0.73	0.3	1.5
Number of Poles	-	8	12	8
Stack length	mm	84	84	84
Stator Lamination weight	kg	18.65	14.11	11.86
Rotor Lamination weight	kg	5.22	5.16	6.15
Armature Winding weight	kg	5.99	7.44	10.57
Rotor copper/magnet Weight	kg	1.3	-	7.67
Total weight	kg	31.6	26.7	36.25
Steel Cost	\$	31.03	25.05	23.41
Copper Cost	\$	39.53	49.10	120.38
Magnet cost	\$	171.60	0	0
Total Cost	\$	242.17	74.16	143.80

Table (3-2) illustrates that the PM machine outperforms its counterparts at 1500 rpm, producing the most significant torque, best efficiency and minimum current density. However, the PM machine's torque generation reduces in comparison to the other two machines at 6000 rpm. This is due to a decrease in torque within the constant power region as speed increases. Observations from the data clearly demonstrate that at 1500 rpm, copper loss resulting from the high current density is the dominant form of power dissipation across all machines. Conversely at (6000 rpm), iron loss becomes more significant due to the increased frequency. IM owing to the presence of copper winding in both the stator and rotor, suffers from particularly high copper loss. On the other hand, SRM is characterized by substantial iron loss arising from the increased flux frequency.

Despite the SRM showing the highest torque density (due to high number of poles) it is not the ideal choice for EVs due to its drawbacks such as torque ripple and acoustic noise. The PM machine, however, stands out as an optimal option for EVs.

Table 3-2 Performance comparison at (a) 1500 rpm and (b) 6000 rpm

(a) Speed: 1500 rpm					
Topology	Torque (Nm)	Copper loss (W)	Iron loss (W)	Efficiency (%)	Current density (A/mm ²)
IPM	303	4328	198	91.3	15.7
IM	297	8591	148	83.1	15.8/12.1
SRM	294	7653	404	85.2	20.1
(b) Speed: 6000 rpm					
IPM	45.6	219	953	96.1	3.75
IM	50.8	730	439	95.2	4.51/3.72
SRM	52.1	306	4074	88.2	4.02

The following comprehensive qualitative comparison shown in Table (3-3) compares various machine topologies specifically tailored for automotive applications. Furthermore, this comparison is specifically focused on RFM, chosen for their superior performance and construction benefits. It excludes machines that require brushes and slip rings, such as DC brushed machines and WFSMs. Furthermore, machines that heavily utilize magnets, such as (IPM and SMPM) machines are omitted from this comparison. In addition, machines with PMs in the stator have been excluded due to the complexities they introduce in the manufacturing process. Acknowledging the critical importance of space, volume and notably field weakening capabilities in EV applications, this comparison emphasizes machines with superior field weakening performance. This ensures that only the topologies with the best capacity to adjust their magnetic fields under high rotational speeds are considered. Factors such as torque density, power density, power factor, efficiency and cost are also evaluated for these topologies. Each machine is assessed based on these parameters and rated qualitatively as ‘High’, ‘medium’ or ‘Low’. Topologies with insufficient field weakening capabilities are removed from consideration in this comparison.

Table 3-3 Comparing machine topologies for automotive applications

Motor type	Power density	Torque density	Power factor	efficiency	Field weakening range	Cost
IM	Medium	Medium	Medium	medium	Medium	Low
SRM	Low	Low	Low	Low	Very High	Very Low
SynREL	Medium	Medium	Low	Medium	High	Very Low
PMa-SynREL	High	High	High	High	High	Medium

The qualitative comparison presented in Table (3-3) demonstrates that SRMs and SynREL machines have low cost. This is mainly attributed to the absence of PMs and copper in the rotor. However, this results in a lower power factor for both types of machines. To address this issue, the incorporation of PMs in PMa-SynREL machines has mitigated the drawbacks associated with SynREL machines, however at a higher cost due to the use of rare-earth magnets. Nevertheless, the cost of PMa-SynREL machines remains lower compared to other PM-based machines, such as IPM machines[70]. IMs exhibit a lower cost than PMa-SynREL machines. However, they have a medium field weakening range and a medium power factor, which are crucial considerations in the design of power converters. Additionally, the

continuous torque/power density of IMs is lower compared to PM-based machines. Field weakening is an important consideration in automotive applications. SRMs have the highest range however, their torque/power density is low. PMA-SynREL machines have a field weakening range that is less than that of SRMs but with higher power/torque density.

3.3 Integrated on-board battery charger

A critical component in the EVs drivetrain is the battery. When comparing EVs battery charging with its ICE vehicle counterpart refuelling stations are widely available for customers whereas battery charging stations are sparsely distributed. Therefore, battery charging for EVs is a potential concern for its customers. Another potential concern is the charging time that takes to charge up the battery, ICE vehicles refuelling process requires minutes to finish[84].

EVs batteries can be charged using two charger types namely off-board chargers and on-board chargers [85]. Off-board chargers are available at special stations whereas, on-board chargers are available anywhere and can be connected directly to a single-phase and three-phase mains. The power flow in both types can be unidirectional or bidirectional. The unidirectional power flow charger has a simplified interconnection with the grid with reduced hardware requirements. On the other hand, bidirectional power flow chargers allow the batteries energy to be injected back to the grid [85, 86].

On-board battery chargers shown in Figure (3-16) have drawbacks on the vehicle when compared with off-board battery chargers it adds more weight, volume and increases the price of the EV. However, on-board battery chargers have a salient merit which it doesn't require an expensive infrastructure [87]. There are two types of on-board battery chargers conductive and inductive chargers. The conductive charging happens on-board with a wire directly connected to the outlet whereas, inductive chargers have a section of the charger off-board and uses the principle of magnetic power transfer therefore, it doesn't require a wire[88]. On-board battery chargers have lower power rating than that of off-board chargers. In order to increase the power rating of on-board battery charger's extra components are required resulting in more weight, cost and volume [89]. This issue can be solved by integrating the charging unit with the existing drivetrain equipment's power electronics and electric motor. This integration leads to reducing additional weight, cost and volume [90]. On-board integrated chargers are classified into slow charging (single-phase) and fast charging (three-phase) [91].

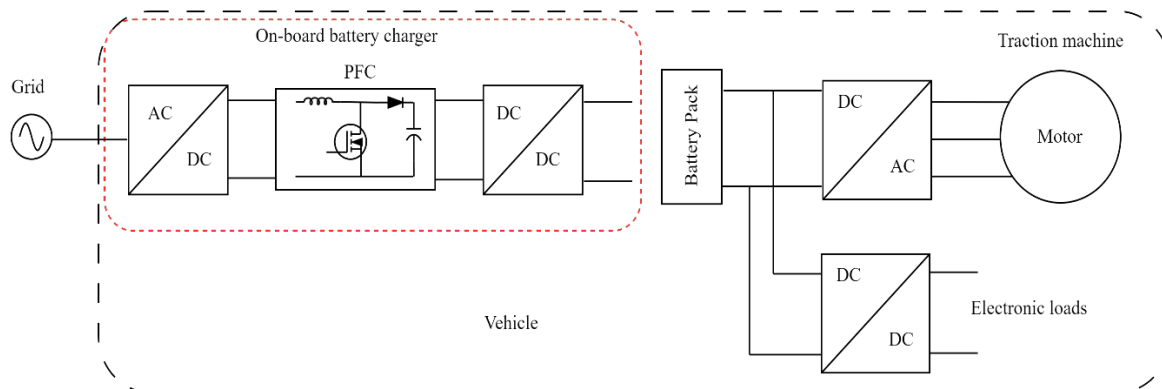


Figure 3-16 On-board battery charger

A single-phase on-board integrated battery charger topology is presented in Figure (3-17) it is composed of two three-phases IMs driven by two separate voltage fed inverters and a bidirectional dc power source (battery). During the charging mode, a single-phase power supply is connected to the motor neutral ports. This topology has the advantage of zero torque in the charging mode, it can use a single motor with two sets of three phase windings. The utilization of a bidirectional dc power source provides the ability of battery energy being injected back to the grid. Another feature of this topology is the transmission and mechanical differential is not required[92]. Hence, the provided topology has a drive system and a battery recharge system that are optimally integrated leading to elimination of additional cost, weight and volume.

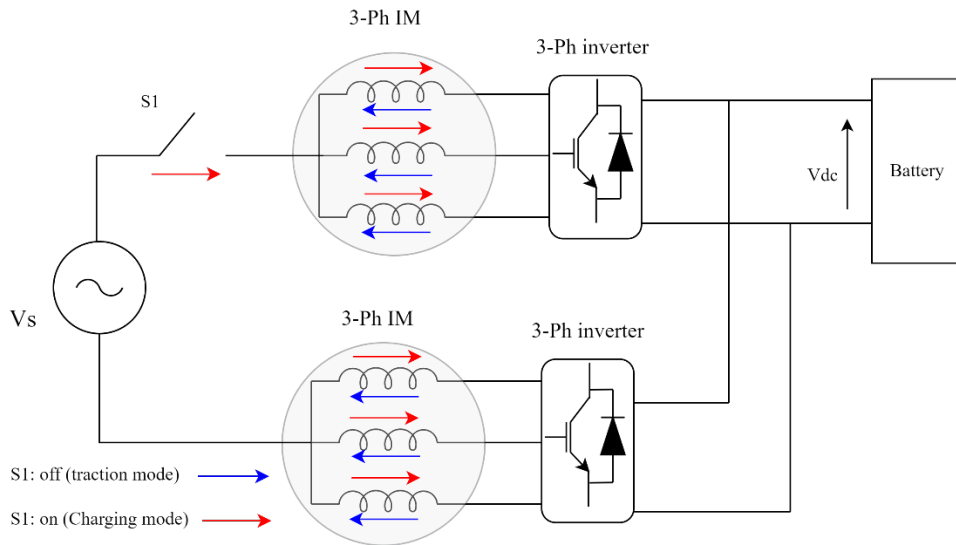


Figure 3-17 Integrated on-board battery charger using two IMs windings

Another single-phase on-board battery charger is shown in Figure (3-18) the drivetrain of this topology is consisted of an IM for the traction function and is driven by a 3-phase conventional inverter that is connected to a battery. The battery consists of 28 lead acid batteries connected in series and each battery is 12 volts, therefore the battery has a nominal voltage equal to 336volt. A filter capacitor is connected across the terminals of the battery so as to damp the voltage transients in both modes traction mode and charging mode. The supply peak voltage can be any value that is lower than the battery voltage so that unity power factor is achieved. The line filter shown in Figure (3-18) connected across the supply terminals is to smooth the line current harmonic distortion.

In the charging mode, the IM windings are reconfigured by means of relays, S2 and S3 are closed while S1 is open. Motor windings will be used as inductors in the charging circuit, phase 2 and phase 3 with inverter are controlled using pulse width modulation PWM to perform as a boost converter. In the traction mode, S2 and S3 are open and S1 is closed and the three-phase IM will be driven by the inverter. This topology allows the battery to be discharged back to the grid, periodic discharging of the battery will lead to improving battery capacity over its life cycle[93].

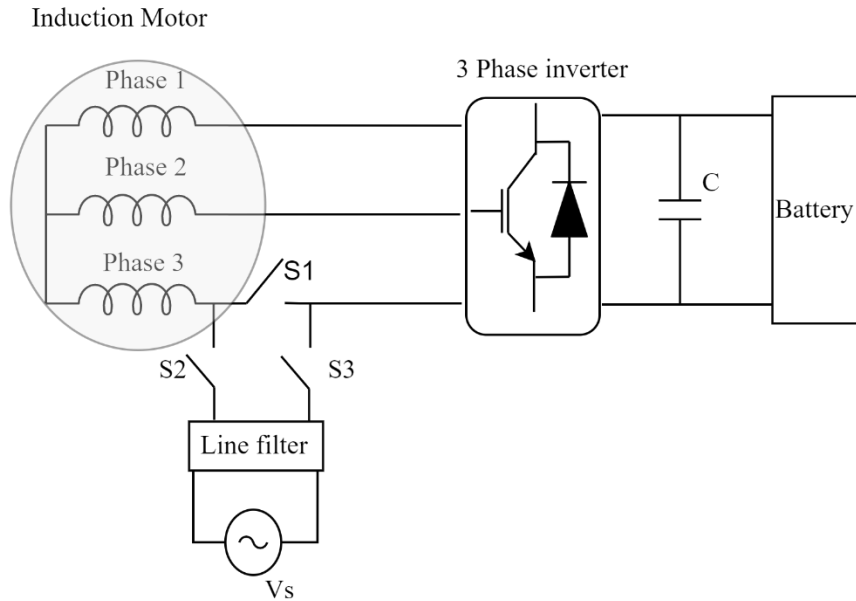


Figure 3-18 Integrated on-board battery charger by reconfiguring one phase of an IM

Figure (3-19) demonstrates a four-wheel drive vehicle equipped with a single-phase on-board integrated battery charger. This topology consists of four 3-phase IMs, each driven by a dedicated inverter connected to the battery. A transfer switch is employed within this topology to alternate between charging and traction modes.

In charging mode, the single-phase power supply is connected to the neutral ports of IM1 and IM2. In this context, the motor windings act as inductors in the charging circuit, converting the supply voltage to the necessary DC voltage. Thus, the inductors of IM1 and IM2 serve as a single-phase boost converter. The inverter switches are toggled on and off simultaneously, ensuring that all motor phases carry the same current. Consequently, this allows for zero torque production. While charging the battery, the transfer switch is set to S2. Under these conditions, IM3 and IM4 function as a DC/DC buck chopper, while IM1 and IM2 continue to operate as a boost converter.

In contrast, during traction mode, the transfer switch is set to S1. All four motors are then driven by their respective inverters at the required frequency. This setup allows for optimal propulsion and energy efficiency[94].

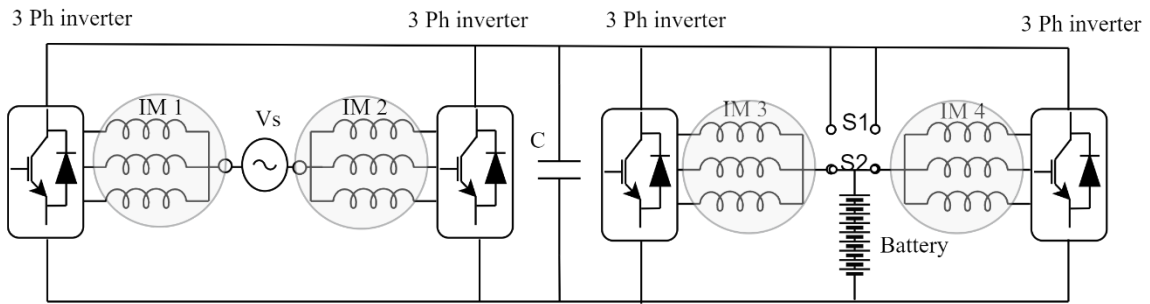


Figure 3-19 Integrated on-board charger using 4-IMs

A single-phase on-board charger shown in Figure (3-20), designed for reuse of the EV drivetrain power components, and installed on an electric scooter. The components used in this topology, include an axial flux PM motor, a three-phase inverter, a rectifier equipped with an LC filter, a filter capacitor, a single-phase supply rated at 110V AC with a frequency of 60Hz, and a 180V-12Ah lead acid battery.

During the charging process, the rectified and filtered supply voltage is converted to DC voltage. The motor inductors along with the inverter, function as a boost DC/DC converter to charge the battery. However, a drawback of this integrated on-board battery charger is the unidirectional flow, which restricts the system to slow charging[95].

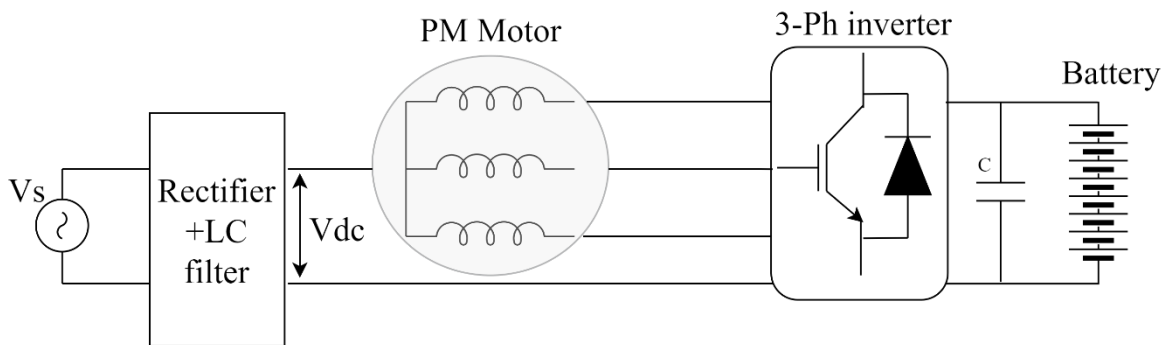


Figure 3-20 Integrated battery charger using a PM motor windings

A single-phase on-board battery charger shown in Figure (3-21), this configuration uses a four-phase SRM driven by a modified miller converter that is formed using two intelligent power modules. This electric drive has five inverter legs with an external leg that operates as a front-end dc/dc boost converter to adjust the battery voltage and only be used during traction mode. The traction mode is changed to the charging function by means of a switch. The SRM windings are reconfigured and with some intelligent power modules to arrange a buck-boost or buck-type switch mode to charge up the battery. Furthermore, power factor correction (PFC) is performed in charging mode, this topology is suitable for low-speed drives such as golf carts and electric scooters etc.[96].

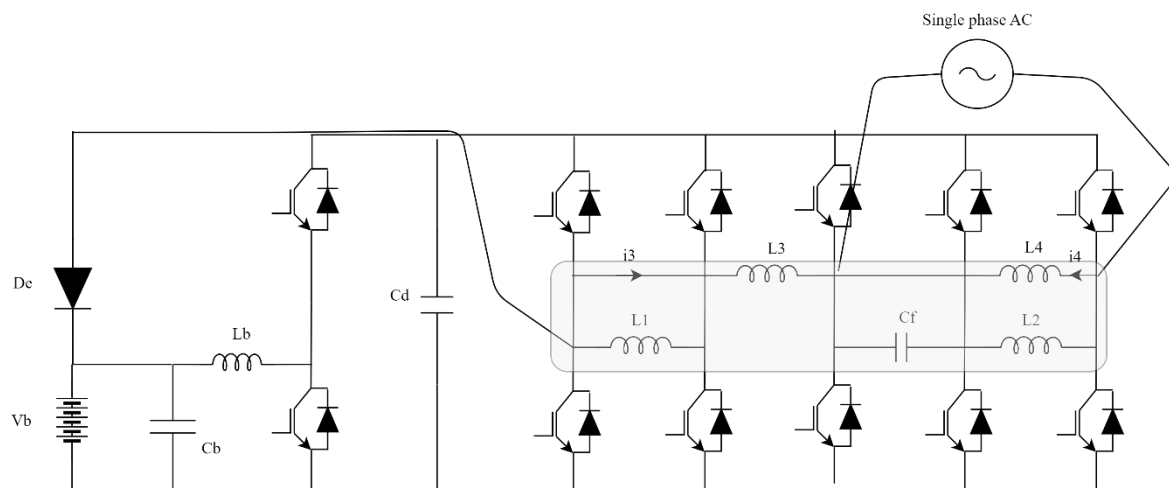


Figure 3-21 On-board integrated charger using a SRM windings

A single-phase machine integrated on-board charger with active power filter (APF) is shown in Figure (3-22). It is composed of a 3-phase SMPM motor, active power filter APF, three phase inverter, quasi-z-source dc-dc converter and battery. In the traction mode, S1 and S2 are closed, and the motor is driven by the 3-phase inverter. In the charging mode, S1 and S2 are open, and the motor windings are used as inductor filters to the grid side and connected to a single-phase supply. Moreover, the first two legs of the inverter are used as PFC while the third leg is connected with APF inductor and capacitor. Integrating an APF in the quasi-z-source rectifier circuit adds the advantage of eliminating the second order harmonic and a reduction in the charger size and weight. The disadvantage of this topology is the use of additional passive components to build the APF [86].

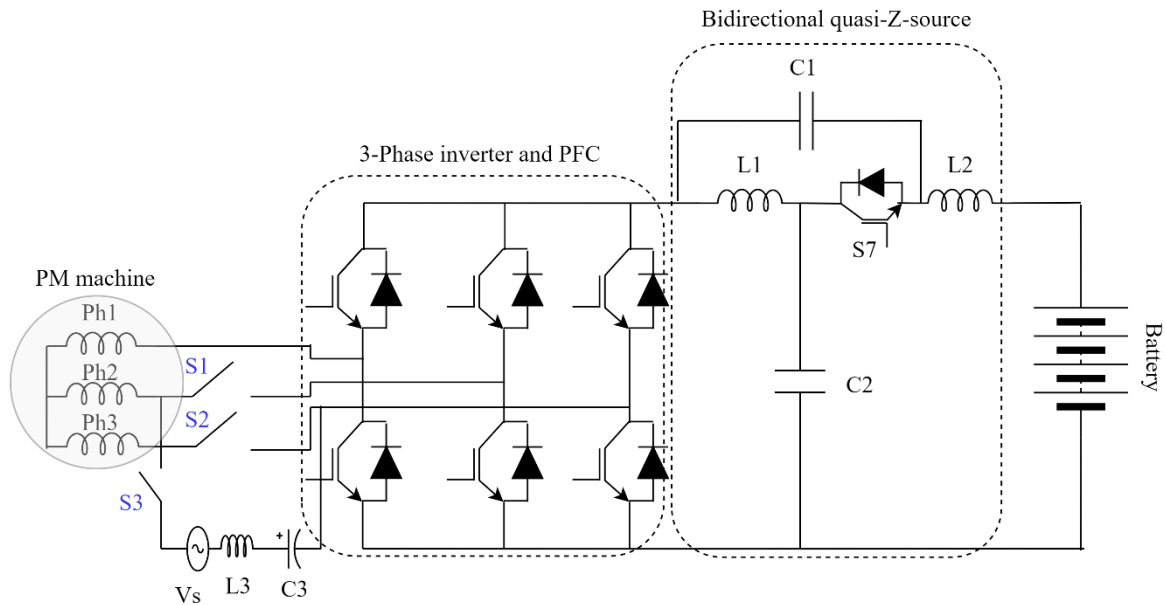


Figure 3-22 Single-phase integrated battery charger using a PM machine winding and an APF

Multiphase machines with single-phase on-board charger are shown in [90]. The presented configurations have already been implemented for a 3-phase on-board battery charger reported in [97-99]. Figure (3-23a) shows a nine-phase motor with a single-phase supply connected to the neutral ports of the first two three-phase windings. This topology requires no hardware reconfiguration for charging/traction modes. Another configuration that uses the same principle is shown in Figure (3-23b) based on a six-phase motor. Moreover, this topology also has the advantage of no hardware reconfiguration is needed. A configuration based on a five-phase motor is shown in Figure (3-23c), this topology employs a switch for the purpose of reconfiguration. Therefore, this topology lacks the advantage in a nine-phase and six-phase configuration that requires no hardware. All configurations support vehicle to grid mode and zero torque average is achieved due to no rotating field is produced in the rotor.

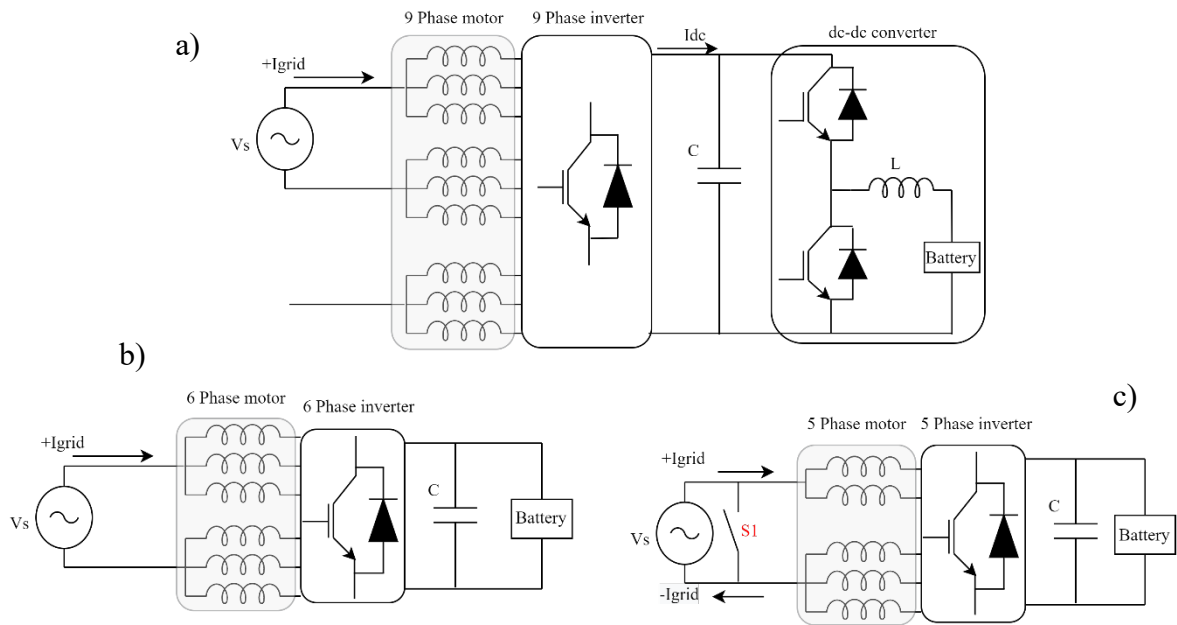


Figure 3-23 Integrated on-board charger using (a) 9-phase winding (b) 6-phase windings and (c) 5-phase windings

Hyundai has innovated an integrated charging system for its PHEV, shown in Figure (3-24). This system is distinguished by its dual-function machines, which can drive the vehicle and operate as a generator. Notably, the generation mode is activated during braking to efficiently recharge the vehicle's battery. This technology also enhances the idle stop and go (ISG) functionality, utilizing the motor for starting and stopping the engine in sync with the vehicle's motion thus aiding in emission reduction. The charger is flexible, accommodating both level 1 and level 2 charging formats. As depicted in Figure (3-24), the setup includes two motors linked to the power grid via a pair of relays. The connection of the supply occurs between the neutral points, with the traction inverters modulating the duty cycle to facilitate PFC, thus serving as active rectifiers while in charging mode. Additionally, a DC-DC converter at the battery end is employed to maintain the DC link voltage. This Hyundai integrated charger design entails certain drawbacks, such as increased size and cost. This is due to the requirement for neutral point access and the incorporation of two motors[100].

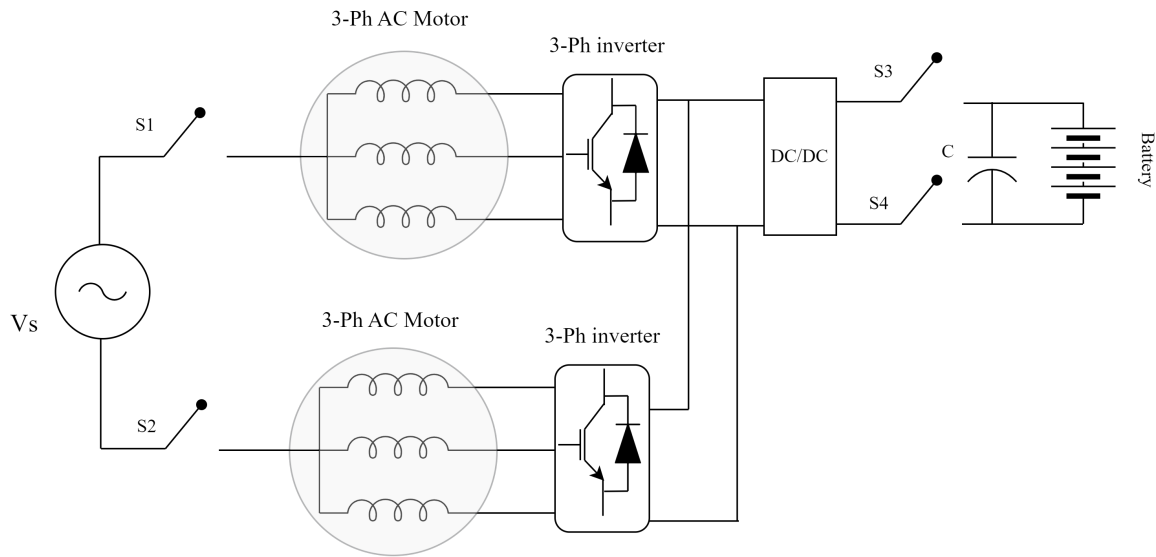


Figure 3-24 Single-phase on-board charger by Hyundai

3.4 Three-phase on-board integrated battery chargers

Fast on-board charger supplied by a three-phase mains is described in [101]. The configuration structure is shown in Figure (3-25) namely, three-phase mains, EMI filter, split-phase machine, three H-bridges, front-end converter and a battery.

In charging mode, the 3-phase supply connects to the split-phase machine. The current injected from the grid splits into opposite directions of equal magnitude, resulting in a cancellation of the magneto-motive force (MMF). Consequently, this leads to zero torque production. Then, the grid currents are rectified, and the front-end converter operates in the buck mode to recharge the DC voltage. In this case the rotor is at standstill however, due to unequal rotor mass or unbalanced currents the rotor will experience inevitable vibrations. The 3-H bridges have the advantage of PFC in the charging process. The downside of this configuration is low winding inductance when charging due to the cancelation of MMF. Moreover, the inductance is nearly equal to the leakage inductance which is too low for an acceptable charger process.

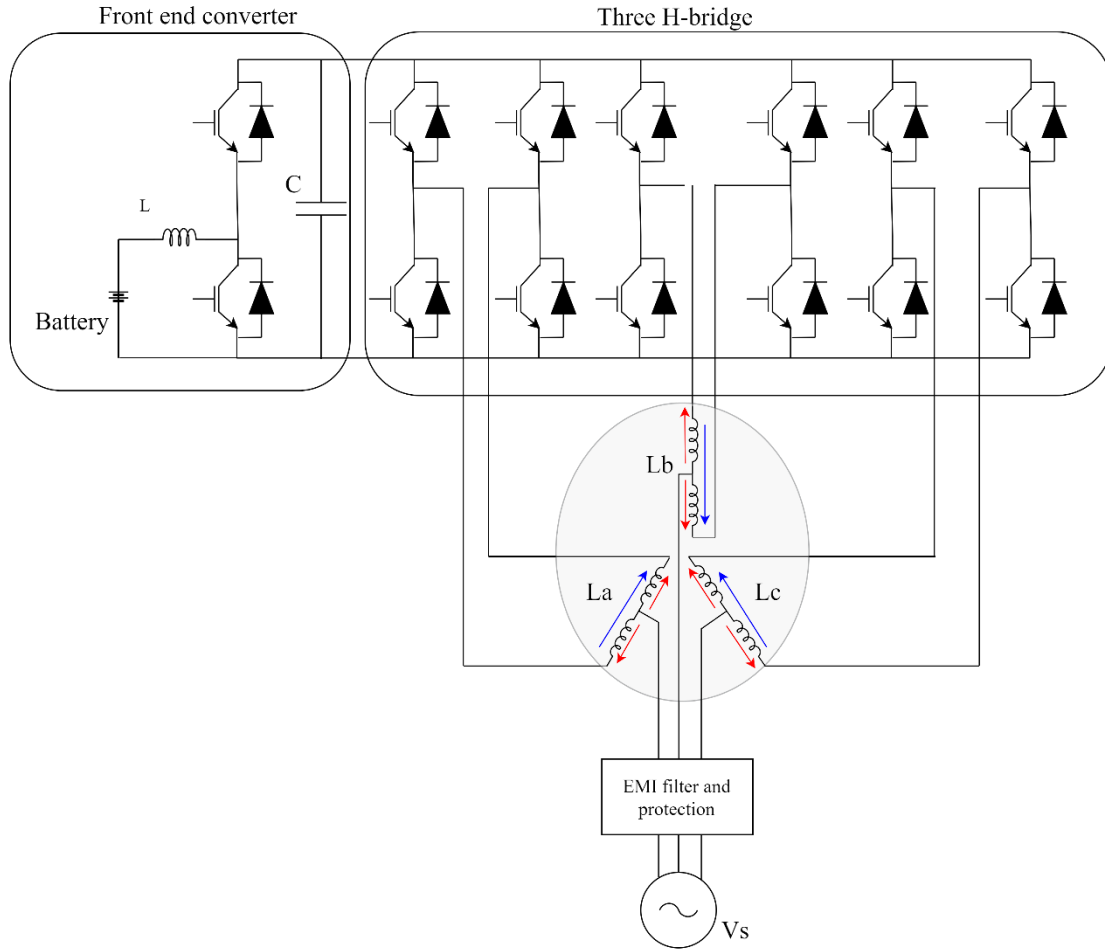


Figure 3-25 Integrated battery charger based on a split-phase machine, red arrows indicate the charging process and the blue arrows the traction mode

A high power 3-phase isolated on-board integrated charger is reported in [102]. This topology employs two sets of 3-phase windings as shown in Figure (3-26). In the traction mode, the six windings are connected in series forming a 3-phase motor powered by the inverter through the battery. While in the charging mode the windings are reconfigured by means of relays-based switches. One set of the three windings is connected to the 3-phase grid and the other 3 windings are connected to the inverter. The windings connected to the inverter will take up the induced voltage and the inverter will use this isolated voltage to recharge the battery forming a 3-phase boost rectifier. Therefore, the inverter is used to control the battery charging based on the induced voltage. This induced voltage is capable of rotating the rotor while charging therefore, a mechanical clutch is required to disconnect the motor from the drivetrain. The voltage in the charging mode is split therefore, the charging power is half of the traction rated power.

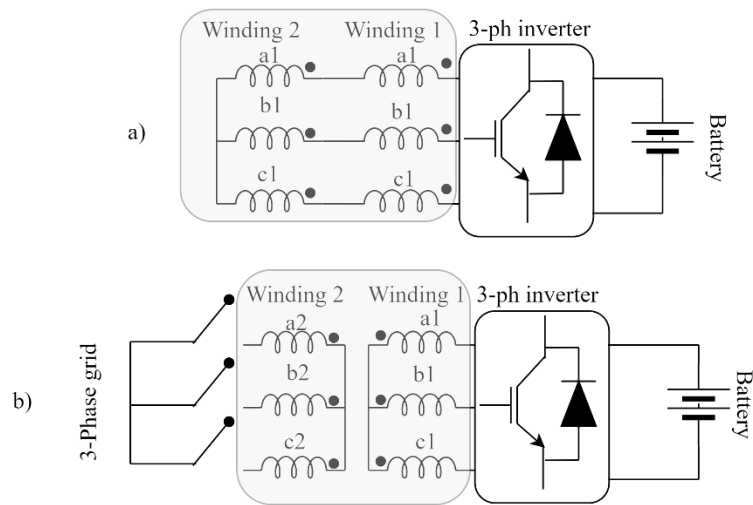


Figure 3-26 3-phase integrated charger using a 6-phase motor windings

An isolated machine integrated on-board battery charger based on a 9-phase IPM motor is reported in[103]. This topology employs a 9-phase IPM motor for traction mode, using high number of phases have the advantage of the following: fault tolerant capability, allow for limp home mode and cancelation of MMF subharmonics for both traction/charging mode. Figure (3-27) shows the windings layout for traction mode, the nine-phase FSCW windings are reconfigured to provide six winding terminals hence, the motor is driven by a 6-phase inverter during traction. In the charging mode, the windings are reconfigured by means of switches, the charging circuit is viewed as a 3-phase (primary windings) to 6-phase (secondary windings) rotating transformer. In this case the charging power will be limited to one-third of the traction rated power.

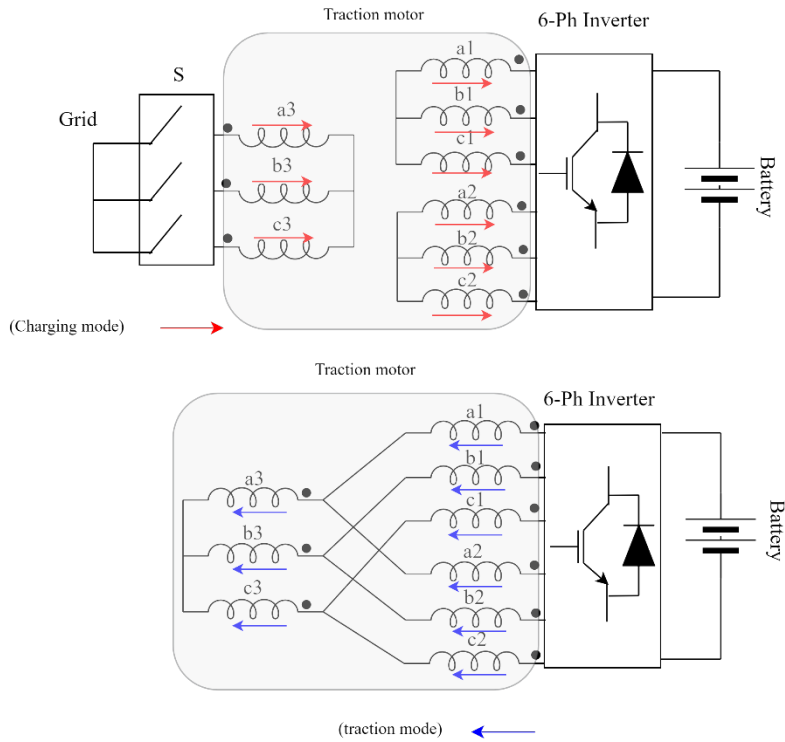


Figure 3-27 3-Phase integrated charger using an IPM (FSCW)

A FSCW for a SMPM motor is reconfigured to be used for an integrated on-board charger shown in [104]. The configuration is composed of a 12-slot 10-pole SMPM motor with six windings, two 3-phase voltage source inverters (VSI), a switch and a battery as shown in Figure (3-28).

In the traction mode, windings (ABC1) are connected in series with windings (ABC2) forming an open-end 3-phase motor. In this case two VSI will drive the motor, having two VSI will give the following advantages improved voltage waveform and the motor can be driven by only one VSI. In the charging mode, switch S is closed, and the motor windings are used as filters in the charging circuit. In order to prevent the rotor from rotating the windings set (ABC1) are reversed so as to cancel the MMF and ensure zero torque production.

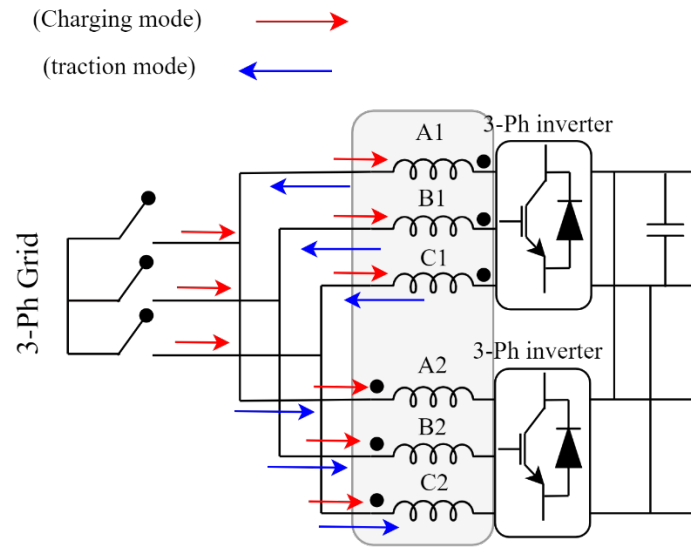


Figure 3-28 Integrated battery charger using a 2*3phase FSCW

On-board traction machine integrated chargers with high phase order have a major disadvantage which is the implementation of power electronics with high number of switches this leads to increasing size and cost. In [105], an on-board integrated charger based on symmetrical six-phase windings with a nine-switch converter is presented. Figure (3-29) shows the structure of the charger. The salient merit of this topology is the utilization of low number of semiconductor switches for both traction/charging mode.

In the traction mode, the symmetrical six-phase motor is driven by a nine-switch converter through the battery. In charging mode, S1 and S2 are open with S3 closed, the nine-switch converter will act as a 3-phase rectifier, and therefore, the symmetrical six-phase will work as filters in the charging circuit. In this mode, unity power factor is achieved at the grid side and zero torque production is reached without the need to employ the so-called phase transportation techniques.

The downside of this on-board charger is the need of a hardware reconfiguration using additional switches to change between traction and charging mode as well as the low DC-link compared with conventional dual 3-phase inverter.

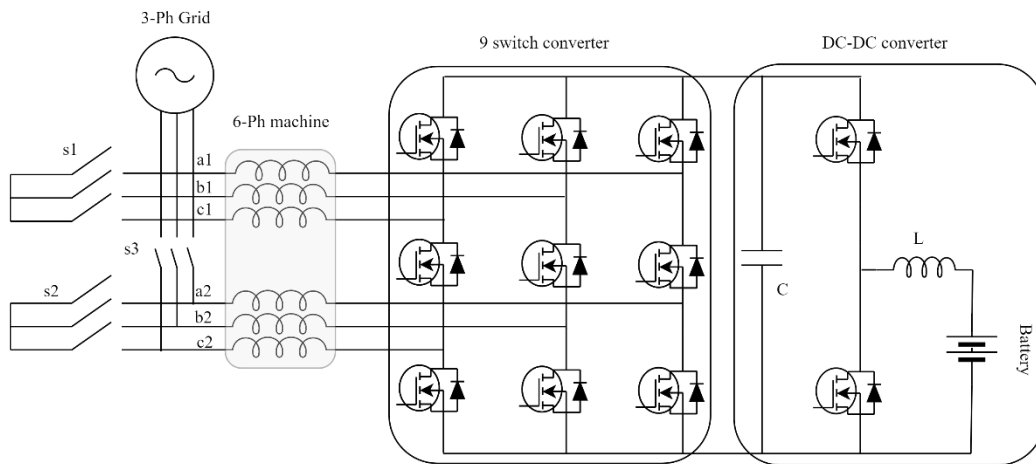


Figure 3-29 Integrated charger based on a 6-phase machine and a 9-switch converter

In [97], a five-phase machine is reconfigured to be used in an on-board battery charger circuit. As shown in Figure (3-30), the configuration comprises a 3-phase grid supply, an EMI filter, two switches, a five-phase motor, a five-phase inverter, and a battery.

In the traction mode, S1 and S2 are closed, and the motor is driven by the inverter through the battery. Furthermore, the EMI filter is short circuited in the traction mode and will not infer in this mode. In the charging mode, a 3-phase supply is connected to the motor windings and the windings are used as inductive filter in the charging process. The supply voltage is rectified and fed into the battery.

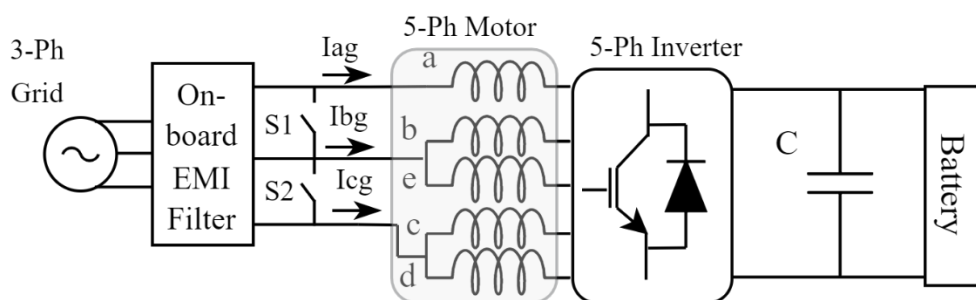


Figure 3-30 3-phase integrated charger based on a 5-phase motor

Another multiphase topology is presented in [106], it is based on a six-phase asymmetrical machine. The topology is shown in Figure (3-31). The six-phase windings are reconfigured by means of switches. In the charging mode, the switches are open, and the 3-phase supply is connected to the motor windings. Phase transportation is used to ensure zero torque production. In the propulsion mode, the switches are closed forming two isolated neutral ports, and the motor is driven by the inverter.

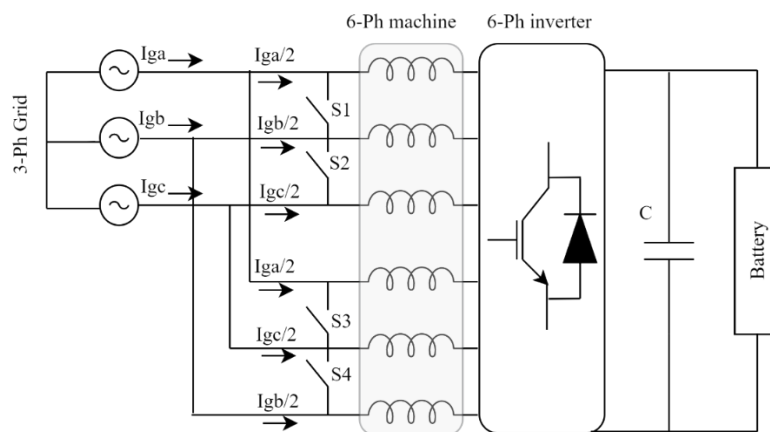


Figure 3-31 3-phase integrated charger using an asymmetrical 6 phase windings

A nine-phase motor for an on-board charger using a 3-phase supply is reported in [99]. The on-board charger for this topology is depicted in Figure (3-32). During the charging mode, the three-phase supply is connected to the natural points of motor. The motor windings in the charging mode are controlled in such a way that all windings produce the same current and zero torque is achieved. This topology has the advantage of no hardware reconfiguration is required. In the traction mode, the system performs as having three isolating neutral ports.

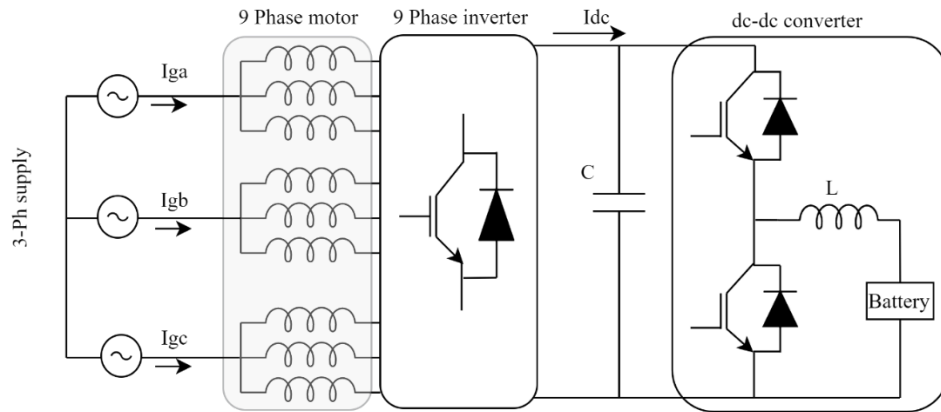


Figure 3-32 3-phase integrated battery charger using a 9-phase motor's neutral points

A three-phase split winding is proposed in [107], this topology is driven by a dual inverter in the traction mode. In the charging mode, a 3-phase utility is connected to the mid points of the phases as shown in Figure (3-33). The flux produced by one winding is cancelled out by the other winding in each phase, hence, in the charging mode no torque is produced. The downside of this configuration is that it has an increased cost because it utilized two inverters.

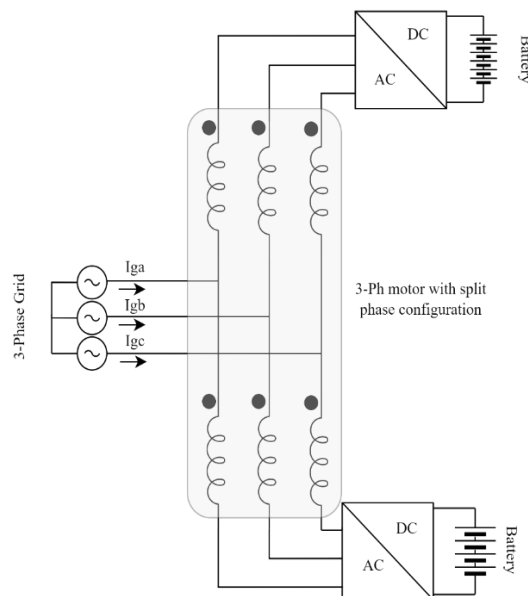


Figure 3-33 3-phase integrated battery charger based on a split phase motor configuration

A high power integrated on-board battery charger is investigated in [108], this topology utilizes a three phase interface converter as shown in Figure (3-34), to achieve high power and avoid extra hardware reconfiguration. In a conventional 3-phase buck converter, energy storage devices such as the dc-inductor and dc-capacitor increase the size and weight, the proposed topology employs the motor inherent magnets as a dc inductor in the charging mode and uses the capacitor of the inverter. Hence, reduced size and weight are achieved.

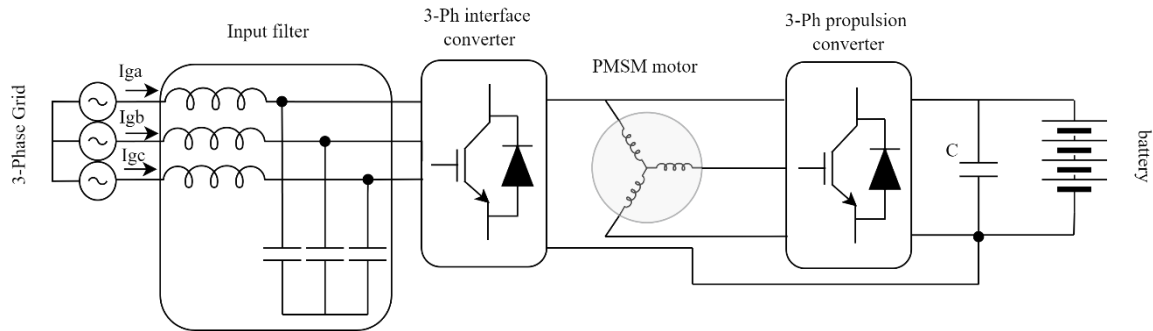


Figure 3-34 Integrated on-board charger using an input filter and machine windings

Figure (3-35) presents a fast charging device by Renault for an EV [109], designed to convert 3-phase grid AC power into DC through a rectifier. This DC is then applied to the vehicle's battery via an inverter. The on-board charger comprises an input filter, rectifier, wheeling diode, motor, inverter, and the battery, capable of interfacing with either single-phase or three-phase power supplies. The stator coils of the motor serve as a buffer filter, using their inductance to stabilize the current and reduce electrical noise. With DC current flowing through the stator windings, the AC motor is rendered torque-free, meaning it will not experience rotational force during the charging process. To protect the motor components and ensure their safety, the current flowing through the motor is carefully regulated to prevent overheating.

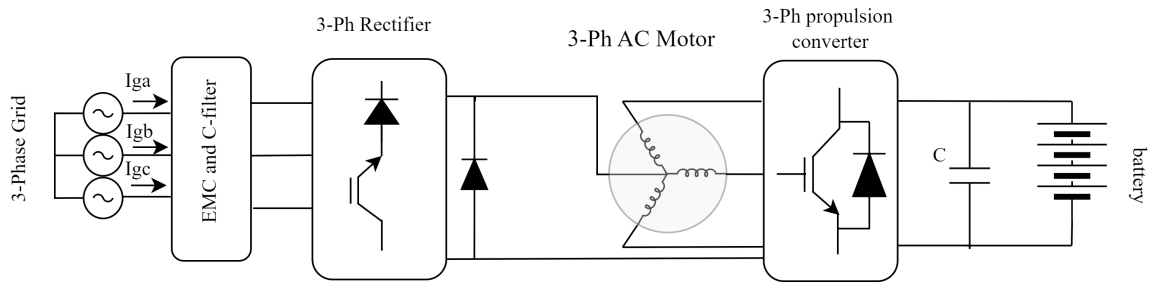


Figure 3-35 Fast integrated charger by Renault

Table (3-4) summarizes the machine integrated for on-board battery chargers in this chapter. It can be seen that the traction motor can employ 3-phase or more. The layouts that utilize a single-phase source exhibit no torque due to there is no rotating field. However, inevitable vibration might occur in these topologies. On the other side, 3-phase supply connected to the traction motor requires specific layouts to avoid the rotor from rotating, such as phase transportation or split phase windings this will lead to field cancelation which results in no torque. However, the inductance will be low.

When traction motor is accessed by neutral points this topology exhibits simplified reconfiguration. However, having the motor phases in parallel in the charging mode reduces the inductance value. Thus, in this thesis a series of layouts will be tested, in both series connections and parallel connection to leverage the motor winding inductance in the charging mode.

Table 3-4 Comparison of traction machine integrated battery chargers

Layout figure	Traction motor phases	Charger supply	Torque in charging mode	Traction motor reconfiguration needed
Figure (3-17)	2*3-phases	1-phase	No	No
Figure (3-18)	3-phase	1-phase	No	Yes
Figure (3-19)	3-phase	1-phase	No	Yes
Figure (3-20)	3-phase	1-phase	No	No
Figure (3-21)	4-phase	1-phase	No	No
Figure (3-22)	3-phase	1-phase	No	Yes
Figure (3-23)	(a) 9-phase (b) 6-phase (c) 5-phase	1-phase	No	Yes for 5-phase configuration
Figure (3-24)	3-phase	1-phase	No	No
Figure (3-25)	3-phase	1-phase	No	No
Figure (3-26)	6-phase	3-phase	Yes	Yes
Figure (3-27)	9-phase	3-phase	Yes	Yes
Figure (3-28)	2*3 phase	3-phase	No	No
Figure (3-29)	6-phase	3-phase	No	Yes
Figure (3-30)	5-phase	3-phase	No	Yes
Figure (3-31)	6-phase	3-phase	No	Yes
Figure (3-32)	9-phase	3-phase	No	No
Figure (3-33)	3-phase	3-phase	No	No
Figure (3-34)	3-phase	DC	No	No
Figure (3-35)	3-phase	DC	No	No

3.5 Summary

This chapter has provided a detailed review of traction machines. PM synchronous machines have emerged as a promising configuration for EV applications due to their high-power density. As this thesis focuses on the design of high-power high-speed applications, a comprehensive qualitative comparison of machine topologies with excellent field weakening capabilities has been conducted. The comparison reveals that the PMA-SynREL machine emerges as the optimal topology to meet the requirements of heavy-duty applications.

Traction machine integrated on-board chargers have the ability to repurpose the windings of the traction motor to function as inductors during charging mode. This chapter has explored both single-phase and three-phase charger supplies. It's clear that single-phase machine integrated chargers don't generate torque since they lack a rotating magnetic field. However, these systems may experience vibrations. On the other hand, three-phase machine integrated chargers necessitate specific designs, such as split phase winding or phase transportation. These designs prevent the rotor from rotating and eliminate the need for a mechanical lock on the rotor. However, these specific layouts have low inductance due to the cancellation of magnetic fields. This aspect of their design could impact the efficiency and performance of the charger and is therefore a factor to consider in their implementation.

Chapter 4. Preliminary Machine Design

4.1 Introduction

In this chapter, the specification requirements and constraints of the traction motor for a heavy-duty truck are presented. A design methodology is introduced in a logical sequence to meet the challenging demands of the required motor. Using this information, a preliminary machine is designed through FEA using Motor-CAD software. An understanding of the multi-physics is essential for the PMA-SynREL machines. Therefore, mechanical and thermal analyses are incorporated into the initial design to better achieve a feasible result.

The understanding of multi-physics and the overall design process represent the highlight of this chapter and a key contribution to knowledge.

4.2 Application specifications and constraints

This section defines the performance requirements and physical constraints of the required traction motor. The design specifications for a BEV heavy-duty commercial electric truck, provided by Cummins Company, are tabulated in Table (4-1). The torque and power characteristic are plotted verse the required speed in Figure (4-1) with the operation regions of the machine.

Table 4-1 Traction machine performance requirements and geometrical constraints

Requirements	Value
Stator outer diameter	≤ 350 mm
Machine maximum length	≤ 350 mm
Active maximum weight	≤ 70 kg
Moment of inertia	≤ 0.4 kg. m ²
Maximum winding temperature	200 °C
Maximum phase current	660 A
DC-link voltage	620 V
Peak Torque @ 5000 rpm	526.8 Nm
Peak Power @ 5000 rpm	274 kW
Rated Torque @ 5000 rpm	401.1 Nm
Rated Power	210 kW
Rated Torque @ 15000 rpm	140 Nm

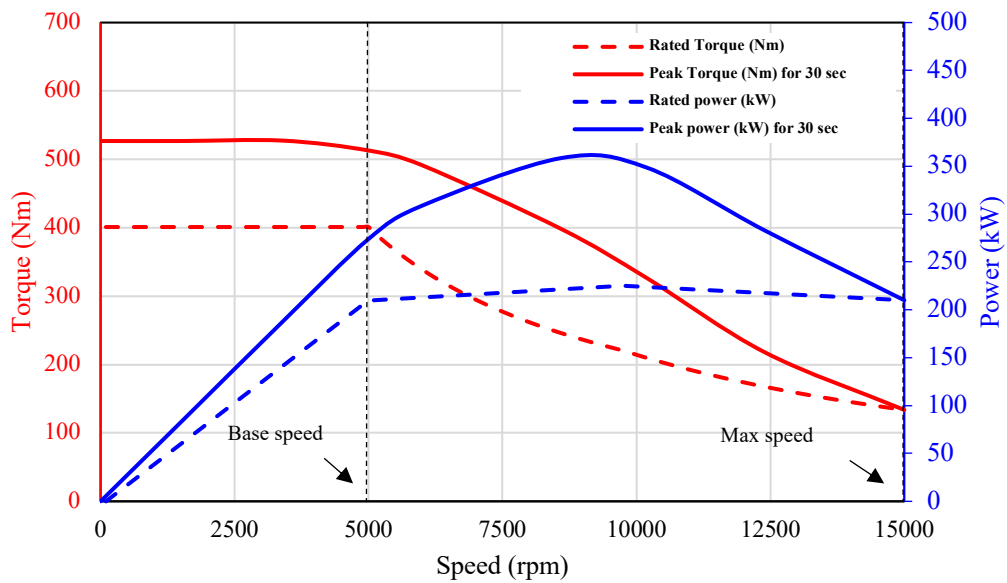


Figure 4-1 Torque/Power vs speed characteristic of required motor from Cummins

Based upon the performance requirements and physical constraints of the machine, it can be inferred that the primary design goals for this specific design revolve around the following aspects:

1) Torque and power characteristic

A peak torque is required at base speed for 30 sec therefore, the motor must be designed to handle this torque and the thermal load produced at this point. The thermal management is of prime importance to ensure reliable operation at peak conditions. The constant rated power range is 1:3. Thus, huge field weakening is required to achieve high top speed. Implementing field weakening requires a control strategy to advance the phase angle of phase current to maintain the voltage beyond the base speed within limits. As the frequency requirement is increased with the speed more energy losses are generated which leads to a drop in efficiency. The use of materials with high saturation limits and increased electric resistivity is important to accommodate the peak current and reduce losses at maximum speed.

2) High power and torque density

Achieving high power density and high torque density are essential prerequisites for applications where compactness, lightweight and high performance are required. High power density is potentially achieved by increasing the speed, while high torque density is attained by incorporating high energy density rare-earth materials. The active mass of the required machine which includes stator, rotor and magnets should be less than 70 kg. High power-to-volume ratio is a key design in application where space constraints are critical. As stated in Table (4-1) the maximum stator outer diameter is 350 mm and maximum machine length is 350 mm, hence a machine volume less than 33.67 L is required. Incorporating high electric steel grade with high-energy rare-earth material and advanced cooling methods are all key design aspect that leads to reduced volume. Therefore, when striving for high power density and increased speed in electric machine design, the overall process naturally evolves into a complex multi-physics issue. This challenge encompasses the electromagnetic, thermal and mechanical aspects, all of which have constrained boundaries that must be carefully considered.

3) Dynamic response

The ability of the designed machine to react quickly to any change in torque and speed is highly demanded in automotive applications. The moment of inertia influences the acceleration and deceleration of the vehicle. Low inertia can enhance vehicle dynamics, driver response, and energy efficiency during acceleration and deceleration. Hence, the designed motor should have a low moment of inertia. Inertia is observed to rapidly increase with increasing the rotor outer diameter. Therefore, at the design stage of the rotor it should be optimized to have a low inertia as feasible and not exceed the maximum inertia $0.4 \text{ kg} \cdot \text{m}^2$.

4.3 Design methodology

Designing a traction motor for an automotive application is a multi-faceted process, encompassing various stages as shown in Figure (4-2) to ensure high performance, efficiency and reliability. Now, after the motor requirements were established in the previous section this help to identify the most suitable motor type. Based upon the performance requirements and physical constraints PMA-SynREL machines are emerging as a viable option to be equipped in the application drivetrain. Its combined features of PM motors and SynREL motors provides an optimal balance of the quantity of magnets incorporated, performance, efficiency, and cost. The presence of PM torque and reluctance torque makes PMA-SynREL exhibit high torque density and high-power density. Further, the preeminent proportion of reluctance torque facilitates the production of significant torque within elevated speed with minimized risk of magnet demagnetization.

The high power required and the huge field weakening range are associated with thermal limitations which can lead to performance degradation, this justifies the use of PMA-SynREL machines that uses less magnetizing current due to the share of magnet and reluctance torque. This results in reduced copper losses and minimizes temperature rise. Hence, high efficiency is achieved at critical operation points such as, peak torque and at maximum speed.

Several notable obstacles exist in the development of PMA-SynREL machines, the primary issue involves the significant torque ripple and mechanical strain experienced by the rotor at elevated peripheral velocities.

After the topology is selected, the next steps are to consider aspects such as the material selection, proper winding layout to be accommodated in the stator with motor sizing to achieve the desired performance. This involves deciding on thermal management to keep the generated heat within limits.

An important aspect of the machine design is the simulation, which helps predict the electromagnetic performance across the wide speed range, temperature rise and mechanical behaviour. In this thesis FEA software (Motor-CAD) will be used to identify the motor performance and highlight any potential issues before physical prototyping. Once the designed motor fits the application requirements it must undergo through more refinement to achieve the highest performance with low weight as feasible as possible. The manufacturability of the optimized motor is a crucial aspect, it highly effects cost. The supply chain stability of rare-earth magnets is important to consider, the rotor design and assembly presents a challenge due to the need of high accuracy in alignment and robust construction. The incorporation of PMs requires precision. The integration of effective cooling methods and the spacing it requires are all important aspects.

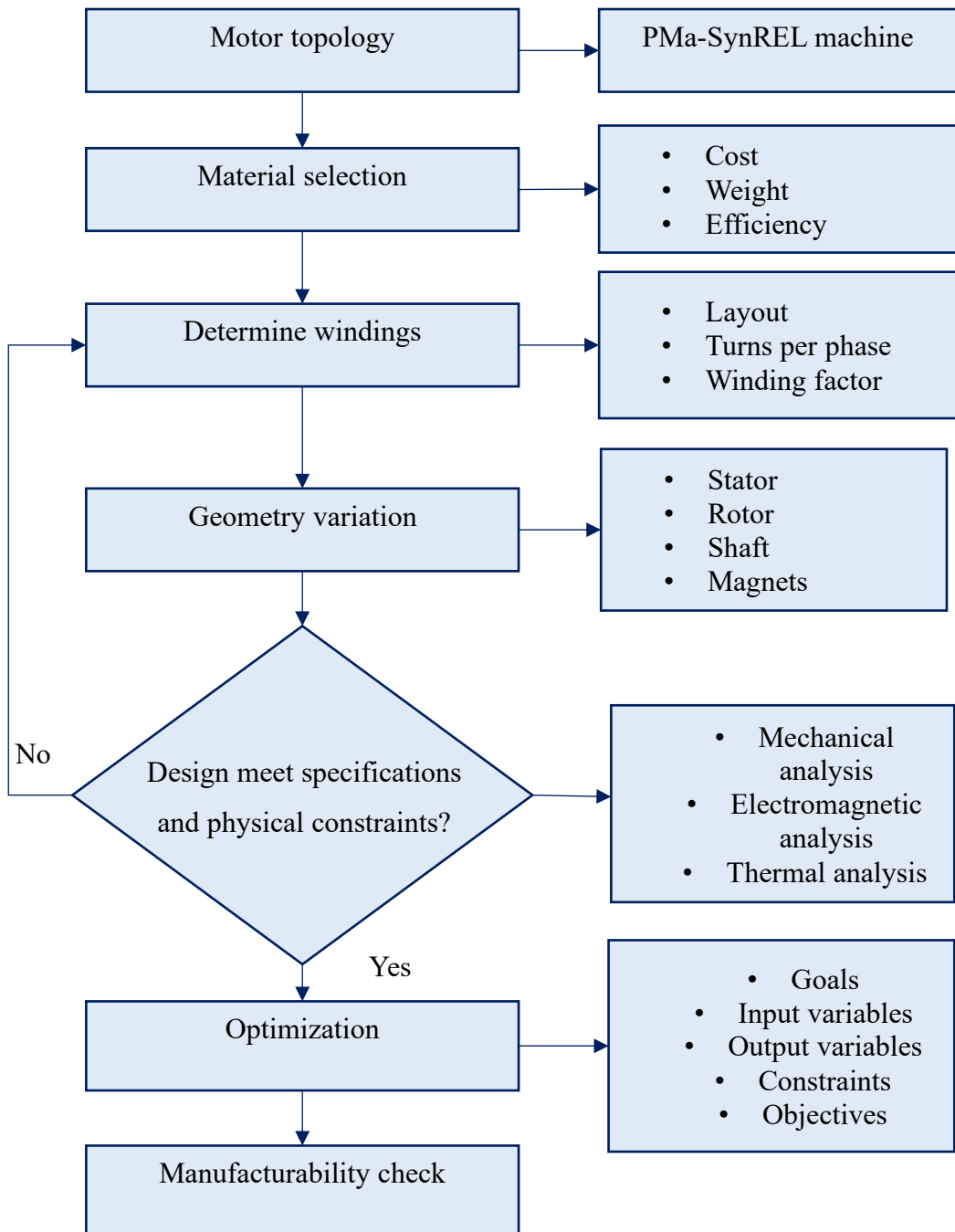


Figure 4-2 Design methodology process

4.4 Optimization workflow

This study incorporates the use of a Multi-Objective Genetic Algorithm (MOGA-II), which is integrated with an automatic procedure executed through MATLAB and the finite element software Motor-CAD. The primary optimization tool used is modeFRONTIER. In the MOGA-II algorithm's evolutionary optimization process, it assesses each traction motor design against objectives while respecting constraints. Over time, the designs converge towards optimal solutions that best fit the multi-objective criteria and constraints. Once convergence is achieved, or after a predetermined number of iterations the process identifies one or more optimal motor designs.

The final output is a set of motor designs optimized to meet the objectives within the given constraints. These designs are then analysed to choose the most suitable one for the specific application of the traction motor. The flow of data and the interaction between the optimizer modeFRONTIER, MATLAB, and Motor-CAD is depicted in Figure (4-3).

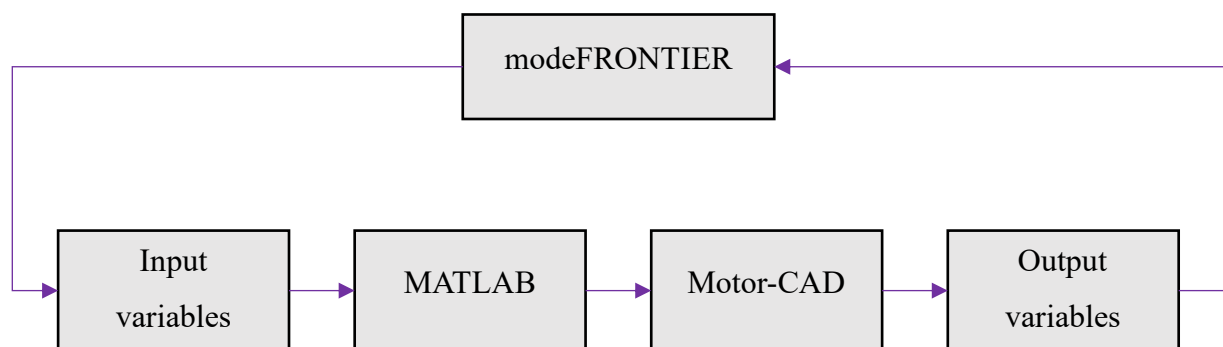


Figure 4-3 Optimization workflow

The workflow in Figure (4-3) can be illustrated as follows:

1. **Input variables:** The process begins with the MOGA-II optimizer in modeFRONTIER. The algorithm generates a diverse set of initial solutions for the traction motor's design parameters. These parameters (input variables) include aspects like motor dimensions, electrical inputs, winding configurations, etc. This initial population of solutions is then fed into MATLAB, serves as an intermediary platform where further processing or transformation of the data can occur if necessary.

2. **Simulation in Motor-CAD:** The processed design parameters from MATLAB are then imported into Motor-CAD. Motor-CAD simulates each motor design variant based on the provided parameters. During this simulation phase, Motor-CAD solves the model to provide the optimizer with performance metrics of the traction motor, such as efficiency, torque, temperature, mechanical stresses and output power.

3. **Output variables:** The output from Motor-CAD, encompassing both the objectives (like active weight, output power) and the constraints (such as maximum allowable temperature, size limitations, and mechanical stresses), is then fed back to the MOGA-II optimizer.

4.5 PMA-SynREL machine torque production

In rotating electric machines, electric power is converted to mechanical power through the medium of magnetic energy. When electric current is applied to the stator windings of the motor a magnetic field is generated. This magnetic field (in the stator) interacts with the magnetic field created by PMs (in the rotor) at the airgap. The interaction between these magnetic fields results in a force acting on the rotor, which leads to its rotation. The fundamental relation between force production F , a current carrying conductor I and the length of the conductor L is expressed in Lorentz equation represented in equation (4.1), a current carrying conductor can be simplified as a continuous flow of electrons moving through it. As a result, when such a conductor is placed within a magnetic field B , it experiences a force acting upon it. Thus, torque in electric machine can be defined as the rotational forced applied multiplied by the perpendicular distance which is the stator bore radius r as shown in equation (4.2).

$$F = IL \times B \quad (4.1)$$

$$T = (F)(r \sin(\theta)) \quad (4.2)$$

For a 3-phase machine, torque T exerted on the stator bore diameter D is expressed by substituting equation (4.1) into (4.2) as follows, where N_{ph} is the number of turns per phase.

$$T = \left(\frac{3}{2}\right) (B)(DL)(N_{ph}I) \sin(\theta) \quad (4.3)$$

The amount of current fed into the stator winding turns per phase (N_{ph}) with respect to the stator bore periphery πD is the electric loading A of the machine, expressed in equation (4.4), the higher the electric loading the higher the torque generated by the machine. However, the increase in electric loading is associated with an increase in copper losses which leads to temperature rise. Therefore, electric loading is governed by the available cooling method.

$$A = \frac{3 \times 2 \times I \times N_{ph}}{\pi \times D} \quad (4.4)$$

$$I = \frac{A \times \pi \times D}{3 \times 2 \times N_{ph}} \quad (4.5)$$

From the electric loading equation (4.4), the current in the machine can be expressed as in equation (4.5) substituting equation (4.5) into (4.3) gives the torque equation in (4.6).

$$T = \left(\frac{D^2}{4} \times \pi \times L_{stack}\right)(B)(A)\sin(\theta) \quad (4.6)$$

Crucial observations can be extracted from the torque expression (4.6), which are summarized as follows:

- (a) Electromagnetic torque is generated due to the interaction of the magnetic fields created by the armature current and the magnetic fields of the rotor magnets, the strength of these magnetic fields depends on the electric loading and magnetic loading and the angle between them denoted as torque angle.
- (b) Electromagnetic torque is proportional to the cylindrical volume of the stator bore. Therefore, for a given volume the only way to increase the torque is to act on the electric loading and magnetic loading. Thus, torque per rotor volume (TRV) is the product of electric loading and magnetic loading and the sine of the torque angle. The TRV is a useful metric to compare the power density of different motors, as it essentially measures how much torque is produced within a given amount of space, this is essentially crucial for EVs, where reducing weight and optimizing space are essential considerations in achieving efficient design and superior performance.

4.6 Limitations of electric loading and magnetic loading

As stated in equation (4-4), the electric loading is dependent on the amount of current fed into the windings of the motor and number of turns per phase. Increasing the current increases the torque generated, but also increases the ohmic losses in the windings which results in temperature rise and reduced efficiency. Further, increasing the number of turns per phase for a given current increase the current density which leads to losses and temperature rise. As mentioned before the electric loading is limited by the available cooling method.

Magnetic loading is the maximum flux density distributed in the air gap, like the electric loading higher magnetic loading in the machine gives more torque production, however, it may cause saturation in the magnetic circuit of stator, rotor and magnetic material. Its increase is associated with a possible rise in core losses such as hysteresis and eddy current losses. It can be optimized by selecting high-quality magnetic material to design efficient magnet circuits. Incorporating high energy PMs in the rotor can provide strong and consistent magnetic fields, which enhance the magnet flux density in the airgap. However, PMs are temperature sensitive and they lose flux density with elevated temperature. So, a balance must be found between thermal limitation and electric and magnetic loading to ensure optimal performance, efficiency and reliability of the machine.

The geometry of a PMA-SynREL machine is composed of two main parts namely, the stator and the rotor as shown in Figure (4-4), the stator is typically composed of laminated steel core and it accommodates the electric circuit (copper windings) in its slots. These windings are arranged in the slots, they are consisted of a number of coils that are connected in a specific layout around the inner circumference of the stator called armature windings. The motor windings are excited with a 3 phase AC current to generate a rotating magnetic field.

The rotor core is characterized by two primary elements: axially magnetized PMs and distinct salient poles with reluctance structure. The salient pole structure is made of laminated iron and are shaped to boost the reluctance torque and maintain the mechanical integrity. Reluctance is an inherent property of magnetic materials, which is related to their ability to conduct magnetic flux, therefore, the rotor of PMA-SynREL is deliberately shaped to create anisotropic magnetic properties. Thus, the magnetic reluctance is changed at different rotor position with respect to

phase excitation. The PMs are magnetized in a parallel direction to the stator to maximise the magnetic torque production.

When, the stator is excited the aim is to maximize the synchronisation between the stator magnetic field and the rotor field (flux due to PMs), the interaction of stator fields with the distinct salient pole of the PMA-SynREL machine causes the magnetic flux to follow to the least magnetic reluctance path (in the rotor) hence, the rotor will align to the d-axis direction as shown in Figure (4-4). As stated, reluctance is changed at different rotor positions. The electromagnetic torque production can be expressed to magnetic torque and reluctance torque as mentioned; hence the following section will represent the equivalent circuit of a PMA-SynREL machine.

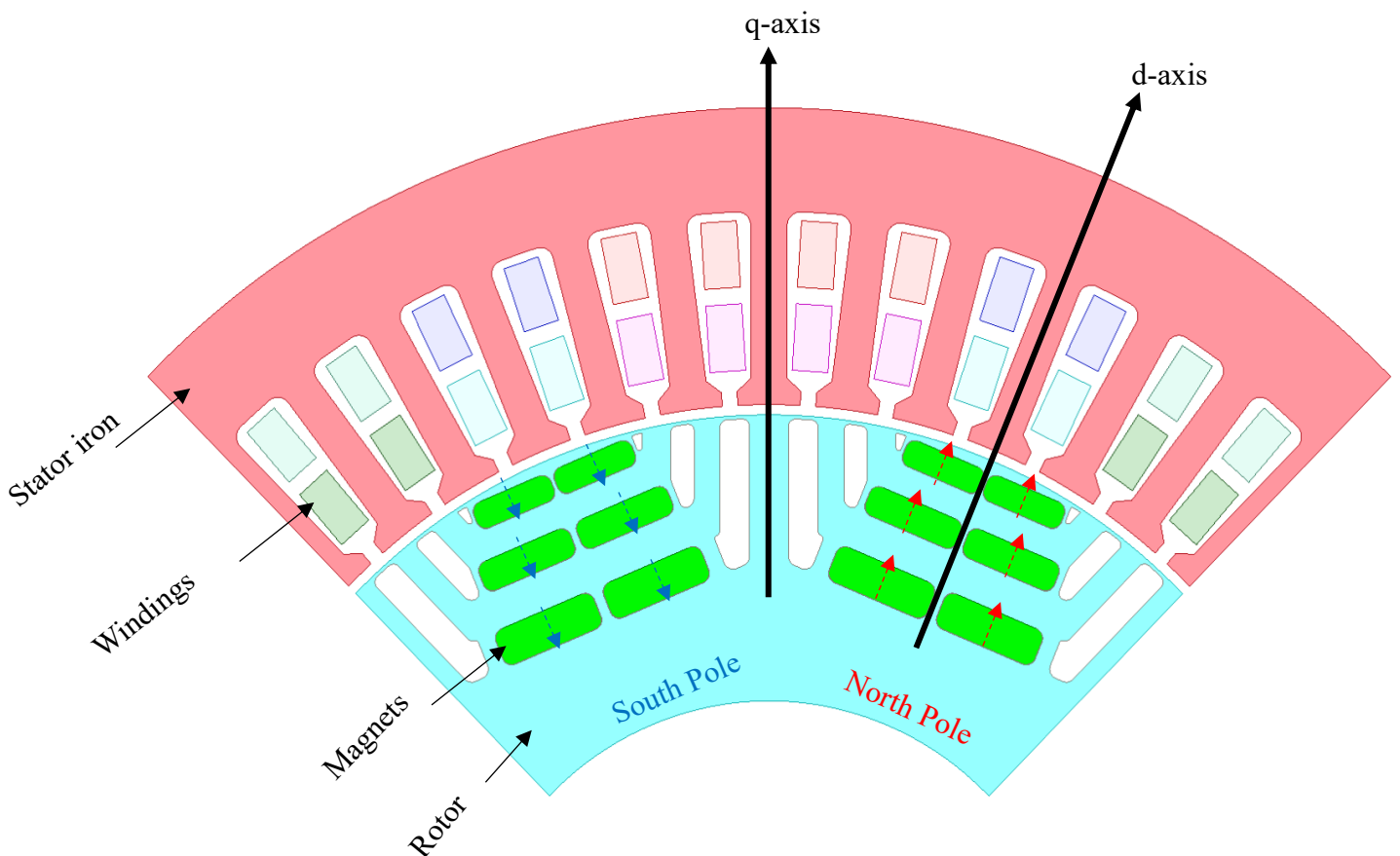


Figure 4-4 PMA-SynREL machine configuration

4.7 PMa-SynREL machine equivalent circuit and basic characteristic

This section outlines the equivalent circuit of the PMa-SynREL machine. As mentioned in the previous section, torque is generated because of the interaction of the magnetic fields of the (stator) and (rotor). The stator windings are connected to an inverter powered by a battery to provide the excitation. The rotor provides constant flux density from the PMs, however, with elevated temperature PMs flux levels reduce. Therefore, the equivalent circuit is composed of the armature windings that have resistance R_s , stator leakage inductance $L_{\ell s}$, magnetizing inductance L_m , and the PM excitation (in the rotor). All these elements interact together to form the electromagnetic torque.

Due to the rotor salient pole as shown in Figure (4-4), PMa-SynREL motor exhibits varying inductance in the q-axis and d-axis. Thus, the equivalent circuit is divided into two separate circuits as shown in Figure (4-5).

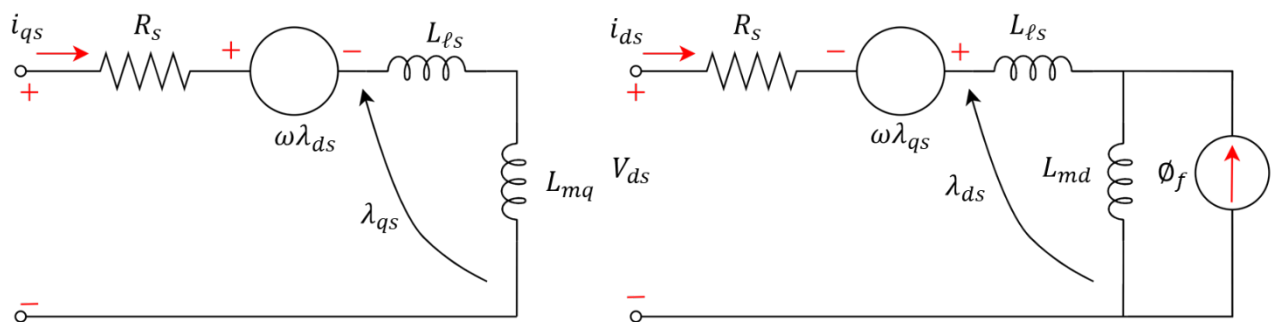


Figure 4-5 Equivalent circuit of a PMa-SynREL machine (a) q-axis and (b) d-axis

The 3-phase equivalent circuit of the PMa-SynREL machine can be transformed to the q-axis and d-axis equivalent circuit using the (park transformation technique). This leads to simplification of analysis as the machine becomes analogous to DC machine, where torque and flux are decoupled, this enables independent control of torque and flux. The q-axis represent the torque component and the d-axis represent the flux component. As discussed in the previous section that PMa-SynREL machine, has a rotating magnetic circuit that is shaped to have salient pole structure. Hence, the d-axis and q-axis inductances influence the distribution of the magnetic flux. As in Figure (4-4), the d-axis is aligned in the direction of PM flux and the q-axis is perpendicular with a lower magnetic flux density. Figure (4-5) shows the equivalent circuit of the d-axis and q-axis circuit. The flux linkages in the d-axis and q-axis circuits are given by equations (4.7) and (4.8), respectively. In these equations, λ_{ds} and λ_{qs} represent the

flux linkages in the d-axis and q-axis, L_{md} and L_{mq} denote the magnetizing inductances in the d-q coordinate system, λ_{PM} is the PM flux, and i_d and i_q are the currents in the d-axis and q-axis of the d-q coordinate system.

$$\lambda_{ds} = (L_{md} + L_{\ell s})i_d + \lambda_{PM} = \lambda_{ds} + \lambda_{PM} \quad (4.7)$$

$$\lambda_{qs} = (L_{mq} + L_{\ell s})i_q = \lambda_{qs} \quad (4.8)$$

The voltage equations for the d-axis and q-axis, based on their equivalent circuits, are expressed in equations (4.9) and (4.10). In these equations, v_{qs} and v_{ds} represent the voltages, ω_r denotes the electric speed, and R_s is the resistance of the stator windings.

$$v_{qs} = R_s i_{qs} + \frac{d\lambda_{qs}}{dt} + \omega_r \lambda_{ds} \quad (4.9)$$

$$v_{ds} = R_s i_{ds} + \frac{d\lambda_{ds}}{dt} - \omega_r \lambda_{qs} \quad (4.10)$$

The input power P_{in} is expressed via the park transformation as:

$$P_{in} = \frac{3}{2} (v_{ds} i_{ds} + v_{qs} i_{qs}) \quad (4.11)$$

Assuming, steady state operation and neglecting losses the input power is equal to output power as in:

$$P_{out} = \frac{3}{2} ((-\omega_r \lambda_{qs}) i_{ds} + (\omega_r \lambda_{ds}) i_{qs}) \quad (4.12)$$

Hence, the electromagnetic torque T_e in equation (4.13) is acquired by dividing the output power P_{out} in equation (4.12) by the mechanical speed yields:

$$T_e = \frac{3}{2} (\lambda_{ds} i_{qs} - \lambda_{qs} i_{ds}) \quad (4.13)$$

Substituting equations (4.7) and (4.8) into equation (4.13) results in a new expression given in equation (4.14), where P represents the number of poles in the machine.

$$T_e = \frac{P}{2} \frac{3}{2} [\lambda_{PM} i_{qs} + (L_{ds} - L_{qs}) i_{ds} i_{qs}] \quad (4.14)$$

The given equation in (4.14) indicates that the produced torque consists of two separate components, which is the magnetic torque shown in equation (4.15) and the reluctance torque component in equation (4.16).

$$T_e = \frac{P}{2} \frac{3}{2} [\lambda_{PM} i_{qs}] \quad (4.15)$$

$$T_e = \frac{P}{2} \frac{3}{2} [(L_{ds} - L_{qs}) i_{ds} i_{qs}] \quad (4.16)$$

The phasor diagram of a PMa-SynREL machine is depicted in Figure (4.6).

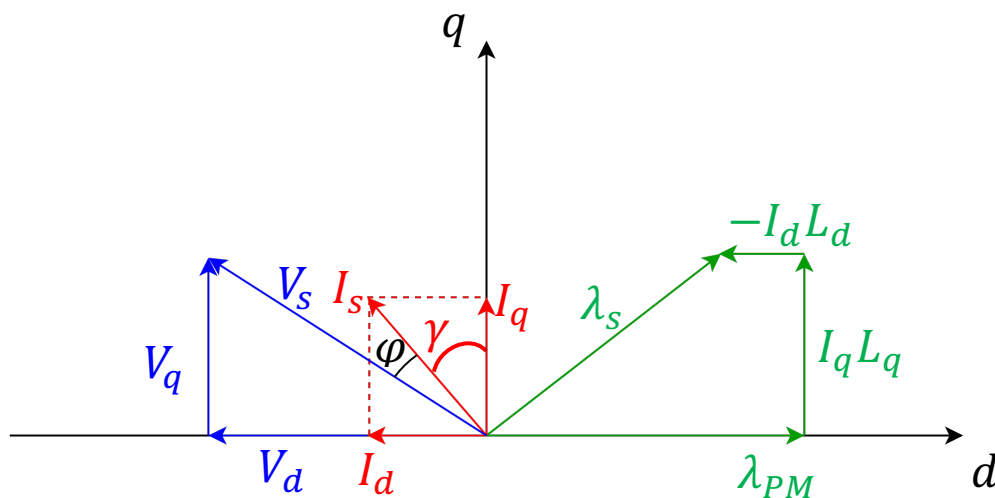


Figure 4-6 Phasor diagram of PMa-SynREL machine

PMa-SynREL machines are driven by an inverter, hence the motor must operate and not exceed the permissible DC voltage limit. As the frequency is increased to achieve higher speeds, the terminal voltage V_s is increased and will continue to increase beyond its rated value as expressed in equation (4.17). In order to keep the voltage at its rated value in the high-speed range, field weakening is required. This is achieved by controlling the phase advance angle γ shown in the phasor diagram in Figure (4-6). Injecting a negative I_d current reduces the total flux linkage in the machine λ_s , by applying a (stator field) that will oppose the PM field thus the motor can

rotate at faster speeds without exceeding the DC voltage limit. As shown in equations (4.18) and (4.19) controlling the phase advance angle γ changes I_q and I_d accordingly. The current magnitude of I_q and I_d should not surpass the maximum limit set for stator current I_{sMAX} as shown in equation (4.20). The reduction of the flux linkage in the d-axis is associated with sacrificing some of the maximum torque.

$$V_s = \omega_r \times \sqrt{\lambda_q^2 + \lambda_d^2} \leq V_{sMAX} \quad (4.17)$$

$$I_q = I_s \cos \gamma \quad (4.18)$$

$$I_d = I_s \sin \gamma \quad (4.19)$$

$$I_s = \sqrt{I_q^2 + I_d^2} \leq I_{sMAX} \quad (4.20)$$

4.8 Torque quality in PMA-SynREL machines

Torque quality is an important aspect that electric machine designers should highly consider, especially when the application is an EV. Torque quality refers to the smoothness and consistency of the generated torque. In PMA-SynREL machine the torque quality is assessed based on the percentage of torque ripple (%). Torque ripple is caused by a combination of pulsating torque and cogging torque, which are explained as follows.

The interaction of the stator non-sinusoidal MMF with the rotor geometry causes pulsating torque. The stator MMF fundamental harmonic interacts with the rotor magnetic field, leading to the generation of the average electromagnetic torque. However, high-order harmonics that are not synchronised with the rotor cause magnetic flux fluctuation, which lead to vibration and noise. Various reasons that cause spatial MMF harmonics, such as non-sinusoidal current caused by supply voltage, type of winding used and slotting effect. Magnetic saturation can distort the flux, which in turn impacts the MMF waveform and increase the harmonic content. Therefore, the design of rotating magnetic circuit (rotor), highly influence the torque ripple. The salient pole structure of PMA-SynREL machine causes magnetic reluctance variation

which causes torque ripple. Therefore, at the design stage proper positioning and sizing of the flux barriers reduce torque ripple[110].

Other phenomena which impact torque quality is cogging torque. Cogging torque primarily arises due to the attractive forces between the PMs in the rotor with the stator teeth. Cogging torque is position dependent, as when the magnets move away from the teeth this cogging torque is minimum. Thus, when the rotor rotates torque fluctuations occur. Mitigation techniques involve stator skewing, optimizing the stator with rotor. Further, as the slot-pole combination impact the cogging torque, the cogging torque frequency and magnitude are dependent on the slot-pole combination.

4.9 Design consideration

4.9.1 Selection of the slot-pole combination

The number of poles is determined by the frequency available from the supply. However, since PMA-SynREL machines are driven by inverters, they allow for a broader range of operational speeds. Considering machine performance, the significance of the slot-pole combination becomes evident. Higher pole counts yield high power density, whereas lower pole counts necessitate more current when they are to deliver the same power density as their high-pole counterparts. This increased current can result in increased copper losses and thermal issues. The high-power density of machines with high pole counts is attributed to the more effective utilization of the magnetic field produced by the stator and rotor. Thus, a greater number of poles results in increased torque generation and enhanced power density, along with a reduction in cogging torque.

It is important to note, however, that the increase in number of poles will increase the electric frequency. Therefore, high iron losses are expected with high number of poles. Thus, the number of poles should be selected in order to achieve the best balance between reduced mass (high torque density) and decreased electric frequency (minimized core losses). The selection of number of slots is important, as it is the place where the windings will be accommodated. For 3-phase windings, 3 slots are required to accommodate 3 phases in each slot, however, each phase will be split into parallel paths thus the number of slots will be a multiple of 3.

Assigning the number of slots and poles, is not an independent decision, these two parameters are interrelated and should be carefully considered together during the design process. The interaction of the slot and poles influence the magnetic field harmonics; hence, the aim is to minimize these harmonics to boost the machine performance. Furthermore, proper selection of slot-pole can reduce cogging torque to have a reduced torque ripple. The slot number should always be even, this provides more symmetry to the design, thus larger proportion of the radial forces would counteract one another. The least common multiple (LCM) and the greatest common divider (GCM) between the slot and pole should be ideally maximized. By employing a high LCM, high frequency cogging torque is obtained, typically leading to a reduced cogging torque amplitude. The larger GCD normally results in lower radial forces, owing to the increased design symmetry[111].

4.9.2 Winding configuration

There are two prevalent winding configurations employed in electric machines. Concentric windings (CWs) overlapping and nonoverlapping, each coil is wound around a single tooth and Distributed windings (DWs) overlapping, coils are spread across a multiple of slots per pole per phase, resulting in a larger coil span. CWs depicted in Figure (4-7), have the advantage of short end windings, resulting in low winding resistance and a high slot fill factor. Consequently, they exhibit lower copper losses and a shorter stack length compared to DWs. Additionally, nonoverlapping CWs offer high inductance, essential for applications that demand a broad speed range. The winding layout is straightforward, simplifying the manufacturing process. However, the significant harmonic content in their MMF, high parasitic losses at high speed and high frequency.

In PM BLAC motors, DWs are extensively utilized due to their sinusoidal magnetomotive force MMF distribution. They provide an improved saliency ratio compared to CWs. As the slot per pole per phase is nearly equal to 1 in DWs, a unity winding factor can be achieved, resulting in high power density. However, DWs have some drawbacks, they are more challenging to manufacture compared to CWs, and their longer end windings lead to increased copper losses. Based on the above, for this thesis the DWs are going to be used as they provide a sinusoidal MMF distribution, which is needed in electric motors employed for EVs [55, 112-114].

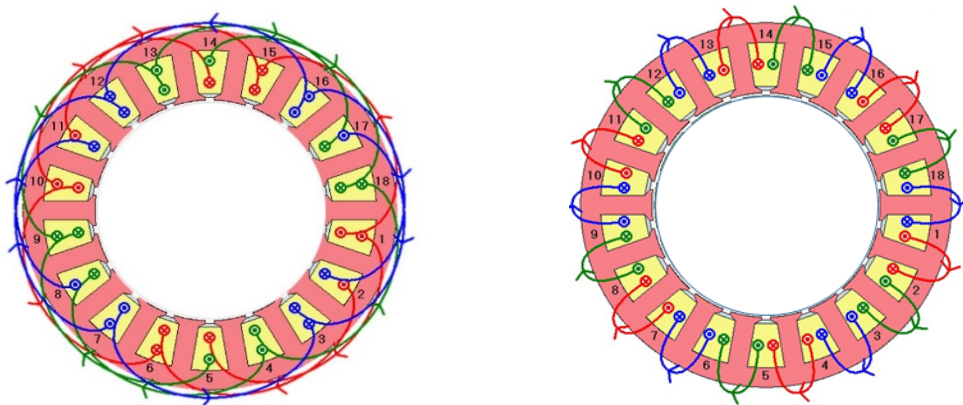


Figure 4-7 Distributed windings represented on the left side and concentrated windings on the right side

4.9.3 Material selection

4.9.3.1 Stator and rotor lamination

The selection of the stator's magnetic circuit material is a crucial determinant of an electric machine's performance, efficiency, and reliability. Utilizing lamination steel with superior magnetic properties, such as high permeability and low coercivity enables the effective conduction of magnetic flux. However, during recurring magnetization and demagnetization circulating currents known as eddy currents are generated leading to an increase in eddy losses. To mitigate these eddy current losses the stator is typically constructed from thin insulated laminations. Furthermore, the thermal conductivity of the chosen material is a significant consideration. A material with excellent thermal conductivity promotes efficient heat dissipation which is crucial for optimal performance. The selected material must also possess sufficient strength to withstand the physical stresses encountered during operation.

The B-H curve, which characterize electric steels have a saturation point that dictates the maximum power density. The flux density of electric steels hits a particular value beyond which it does not increase further, this threshold is known as the saturation point. Incorporating different additives, such as silicon to the metal can enhance this saturation point. A higher saturation value allows for a higher applicable flux density, thereby increasing the torque density of the machine. Each distinct addition to the steel alters the loss profile, which depends on several factors, including the frequency (f), the flux density (B). There is also material specific constant for hysteresis losses (k_h) and for eddy currents losses (k_e). A simplified representation of this is provided by the Steinmetz equation (4.21). These losses determine the maximum flux density and frequency that can be utilized while preserving high efficiency for a particular material.

$$P_{total} = k_h f^\alpha B^\beta + k_e f^2 B^2 \text{ (W/kg)} \quad [115] \quad (4.21)$$

The saturation point and loss profile of the stator play a crucial role, but the mechanical strength of the rotor is equally important. In specific machine configurations and applications, such as PMA-SynREL machine for automotive application. The machine speed is high, and the torque is high as well. Optimizing the rotor magnetic circuit is an important aspect to boost the machines performance. Having the PMs embedded in the rotor surface and enhancing the

proximity of PMs closer to the air gap significantly boost the machines performance. However, the high-speed rotation of the rotor exerts centrifugal forces on the PMs, thus imposing a limit on how close they can be to the rotor surface. The more robust the rotor material the less fragile it will be to mechanical stress. Thus, allowing the PMs position to be optimized as feasible as possible to maximize the motors performance[116].

EVs traction motors necessitate high power and high frequency operation which requires high-quality electric steel. Thus, careful selection of the stator and rotor material is a pivotal aspect of electric machine design. Figure (4-8) depicts a range of high-performance electric steels, characterized by their losses and yield strength. Silicon iron is denoted by blue marks, whereas cobalt iron is represented by red marks. For the stator material, low losses are crucial hence common usage of 10JNEX900 and NO20. While for the rotor the HXT steels are widely used in rotors due to their impressive strength and low loss characteristic. Their high strength properties make them an optimal choice for applications demanding robust rotor materials[117]. In this thesis, material NO10 for the stator and 35HXT780T for the rotor will be used. The materials characteristics are shown in Figure (4.9).

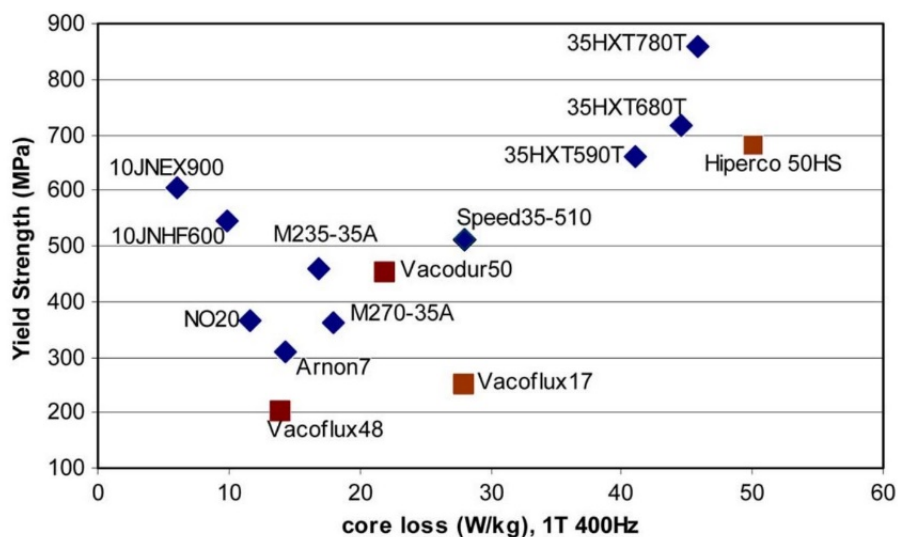


Figure 4-8 High performance electric steel[117]

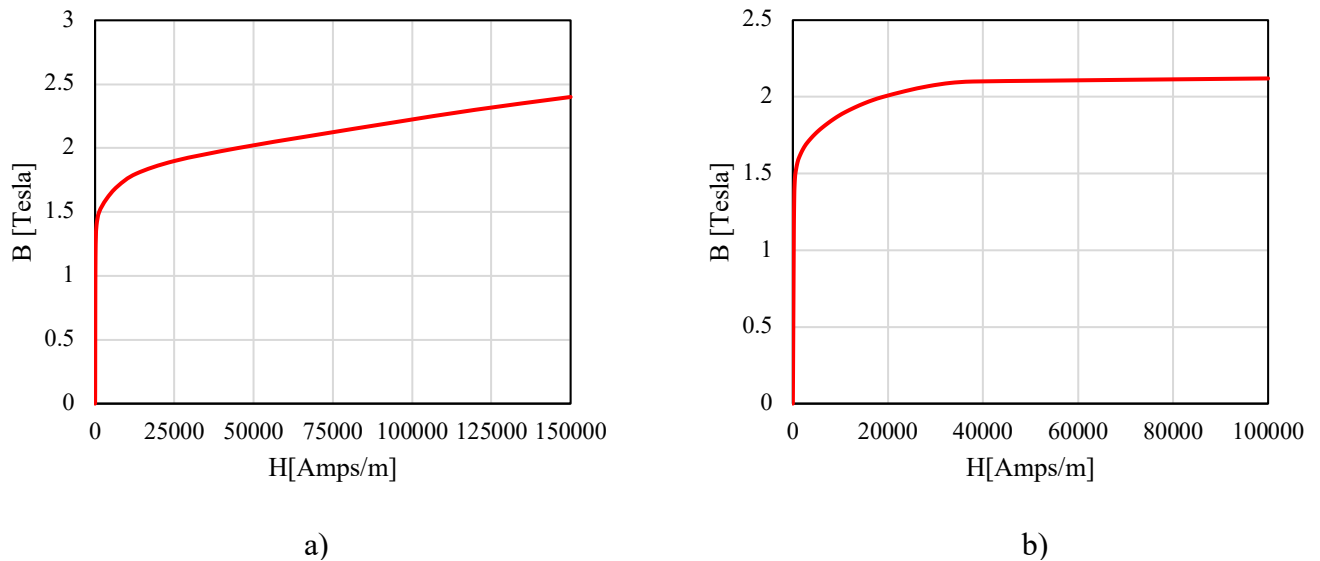


Figure 4-9 (a) N10 0.1 iron characteristic for the stator and (b) 35HXT780T iron for the rotor

4.9.3.2 *Permanent magnet material*

One of the most important components of a PMA-SynREL machine is the PMs, since it allows a persistent magnetic field to be maintained without the use of external energy. In PMA-SynREL machines these magnets are accommodated in the rotor flux barriers, they play a vital role in the performance of PMA-SynREL machine as they increase the torque density and efficiency. A PMs intrinsic magnetic properties produce a constant magnetic field. The performance of a PM is primarily dependent on its coercivity and remanence. A magnet with high coercivity exhibit greater immunity to demagnetization, while a magnet exhibiting high remanence is indicative of a more robust magnetic field.

The incorporation of the suitable PMs type in the construction of PMA-SynREL machines necessitate careful investigation. The selection of an ideal type is heavily influenced by factors such as its commercial accessibility, inherent magnetic and energy density properties, as well as its operating temperature capabilities. Commonly employed types of PMs include Samarium Cobalt (SmCo), Neodymium Iron Boron (NdFeB), AlNiCo, and Ferrites. Each type exhibits unique magnetic characteristics making it uniquely suited to specific applications. For example, Ferrite magnets demonstrate a moderate energy density and are relatively cost effective. AlNiCo magnets, in comparison outperforms all other magnetic material in terms of temperature operation. However, its performance is constrained due to inherent low coercive force. Contrastingly, NdFeB magnets are distinguished by their superior energy density values, although their maximum operating temperature is restricted to 230 C [118]. SmCo and NdFeB

both belong to the rare-earth magnet family. SmCo magnets outperform NdFeB magnets in handling heat, as they resist demagnetization better at high temperatures. They are also more affordable, mainly because NdFeB magnets use a lot of dysprosium, which is a costly rare-earth element. However, NdFeB magnets still lead the market in terms of energy strength[119].

4.9.4 Electromagnetic losses and efficiency

When an electric machine is operating, losses of energy occur within the machine reducing its efficiency and overall performance. Efficiency represents the proportion of electric power converted into mechanical power in EVs to propel the vehicle. Low efficiency traction machines have a significant impact on a EVs performance, especially in terms of battery life and range. Low efficiency implies that a significant portion of the electric energy is lost during the conversion process. These losses often manifest in the form of heat, vibration, and noise. The impact of a low efficiency traction machine on the vehicle's battery is that it consumes more power to deliver the same output power of a high efficiency machine. This increase in power consumption leads to the battery depleting more active power, thus the vehicle range is reduced for a single battery charge.

In order to design, analyse and optimize traction machines it is essential to have a thorough understanding of these losses. Generally, electric machines losses are classified into four main categories, ohmic losses, magnetic core losses, mechanical losses and stray losses[120]. The following section will focus on the electromagnetic losses in traction machines.

a. Ohmic losses:

In PM machines, ohmic losses are primarily due to the resistance of the machine's stator winding due to the rotor is free from copper. These losses (DC losses) are proportional to the square of the current i , as indicated in equation (4.22), and are therefore load dependent.

Additionally, they can also be frequency-dependent (AC losses). As the speed of the motor increases the frequency increase leading to an increase in the skin effect. This effect causes the current to concentrate on the outer surface of the conductor, effectively reducing its cross-sectional area and increasing its resistance. This leads to higher copper losses. To mitigate skin effect losses, one approach is to divide conductors into several strands as illustrated in Figure (4-10).

At high operating frequencies, particularly in the range of hundreds of Hertz, AC losses become a significant contributor to total losses in traction motors. An effective method to reduce these AC losses is by using multi-strands and positioning the windings away from the slot opening. This technique can decrease AC losses by at least 79.2%.

In machines operating at frequencies up to 500 Hz, proximity losses and flux leakage are the dominant factors, while at frequencies up to 2000 Hz skin effect losses becomes a concern. In traction motors, proximity losses predominantly affect base speed AC losses, whereas at maximum speed, skin effects losses are more dominant. However, by reducing the conductor diameter below the skin depth, the skin effect issue can be effectively addressed[121].

Research has shown that for high frequency machines (over 1 kHz), unconventional design choices such as a reduced copper fill factor and thinner strands can lead to increased efficiency. These factors are vital for cooling requirements. Addressing these losses early in the design phase can have a positive impact on the cooling system, potentially reducing its size, mass and cost[122].

$$P_{cu} = i^2 \times R_{DC} \quad (4.22)$$

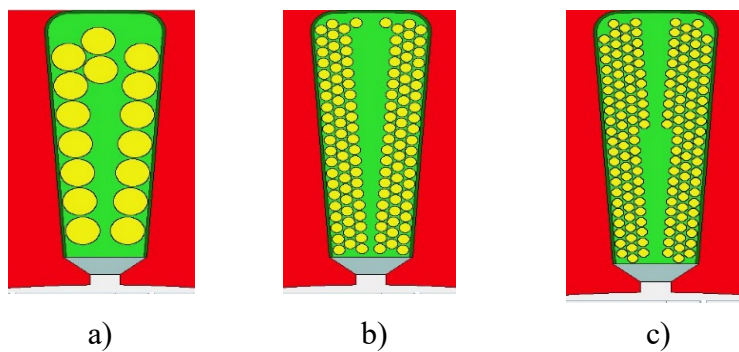


Figure 4-10 Double-layer per slot (a) 8 turns/1strand (b) 8 turns/8strands and (c) 8 turns/10 strands

b. Iron losses:

Iron losses are classified as hysteresis losses and eddy current losses. Eddy current losses are caused by the induced currents circulating within the core by the variable magnetic field. These losses are directly proportional to the square of both frequency (f) and the flux density (B). The material thickness (t) also is an important factor that increases the eddy current losses in the magnetic material core as shown in equation (4.23). Therefore, it is customary in the area of electric machines, that the stator and rotor are divided into laminated steel to increase the material electric resistivity. The thinner the laminations the less eddy currents will be produced[123]. Hysteresis losses occur due to the continuous magnetization and demagnetization of the core material. These losses are proportional to the flux density and frequency as shown in equation (4.24). Several constants, derived from the material's properties, are associated with hysteresis and eddy current losses. These include k_h , α , and β for hysteresis losses, and k_e for eddy current losses as shown in equation (4.23) and (4.24).

$$P_e = k_e f^2 B^2 t^2 \quad (4.23)$$

$$P_h = k_h f^\alpha B^\beta \quad (4.24)$$

c. Permanent magnet losses:

PMs have an inherent sensitivity to temperature, which affects their magnetic properties. The Curie temperature is a critical point where the magnetic properties of PMs begin to degrade due to heat. Therefore, choosing a high-quality PM becomes crucial to maintain a high magnetic flux even at elevated temperatures. It's also important to note that strong external magnetic fields from the stator can interfere with the rotor PMs, leading to demagnetization.

Similar to how the stator and rotor iron are laminated into thin sheets to minimize eddy currents, the magnets can also be segmented to achieve the same effect. The placement of magnets is equally important, as reducing the airgap moves the rotor's magnets closer to the stator, leading to higher losses in the magnets. Therefore, machine designers must optimize both the stator and rotor designs to minimize magnet losses and enhance efficiency.

When PMs are embedded in the rotor lamination, a rotor material with high resistivity can help mitigate eddy currents. A rotor with high magnetic permeability improves the magnet flux

linkage between the stator and rotor, reducing PM losses. The cooling method implemented should also ensure that PMs are effectively cooled down to preserve their magnetic properties.

4.9.5 Cooling options

As mentioned in the previous section, machine losses cause a reduction in efficiency, the output mechanical power will decrease, and hence the battery of the vehicle will deliver more power to maintain the required output power. The machine losses are a primary source of heat. To prevent excessive heat from damaging the machine's components, it is necessary to cool down the hot spots. If the machine is over the permissible temperature limit, the winding insulation will be damaged, the iron core will degrade, and the PMs will not provide adequate flux. In all operating conditions of the machine, it is critical that the machine maintains a safe temperature. A traction machine used in an EV application is most likely to reach its highest temperature at times of peak power and maximum speed. Therefore, it is crucial to estimate losses in order to select a cooling system that will limit the rise in temperature.

At the design stage of the machine, thermal analysis is coupled with electromagnetic analysis in FEA software. This is to design a machine that has a high power to mass ratio as feasible as the cooling method can maintain temperature within limits. While increasing the current density during the design stage leads to a lower machine volume, the upper limit of the density is limited by the cooling methods available to the designer.

Water-Jacket is a cooling system that is used widely in traction motors for EVs. It is integrated in the machine housing. Its principle of operation is it circulate a liquid coolant around the stator surface to absorb the generated heat. The inlet liquid can be ethylene, glycol, deionized water or dielectric fluids[124]. Another cooling method is spray cooling. Spray cooling is a closed-loop system comprised of a coolant, tank, pump, spray nozzles, and a cooling temperature module. The pump boosts the pressure of the fluid from the tank to the spray nozzle. Afterwards, the nozzle disperses the coolant over the heated surfaces as tiny droplets. A temperature regulation unit collects the liquid coolant or as a blend of liquid and vapor in a dual-phase system to remove absorbed heat and prepare the coolant for recirculation[125].

In this thesis, two cooling systems water-jacket and spray cooling will be investigated in the design process. The aim is to design a machine that meets the required specifications, the

cooling options will be tested on the machine in simulations. The decision on which cooling system will be used, is going to be determined in the design process.

4.10 Initial machine design

In this section the design process is commenced, after identifying the machine specification in section (4.2). The machine configuration is identified, decisions about key parameters of the motor such as number of slot-pole, winding type, material have been justified in section (4.9).

This section focuses on the design of an 8-pole 48-slot PMA-SynREL machine. 8-pole 48-slot machine shows a good compromise of speed and frequency. Furthermore, the slot per pole per phase is equal to 2. The winding factor is equal to 0.966.

4.10.1 Stator sizing

Based on the machine specifications tabulated in Table (4-1), the preliminary design stage is initiated. An important factor in sizing a traction machine is the available supply DC voltage, which is 620 Volts. The maximum RMS phase voltage E_{MAX} can be calculate by equation (4.25), where V_{dc} is the DC bus voltage. Thus, the design must operate within this voltage constraint.

$$E_{MAX} = \frac{V_{dc}}{\sqrt{6}} \quad (4.25)$$

This initial design, which intends to use distributed windings requires that the number of slots per pole per phase q be an integer. This is explained in equation (4.26), where Q represents the total number of slots, p is the number of pole pairs, and m denotes the number of phases. The winding factor k_w represented in equation (4.27) is an important factor that determines how effective the machine voltage produces effective magnetic field, it is influenced by q . In this initial design, an 8-pole 48-slot PMA-SynREL machine will be investigated which has a winding factor equal to 0.966.

$$q = \frac{Q}{2pm} \quad (4.26)$$

$$k_w = \frac{\sin\left(\frac{\pi}{6}\right)}{q \sin\left(\frac{\pi}{6q}\right)} \quad (4.27)$$

An initial assumption based on envelop size is made, the stack length is set to 200mm which is less than the maximum axial length of the machine envelop by 44%. The available cooling method is water-jacket in the initial design phase, therefore an electric loading equal to 99 kA/m and the continuous RMS current density 10 A/mm^2 is assumed[126]. The torque is developed as in equation (4.28), where D is the stator bore diameter, k_w is the winding factor, L_{stack} is the stack length of the motor, B is the fundamental airgap flux density RMS value and A is the electric loading. In equation (4.28), the stator bore diameter is not known but the required peak torque is known. Thus, based on equation (4.29) the initial stator bore diameter is established. It is critical to note that the stator bore diameter must be design based on the peak torque of machine. Although, it is required for 30s as stated in the specification, the stator bore diameter has to be designed to prevent any excessive saturation at this peak torque and associated thermal limit.

$$T = \frac{\pi}{2} \cdot k_w \cdot D^2 \cdot L_{stack} \cdot B \cdot A \quad (4.28)$$

$$D = \sqrt{\frac{2T}{k_w \cdot \pi \cdot L_{stack} \cdot B \cdot A}} \quad (4.29)$$

The flux per pole ϕ is determined using equation (4.30). It's important to note from this equation that any increase in either the stack length L_{stack} or the stator bore diameter D results in a higher flux per pole. This implies that as the volume increases, more flux is generated leading to greater torque production.

$$\phi = \frac{\pi D}{2p} L_{stack} B \quad (4.30)$$

The number of turns per phase N_{ph} can now be calculated from equation (4.31), where I is the maximum RMS current the supply can provide, it is available in the machine specifications 660 Amps RMS.

$$N_{ph} = \frac{A \cdot \pi D}{2 \cdot m \cdot I} \quad (4.31)$$

The RMS electromotive force (EMF) per phase, as outlined in equation (4.32), is determined by several key factors. These include f representing the electrical frequency, k_w the winding factor, ϕ the flux per pole and N_{ph} the number of turns per phase. In light of these factors, it is essential to design all components that influence the EMF in alignment with the constraints of the available supply RMS voltage. This ensures that the machine operates efficiently and safely within the prescribed voltage limits, especially at its maximum speed.

The sensitivity of EMF to frequency changes is an important aspect to consider. This becomes particularly crucial when the machine operates at its maximum speed of 15,000 rpm. At this speed, the EMF must comply with the supply RMS voltage limit, as shown in equation (4.25). To achieve this compliance, flux weakening strategies are applied at high speeds.

$$E_{ph} = 4.44 f k_w N_{ph} \phi \quad (4.32)$$

After, the stator bore diameter D was determine in equation (4.29), the slot pitch λ_s , pole pitch λ_p can be computed by applying equations (4.33) and (4.34).

$$\lambda_s = \frac{\pi D}{Q} \quad (4.33)$$

$$\lambda_p = \frac{\pi D}{2p} \quad (4.34)$$

The tooth width w_{tooth} and yoke width w_y can be computed by applying equations (4.35) and (4.36), where B_{peak} represents the fundamental peak of airgap flux density, B_t is the saturation tooth flux density and B_{bi} is the saturation back iron flux density.

$$w_{tooth} = \frac{B_{peak} \cdot \lambda_s}{B_t} \quad (4.35)$$

$$w_y = 0.5 \cdot \frac{B_{peak} \cdot \lambda_p}{B_{bi}} \quad (4.36)$$

As the current density is set at 10 A/mm^2 and the fill factor is 0.45. The copper area in all slots S_{cu_all} is calculated as shown in equation (4.37). Increasing the number of turns per phase N_{ph} or current I for a fixed current density and fill factor would require an increase in copper area.

$$S_{cu_all} = \frac{2mIN_{ph}}{J \cdot k_{fill}} \quad (4.37)$$

After the copper area is found in equation (4.37), the back iron diameter D_{bi} which is the stator bore diameter plus the slot depth is calculated by computing equation (4.38) and (4.39), in equation (4.38) a 0.5 factor is introduced due to that other nonconductive material also occupies the slot.

$$S_{cu_all} = 0.5 \frac{\pi}{4} (D_{bi}^2 - D^2) \quad (4.38)$$

$$D_{bi} = \sqrt{\frac{8S_{cu_all}}{\pi} + D^2} \quad (4.39)$$

The stator outer diameter D_{so} can be calculated by equation (4.40).

$$D_{so} = D_{bi} + 2w_{bi} \quad (4.40)$$

4.10.2 Rotor sizing

The sizing of the rotor in PMA-synREL machines is crucial. This rotor includes flux barriers, as indicated in Figure (4-11). It's vital to properly size the rotor islands thickness ($wb1, wb2, wb3$) shown in Figure (4-11) to carry the flux without causing saturation, which would negatively impact performance. The flux barrier's inner thickness ($h1, h2, h3$), outer thickness ($b1, b2, b3$), inner width ($w1, w2, w3$) and rotor island's ($wb1, wb2, wb3$) dimensions significantly affect the reluctance torque. Sizing these dimensions is essential to enhance the reluctance torque and reduce the amount of magnets needed.

PMs are employed to saturate the iron islands, thus improving the machine's power factor. Radial and tangential ribs as indicated in Figure (4-11) are incorporated to ensure the rotor's mechanical integrity. In terms of magnet thickness and width, it is initially assumed to correlate with the flux barrier dimensions. All flux barriers inner thickness (h_1, h_2, h_3) and rotor islands thickness (w_1, w_2, w_3) are presumed to have equal dimensions initially. The radial and tangential ribs of the rotor are designed to be 0.5 mm thick, which is the minimum due to manufacturing constraints. The web thickness (x, y, z), as shown in Figure (4-11), is critical for minimizing torque ripple. Primarily, it is assumed that all web thicknesses are equal. The flux barrier outer thickness denoted as (b_1, b_2, b_3) in Figure (4-11) are important not only to boost reluctance torque but to maintain the mechanical integrity. Initially, it is assumed that all flux barrier outer thicknesses are equal. In the optimisation, the inner width (w_1, w_2, w_3) is calculated automatically.

During the optimization phase, all rotor parameters are fine-tuned to maximize torque and minimize magnet usage. A key aspect is maintaining mechanical integrity while balancing electromagnetic and mechanical performance.

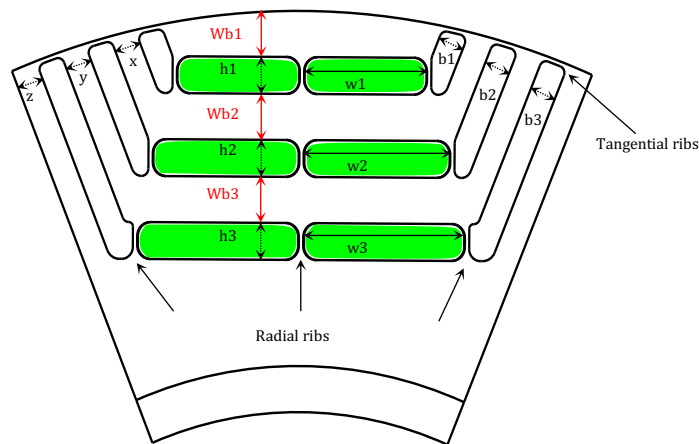


Figure 4-11 Rotor sketch of a PMA-SynREL machine

The initial design is refined using the modeFRONTIER commercial genetic algorithm software by ESTICO. This process is supported by a comprehensive MATLAB script, which included all geometric inputs and detailed electric input parameters for integration with Motor-CAD. The script is designed to transfer crucial operating point data to Motor-CAD, enabling the

precise calculation of key motor performance metrics such as peak torque at base speed, continuous torque at base speed and maximum speed torque. Furthermore, the script is tailored to address potential geometric overlaps due to rotor parameter configurations, ensuring their avoidance. Table (4-2) presents the ranges and initial values of both stator and rotor geometric variables.

Table 4-2 Geometry initial values and optimization range

Stator variables (mm)	Initial value	Range
Back iron	17.1	12-21
Tooth width	5.8	4-7
Slot depth	26.9	20-33
Slot opening	2.2	1.5-3
Tooth tip depth	1	1-3
Rotor variables (mm)	Initial value	Range
wb1,wb2,wb3 (rotor islands thickness)	5	1-6
h1,h2,h3 (flux barriers inner thickness)	5	1-6
b1,b2,b3 (flux barrier outer thickness)	6	1-6
x,y,z (web thickness)	3	1-6
Radial ribs	3 mm	0.5-3

4.10.3 Machine dimensions and materials

The dimensions, material and winding characteristics of the designed PMA-SynREL machine, as depicted in Figure (4-12), are detailed in Tables (4-3), (4-4) and (4-5).

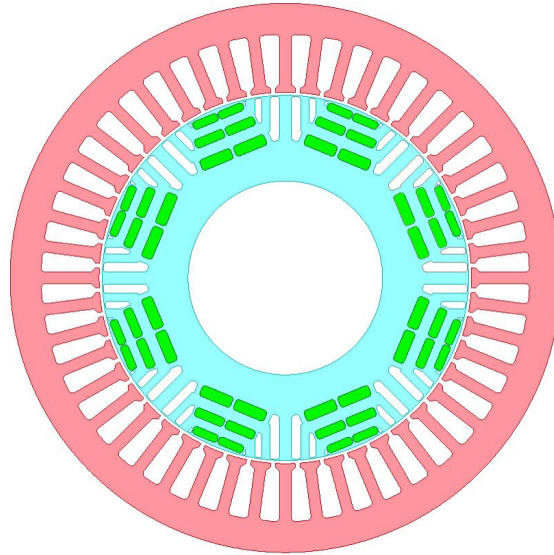


Figure 4-12 Geometry model 8-pole 48-slot

Table 4-3 Radial and axial dimensions of the 8-pole 48-slot

Radial Dimensions	Value
Back Iron	14 mm
Tooth width	5.5 mm
Slot opening	2.36 mm
Tooth tip	2 mm
Number of slots	48
Slot depth	28 mm
Air gap	1.5 mm
Rotor outer	177 mm
Number of poles	8
Number of flux barriers	3
Axial Dimensions	Value
Stack Length	195.5 mm
L/D	1.10

Table 4-4 Machine materials and weight

Component	Material used	Weight (kg)
Stator	N10 0.1 strip	27.51 kg
Rotor	35HXT780T	17.57 kg
Magnets	NdFeB-N42UH	4.93 kg
Windings	Copper pure	13.65 kg
Total active weight		63.66 kg

Table 4-5 Windings Characteristics of machine windings

Design	Value
Winding type	Distributed windings
Winding layers	Double-layer
Parallel Paths	8
Number of turns per phase	16

4.11 Winding type

This motor employs a three-phase supply, phase A, B and C. Thus, the motor requires 3 slots to accommodate 3 phases. However, the designed motor has 8 parallel paths as shown in Figure (4-13b) for each phase, equal to the number of poles. This will reduce the current fed into the slot, and it will be easy to manufacture a coil with a reduced cross section. The type of windings is a distributed winding, the windings are distributed over several slots per pole per phase. Each slot accommodates two turns (double-layer), this leads to more sinusoidal magnetic field that can improve the motors efficiency and torque production.

The number of slots per pole per phase is equal to 2 which is an integer that leads to a winding factor nearly equal to 1. This leads to making the motor more effective at producing a magnetic field from the current supplied. The amount of copper occupied to the slot area is identified as the fill factor. The fill factor is identified as the ratio between the areas of the occupied copper in the slot over the slot area. Theoretically, 100% fill factor ratio will give the highest power and lower copper losses. However, practically the slot area is occupied by slot insulation, conductor insulation and unavoidable gaps. Therefore, fill factor ratio is always lower than

100%. The wire shape also contributes to identify the fill factor ratio. Employing high fill factor will lead to manufactory complexity therefore, 45% fill facto ratio is selected in this project.

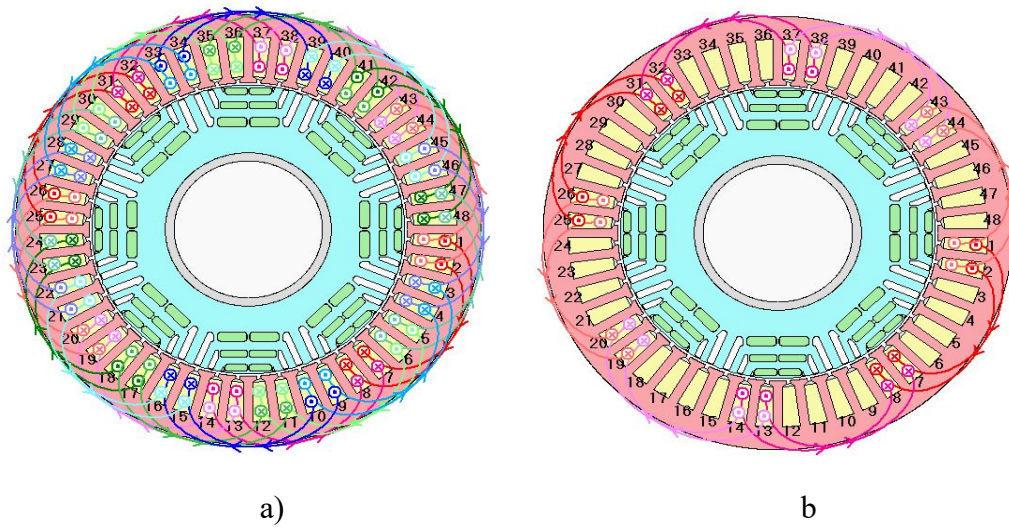


Figure 4-13 (a) 3-phase distributed windings (b) phase A with 8 parallel paths

Figure (4-14) illustrates different fill factor values. It can be observed that an increase in the fill factor leads to more copper occupying the slot area. This results in higher efficiency due to reduced copper losses. However, this also reduces the space available for the flow of cooling air. Consequently, the selection of the fill factor often involves a compromise between copper utilization and thermal management. A fill factor of 0.45 has been chosen, signifying that 45% of the slot volume is filled with copper, while the remaining 55% is occupied by insulation, air, and other non-conductive materials.

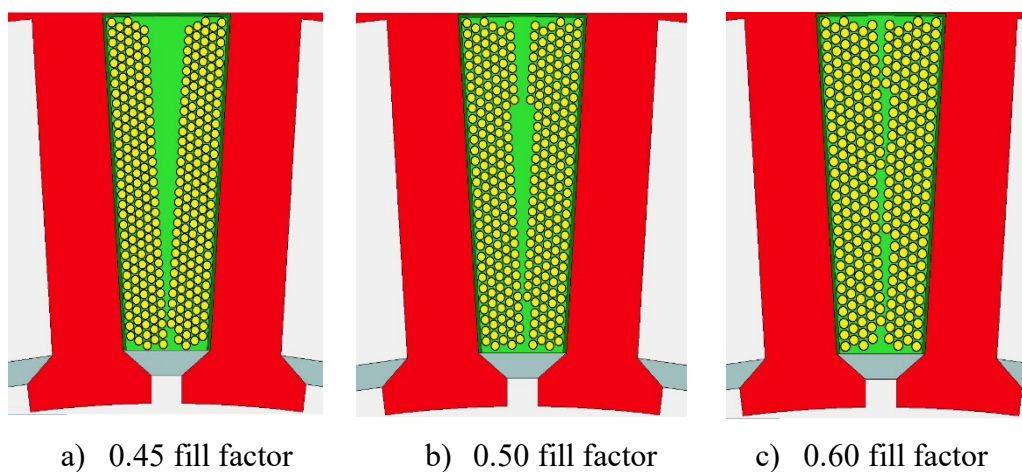


Figure 4-14 Slot with different fill factor

Equation (4.41) presents the formula for current density, which is a key factor in the design process. This equation involves various elements: I represents the electric current, a denotes the parallel paths, n is the number of turns per coil, S_{slot} is the area of the slot, and k_{fill} signifies the fill factor. Current density, defined as the amount of electric current per unit cross-sectional area of the copper windings, is crucial for design considerations. As increasing the current density increase the torque of the machine, hence a reduce machine weight can be achieved. However, a balance must be reached between fill factor k_{fill} and slot area S_{slot} and number of turns per coil n . More importantly, heat generation is correlated to current density and what governs the available current density is the available cooling method.

$$J = \frac{I}{a} \times \frac{2n}{S_{slot} \times k_{fill}} \quad (4.41)$$

4.12 Electromagnetic results

The input power to the machine is restricted by the available DC-link voltage and the maximum RMS current. Thus, it must be ensured that the designed motor does not operate outside these limits. By imposing a balanced three-phase current supply, the peak torque and continuous torque at base speed (5000 rpm) and continuous torque a maximum speed (15000 rpm) are achieved as shown in Figure (4-15).

It can be seen that the designed motor generates 578 Nm electromagnetic torque at base speed (5000rpm) with a 660 (RMS) Amps peak current. The corresponding torque ripple is 16.7 % this is due to the saturation effect as shown in the flux density plot Figure (4-18a). While for the continuous current 460 RMS Amps the motor generates a 412 Nm electromagnetic torque at base speed (5000rpm), the torque ripple for the continuous torque is 14 % less than the torque ripple at peak current due to less saturation effect as shown in the continuous flux density plot Figure (4-18b).

At maximum speed (15000 rpm), the motor generates a torque equal to 184 Nm with 35.34 % torque ripple as shown in Figure (4-15). This reduction in torque at maximum speed is due to the flux weakening control strategy to keep the motor voltage within the permissible voltage limit of the inverter. As the motor speed is increasing the frequency of the current is increased hence, the voltage will reach its rated value. Flux weakening becomes required and a negative

Id-current is required to oppose the magnets flux. The high torque ripple at top speed is 35.34 % this is due to the motor inherent characteristics and the nature of the flux weakening process.

For heavy-duty trucks, it's essential to reduce the torque ripple from 35% to 10% at maximum capacity. Torque ripple presents a significant challenge in PMA-SynREL machines. To address this, machine designers often employ mitigation techniques like rotor skewing[34, 127]. In this design, when operating at its maximum speed, the electromagnetic torque reaches 184 Nm exceeding the machine's target of 140 Nm. Therefore, introducing rotor skewing at a later stage is an effective strategy to manage the torque ripple issue while preserving the average torque.

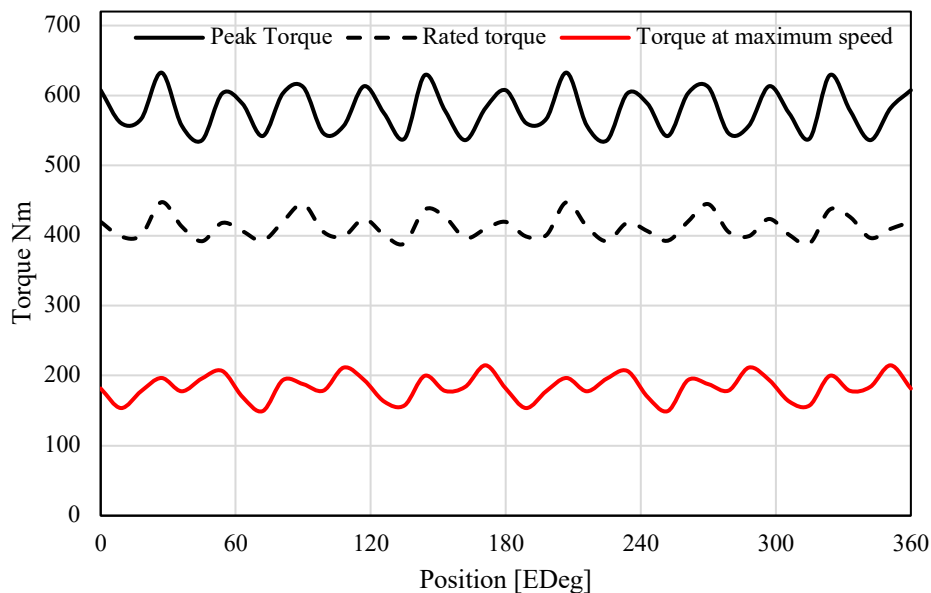


Figure 4-15 Electromagnetic output torque for peak and rated operation at base speed and rated torque at maximum speed

The torque and speed profile is shown in Figure (4-16) for peak and continuous operation. The peak operation is capable to reach a base speed of (6000 rpm) and the continuous torque reached a base speed of (6500 rpm). The voltage supply of the inverter determines the base speed, for the peak operation field weakening started earlier the rated operation due to the saturation, the flux from the rotor and stator contribute to increase the voltage beyond its limits therefore, field weakening is applied to keep the voltage within limits. Hence, having the voltage controlled by MTPA (maximum torque per ampere) technique by adjusting the phase advance angle to have a constant power range.

Figure (4-17) depicts the phase voltage with speed for the rated operation (continuous current), the applied control strategy attempts to find the phase advance angle which gives the maximum torque per ampere. Once the voltage reaches its rated value the phase advance angle is changed with speed to keep the voltage within limits. The phase advance angle is important to be optimized to find the highest torque at base speed and maximum speed. It can be seen from Figure (4-17), that the phase advance is increased to reach a value 78.86. Table (4-6) compares the results of this initial design at base speed (5000 rpm) and maximum speed (15000 rpm) with the machine targets.

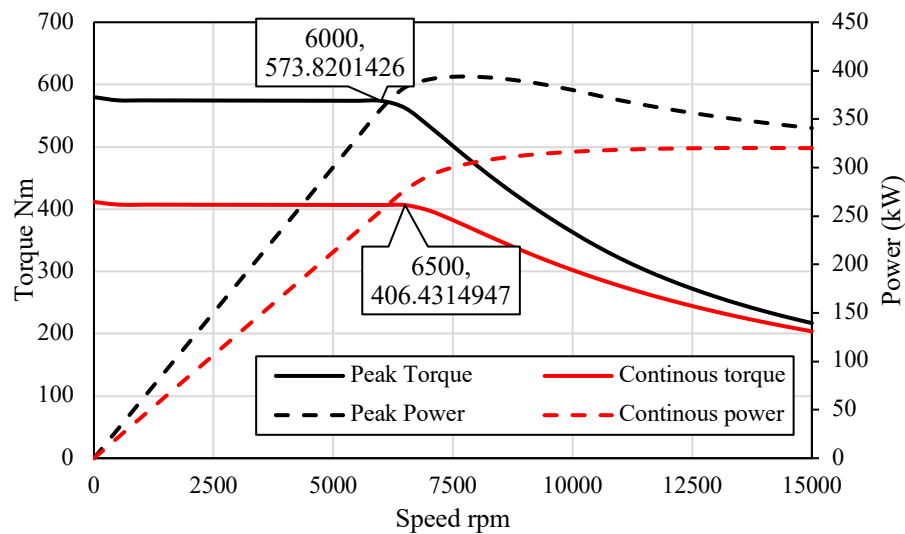


Figure 4-16 Output Torque /Power vs speed

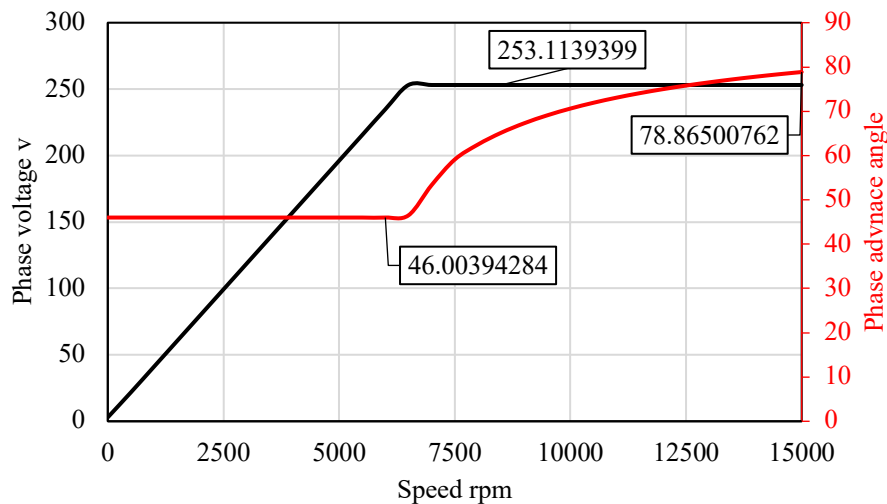


Figure 4-17 Phase voltage across speed and the phase advance angle

Table 4-6 Comparison of initial machine design to machine target

Requirements	Target	Initial design	
Maximum phase current	660 A	660 A	✓
DC-link voltage	620 V	620 V	✓
Peak Torque @ 5000 rpm	526.8 Nm	573 Nm	✓
Peak Power @ 5000 rpm	274 kW	300 kW	✓
Rated Torque @ 5000 rpm	401.1 Nm	406.74 Nm	✓
Rated Power @ 5000 rpm	210 kW	213 kW	✓
Rated Torque @ 15000 rpm	140 Nm	172 Nm	✓

The flux density plots for the designed PMA-SynREL motor depicts the magnetic flux density within various operating regions as shown in Figure (4-18). At base speed, there are two operating regions peak torque and continuous torque. The current in this region is changed based on the needed torque, peak torque which draws a 660 RMS current from the supply while the continuous torque requires a 460 RMS current. The magnetic flux density varies in this region, as it primarily determined by the current in the motor windings and the phase advance angle as shown in Figure (4-18a) and (4-18b).

At maximum speed, the motor operates in the flux weakening region. The magnetic field is reduced by advancing the phase advance angle to prevent the motor voltage from exceeding the DC-link voltage as shown in Figure (4-18c).

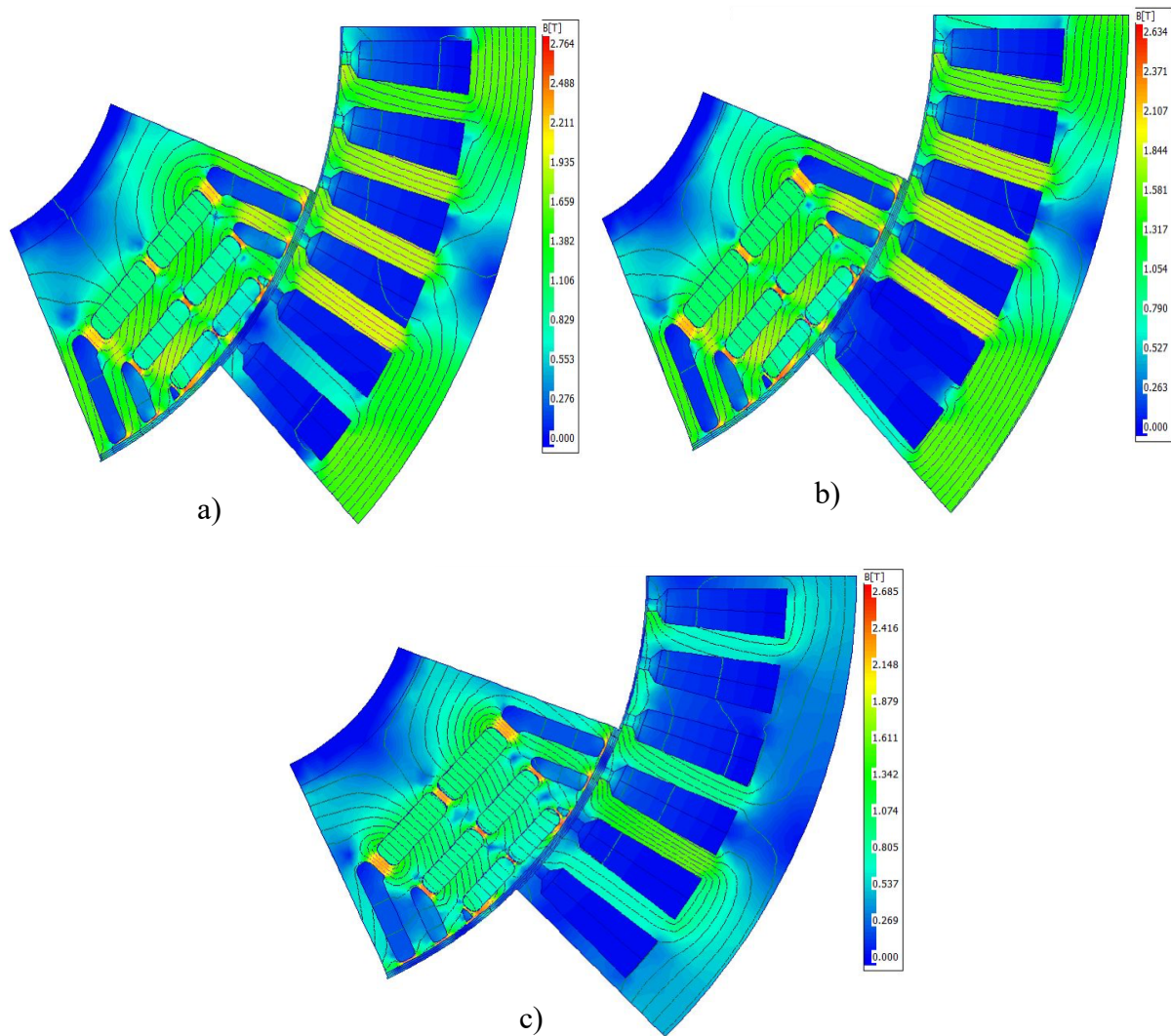


Figure 4-18 Flux density distribution at (a) Peak torque base speed (b) Continuous torque base speed and (c) Continuous torque max speed

4.13 Reluctance torque vs magnetic torque

The following section will show the breakdown of reluctance torque and magnetic torque for the designed motor. It will emphasise the impact of having magnetic torque with reluctance torque to achieve high torque at all operating conditions in the machine. Figure (4-19) depicts the share of reluctance torque with magnetic torque. The contribution of the reluctance torque to the total output torque appears to be more significant than that of the magnetic torque. However, the magnetic torque which constitutes 32.14% at maximum speed is essential for enhancing the total torque. This is particularly noticeable in the field weakening range, where the significant contribution from the magnetic torque helps to offset the reduction in reluctance torque. The phase advance angle is optimized in all operation conditions to find the maximum overall torque.

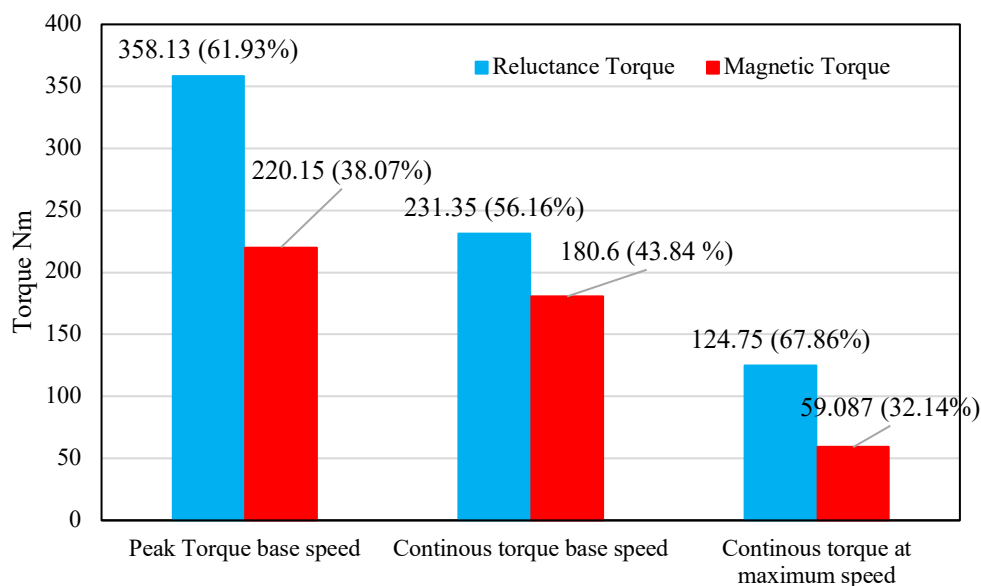


Figure 4-19 Magnetic Torque and Reluctance Torque share at all operation conditions base speed(5000rpm) and Maximum speed (15000 rpm)

4.14 No-load test

A critical characteristic of electric machines is the back-EMF. In PMA-SynREL machines, magnets are placed in the rotor. When the motor operates the inverter supplies voltage to its terminals to generate the rotating magnetic field which then creates torque causing the rotor to spin. As the rotor spins the PMs field cuts through the armature windings in the stator and induces voltage in the windings. This induced voltage is the back-EMF. The magnitude of the back-EMF is proportional to the speed of the motor. Therefore, as the motor speeds up the

back-EMF increases, reducing the net voltage across the windings and thus reducing the current draw. Back-EMF is a critical characteristic and hence, analysing the back-EMF waveform can yield several important insights. Irregularities in the back-EMF waveform can indicate issues like cogging torque and torque ripple which can affect the motor performance. By analysing the Fast Fourier Transform (FFT) of the back-EMF waveform, the presence of harmonics can indicate non-ideal operation. From the motor specifications the maximum speed is 15000 rpm, this indicates that the back-EMF magnitude will be high, however, with control strategy applied the PMs flux will be weakened by a negative I_d to reduce the total flux of the machine at elevated speeds.

As shown in Figure (4-20), the back-EMF is increasing linearly with speed. Therefore, field weakening is required to limit the effect of PMs in the rotor to keep the voltage supply within limits. Furthermore, the Back-EMF Line-Line at maximum speed is shown in Figure (4-21a). It is evident that the back-EMF waveform is not nearly sinusoidal. The FFT of the back-EMF waveform is shown in Figure (4-21b), from the harmonic spectrum it is clear the 3rd harmonic is not present, this is due that the machine employs a balanced 3-phase star connection, and thus triple harmonics are in phase. In this context, the harmonics that are of concerned are 5th, 7th and 11th harmonics. With rotor skewing a more sinusoidal back-EMF can be achieved. This will be reflected on the machines torque ripple at maximum speed.

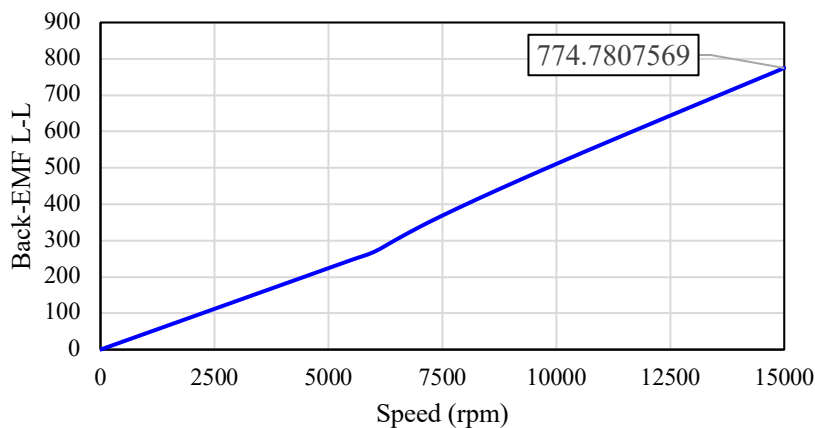


Figure 4-20 Back-EMF Line-Line with speed (rpm)

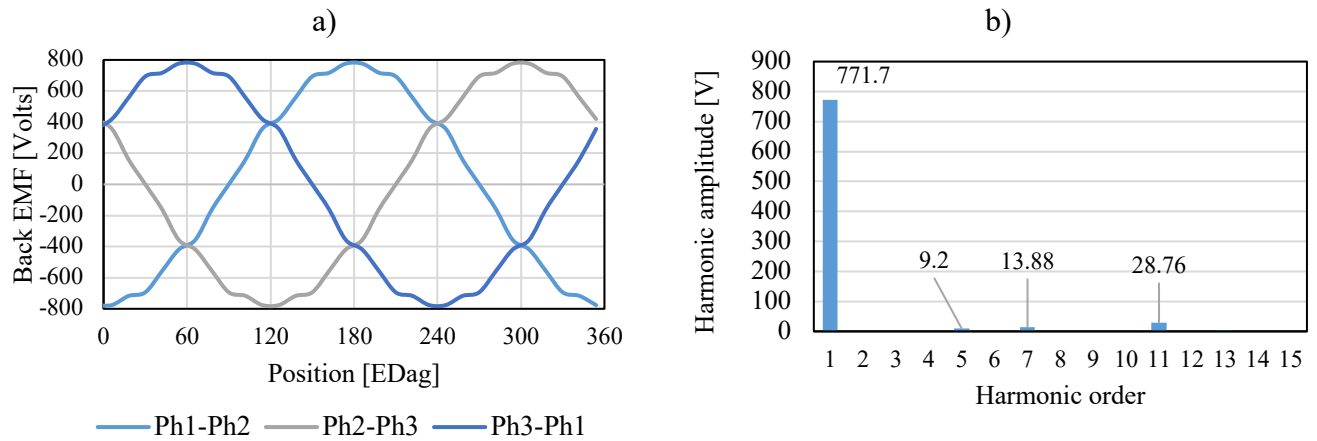


Figure 4-21 (a) back-EMF Line-Line at 15000rpm (b) FFT of Back-EMF at 15000rpm

4.15 Electromagnetic losses and efficiency of the designed machine

This section identifies the losses of the designed machine. During the energy conversion from electrical to mechanical some of that energy is lost and manifested as heat. The machine efficiency can be improved by looking at the quality of the materials used to conduct the energy. The cooling option to manage the heat and prevent overheating is decided based on the amount of heat generated. The aim of this section is to identify the losses behaviour in the machine.

The copper losses in the machine, are due to the winding resistance and the skin effect that happens with the frequency increasing. Figure (4-22a), illustrate the copper losses of the machine during the rated torque operation. It is clearly evident that the copper losses become dominant at high speed. The cooling system must be efficient and capable to maintain the temperature of the winding below 180C to prevent overheating.

The stator iron losses are shown in Figure (4-22b), due to the magnetization and demagnetization of the stator core, iron losses arise this include hysteresis and eddy currents. These losses are directly affected by the frequency of the current. Beyond the base speed, field weakening occurs resulting in a reduction of the machine field. This decrease can initially mitigate the stator losses. However, as the speed continues to increase these losses will persistently increase due to the corresponding rise in frequency. The rotor iron losses are represented in Figure (4-22c), like the stator iron the rotor iron is having hysteresis losses and eddy current losses, and as the rotor is moving the nature and magnitude of these losses look different from the stator losses. Furthermore, the rotor slots have PMs embedded, the magnets

start to lose their persistent flux magnitude when exposed by an external field from the stator, as mentioned earlier that the eddy currents are directly affected by the frequency, the magnet losses increase with speed as shown in Figure (4-22d).

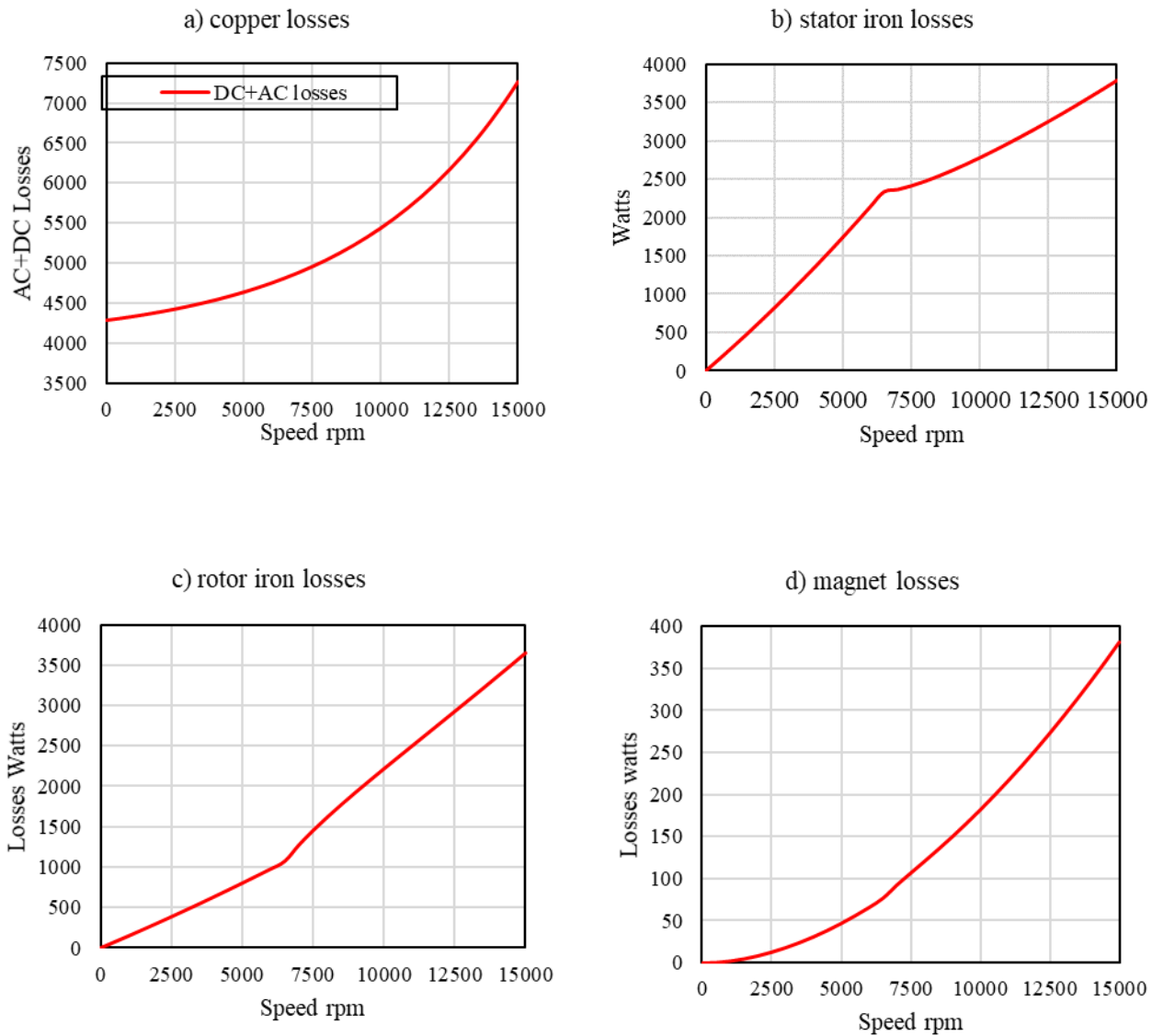


Figure 4-22 Electromagnetic loss (a) copper losses (b) stator iron losses (c) rotor iron losses and (d) PM losses

At top speed (15000 rpm) it is clear from Figure (4-22) that machine losses at this speed are significant compared to the base speed (5000 rpm). However, efficiency at top speed is maintained at 96.4 %. The reason is, at top speed flux weakening is applied thus, the power factor is improved. At top speed the power factor is 0.95 whereas at base speed its 0.81 as shown in Figure (4-23). This helps draw more power from the inverter and consequently more

output power is achieved to recover the power losses. Continuous operation efficiency plot is shown in Figure (4-24).

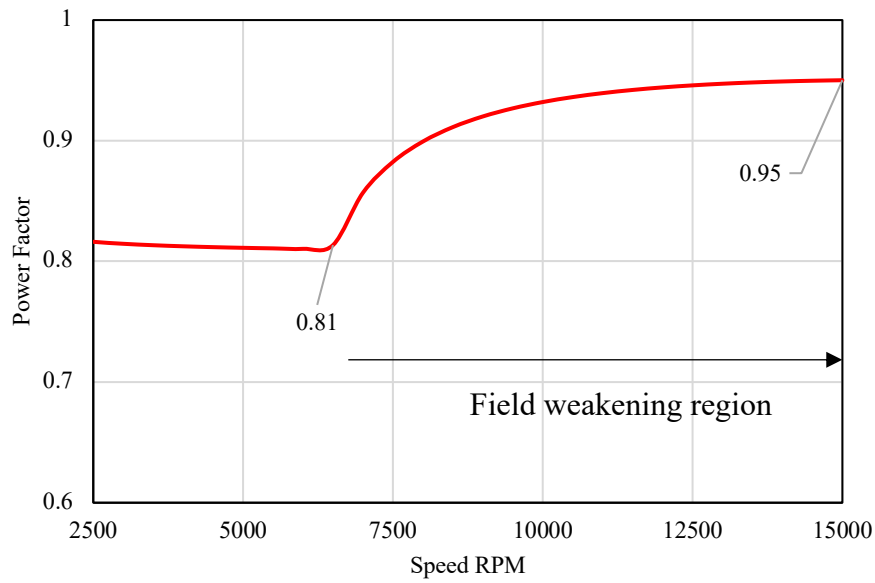


Figure 4-23 Power factor of machine at rated power

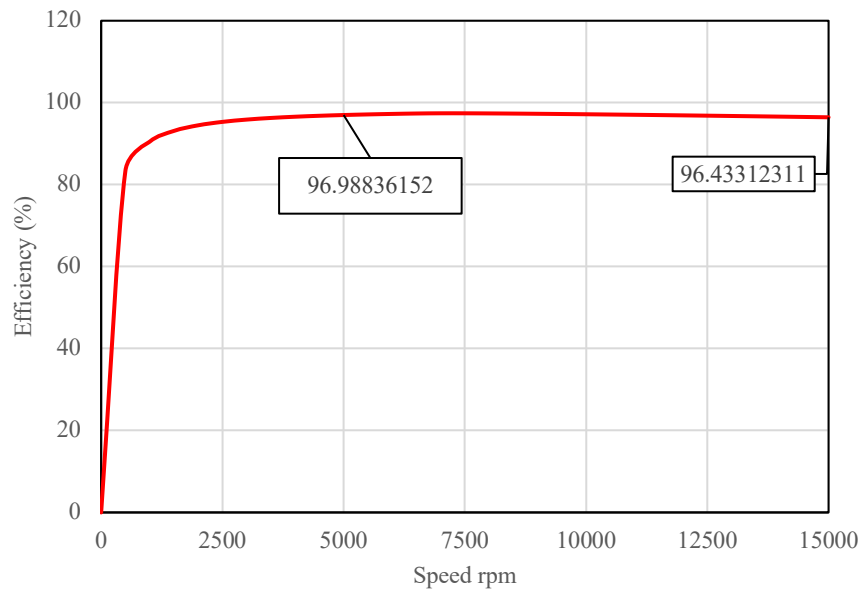


Figure 4-24 Efficiency of machine at rated power

4.16 Thermal management

An important aspect during the design stage is the thermal management. It has a direct effect on the machine's performance. The cooling of the motor can improve torque capability, lifetime, and overall efficiency. Furthermore, excellent cooling allows for the reduction of the motor's weight and size without sacrificing its performance. In order to obtain accurate results, the thermal study has to be integrated with the electromagnetic performance analysis. There are different thermal analysis techniques such as, traditional thermal analysis, numerical methods (FEA/CFD) and lumped circuit models. In this project, the same software, Motor-CAD, used for electromagnetic analysis, will also be used for the thermal section. It employs a lumped circuit model; this technique is accurate and requires short amount of time. Two concepts of cooling are investigated in this section, water-jacket and spray cooling.

The electromagnetic losses for continuous torque are shown in Figure (4.22) they will be sent to the thermal model to evaluate the temperature rise first considering water Jacket. A transient check of temperature rise is conducted on the machine at the base speed due to the motor has peak and continuous torque with different current rating, it must be ensured that the temperature is within limits. A steady-state analysis is performed at the maximum speed to evaluate the temperature. Since the continuous current is sufficient to meet the power requirements at this speed, no transient occurs at this point. The cooling systems used and their fluid properties are shown in Table (4-7).

It is clear that the motor is having a high winding temperature at base speed transient analysis 358 C beyond the permissible limit which is 180 C as shown in Table (4-8) this is mainly due to the peak torque current. On the other side, at maximum speed this is less due to there is no peak current 244C as shown in Table (4-8). As shown in the previous section the electromagnetic losses are dominant at maximum speed. The magnets have a temperature of 411.6 C at base speed and exhibit a temperature of 161.7 C at top speed, this due to the change of current from 660 Amps to 460 Amps. After this initial check of the motor temperature at different operating regions it is clear that the motor is over heated.

At this stage, two options are available to cool down the motor to its safe limits. First, the current density of the motor could be lowered to reduce the temperature. However, this will lead to having a high active weight. The current motor is having an active weight of 68 kg

which is closer to the machine target. So, it is decided to use another cooling system which is a spray cooling method. 12 nozzles are located at the front and rear to target the hot spot of the machine which is the end windings.

The implementation of both water-jacket and spray cooling systems helped to cool down the temperature of the machine. Table (4-8) shows the winding temperatures reduced by 57% at peak current. Furthermore, the winding temperature at top speed reduced by 25.61 %.

Table 4-7 Cooling systems and fluid characteristic

Cooling System	Housing Water-Jacket	Spray Cooling	Inlet Temperature
Fluid Data	10 litre/m	10 litre/m	65C
Fluid Property	EGW 50/50	ATF134 Fluid	40C

Table 4-8 Temperature results using Water-Jacket and Water-Jacket + Spray cooling

@ Peak Current (660 Amp) , base speed (5000 rpm)		
Cooling Method	Windings Temperature	Magnets Temperature
Water-Jacket	358 °C	411.6 °C
Water-Jacket + Spray Cooling	152.4 °C	67.5 °C
@ Continuous Current (460 Amp) , base speed (5000 rpm)		
Cooling Method	Windings Temperature	Magnets Temperature
Water-Jacket	239.9 °C	237.6 °C
Water-Jacket + Spray Cooling	131.5 °C	66.6 °C
@ Continuous Current (460 Amp) , Top speed (15000 rpm)		
Cooling Method	Windings Temperature	Magnets Temperature
Water-Jacket	244 °C	161.7 °C
Water-Jacket + Spray Cooling	181.5 °C	125.6 °C

4.17 Demagnetization analysis

Demagnetization analysis is crucial in the design and operational effectiveness of traction machines. It's particularly important because the performance of PMs is compromised at high temperatures, where they are vulnerable to demagnetization. This possible demagnetization condition leads to a decline in the machine's overall performance. Analysing the risk and impact of demagnetization ensures efficient and reliable functioning of the machine.

The employed magnet N42UH temperature peaks at maximum speed, reaching 126°C as indicated in Table (4-8). According to the data sheet provided in Figure (4-25), the N42UH magnet can operate safely at temperatures up to 180°C. The purpose of the following analysis is to examine N42UH magnets at a temperature of 150°C. This is achieved by setting the phase advance angle to 90 degrees, which results in the injection of stator current into the negative d-axis. This examination aims to thoroughly investigate any vulnerabilities to the effects of demagnetization during normal operation at maximum speed.

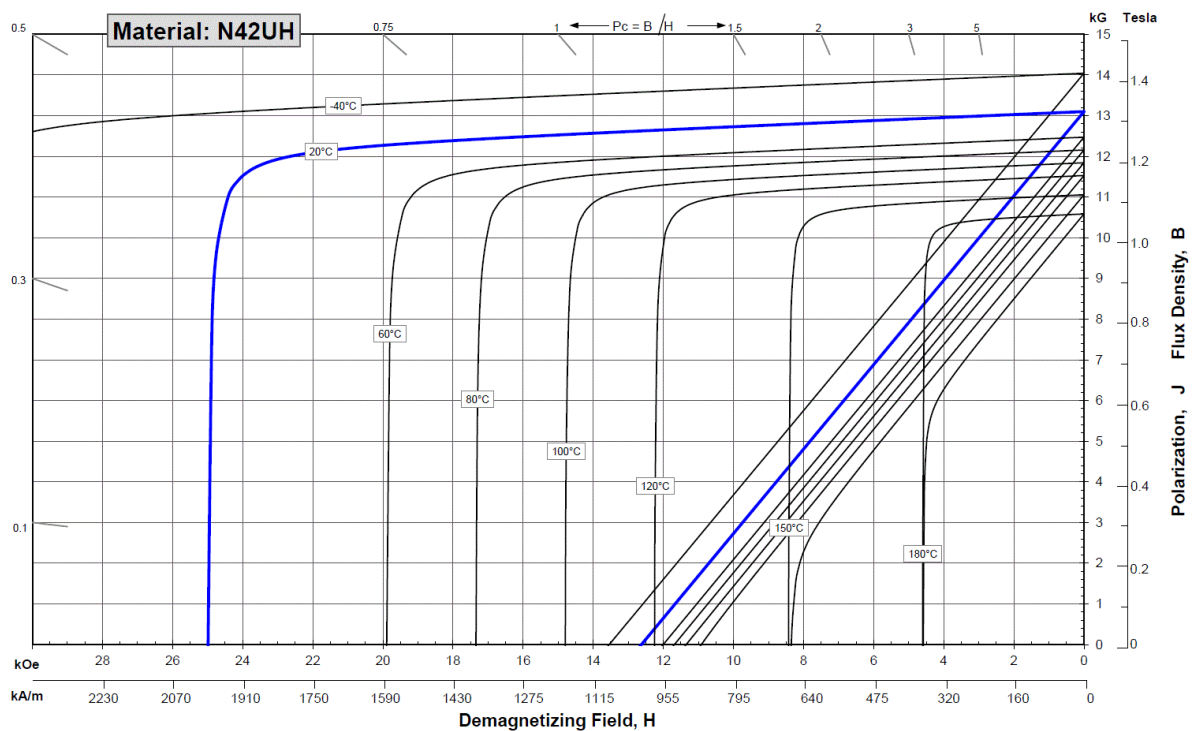


Figure 4-25 N42UH demagnetization curves[128]

The demagnetization analysis presented in Figure (4-26) clearly indicates that the magnets are not at risk of demagnetization. This conclusion is supported by the data in Figure (4-25), showing that for N42UH at 150°C, the B_{knee} point is 0.1975 T. Notably, the magnet nearest to the air gap experiences a slight loss of flux density. However, despite this minor flux density reduction the magnets maintain their operational integrity. Thus, it can be confidently stated that under normal operating conditions the magnets are functioning within safe parameters.

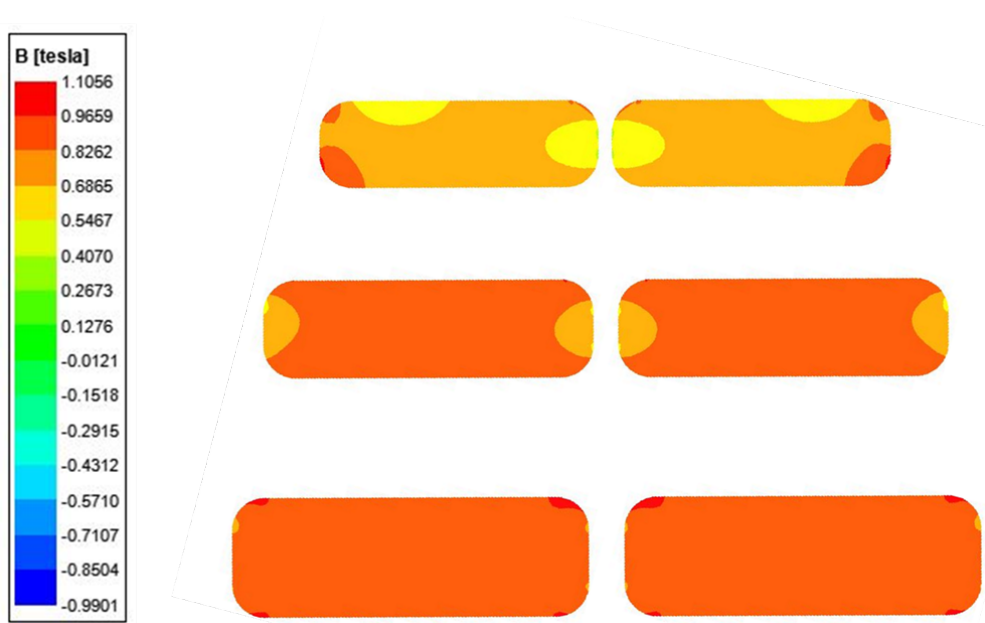


Figure 4-26 N42UH 150 C magnets at maximum speed, with 90-degree phase advance angle

4.18 Mechanical check

The rotor of PMa-SynREL machines is designed with radial and tangential ribs to maintain the mechanical integrity, at elevated speeds the rotor is vulnerable to high stress if not designed well. Peripheral speed is an important parameter to consider in the design and operation of high-speed PM motors. Peripheral speed refers to the linear velocity at the outer surface of the motor, and it is directly proportional to the motor's rotational speed and diameter. To understand this a sensitivity analysis is done, the rotor outer diameter is varied to increase the peripheral speed as shown in Figure (4-27), and this led to increasing the rotor stresses. The peripheral speed can impact the mechanical stress on the motor in several ways. First, higher peripheral speeds can increase the centrifugal forces acting on the rotor and stator, which can cause deformation and distortion of the motor components. This can lead to increased mechanical stress and ultimately, mechanical failure.

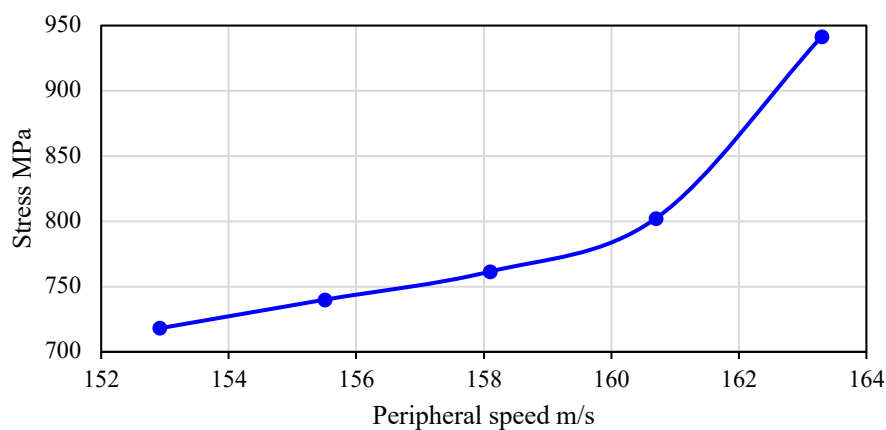


Figure 4-27 Peripheral speed impact on rotor stresses

Iron ribs in PMa-SynREL machines serve to reduce mechanical stress in the rotor core of the motor by distribute the magnetic forces more evenly across the core. However, introducing iron ribs in the magnetic circuit increase the flux leakage, if not optimized well. Therefore, the rotor iron ribs should be optimized in a multi-physis optimization to compromise both mechanical and electromagnetic performance. To mitigate the impact of peripheral speed on mechanical stress, several design and operational considerations should be considered. The motor's peripheral speed should be limited to a safe range based on the size, power rating and operating conditions of the motor. Furthermore, the motor's rotor and stator core should be designed and manufactured to withstand the centrifugal forces and vibrations that may occur at higher peripheral speeds. This may involve the use of high-strength materials and additional

support structures such as iron ribs. In this machine as stated previously the rotor material used is 35HXT780T. The designed machine has a periphery speed equal to 139 m/s. A 10% safety factor is added, so it is checked at 152 m/s and the speed is 16500 rpm. As seen in Figure (4-28), that with speed the rotor stresses increase due to increased peripheral speed.

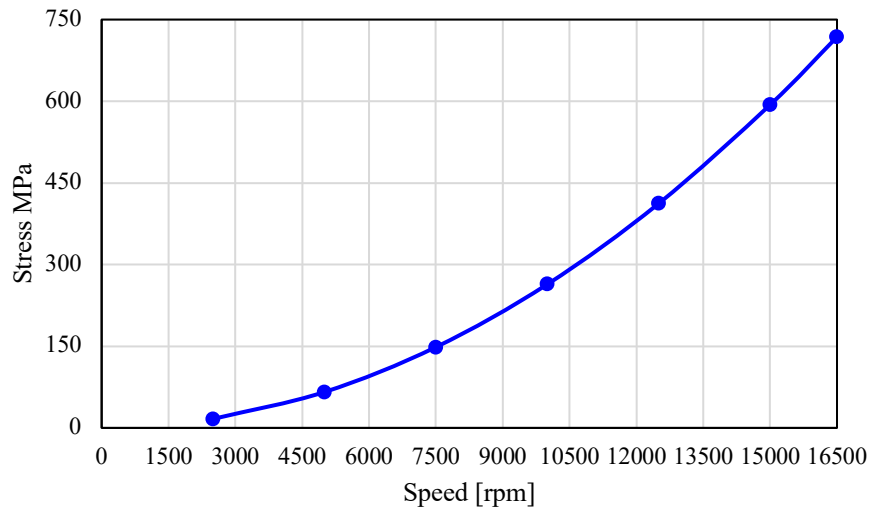


Figure 4-28 Rotor stress with speed variation

The sizing of the rotor outer diameter is critical, increasing the periphery speed increases the stress on the rotor. Further, high speed applications are vulnerable to centrifugal forces, operating at high speed is critical due to high stresses. It is necessary to round the edges of the magnets to spread out the stress more evenly and to reduce the risk of mechanical failure. Sharp edges of the flux barriers and magnets leads to high stress as shown in Figure (4-29), the stress is 1049.016 MPa. Contrastingly, rounded magnets and flux barriers shown in Figure (4-30) have led to a stress equal to 718 MPa which is lower than the material yield stress. Therefore, rotor with sharp edges has 31.56% more stress than the rotor with rounded magnets.

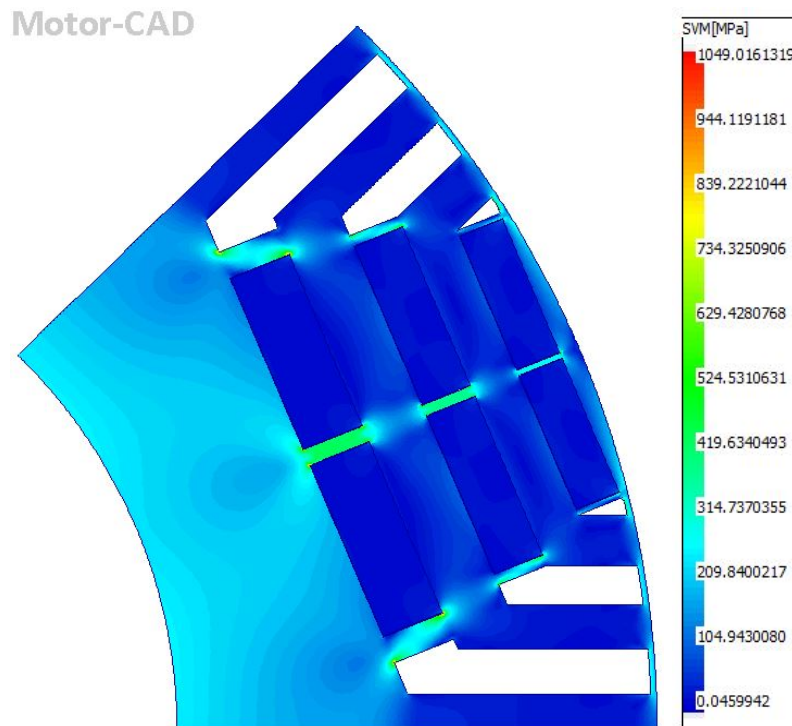


Figure 4-29 Sharp edges flux barriers and magnets equal to 1049.016 MPa

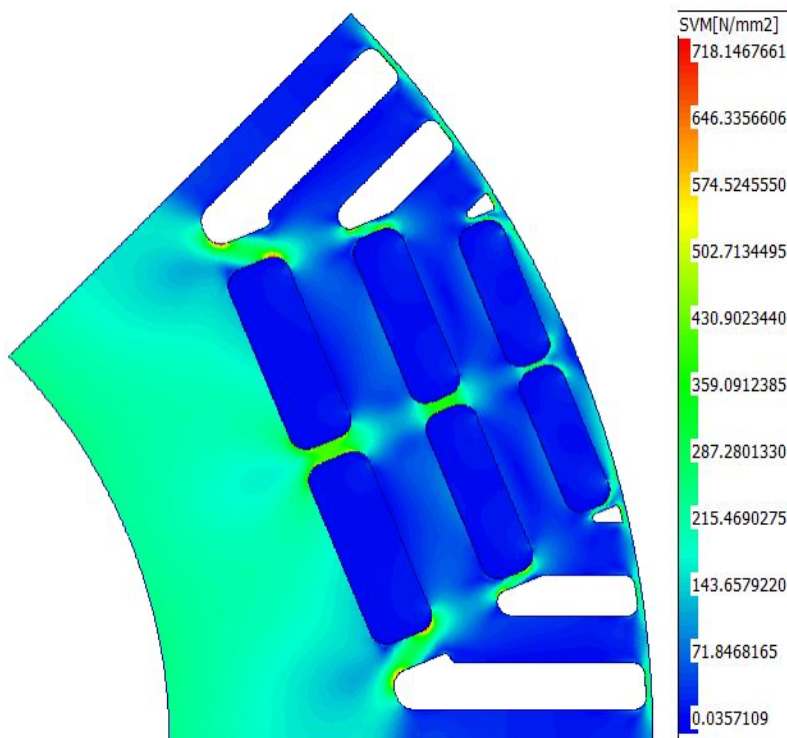


Figure 4-30 Rounded flux barriers and magnets with a stress equal to 718.14 MPa

Table (4-9) represents the PMa-SynREL machine physical dimensions and materials used. It compares the results achieved in this chapter with the target requirements.

Table 4-9 PMa-SynREL machine physical dimensions and materials

Parameter	Target	Value	
Stator Outer diameter (mm)	350	264	✓
Rotor outer diameter (mm)	-	177	
Axial length (mm)	350	195.5	✓
Air gap (mm)	-	1.5	
Slot-pole	-	48-8	
Winding Layout	-	Distributed Windings	
Turns Per Coil	-	8	
Turn Per phase	-	16	
Peak Current density	-	13.93 A/mm ²	
Continuous Current density	-	9.7 A/mm ²	
Peak Power @ 5000 rpm	274 kW	299 kW	✓
Continuous Power @ 5000 rpm	210 kW	212 kW	✓
Peak Torque @ 5000 rpm	526.8 Nm	571.64 Nm	✓
Continuous Torque @ 5000 rpm	401.1 Nm	405.16 Nm	✓
Continuous Torque @ 15000 rpm	140 Nm	178.74 Nm	✓
Peak Power @ 15000 rpm	210 kW	280 kW	✓
Stator Material	-	N10 0.1strip	
Rotor Material	-	35HXT780T	
PM material	NdFeB	N42UH	✓
Active Weight	70 kg	63 kg	✓
Machine Volume (L)	30	10.7	✓

4.19 Summary

A 299 kW PMA-SynREL machine was designed for a heavy-duty truck application that has a high peripheral speed 139 m/s. The designed machine is a 48-slot 8-pole machine. Incorporating NdFeB magnets in the design has helped to increase the machine power to mass ratio to 4.7 kW/kg. Using two cooling methods to cool down the motor was a key enabler to maintain the active weight within the requirements. The cooling systems used are water-jacket and spray cooling. The chapter brings to light the critical parameters required to enhance the performance of the PMA-SynREL machine through a comprehensive understanding of multi-physics aspects. Detailed knowledge of the electromagnetics, thermal management, mechanical structure and their interdependencies in a high peripheral speed PMA-SynREL machine is crucial in its design and operation optimization for an application like heavy-duty trucks. The insights gained from this chapter will guide for more efficient, high-performance EV trucks.

- 1) PMA-SynREL machines exhibits a strong prospect to dominate the heavy-duty vehicles market.
- 2) The high power to mass ratio achieved from the designed PMA-SynREL machine is a prerequisite that is required in the EV market.
- 3) The field weakening capability of PMA-SynREL machines has met the challenging requirements of the heavy-duty truck. Thus, a constant power range was achieved.
- 4) Critical parameters in the PMA-SynREL machine needs more investigation for high-power high-speed applications such as the rotor iron ribs that needs to be sized carefully to strike a balance between the electromagnetic performance and mechanical integrity.
- 5) The torque quality is an important aspect, at elevated speeds torque ripple increase hence, proper positioning of flux barriers at the design stage is important. However, further techniques might be required such as rotor skewing.

Chapter 5. Dual Purpose Traction Machines

5.1 Introduction

The traction motor in EVs is the core of the drive, designing an efficient and high-power high-torque performance machine is required for the traction mode. In the charging mode of the vehicle, generally the traction motor is not engaged in the charging circuit. The potential of using the traction motor inherent magnets (windings) for an on-board battery charger is the aim of this chapter. Allowing the motor to serve as a dual purpose for the EV could lead to more integrated vehicle architecture. It can reduce the need for additional components thereby saving both cost and space of the vehicle. One key concern is the impact of the rotor rotation and vibration on the effective functioning on this dual-purpose arrangement. As the traction motor windings will serve as an input filter (inductor) for the battery charger, current in the windings could lead to rotation or vibration. Another crucial consideration is the amount of inductance a machine can provide for filtration purposes.

In the traction mode, the winding inductance is a vital parameter influencing the efficiency, performance, and control of the traction motor. The motor's inductance is influenced by a variety of factors. These include the motor's design and its specific type, core material with its magnetic properties, dimensions of the air gap, and the winding layout which impacts the magnetic field distribution. Each of these elements plays a crucial role in the overall inductance of the motor. This chapter explores the possibility of reconfiguring a SMPM motor winding, a series of layouts are simulated to highlight the potential of leveraging the motor winding inductance. Furthermore, the implications of using a traction motor as an inductor are investigated. The rotor dynamics and torque exerted for each layout is investigated. The layout which exhibits the highest inductance is implemented on the PMA-SynREL machine designed in chapter 4. The implementation of PMA-SynREL machine in a 3-phase charging system is also covered.

5.2 Traction motor characteristics

The motor used in this chapter is a 6-pole 36-slot SMPM traction motor, this motor is chosen for this investigation as generally SMPM motors have larger airgap than PMA-SynREL machines, this leads to the motor inductance to be lower. Thus, the attempt is to increase the motor inductance for the charging purpose by examining a series of layouts. The implications of using a motor for a dual purpose are amplified for the SMPM as they have a larger air gap width, and the magnets are directly facing the air gap. Having the PMs adjacent to the airgap is a key concern as the magnets can be vulnerable to demagnetization. Table (5-1) represents the motors physical dimensions and Figure (5-1) depicts the SMPM geometry. The materials used for this motor are tabulated in Table (5-2).

Table 5-1 Traction motor physical dimensions

Component	Dimension (mm)
Stator Outer Diameter	164
Rotor Outer Diameter	64
Air gap	2
Band Thickness	4
Magnet Thickness	10
Tooth width	4.3
Tooth tip	1.9
Slot Opening	2
Shaft Diameter	24
Stack Length	80.2
Back Iron	10

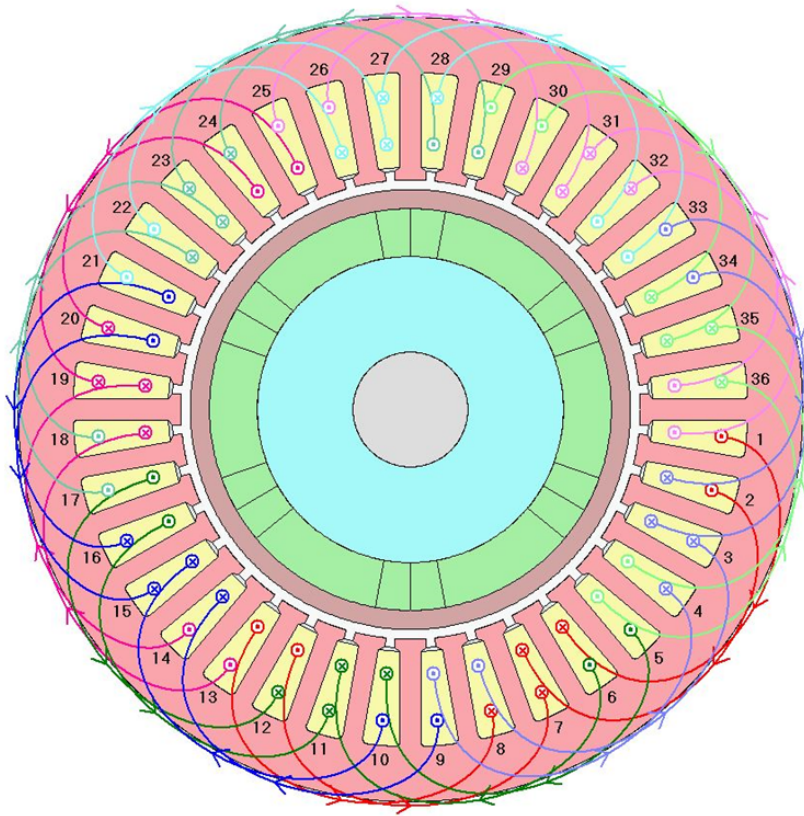


Figure 5-1 6-pole 36-slot SPM machine

Table 5-2 SPM machine materials

Component	Material
Case	Aluminium 6160
Stator Core	10JNEX900
Windings	Copper and insulation
Stator Sleeve	Glass fibre
Banding Sleeve	E-carbon fibre
Magnet	Samarium Cobalt
Rotor and shaft steel	17-4 PH

5.3 Winding arrangement

The 6-pole 36-slot SMPM motor shown in Figure (5-1), employs 3-phase distributed windings. The windings are spread over several slots per pole. The windings characteristics are tabulated in Table (5-3). Each phase has 3 parallel paths as shown in Figure (5-2). The motors slot-pole combination allows the motor to be driven for the traction mode in a different way, **(3-phase)** inverter driven, **(3 by 3)** phase inverter driven, and an open-end configuration all shown in Figure (5-3), (5-4) and (5-5).

Table 5-3 6-pole 36-slot winding characteristics

Component	Material
Winding Layout	Distributed Windings
Number of Layers	2 layers
Turns per coil	4 turns
Turns per Phase	16 turns
Parallel Paths	3 paths

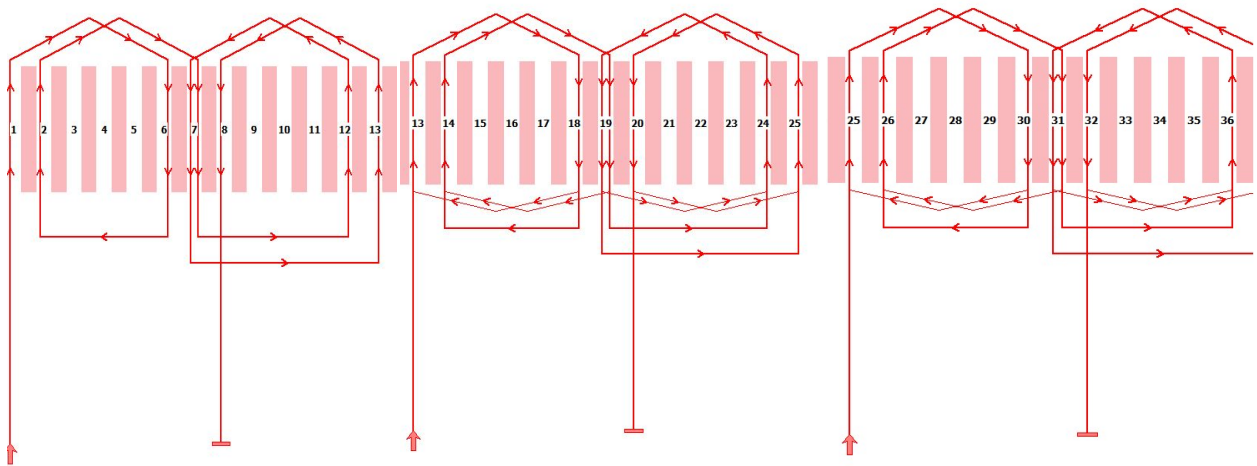


Figure 5-2 Phase A with 3 paths open end

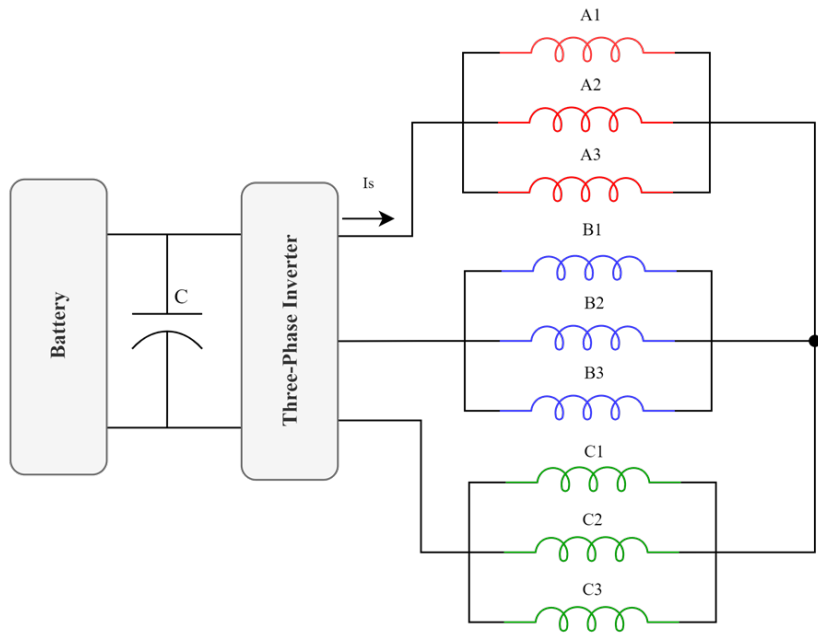


Figure 5-3 **3-Phase** inverter drive configuration

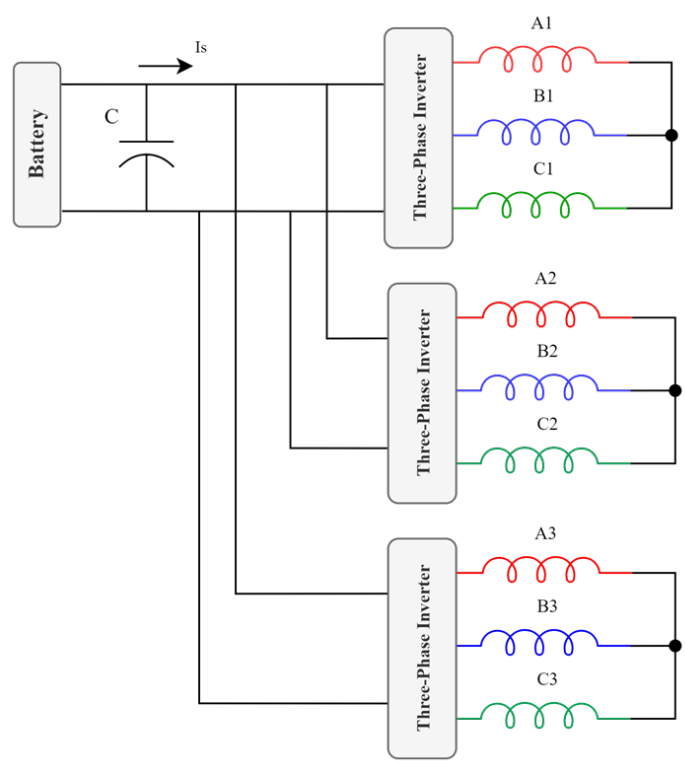


Figure 5-4 **3 by 3**-phase drive configuration

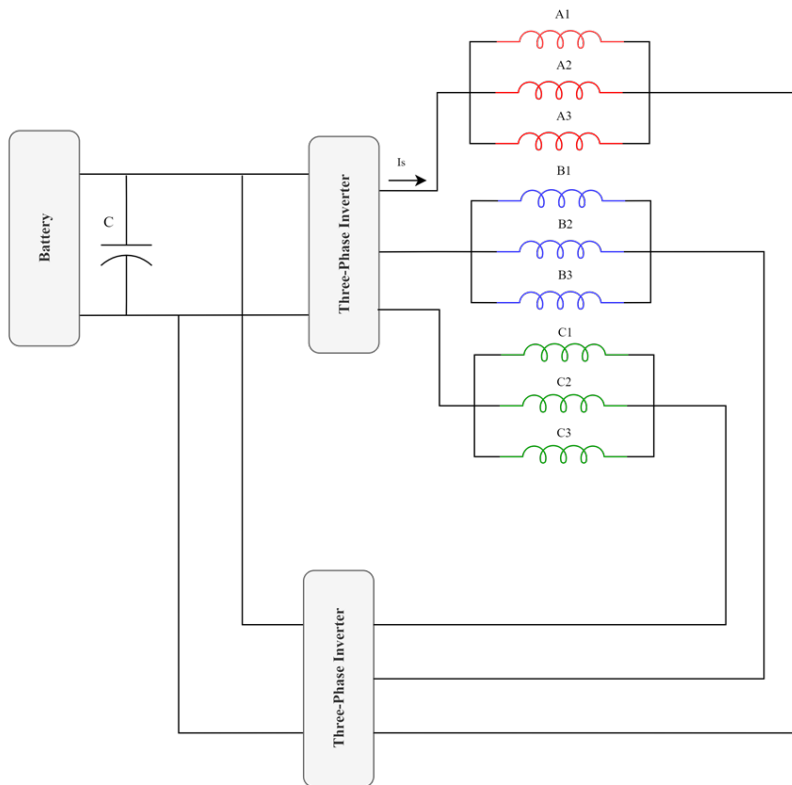


Figure 5-5 2 by 3-phase inverter open end configuration

5.4 Traction mode specifications

The specifications of the SMPM motor are represented in Table (5-4). The motor is designed to deliver a continuous power of 90 kW.

Table 5-4 Traction motor specifications

Component	Value
Input current (Amps)	300
Operating speed (rpm)	0-32000 rpm
Continuous power with 570 Vdc	90 kW
Torque at base speed (20krpm)	42 Nm
Efficiency (%)	95

5.5 Traction mode self and mutual inductance

In this section the aim is to investigate the motor inductance characteristics in the traction mode. As the motor employs 3-phase distributed windings, phase (A) has a self-inductance equal to 31.28 uH and mutual inductance 8 uH as shown in Figure (5-6), the mutual inductance arises from the magnetic coupling between the different phases of the motor and is influenced by the specific winding layout and design of the motor. As mentioned previously this inductance is a result of the number of turns and core material used, these factors have an impact on the inductance value.

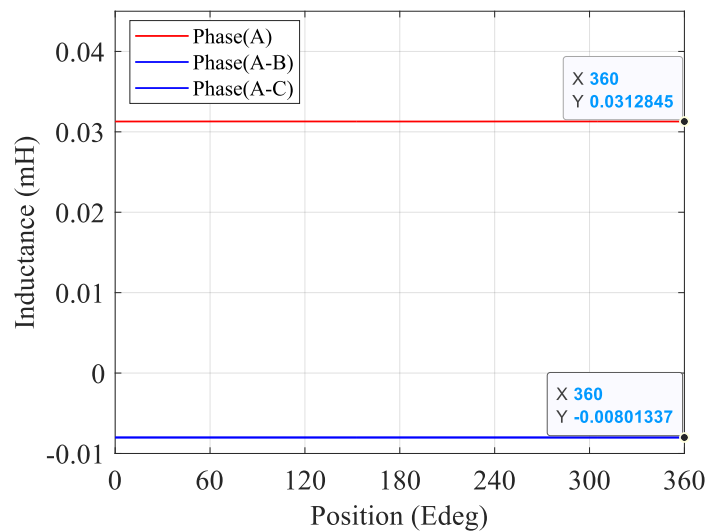


Figure 5-6 Self and mutual inductance for Phase (A)

5.6 Using the traction machine for dual purpose

The motor is driven by a 3-phase inverter like the one shown in Figure (5-3). The phases are joined by a neutral connection to have a balance 3-phase supply. Each phase is composed of 3-parallel paths as described in the winding characteristic in Table (5-3). Exploring the potential of leveraging the traction motor inherent magnets (Windings) for the use as an input filter for an integrated battery charger. This leads to eliminating commonalities on the EV drivetrain. Maximizing the inherent resources of the motor and reduce the need for additional components leads to cost reduction, and weight and space savings.

The following section will explore the 6-pole 36-slot SMPM motor, the main tasks revolve around:

- 1) Purpose a series of layouts (winding connections) to understand how the inductance value is changed from one layout to the other.

- 2) Understand the feasibility of the proposed layout by highlighting the number of switches necessary to transition between the traction modes and charging mode.
- 3) Investigate rotor dynamics, to observe if the rotor rotates or vibrates significantly during the charging mode due to magnetic fields induced by charging current. The vibration caused by the excitation of the motor windings is a critical factor that can affect the reliability of the traction motor to be used as an input filter (inductor).
- 4) Measure the inductance of each layout practically and compare with simulation results.
- 5) Measure the vibration of each layout, and compare the layouts based on the vibration magnitude.

5.7 Experimental rig setup for SMPM motor inductance and vibration testing

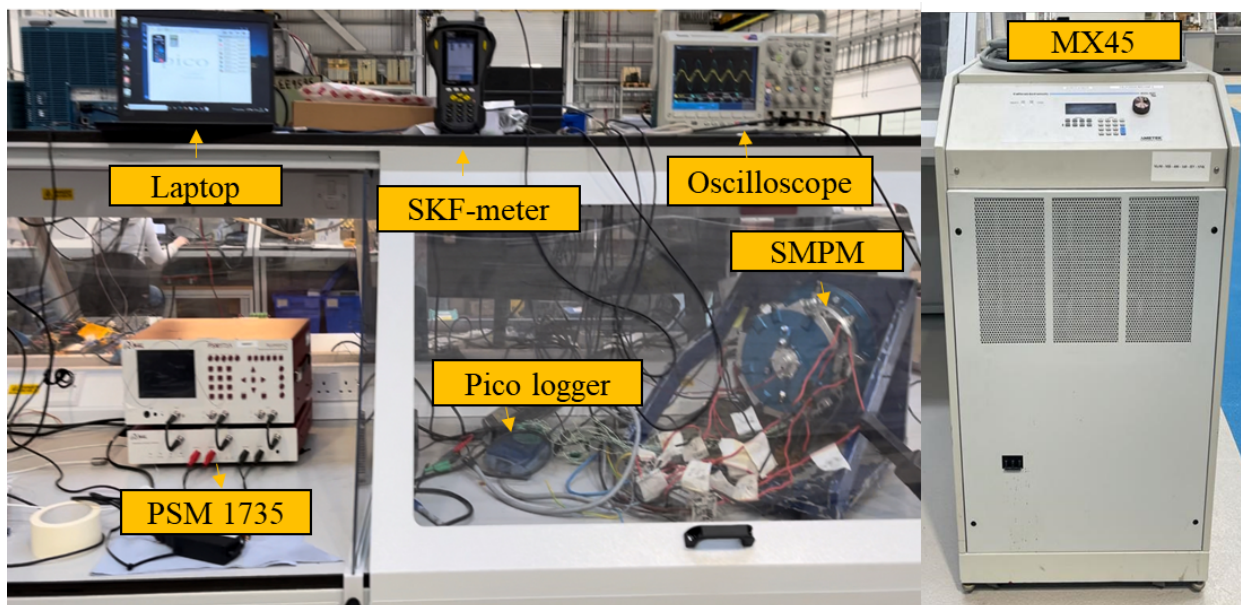


Figure 5-7 Experimental rig setup

Figure (5-7) shows the experimental rig configuration: The experimental setup is designed to provide a robust and comprehensive assessment of the SMPM motor's inductive properties and associated vibration. The primary source of controlled input current is an MX45 power source, operating at a frequency of 50Hz. This allowed for a standardized input current, ensuring a reliable basis for all subsequent readings and measurements. To amplify the circuit impedance, a resistive load rated at 1.1 ohms and 5000 watts is incorporated into the setup. The circuit's impedance is increased to increase the voltage drop. An impedance analyser is employed to measure the inductance of the motor for each layout at 50Hz. To capture the motor's vibrations, an SKF vibration meter is positioned on the motor housing. Two sensors are placed at 90-

degree angles to each other to capture a holistic view of the motor's vibrations. The SMPM motor is securely mounted on a flange. This not only provided stability during operation but also ensured consistency across different tests, helping to eliminate potential discrepancies in the data due to variable motor placement.

5.8 Aligning the rotor position to the d-axis

A low-level DC current is applied to the motor windings. A star connection is obtained as shown in Figure (5-8). Injecting a DC current to the windings will make the winding act as a PM. As the phasor diagram demonstrates, the resultant magnetic field propagates in the direction of phase (A). The rotor which also has PMs on its surface will feel a force due to the magnetic field created by the stator. Thus, it will align itself along the d-axis which is defined by the stators magnetic field.

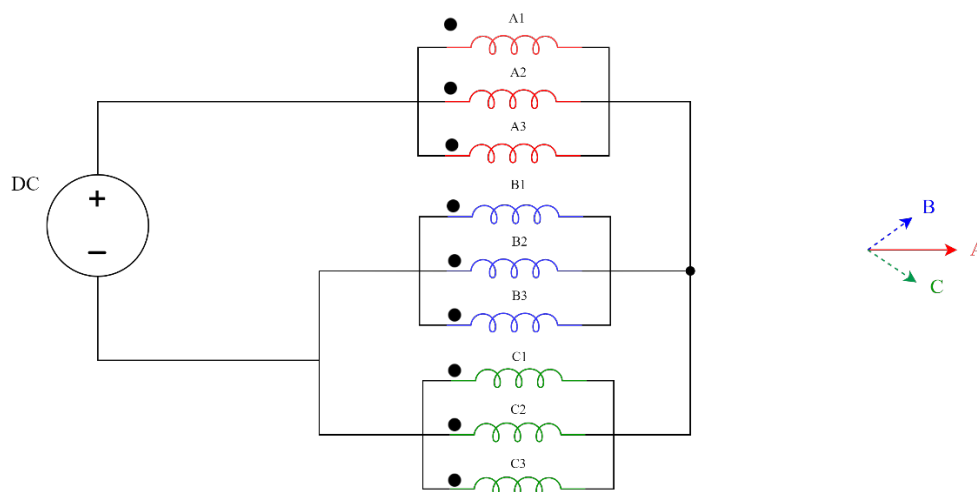


Figure 5-8 Star connection of the 3-phase motor

The supply current is fixed to 60 Amps (rms) this is to amplify the implications of vibration. In laboratory conditions, sometimes it is necessary to amplify certain operational conditions to accurately capture and analyse the characteristics of the system. In the experiment, increasing the current flowing through the motor is used to magnify the vibration, thereby making it more detectable by the SKF vibration meter. When a current passes through the motor windings, it generates a magnetic field. The interaction of this magnetic field with the PMs on the rotor can lead to physical movement or vibration, even while the rotor is stationary. This amplified vibration allows the SKF vibration meter to take more accurate measurements, as it might be less responsive to smaller, more subtle vibrations. The supply frequency is fixed to 50Hz to

compare the frequency components obtained from the SKF vibration meter with the simulation torque FFT. The 6-pole 36-slot SMPM motor is shown in Figure (5-9), the terminal windings of the SMPM are accessible as shown in Figure (5-9), which enables various connection possibilities.

The first step is to measure the inductance for all layouts and compare them with the simulation results. Then, each layout will connect to the resistive load and injected with a 60Amps (rms) current at 50Hz to capture the vibration of each layout. The 60Amps (rms) is 20% of the motor rated current in the traction mode which is 300 Amps (rms). This is to ensure that the windings don't get over heated. For a fair comparison the rotor position is fixed to the d-axis and the supply is set to current mode to ensure all layouts have a 60Amps (rms) 50 Hz current.

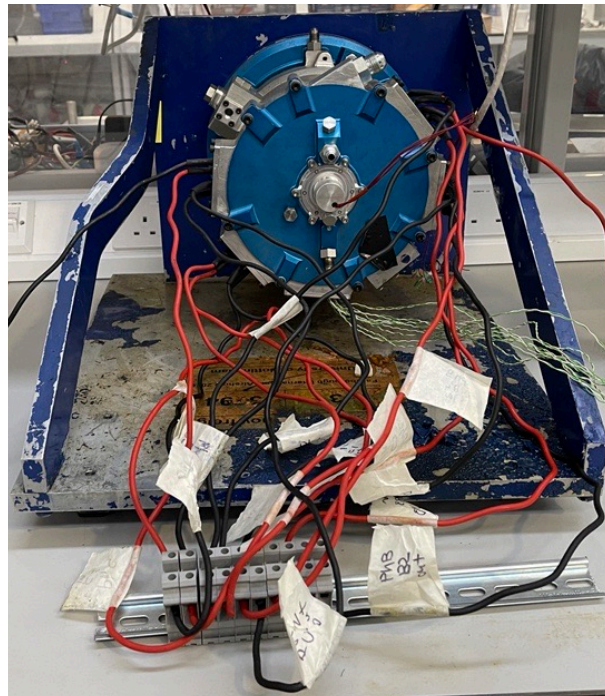


Figure 5-9 6-pole 36-slot SMPM motor connections

5.9 Simulation and experimental results

Single-phase charging can be any home socket. Mode-1 charging is a slow charging mode that is rated at 13 Amps. In the following simulation results the supply current used is a 42Amps (rms)/60 Amps (peak) at 50Hz. The reason for increasing the current is to resemble the right saturation levels. Layout (1) is depicted in Figure (5-10), all parallel paths are connected in series. All coils have the same polarity. In this context, polarity refers to the direction of the magnetic field induced by the current flowing through the coil. Furthermore, connecting multiple coils with the same polarity in series increases the magnetic field.

The flux density plot is shown in Figure (5-11), it is clear that the magnets maintained their flux density, thus the injected current is within the permissible range. The rotor's response to excitation is a critical aspect to consider, as it provides invaluable insights into the functionality of the traction motor windings in the charging circuit. Specifically, observing this response is key to understanding how the motor windings behave as an inductor within the system. By studying the rotor's behaviour and the changes in torque and its FFT, clearer understanding of the inherent inductive properties of the windings and their effects on motor operation can be gained. The analysis initiates with a depiction of the rotor's behaviour from 0 seconds to 2 second. Following this initial observation period, both the torque and its FFT are captured during the subsequent time interval between 1 second and 2 seconds. This latter interval is specifically considered to scrutinize and assess the steady state region of operation.

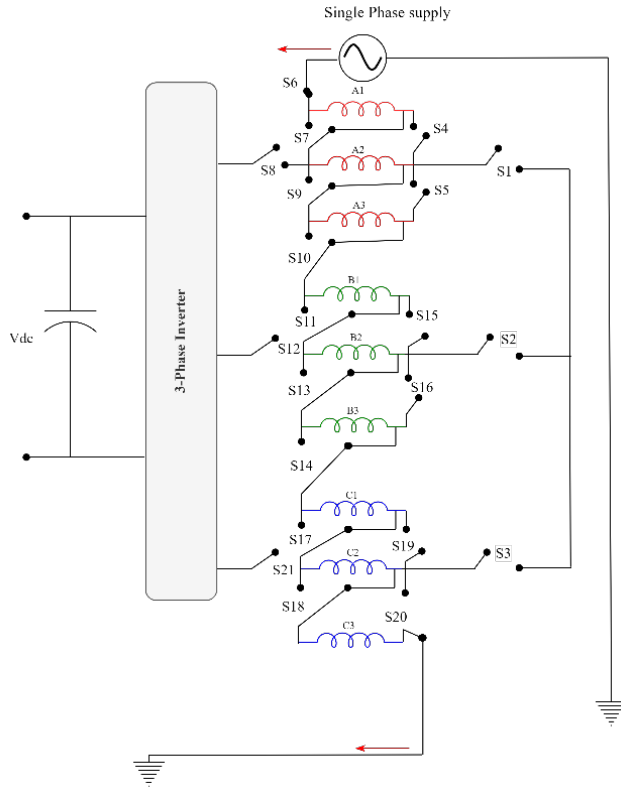


Figure 5-10 Winding connection Layout (1)

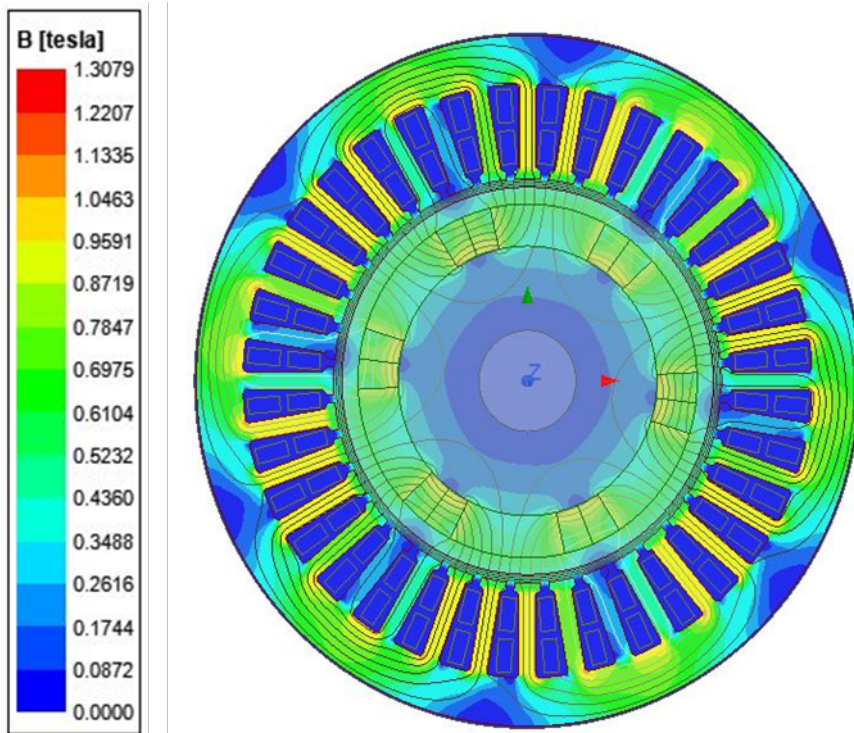


Figure 5-11 Flux distribution plot layout (1)

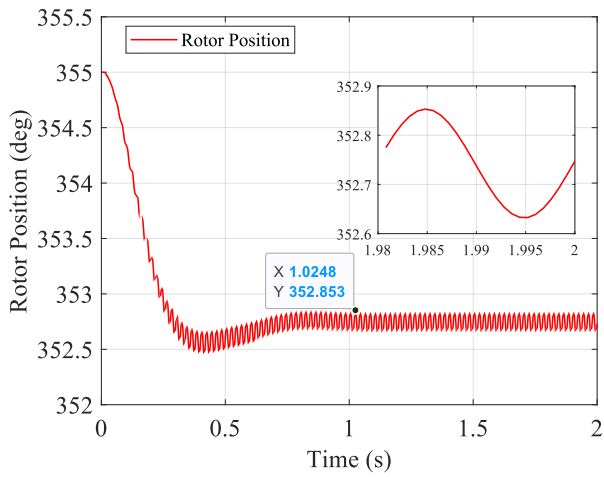
Layout (1) inductance is measured in the simulation, its value is equal to 440uH. The software used in this analysis is ANSYS-Maxwell. The inductance measurement acquired from simulations is compared with the experiment results shown in Table (5-5). The inductance measurement from the experiment is lower than the simulations by 16.7%. This discrepancy requires more investigation. This layout utilizes all motor coils, the inductance in this layout 366 uH is 76.5% higher than the coil inductance A1 which is 86uH. The switches that are required for the transition from the traction mode to the charging mode are 21 switches.

After the inductance measurement, the first step is to setup the motion for a mechanical transient. The effects of the moving parts on the electromagnetic field are accounted in the simulation. In the transient solver the time span is identified to be 2 seconds with 0.008 seconds steps. This is to observe the rotor dynamics. The motors inertia is set in the simulation to 0.0037018 kg.m². As expected, this layout produces a torque at 50Hz equal to 0.71Nm shown in Figure (5-12c), which is the current frequency, the torque FFT is shown in Figure (5-12d). The initial position of the rotor is set at 355 degrees. It reached a steady state within one second. As illustrated in Figure (5-12a), the rotor rotates at a magnitude of 0.2 degrees during the time interval between 1.98 and 2 seconds.

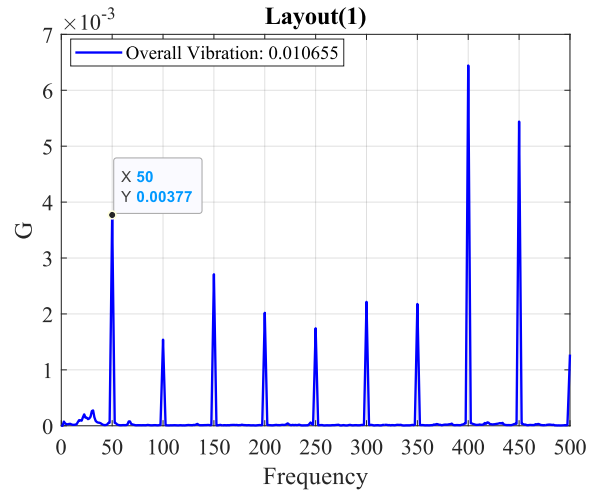
Furthermore, the vibration meter frequencies are depicted in Figure (5-12b). Due to the excitation current that has a frequency of 50 Hz, magnetic field interact with the motor windings and the magnetic core, causing them to vibrate. The frequency of the vibration would typically be at the same frequency as the electrical excitation, in this case, 50Hz or its multiples. The excitation frequency is captured at the 50 Hz component with a magnitude of 0.00377 G. The overall vibration of this layout is 0.010655 G. As can be seen in Figure (5-12b), harmonics are presented in vibration spectrum. The 8th harmonic is the significant one equal to 0.006 G, the presence of harmonics is attributed to the layout configuration and slot-pole combination.

Table 5-5 Inductance comparison between simulation and experiment results layout 1

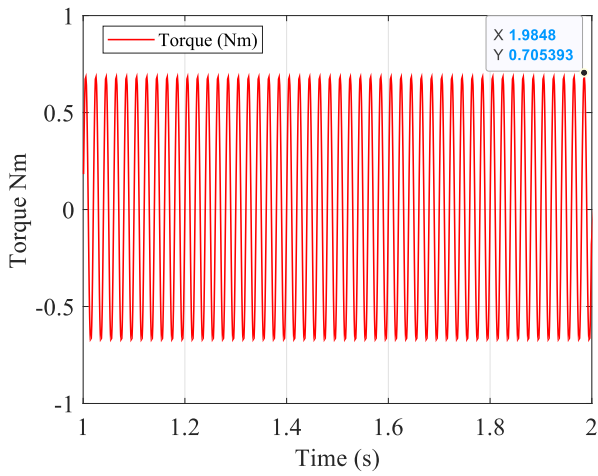
Inductance @50 Hz	Simulation	Experiment	Difference
	440 uH	366.1 uH	16.79%



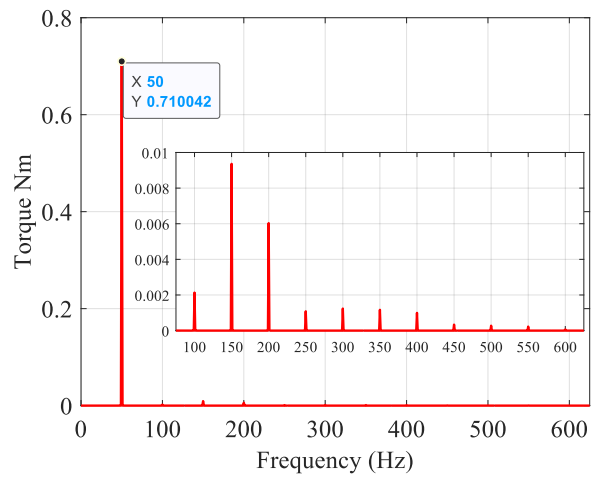
(a) Rotor position



(b) Vibration



(c) Torque (Nm)



(d) FFT of Torque

Figure 5-12 Layout-1 results

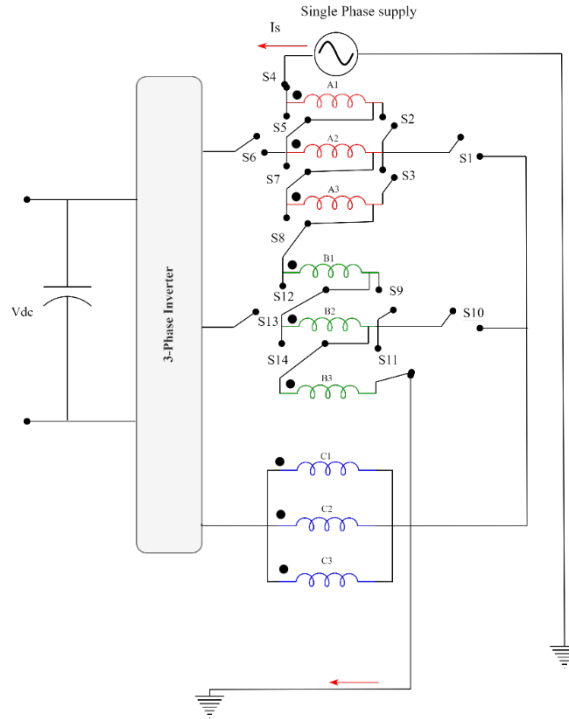


Figure 5-13 Schematic of layout (2) connections

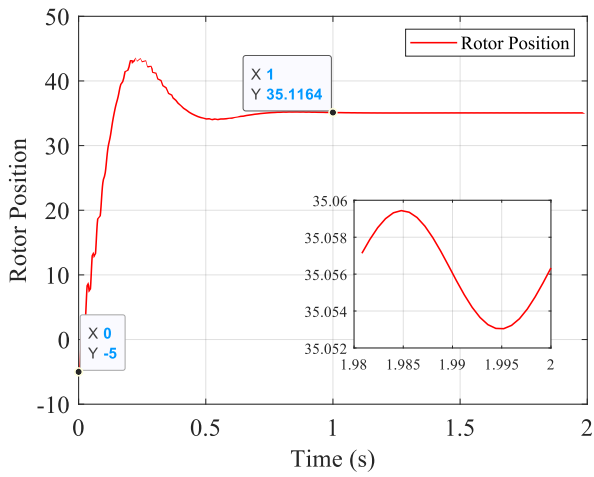
Layout (2) shown in Figure (5-13) unlike layout (1) utilizes phase (A) and (B) coils, this layout reduces the number of switches compared to layout (1) however, this is associated with a decrease in the inductance 334 uH, 8.7% less than layout (1). The inductance measured in the lab is 334.3 uH shown in Table (5-6) which is less than the simulation inductance by 19%. This layout requires 14 switches for the reconfiguration which is less than layout (1) by 7 switches.

As seen in Figure (5-14a), the rotor initial position is -5 deg which is 355 deg, the rotor reaches its steady state at 1sec. The oscillations experienced by the rotor within the time interval of 1 second to 2 seconds are remarkably minimal, measuring only 0.005 degrees as shown in Figure (5-14a). This is due to the torque induced in the steady state which is equal to 0.021 Nm at 50Hz shown in Figure (5-14c) and the torque FFT is shown in Figure (5-14d).

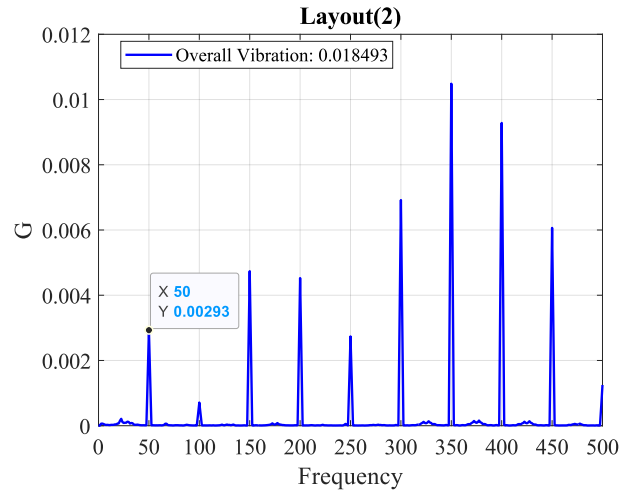
The vibration of this layout is depicted in Figure (5-14b), the overall vibration magnitude is 0.018 G. The multiples of the excitation frequency are present. The 50 Hz component has a magnitude of 0.00293 G. The harmonics are presented due to layout configuration.

Table 5-6 Inductance comparison between simulation and experiment results layout 2

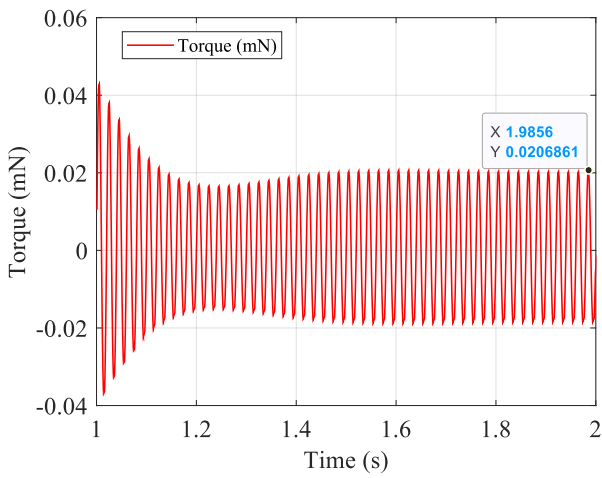
Inductance @50 Hz	Simulation	Experiment	Difference
	413.4 uH	334.3 uH	19.13 %



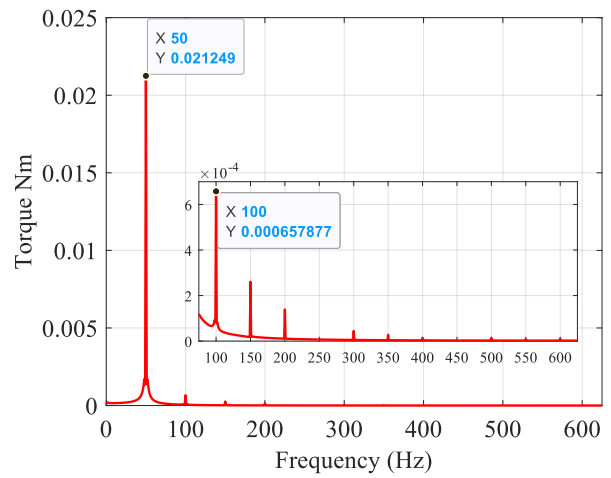
(a) Rotor behaviour



(b) Vibrations



(c) Torque (Nm)



(d) FFT of Torque

Figure 5-14 Layout-2 results

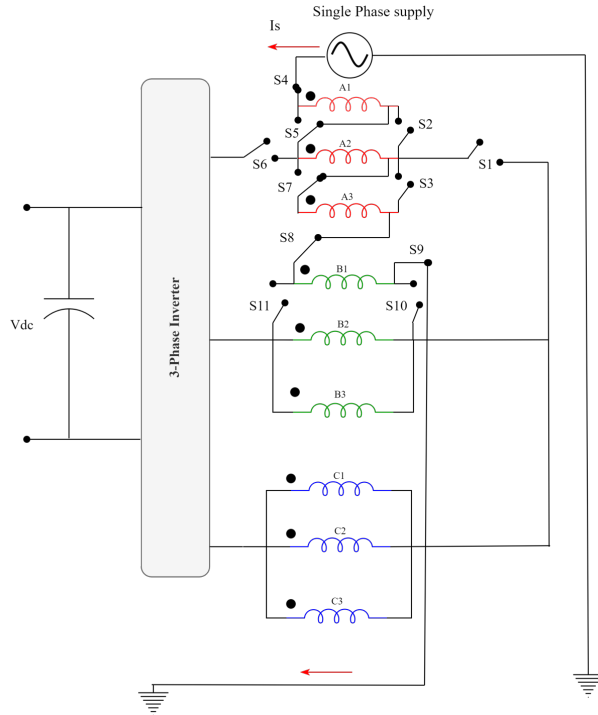


Figure 5-15 Schematic of layout (3) connections

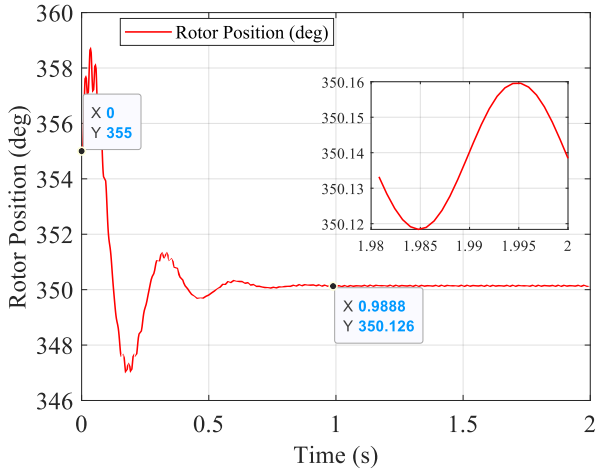
Layout (3) utilizes phase A coils with a coil from phase (B) to enhance the inductance shown in Figure (5-15). Therefore, this layout has an inductance equal to 324.2 μH . Table (5-7) shows the variation in inductance between lab measurements and simulation results, the inductance measured in the lab is higher by 7.23% this is due to the end windings.

The rotor position aligned with the stator field therefore, the rotor changes its position by 5deg as shown in Figure (5-16a). The torque at 50 Hz has a magnitude equal to 0.13 Nm shown in Figure (5-16c) that results in rotor oscillations with magnitude equal to 0.04 degrees from time interval 1.98sec to 2sec. The torque FFT is shown in Figure (5-16d).

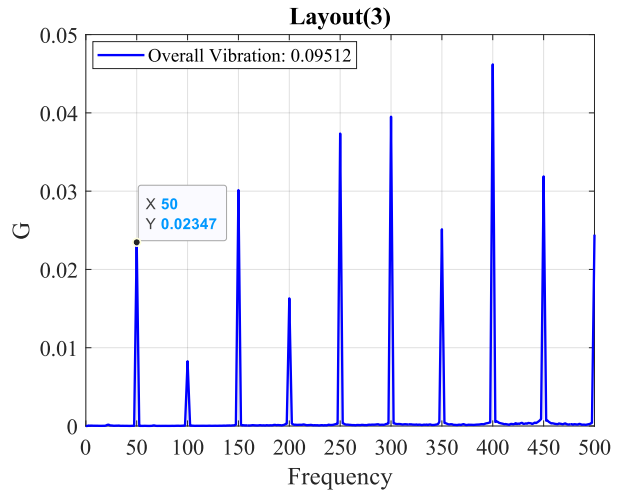
The vibration of this layout is depicted in Figure (5-16b), the overall vibration magnitude is 0.09512G. The multiples of the excitation frequency are present. The 50 Hz component has a magnitude of 0.02347 G. The harmonics are presented due to layout configuration.

Table 5-7 Inductance comparison between simulation and experiment results layout 3

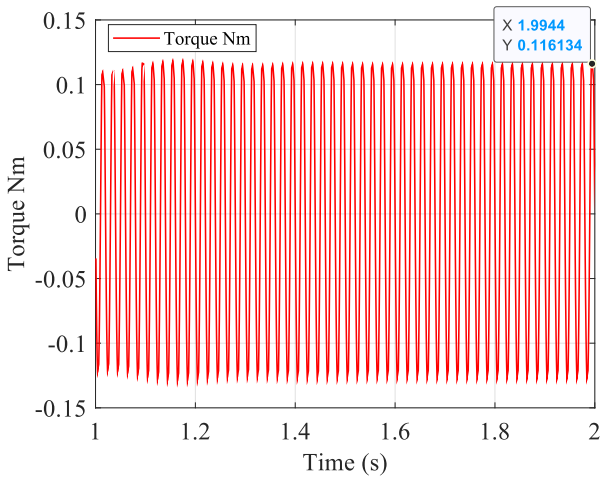
Inductance @50 Hz	Simulation	Experiment	Difference
	302.35 uH	324.2 uH	7.23 %



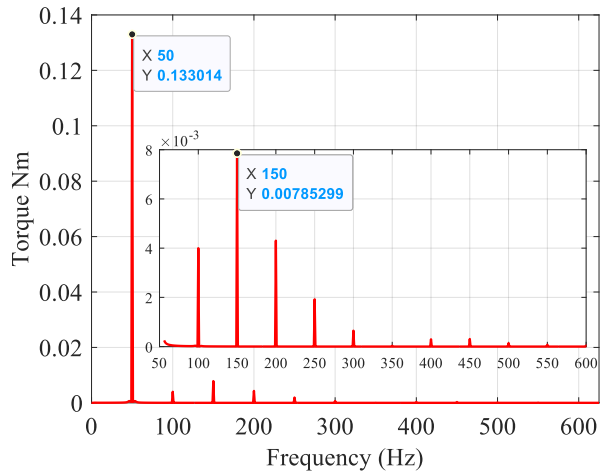
(a) Rotor Position



(b) Vibration



(c) Torque (Nm)



(d) FFT of Torque

Figure 5-16 layout_3 results

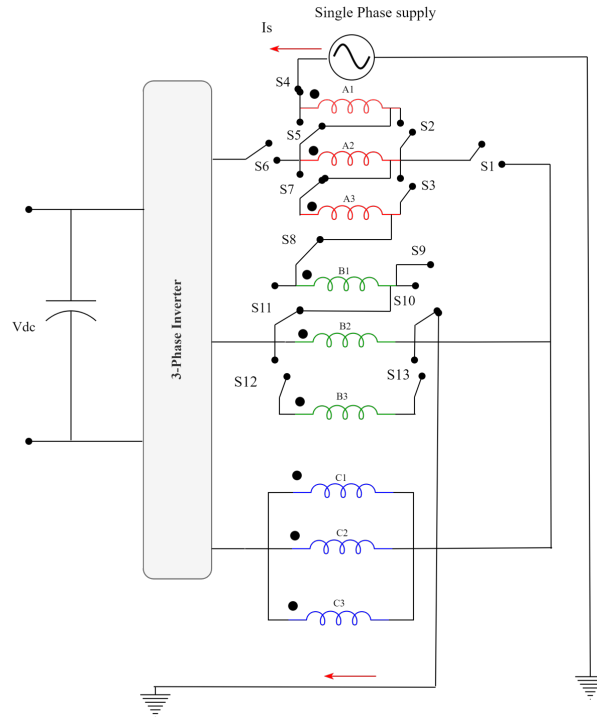


Figure 5-17 layout_4 winding schematic

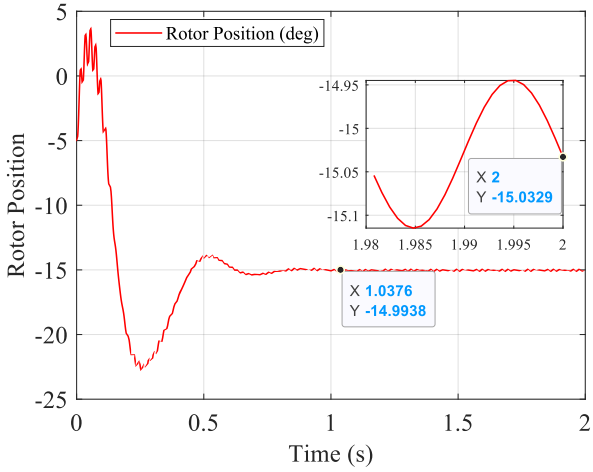
Layout (4) shown in Figure (5-17) is similar layout (3), with adding coil B2 in the circuit. Layout (4) has an inductance equal to 321.3 μH as shown in Table (5-8). 13 switches are required for the transition from traction mode to charging mode.

The rotor changes its initial position by 10 (degrees) to align with stator field as shown in Figure (5-18a). The torque is 0.5 Nm at 50Hz shown in Figure (5-18c) and the torque FFT is shown in Figure (5-18d). The rotor oscillations with a magnitude equal to 0.15 degrees from time interval 1.98sec to 2sec.

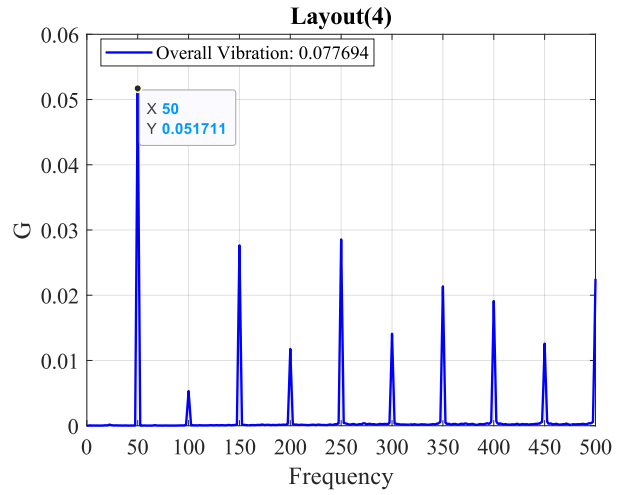
The vibration of this layout is depicted in Figure (5-18b), the overall vibration magnitude is 0.077694 G. The multiples of the excitation frequency are present. The 50 Hz component has a magnitude of 0.051711 G. The harmonics are presented due to layout configuration.

Table 5-8 Inductance comparison between simulation and experiment results layout 4

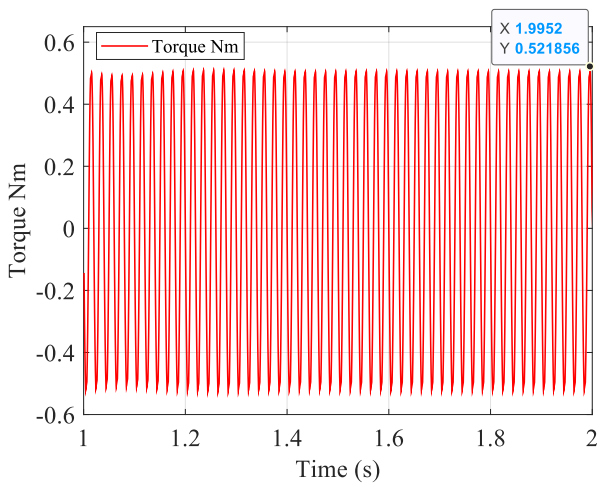
Inductance @50 Hz	Simulation	Experiment	Difference
	351.3 uH	375 uH	6.32%



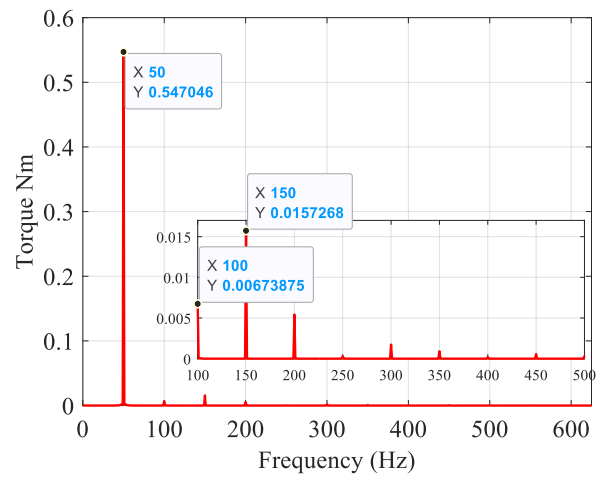
(a) Rotor position



(b) Vibration



(c) Torque (Nm)



(d) FFT of Torque

Figure 5-18 Layout_4 results

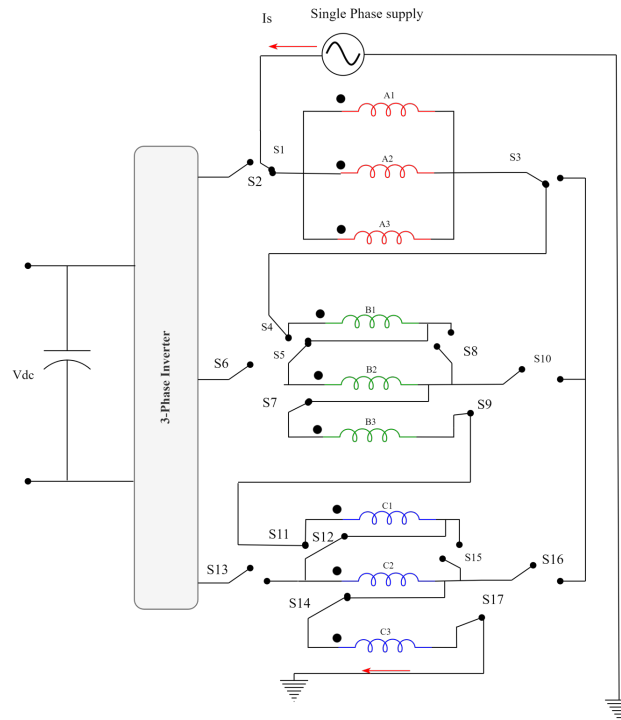


Figure 5-19 Layout-5 winding schematic

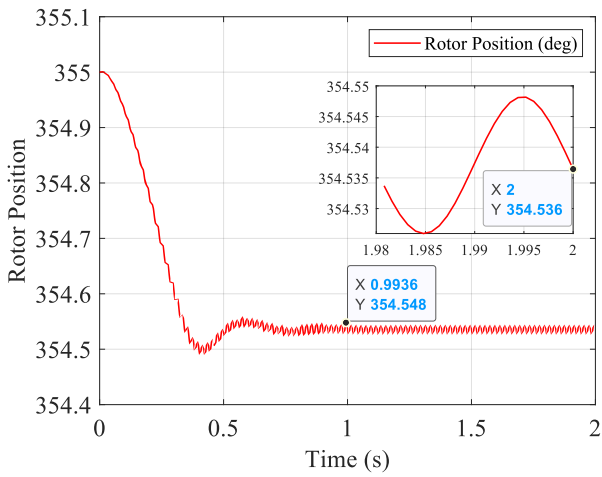
Layout (5) shown in Figure (5-19) has all phases connected in series. Coil phase A is connected in series with phase B and C, phase A is connected in parallel unlike phase B and C that are connected in series. The inductance of this layout is 329 μH as shown in Table (5-9). This increase in inductance is associated with an increase in the number of switches required for reconfiguration. In this layout 17 switches are required for the reconfiguration.

As all coils are excited the rotor position shifted from initial position by 0.464 degrees as shown in Figure (5-20a). The torque in this layout at the supply frequency is equal to 0.07 Nm as shown in Figure (5-20c), the torque FFT is shown in Figure (5-20d).

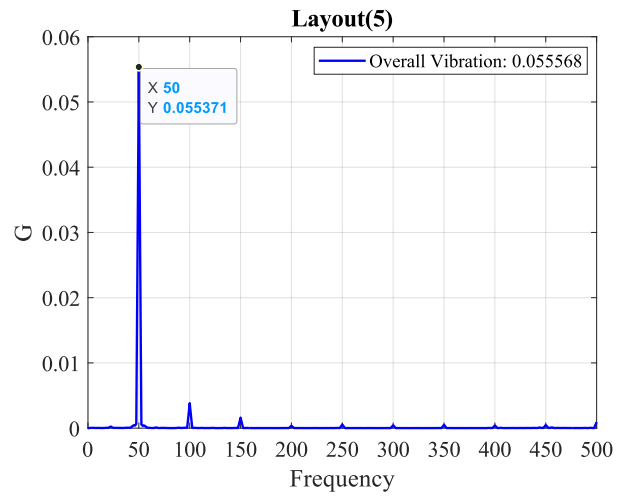
The vibration of this layout is depicted in Figure (5-20b), the overall vibration magnitude is 0.0027022G. The multiples of the excitation frequency are present. The 50 Hz component has a magnitude of 0.002676 G. The harmonics are presented due to layout configuration.

Table 5-9 Inductance comparison between simulation and experiment results layout 5

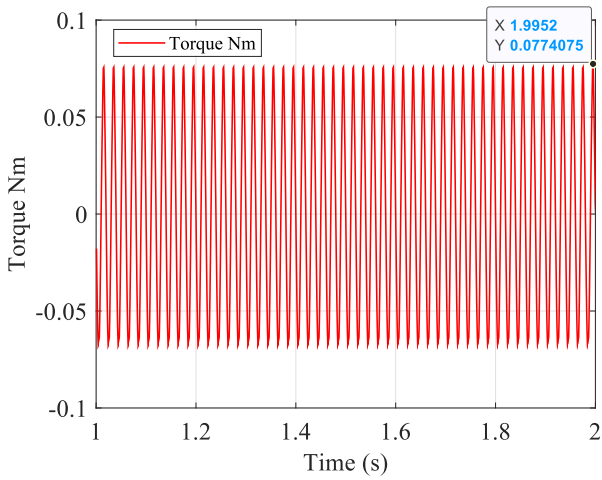
Inductance @50 Hz	Simulation	Experiment	Difference
	363.14 uH	329 uH	9.4 %



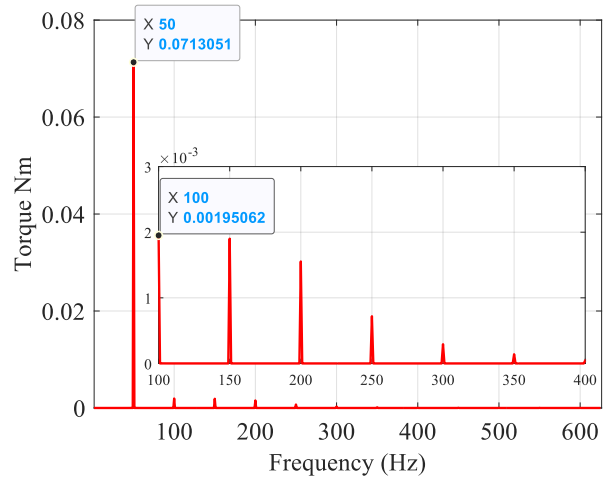
(a) Rotor position



(b) Vibration



(c) Torque (Nm)



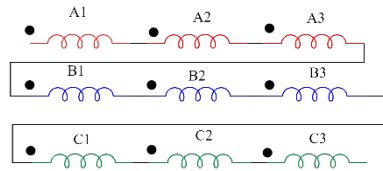
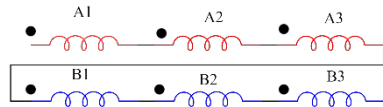
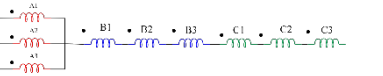
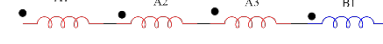
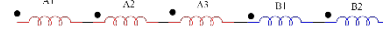
(d) FFT of Torque

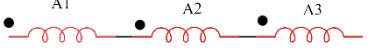
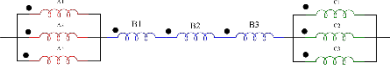


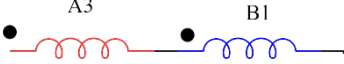
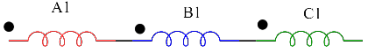
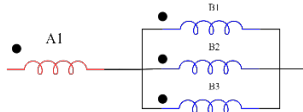
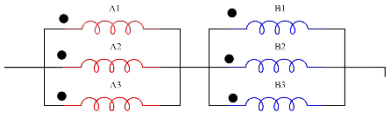
Figure 5-20 Layout_5 results

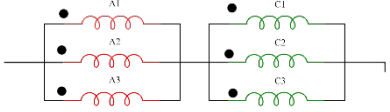
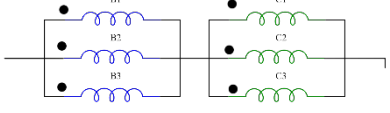
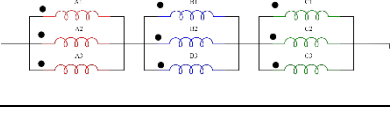
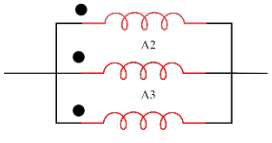
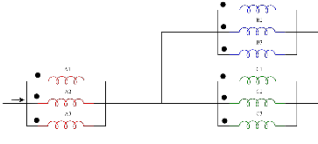
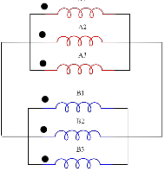
5.10 Layout comparison

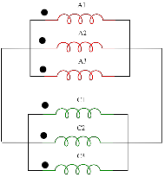
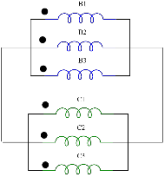
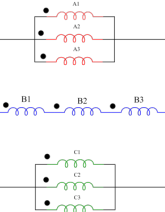
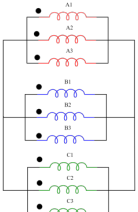
Table (5-10) serves as a comprehensive summary of all the layouts discussed in this chapter. It offers a side-by-side comparison of each layout, allowing for a clear and direct analysis of their respective characteristics and performance metrics. For layouts, those that depict rotor angles exceeding the limit of 15 degrees are considered outside the optimal range and are therefore coloured in red.

Table 5-10 Comparative evaluation of potential layouts for using the traction machine as an inductor

	Layout	Inductance (uH)	Torque @ 50 Hz (Nm)	Switches required for reconfiguration	Rotor Shift (deg)	Vibration (G)
1		366.1 uH	0.7 Nm	21	2.2 (deg)	0.011 G
2		334.3 uH	0.02 Nm	14	40.11 (deg)	0.019 G
3		329 uH	0.07 Nm	17	0.5(deg)	0.056 G
4		324.2 uH	0.13 Nm	11	5 (deg)	0.095 G
5		321.3 uH	0.55 Nm	12	20 (deg)	0.138 G

6		306 uH	0.02 Nm	7	0.021 (deg)	0.006 G
7		240 uH	0.09 Nm	11	19 (deg)	0.018 G
8		183 uH	0.01 Nm	7	0.018 (deg)	0.123 G
9		178.2 uH	0.12 Nm	10	1.17 (deg)	0.10 G
10		168.8 uH	0.37 Nm	5	27 (deg)	0.138 G
11		165 uH	0.34 Nm	10	3.39 (deg)	0.082 G
12		99.3 uH	0.41 Nm	8	27 (deg)	0.098 G
13		45.7 uH	0.36 Nm	6	27 (deg)	0.027 G

14		45.17 uH	0.32 Nm	6	18 (deg)	0.031 G
15		44.70 uH	0.14 Nm	6	1.5 (deg)	0.003 G
16		42.91 uH	0.09 Nm	9	1 (deg)	0.002 G
17		35.36 uH	0.065 Nm	3	1.2 (deg)	0.003 G
18		28.5 uH	0.104 Nm	10	1.6 (deg)	0.002 G
19		12.38 uH	0.88 Nm	5	20 (deg)	0.031 G

20		12 uH	0.83 Nm	8	11 (deg)	0.030 G
21		12 uH	0.14 Nm	6	3.3 (deg)	0.016 G
22		8.50 uH	0.55 Nm	11	20 (deg)	0.012 G
23		5.67 uH	0.09 Nm	7	4 (deg)	0.002 G

5.11 Functionality of PMA-SynREL machine as an inductor

The knowledge acquired from investigating the use of SMPM machine as an inductor shows that the motor windings can be used as an inductor with the rotor oscillating at the supply frequency. The oscillations shown on the SMPM motor are minimal. This section aims to investigate layout 1 on the PMA-SynREL machine presented in chapter 4, which is the candidate to be employed for a heavy-duty truck application.

Table (5-11) shows the geometrical differences between the SMPM machine vs PMA-SynREL machine. It is clear that the PMA-SynREL machine exhibit a reduced airgap and increased volume compared to the SMPM machine. Both machines have the same number of turns per phase as shown in Table (5-12), however due to the volume and reduced airgap of the PMA-SynREL layout (1) has a higher self-inductance by 97%. Layout (1) has all phases connected in series with all parallel paths in series.

Table 5-11 Geometry comparison SMPM machine vs PMA-SynREL machine

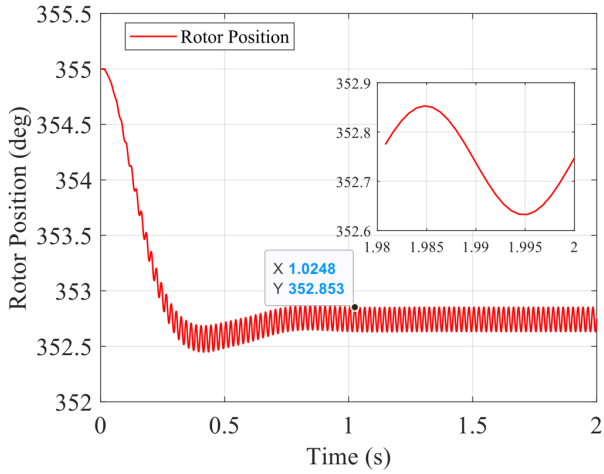
Machine topology	SMPM machine	PMA-SynREL machine
Slot/pole	36/6	48/8
Stator outer diameter (mm)	164	264
Stator bore (mm)	96	180
Air gap (mm)	2	1.5
Stack length (mm)	80.2	195.5
Volume (L)	1.69	10.70

Table 5-12 Winding characteristics of SMPM machine vs PMA-SynREL machine

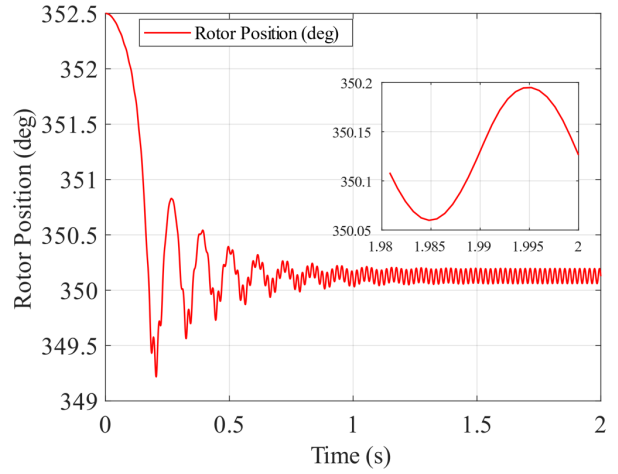
Machine topology	SMPM machine	PMA-SynREL machine
Winding layout	Distributed windings	Distributed windings
Winding layers	2	2
Turns per coil	4	8
Turns per phase	16	16
Parallel paths	3	8
Self-inductance	33.29 uH	189.6 uH
Mutual inductance	8.0 uH	66.05 uH
Layout (1) inductance	360 uH	14.6 mH

Figure (5-21) illustrates the outcomes of using the electric motor as an inductor. The PMA-SynREL machine has an increased peak torque compared to the SMPM machine due to several reasons, increased inductance, reduced air gap, magnet grade and a higher rotor outer diameter. It is evident both topologies have a zero average torque as shown in Figure (5-21) due to the supply current which is a single-phase rated at 60 Amps peak at frequency of 50 Hz.

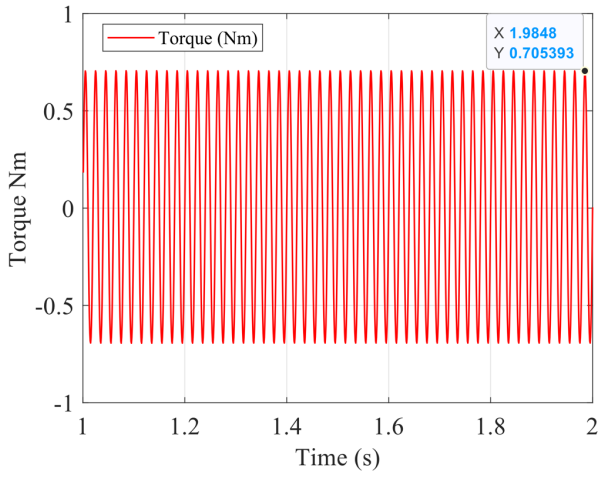
The rotor dynamics for both topologies show that the rotor oscillates in the steady state region at 0.1 degrees for the SMPM machine and 0.15 degrees for the PMA-SynREL machine. This is due to the 50 Hz torque component shown in the FFT of torque in Figure (5-21). As both machines have different slot-pole combination the rotor dynamics at the transient region are different.



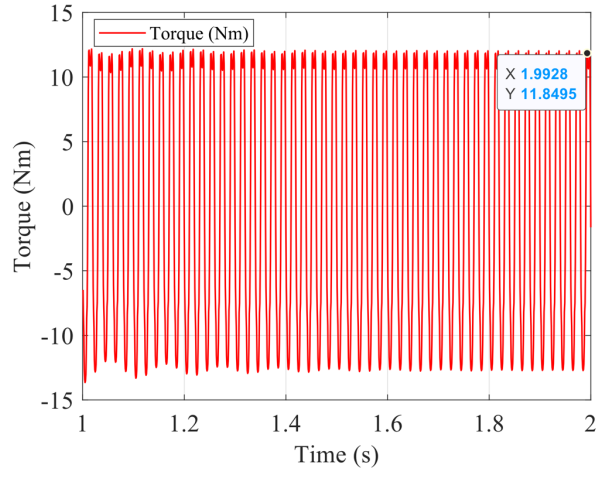
(a) Rotor position (SMPM motor)



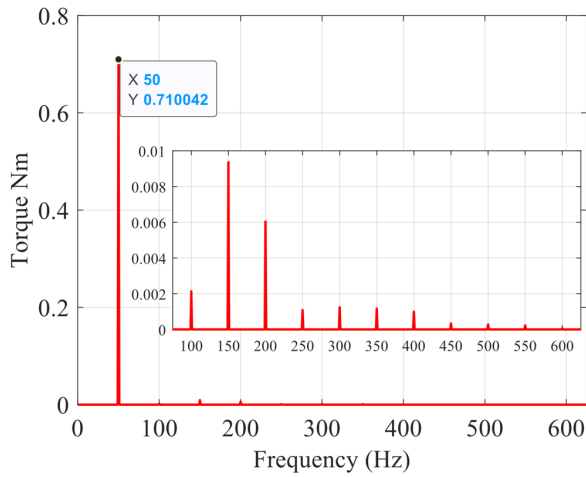
(b) Rotor position (PMA-SynREL motor)



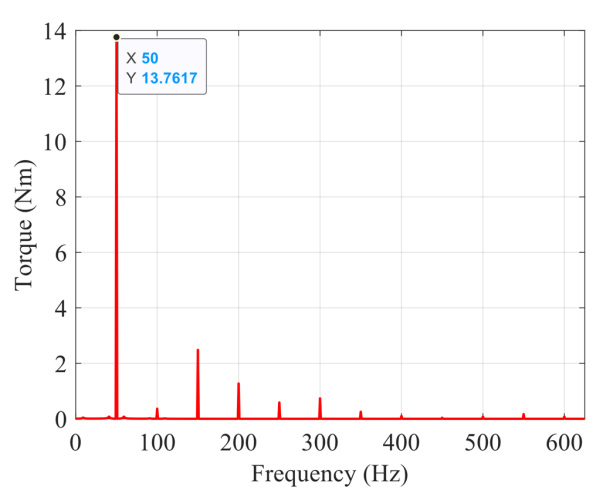
(c) Torque (Nm) (SMPM motor)



(d) Torque (Nm) (PMA-SynREL motor)



(e) Torque FFT (Nm) (SMPM motor)



(f) Torque FFT (Nm) (PMA-SynREL motor)

Figure 5-21 SMPM vs PMA-SynREL (machine as an inductor)

5.12 Heavy-duty machine as a high current density inductor for a three-phase charging system

This thesis primarily focuses on the application of a heavy-duty commercial electric truck, considering that single-phase charging is generally limited to slow charging, investigating three-phase charging is of prime importance. Utilizing the heavy-duty PMA-SynREL machine as an inductor in a 3-phase charging circuit presents certain challenges. A notable issue is the rotating magnetic field generated during the charging process, which has the potential to rotate the rotor. To address this, it's essential to employ techniques aimed at cancelling or opposing the rotation of the magnetic field. Successfully achieving this would keep the rotor stationary, thus eliminating the need for a mechanical lock on the rotor a measure that would otherwise be necessary to prevent the rotation of the rotor. This approach is critical for the effective and safe integrating the traction motor windings in a 3-phase charging circuit.

The PMA-SynREL machine designed in chapter 4 is characterized by a three-phase balanced distributed windings, where each phase consists of eight parallel paths. In a three-phase system, balanced currents are injected into phase A at zero degrees, phase B at -120 degrees, and phase C at -240 degrees establishing a rotating magnetic field that moves in a clockwise direction and induces torque. If phases B and C are swapped, the rotor's motion direction will reverse, causing it to rotate anticlockwise. The motor windings need flexibility to cancel or oppose the rotating field pattern using another set of three-phase windings.

The motor initially features a design with eight parallel paths per phase. This configuration is modified by dividing the eight paths into two sets, each comprising four parallel paths. This alteration effectively transforms the motor into a dual three-phase system, differing from the standard single three-phase setup. This reconfiguration is done through a reconnection of the existing coils, not by adding or physically altering the motor's components. The primary advantage of this reconfiguration is the enhanced flexibility in electrical connections. The schematic in Figure (5-22) illustrates a dual three-phase arrangement with open-end windings connected to two three-phase inverters and a battery, the winding layout is shown in the radial view of the motor in Figure (5-24).

In the traction mode, the dual three-phase windings are connected in series to form a balanced three-phase system, as depicted in the vector diagram in Figure (5-23a). During the charging

mode, S_Grid is activated resulting in the motor windings being reconfigured into a parallel setup as A1-A2, B1-B2, and C1-C2. Owing to the spatially symmetrical phase windings, the field generated by A1 is counteracted by A2 and similarly for the other phases as shown in the vector diagram in Figure (2-23b). Therefore, the resultant field is nullified, ensuring the machine maintains zero average torque.

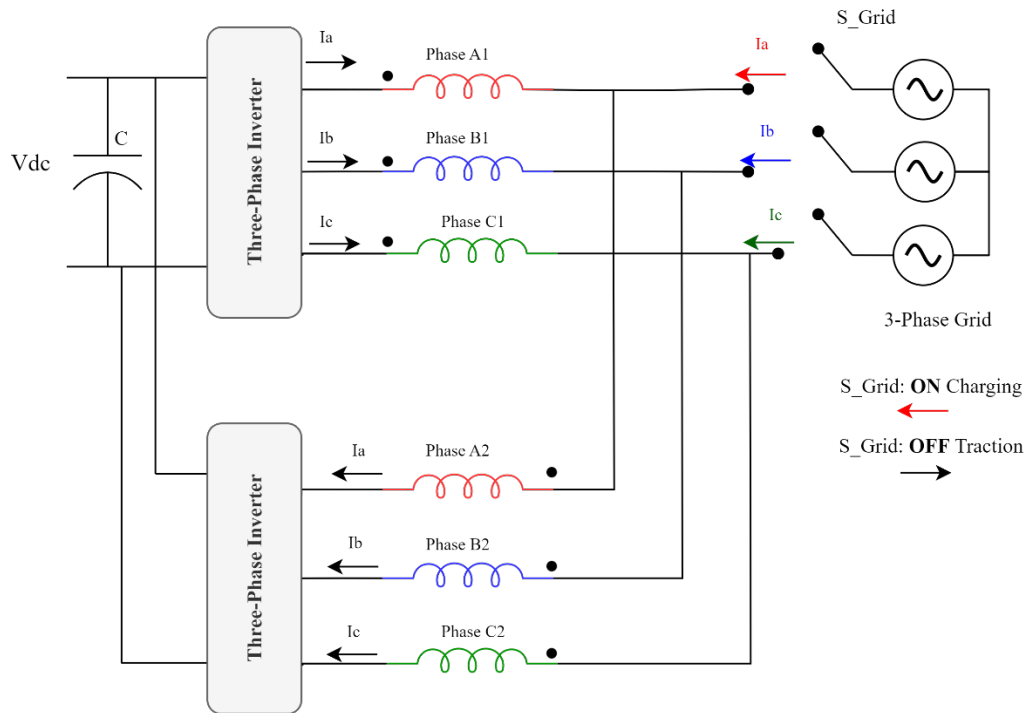


Figure 5-22 Dual three phase symmetrical winding layout

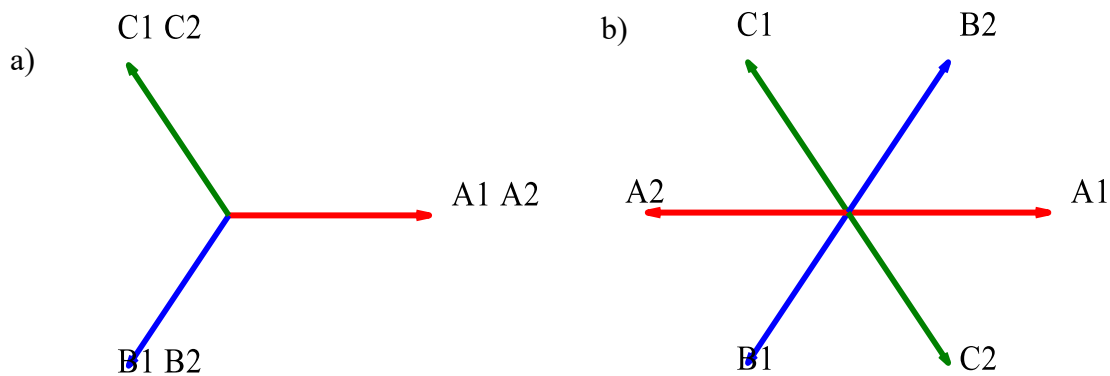


Figure 5-23 Phasor diagram (a) Traction mode (b) Charging mode

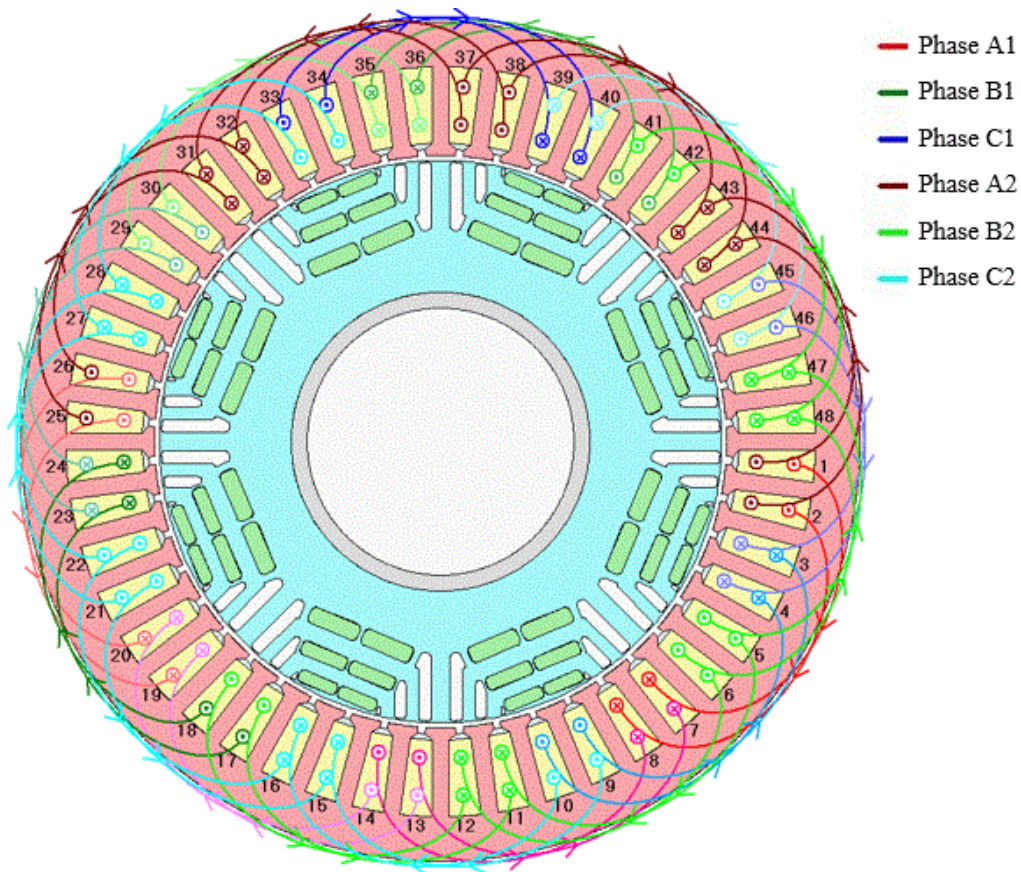


Figure 5-24 8-pole 48-slot PMA-SynREL machine (Dual three phase symmetrical windings)

In traction mode, A1-A2 are connected in series and similarly for phase B and C. This specific series connection has led to a notable increase in inductance, reaching 0.7239 mH. This is a significant rise compared to the inductance observed in the standard single three-phase connection with eight parallel paths, previously measured at 0.1896 mH. This change underscores the substantial impact that winding configuration and connection type can have on the electrical characteristics of the machine. In charging mode, the configuration of the PMA-SynREL machine is adjusted to ensure effective magnetic field cancellation. This is achieved by introducing the supply current into A1 in a direction opposite to that of A2, creating a magnetic field that is 180 electrical degrees out of phase A2 field and similarly for phase B and C. This configuration results in a significant decrease in the phase self-inductance, which drops to 4.2286 μ H, as detailed in Table (5-13). This approach is crucial for cancelling the magnetic field effectively, thereby ensuring the charging mode operates efficiently and effectively. It is critical to note that these measurements were recorded with the rotor position at 352.5 degrees.

The impact of changing the rotor position on inductance demonstrated that, within this layout the inductance remained stable.

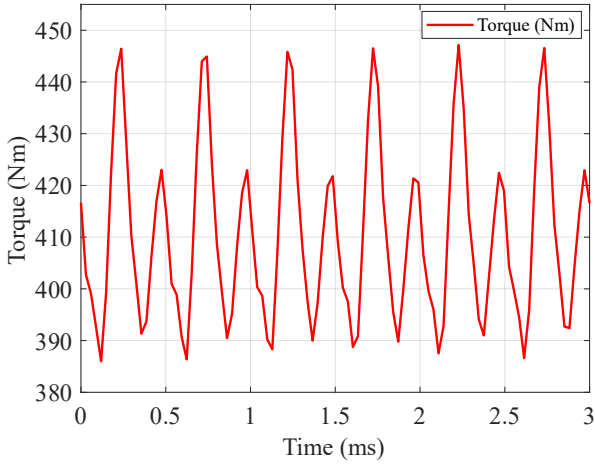
Table 5-13 Inductance measurements in traction and charging mode (dual 3-phase symmetrical windings)

Traction mode inductance	Charging mode inductance
0.7239 mH Phase A1 series with Phase A2	4.2286 uH, Phase A1 parallel with Phase A2
	4.2256 uH, Phase B1 parallel with Phase B2
	4.2256 uH, Phase C1 parallel with Phase C2

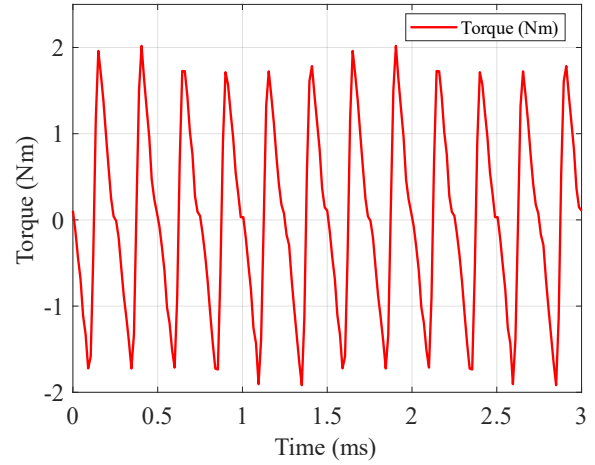
5.13 Simulation results of the dual 3-phase symmetrical layout

In the traction mode, the PMA-SynREL machine in the dual 3-phase symmetrical layout is rated for a peak current of 325.25 Amps, which aligns with the continuous output torque of the machine. This current rating is utilized as a reference point for evaluating the machine's behaviour in charging mode. The performance of the PMA-SynREL machine in traction mode is first illustrated in Figure (5-25a), which demonstrates an output torque of 410 Nm at a base speed of 5000 rpm.

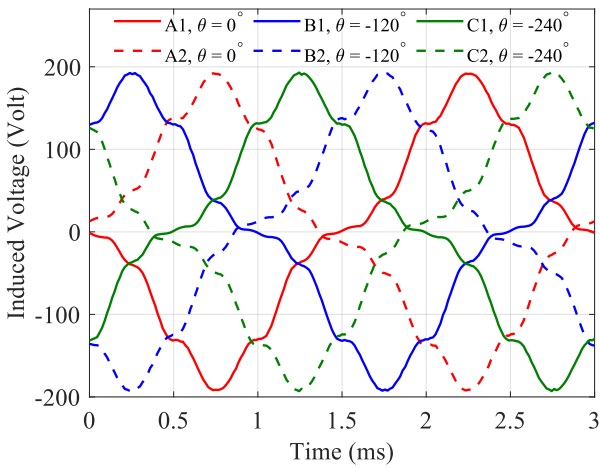
The investigation of the charging mode is initiated at the base speed of 5000 rpm. This is a critical parameter since synchronous machines are designed to produce torque at synchronous speeds. The findings, detailed in Figure (5-25b), reveal that the average torque is effectively zero, with the torque fluctuating between positive and negative values. This fluctuation is indicative of rotor oscillations within the machine. To investigate the machine's dynamics, a transient analysis is conducted at a grid frequency of 50Hz. The results from this analysis confirm the previous observations, indicating a zero average torque as shown in Figure (5-25f). Moreover, it observed that the rotor oscillates at the supply frequency in the steady-state region, and the magnitude of these oscillations is low as shown in Figure (5-25e). The induced voltage shown in Figure (5-25c) and the flux linkage shown in Figure (5-25d), clearly represents that A1, B1 and C1 are in the opposite direction of A2, B2 and C2.



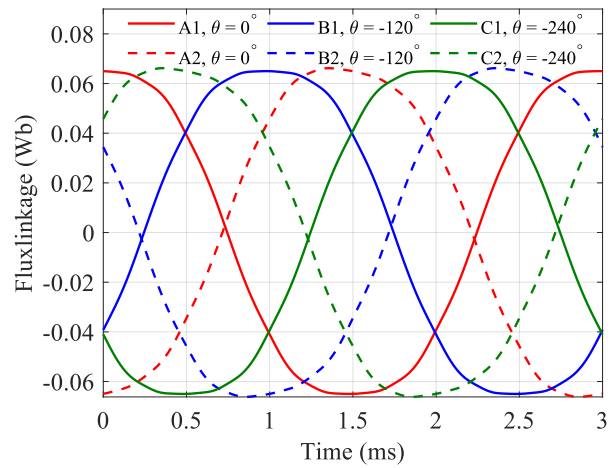
(a) Torque in traction mode at 5000 rpm



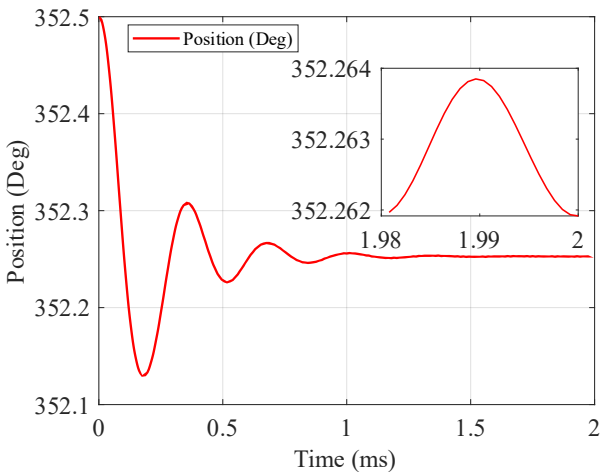
(b) Torque in charging mode at 5000 rpm



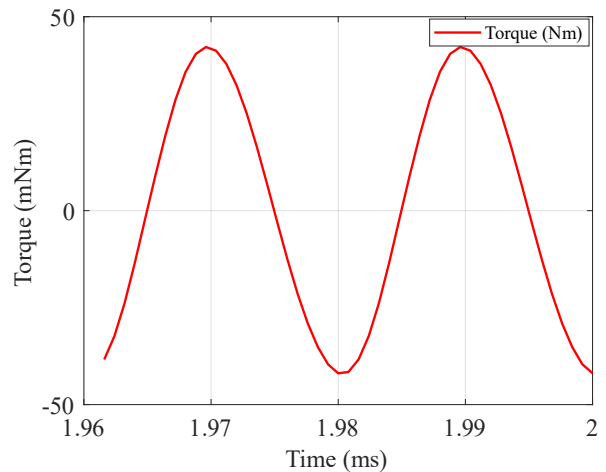
(c) Torque in charging mode steady state **mili N**



(d) Flux linkage at charging mode



(e) Rotor position charging mode



(f) Torque in charging mode (transient analysis)

Figure 5-25 Dual 3-phase symmetrical windings (traction and charging) results

The symmetrical winding layout of the machine investigated previously in Figure (5-22), upon thorough analysis, has demonstrated its ability to operate without generating torque in the charging mode. This section aims to investigate this layout by proposing a reconfiguration of each phase into a series connection. Previously, each phase was composed of four parallel paths. Transitioning to a series connection is expected to significantly enhance the inductance, a critical factor for the machine’s performance as an inductor. However, this modification necessitates a greater number of switches to facilitate the reconfiguration from parallel to series paths. As depicted in Figure (5-26), achieving the series connection of A1 coils with A2 coils requires the integration of 16 switches. Additionally, an investigation into the rotor dynamics is necessary. This exploration will focus on examining the impact of this increased inductance on the machine’s overall operational dynamics.

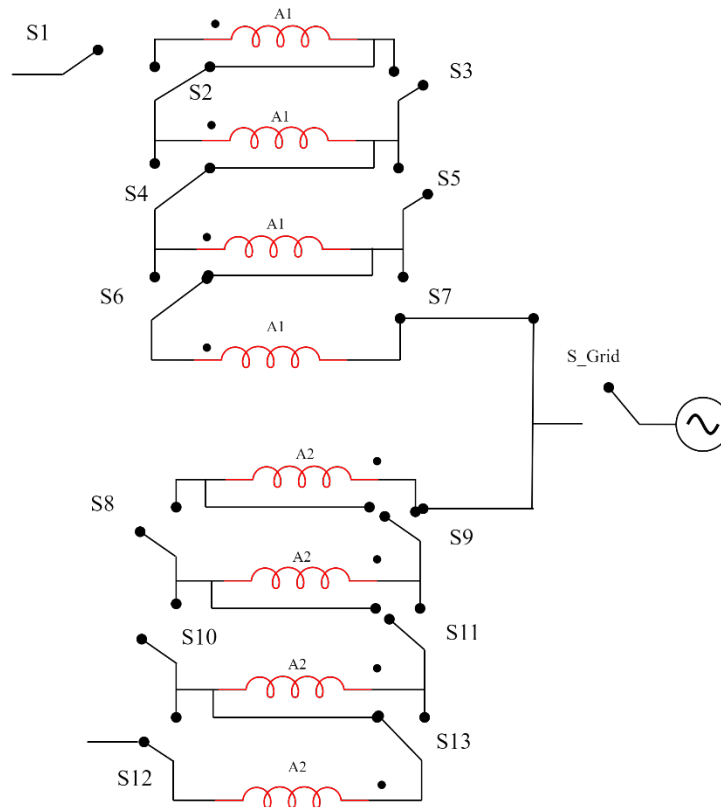
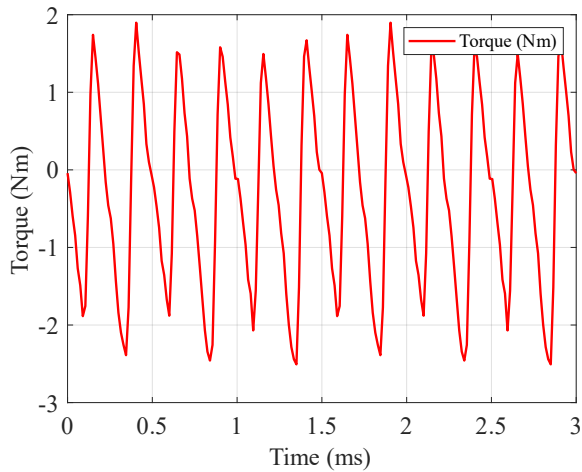


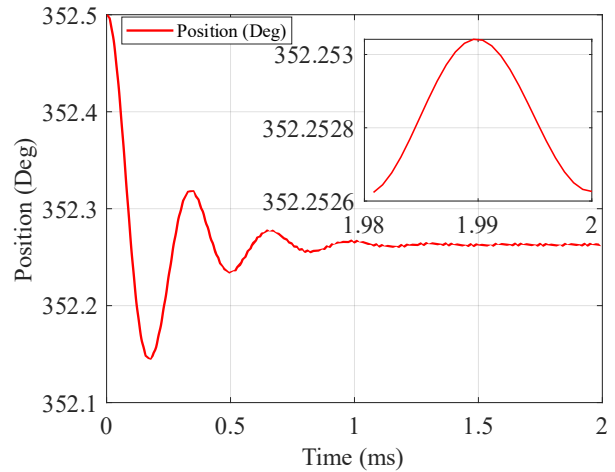
Figure 5-26 Dual 3-phase symmetrical layout (Phase A1 and A2) in series

As expected, the inductance has increased in this layout to 67.6691 uH. Furthermore, this new configuration proves that this symmetrical dual 3-phase distributed winding is torque-free. Due to the increased inductance the torque has increased as shown in Figure (5-27a). In the parallel connection shown in Figure (5-25f) the peak torque in the transient analysis within the interval

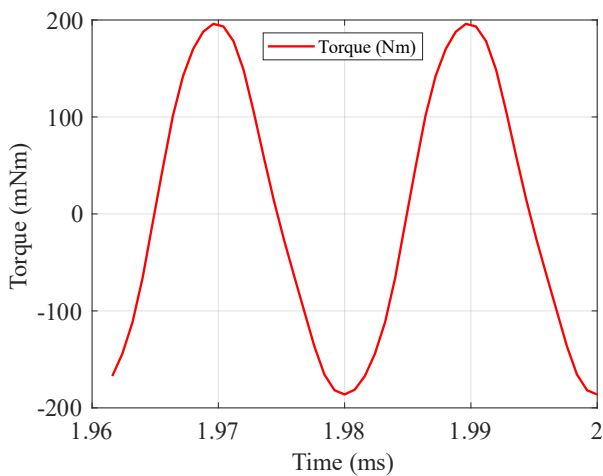
of 1.92 ms to 2 ms was less than 50 mNm, whereas in this connection it has surpassed 50 mNm peak torque. The rotor position, as depicted in Figure (5-27b) reveals that the magnitude of oscillations in the steady state region is minimal. This observation indicates that the impact of the increased inductance on the rotor dynamics is relatively negligible in terms of causing significant oscillations.



(a) Torque in traction mode at 5000 rpm



(b) Rotor position charging mode



(c) Torque in charging mode (transient analysis)

Figure 5-27 Results of dual 3-phase symmetrical layout all paths in series per phase

5.14 Simulation results of the dual 3-phase asymmetrical layout

This section aims to investigate an asymmetrical dual three-phase connection as an inductor for the charging mode. This configuration, as shown in Figure (5-28), employs dual three-phase windings offset by a spatial angle of 30 degrees. Unlike the symmetrical dual three-phase configuration, the asymmetrical layout requires additional switches. This configuration requires four switches, as shown in Figure (5-28) to transition from traction to charging mode. This facilitates the reconfiguration of the windings. In this layout, each winding phase consists of eight parallel paths.

Phase transposition is applied to alter the phase sequence. During charging mode, the grid phases are connected as follows: I_a to (C2-B1), I_b to (A1-B2), and I_c to (A2-C1). The spatial angle between the connected phases in the charging mode is 150 degrees as opposed to the symmetrical layout which has a spatial angle of 180 degrees. Figure (5-29b) illustrates the resultant magnetic field, which is positioned centrally to the excited phases and exhibits a reduced magnitude. The winding layout is shown in the radial view of the motor in Figure (5-30).

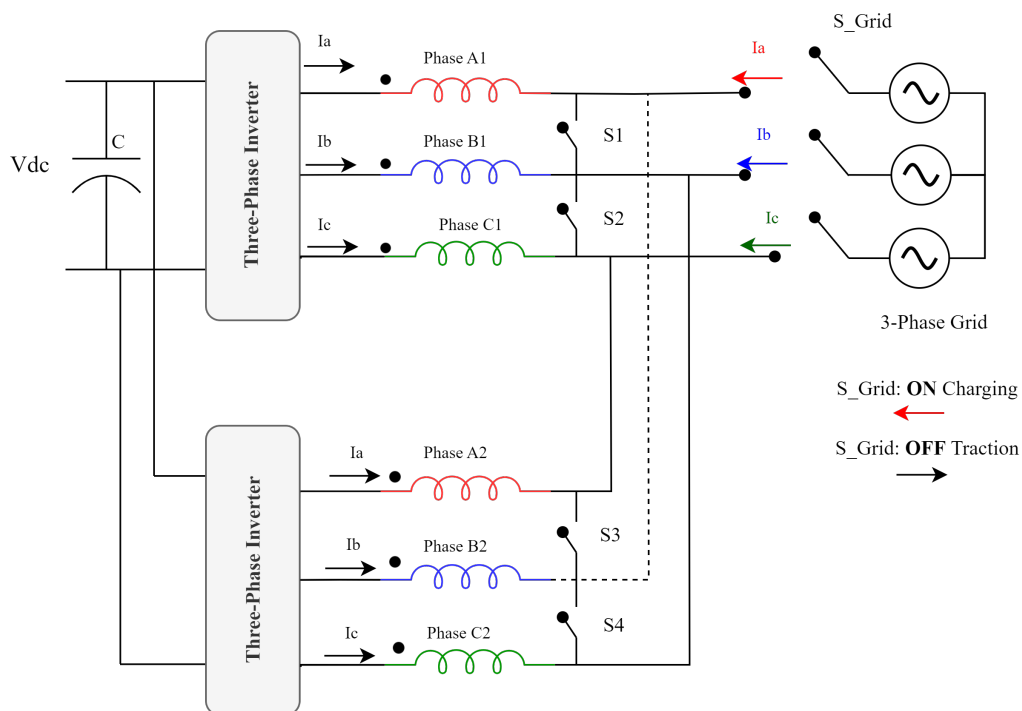


Figure 5-28 Dual three phase asymmetrical winding layout

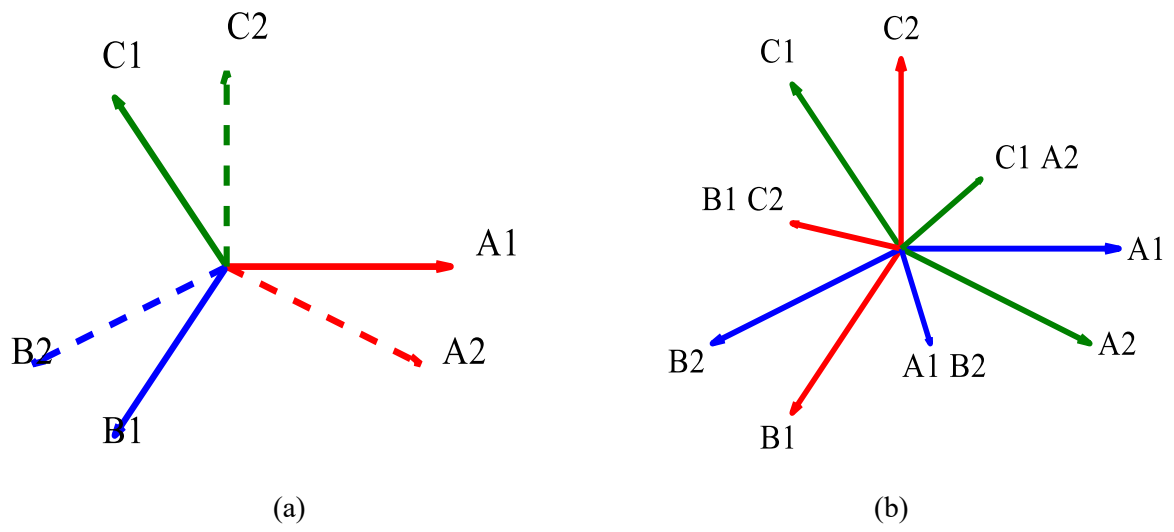


Figure 5-29 Phasor diagram for asymmetrical layout (a) Traction mode (b) Charging mode

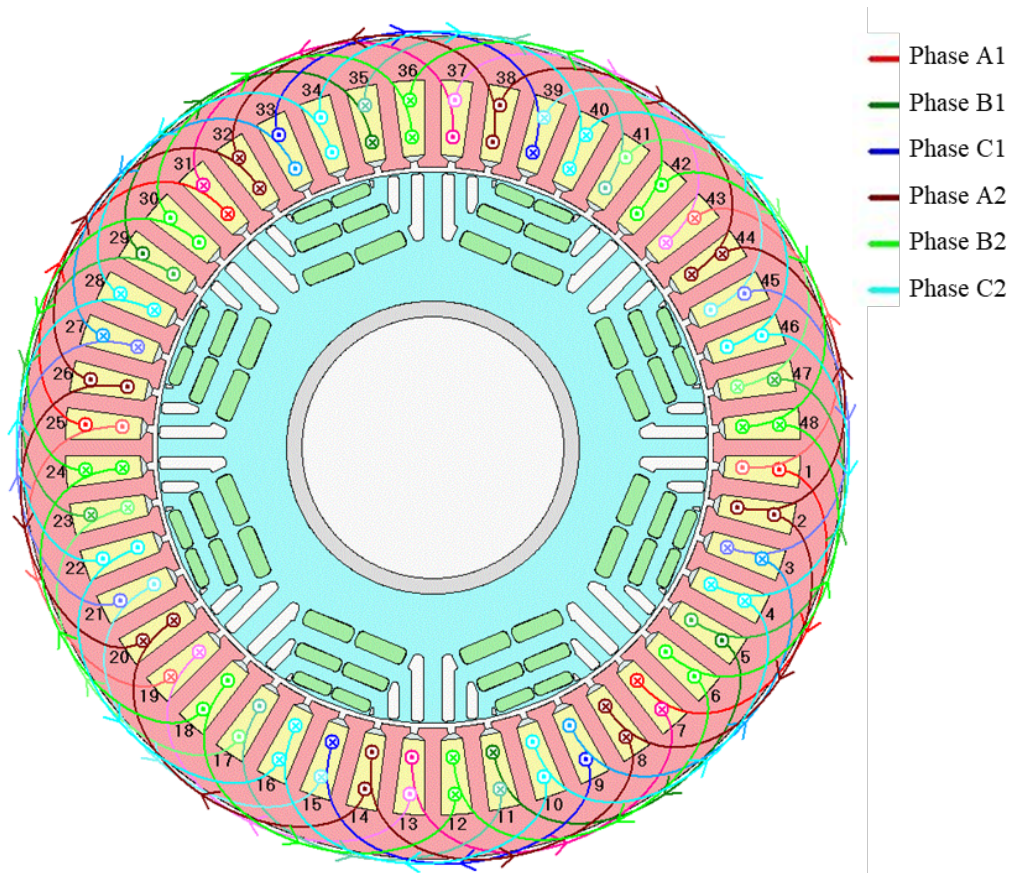


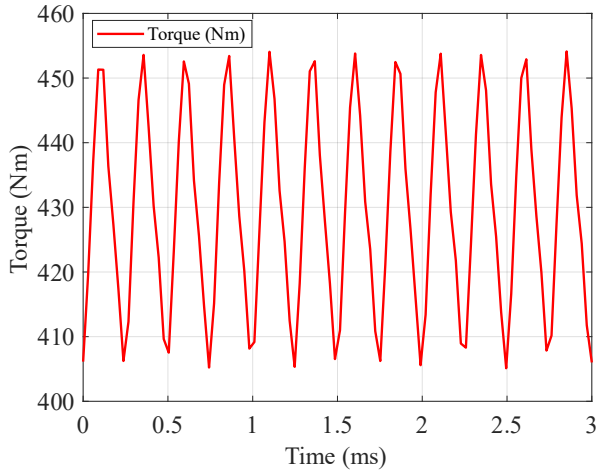
Figure 5-30 8-pole 48-slot PMA-SynREL machine (Dual three phase asymmetrical windings)

In traction mode, the closure of switches S1-S2 and S3-S4 establishes two neutral points within the system. The measured inductance shown in Table (5-14) for each phase in this mode is 82 uH. This reduced inductance per phase can be attributed to the fact that the dual three-phase asymmetrical windings are not interconnected in traction mode as in the symmetrical open end dual 3-phase connection, furthermore, each phase consists of eight parallel paths. In charging mode, the inductance of Phase A1-B2 is recorded at 23.04 uH. This represents 81.6% increase in inductance compared to the symmetrical layout inductance 4.2286 uH, which is attributable to the presence of a resultant magnetic field. The inductance measurements were taken with the rotor positioned at 356.25 degrees. At this specific position, the rotor is aligned with phases B1 and C2, which means that the influence of the rotor's PM field is most pronounced on the inductance of phase B1-C2. Therefore, the inductance characteristics of this asymmetrical layout are influenced by the rotor position during charging mode.

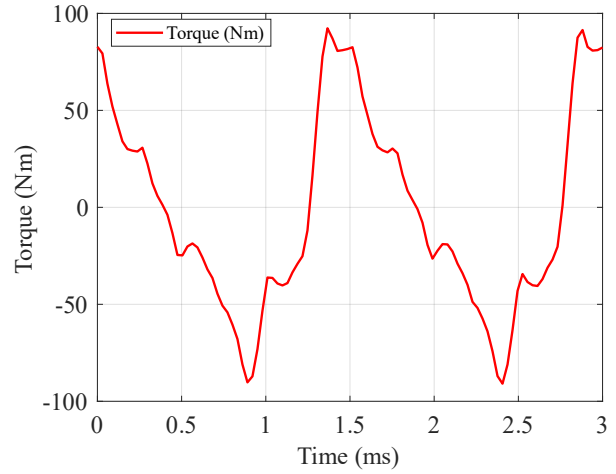
Table 5-14 Inductance measurements in traction and charging mode (dual 3-phase asymmetrical windings)

Traction mode inductance	Charging mode inductance
82uH, Phase A1	23.04 uH, Phase A1 parallel with Phase B2
	19.720 uH, Phase B1 parallel with Phase C2
	23.12 uH, Phase C1 parallel with Phase with A2

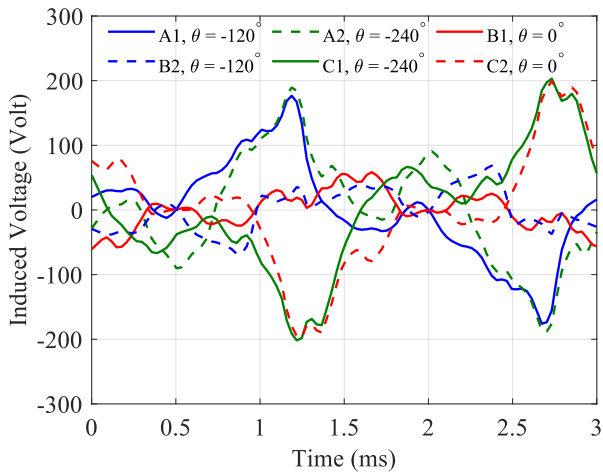
The traction mode is examined first at 650.5 peak current, the traction mode average torque is 430 Nm. The windings are reconfigured to the charging layout, in this mode the motor exhibit a zero average torque at the base speed of the motor as shown in Figure (5-31b). A transient analysis is examined on this layout with the current frequency set to 50 Hz, it shown in Figure (5-31e) that the rotor reaches steady state at 1ms and oscillates at grid frequency with low magnitude. Due to the reduced frequency from 333.333 Hz to 50 Hz, the torque in the transient analysis is less distorted as in Figure (5-31f). The spatial angle 150 degrees between the connected phases in the charging mode is reflected on the flux linkage of in Figure (5-31d) and induced voltage in Figure (5-31c).



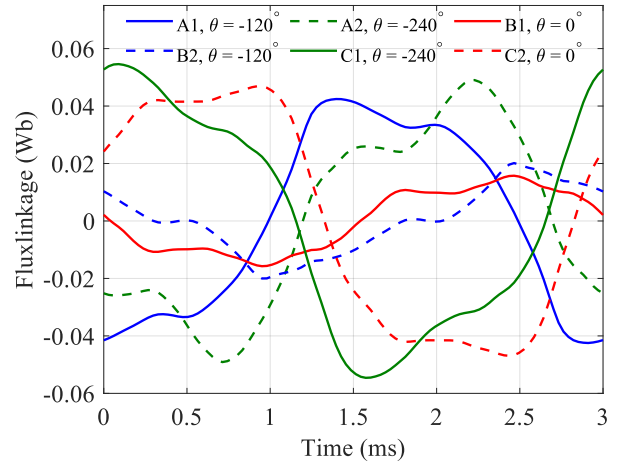
(a) Torque in traction mode at 5000 rpm



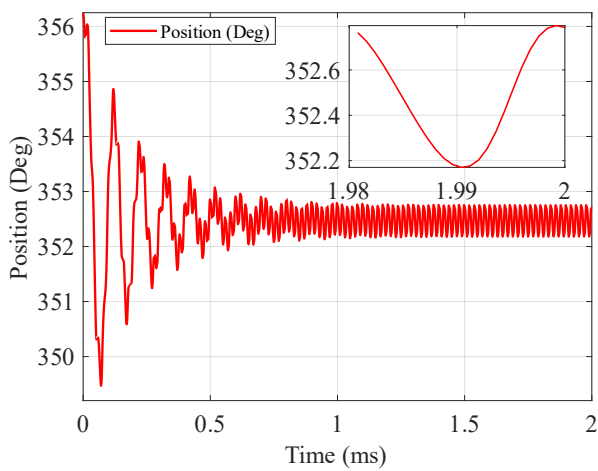
(b) Torque in charging mode at 5000 rpm



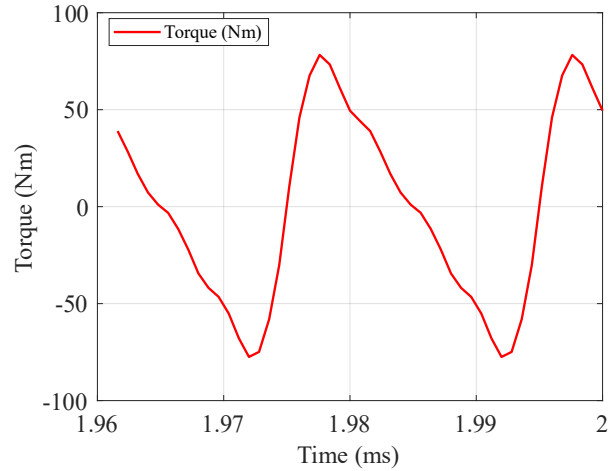
(c) Torque in charging mode steady state **mili N**



(d) Flux linkage at charging mode



(e) Rotor position charging mode (transient analysis)



(f) Torque in charging mode (transient analysis)

Figure 5-31 Dual 3-phase asymmetrical windings (traction and charging) results

The following section will investigate the asymmetrical winding layout in the charging mode by reconfiguring each phase into one path instead of eight parallel paths, this will assist in increasing the inductance and assessing the layout more in the charging mode. Figure (5-32) depicts the reconfiguration connection of A1-B2, and similarly this will be applied on all phases.

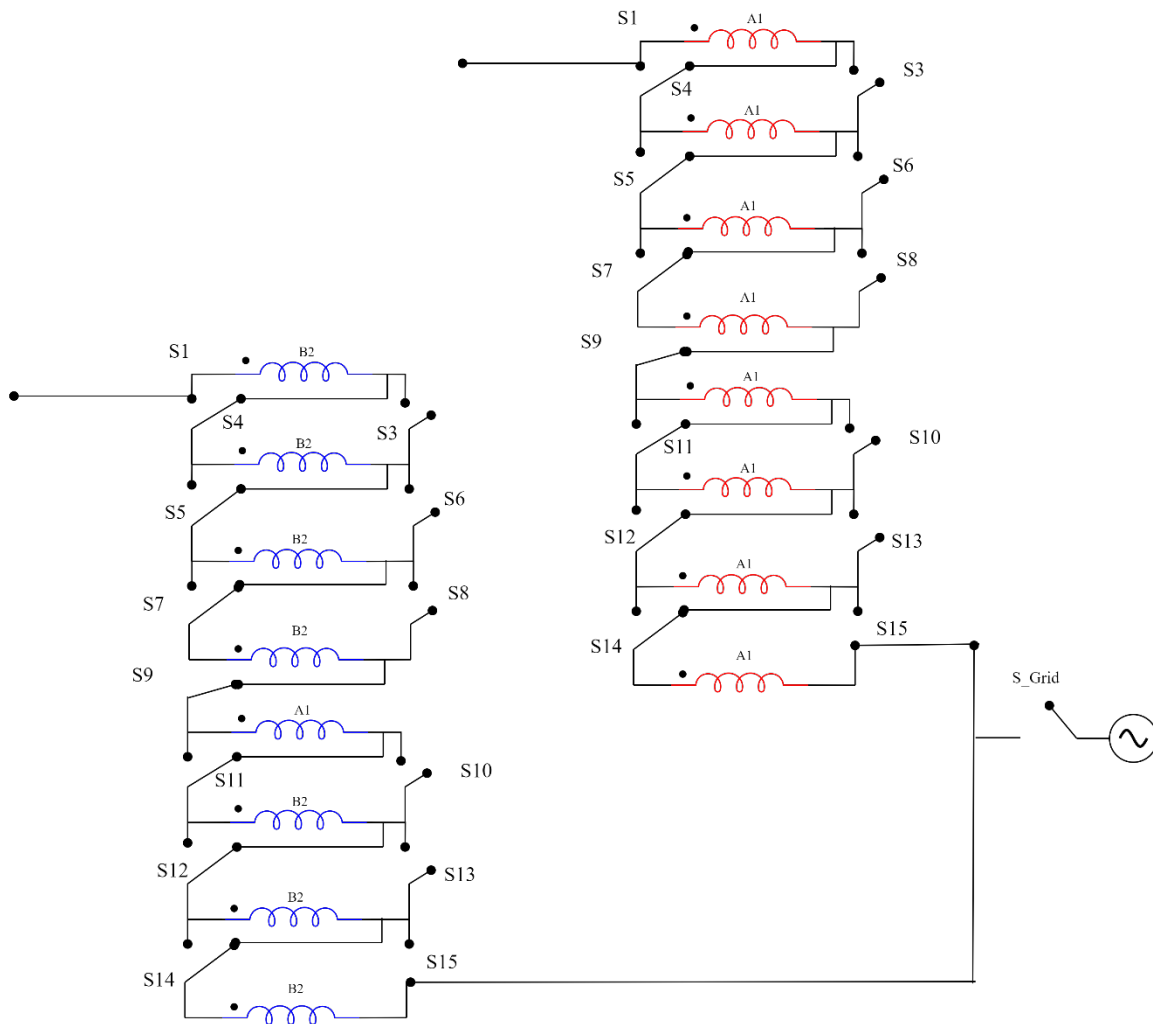
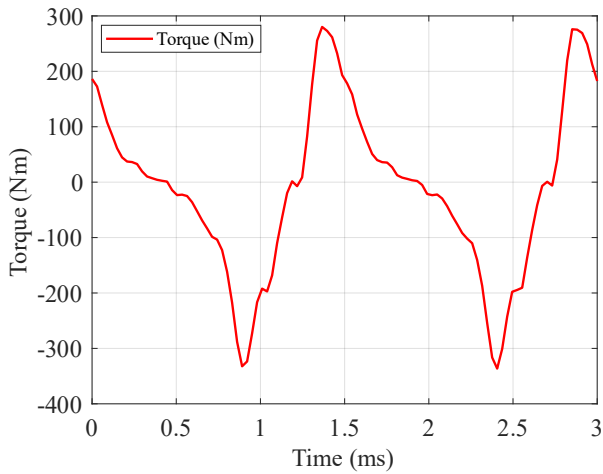
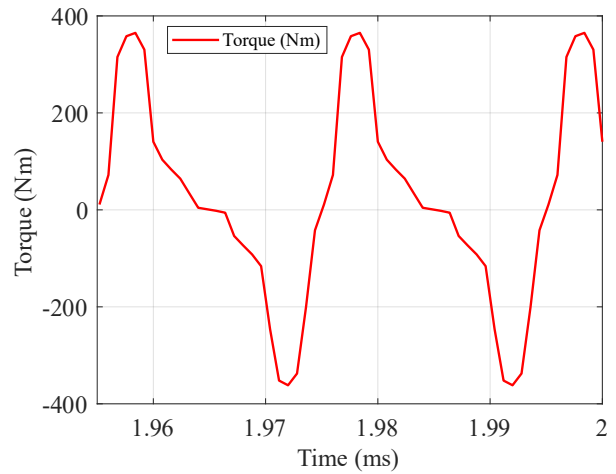


Figure 5-32 Dual 3-phase asymmetrical layout (Phase A1 and B2) in series

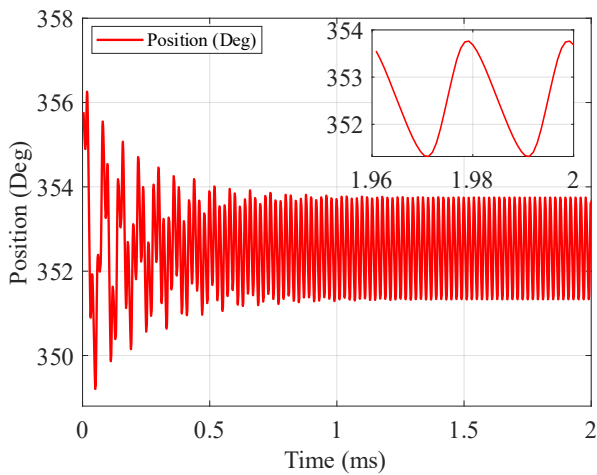
Each phase in this layout will require 15 switches, to facilitate the charging configuration with all paths in series. As expected, the inductance has increased to 1.5077 mH and as shown in Figure (5-33a), the torque is fluctuating between the positive and negative. In the transient analysis, the torque is captured in the steady state region in Figure (5-33b), with average torque equal to zero. The rotor position is shown in Figure (5-33c), at steady state the magnitude of rotor oscillation is minimal.



(a) Torque at 5000 rpm



(b) Torque during transient analysis



(c) Rotor position in transient analysis

Figure 5-33 Results of dual 3-phase asymmetrical layout all phases paths in series

5.15 Thermal management in charging mode

The reconfiguration of the machines parallel paths into series as shown in Figure (5-26) and Figure (5-32), will alter the resistance and current density of the machine therefore, the input current must be reduced in those configurations to keep the current density of the traction motor to its designed value 9.71 A/mm². This ensures that the windings of the machine are within temperature limits. An important aspect of the functioning of the traction machine as a high current density inductor is to ensure that the magnets are not exposed to high temperature from the windings.

This section will look at the temperatures of the symmetrical dual 3-phase layout in Figure (5-22) and the asymmetrical dual 3-phase in Figure (5-28). Both layouts were examined to produce the same copper losses at a current density equal to 9.71A/mm². As the grid frequency is 50 Hz, it is expected that the iron components are not of concern, the only components of concern are the copper (DC losses) and magnet temperature.

The temperatures shown in Table (5-15), are acquired with the traction machine cooling systems (water-jacket and spray cooling) are activated. This means if the charging point supports high current, the heavy-duty traction machine with its integrated cooling is capable of operating as a high current density inductor in the charging circuit with safe temperature limits.

Table 5-15 Windings and magnets temperature during charging mode

Component	Symmetrical layout Figure (5-22)	Asymmetrical Layout Figure (5-28)
Windings	109.7 C	109.9 C
Magnets	42.6C	42.6 C

5.16 Summary

This chapter provides an insightful exploration into the potential of employing traction motor windings as an inductor. The subject motor is a SMPM motor, which features a distributed double-layer winding, a common configuration found in EV motors and certain types of industrial motors. The research affirms the possibility of using the traction motor windings as an inductor. It is found that the layout of the winding directly impacts the circuit's inductance, a crucial parameter for effective power input filtration. Interestingly, this chapter found that an increase in layout inductance correlates with a higher number of required switches for reconfiguration, suggesting greater complexity and possible increases in switching losses.

Injecting the motor with a current leads to the generation of torque, which prompts the rotor to oscillate at the same frequency as the supply. Despite this, the induced torque and resulting oscillation are relatively minimal indicating that they shouldn't notably interfere with the motor's operation as an inductor. The study further revealed that the rotor's initial position and the placement of the excitation field significantly influence the rotor's behaviour. Observing the rotor's movement provides key insights into the interaction between the stator's magnetic field and the PMs on the rotor, where it's seen that the PMs induce rotor oscillation in response to supply excitation.

In this investigation, the focus was on examining a series of layouts involving SMPM machine windings. The layouts underwent lab evaluation to measure their inductance, after which a 60A RMS current at a frequency of 50 Hz was applied to take vibration measurements using a vibration meter.

Across all layout configurations, there was a consistent presence of a 50Hz component in the vibration meter readings. This reoccurring 50Hz component is due to the excitation current frequency. Discrepancies were also noted between the inductance values measured in the lab and those predicted by the simulation in some layouts. These could be due to the actual effects of end windings and mutual inductance, possibly overlooked in the simulation models.

The investigation done on the SMPM machine shows that connecting all phases in series with all parallel paths in series yield the highest inductance. This layout was implemented on the PMA-synREL machine which is the candidate for the heavy-duty truck applications. The results

show that the PMA-SynREL machine exhibit higher inductance in layout 1 this was attributed to reduced airgap length and increased volume. The results show that both the SMPM machine and the PMA-synREL machine exhibit zero average torque. Furthermore, both topologies show a 50Hz component in the FFT of the torque due to the supply current.

The use of the high power PMA-SynREL machine as an inductor has been further investigated in a 3-phase charging system, this is due to the importance of 3-phase charging for heavy-duty commercial vehicles. Two techniques have been used, dual 3-phase symmetrical layout and dual 3-phase asymmetrical winding layout. All methods are torque-free in the charging mode. Reconnecting the 3-phase setup to a dual 3-phase setup gave more degrees of freedom to exploit the traction machine windings in the charging mode to achieve zero torque. All techniques applied in the 3-phase charging mode used the machine's continuous rated current in traction mode. In the thermal aspect of using the traction machine as a high current density inductor, DC losses were the cause of heat in the windings, which could make the magnets vulnerable to demagnetization. However, with the activation of the traction machine's cooling system including spray cooling and water-jacket, the PMA-SynREL machine can be used as a high current density inductor in the charging mode within safe temperature limits.

Chapter 6. Optimization of Various Slot-Pole Configurations of PMA-SynREL Machines

6.1 Introduction

Understanding the impact of increasing the number of poles of PMA-SynREL machines is the aim of this chapter. Chapter 4 comprehensive exploration of an 8-pole machine provided an understanding of the multi-physics of the machine for high peripheral speed. However, one critical aspect merits further exploration which is the pole count variation. Given the important balance required to achieve in the design of high-power high-speed machines, which is striking a balance between the electromagnetic, mechanical and thermal performance. This chapter compares between 5 different slot-pole PMA-SynREL machines, all machines will be optimized to achieve the lightest weight as feasible. The same external cooling will be used for all machines.

The contribution to knowledge of this chapter is the exploration between the pole count and weight for a fixed outer rotor diameter of a high-power high speed PMA-SynREL machine. Moreover, the trade-off between rib thickness and pole count, as well as current density and back iron. The impact of design constraints, how they interact and counterbalance each other.

6.2 Slot-pole combination

In the comparative study of different slot-pole for PMA-SynREL machines, the number of slots per pole per phase (SPP) is a crucial factor. Having the same SPP for all the configurations ensures a fair comparison. The SPP is a key parameter that dictates the machines performance and overall characteristic. This includes the winding distribution, magnetic field harmonics. It is also important to note that maintaining equal SPP across different configurations may introduce other challenges, especially when moving to higher pole numbers. The number of slots increases with the number of poles when aiming for a fixed SPP for all configurations as shown in Table (6-1). This could lead to higher complexity in the machines geometric design and manufacturing process.

Table 6-1 Winding Factor and SPP for different slot-poles

Slot/Poles		6	8	10	12	14
24	k_w		1	0.588		0.766
	SPP		1	0.8		0.571
36	k_w	0.966	0.945	0.942	1	0.551
	SPP	2	1.5	1.2	1	0.857
48	k_w		0.966	0.954		0.937
	SPP		2	1.6	1	1.143
60	k_w		0.951	0.966		0.95
	SPP		2.5	2		1.429
72	k_w	0.958	0.96	0.954	0.966	0.954
	SPP	4	3	2.4	2	1.714
84	k_w		0.953	0.952		0.966
	SPP		3.5	2.8		2

In this thesis SPP is set to 2. Further, the topologies that will be considered are (6-pole 36-slot), (8-pole 48-slot), (10-pole 60-slot), (12-pole 72-slot) and (14-pole 84-slot). Increasing the number of poles of the machine increase the electric frequency for a given speed which will increase the iron losses of the machine. Furthermore, increasing the number of poles reduces the back iron of the stator as the flux will follow a shorter path. Hence, a reduction in stator iron can be achieved with high-pole count.

6.3 PMA-SynREL machine geometry

The design of the rotor in a PMA-SynREL machine heavily relies on the correct positioning of the flux barriers ($wb1$, $wb2$, $wb3$, and $wb4$) starting from the rotor's centre shown in Figure (6-1). This configuration determines the d-axis flux path. Moreover, the thickness ($h1$) and width of the magnets ($w1$) are also crucial as PMA-SynREL machines offer advantages over other PM machines, due to the reduced PM quantity. This consideration should be part of the optimization process to enhance electromagnetic performance with fewer magnets. As PMs are temperature sensitive, a reduction in quantity can decrease the machine's overall sensitivity to temperature. The web thickness, denoted as x , y and z in Figure (6-1) requires precise positioning which significantly influences the torque ripple. Furthermore, the introduction of iron ribs coloured in red in Figure (6-1), both radially and tangentially is necessary to preserve mechanical integrity. Including centre and inner ribs reduces the mechanical stress on the rotor. However, these ribs can increase leakage flux potentially diminishing the motor's performance. This situation underscores the importance of conducting a multi-physic optimization that considers electromagnetic, mechanical and thermal analyses.

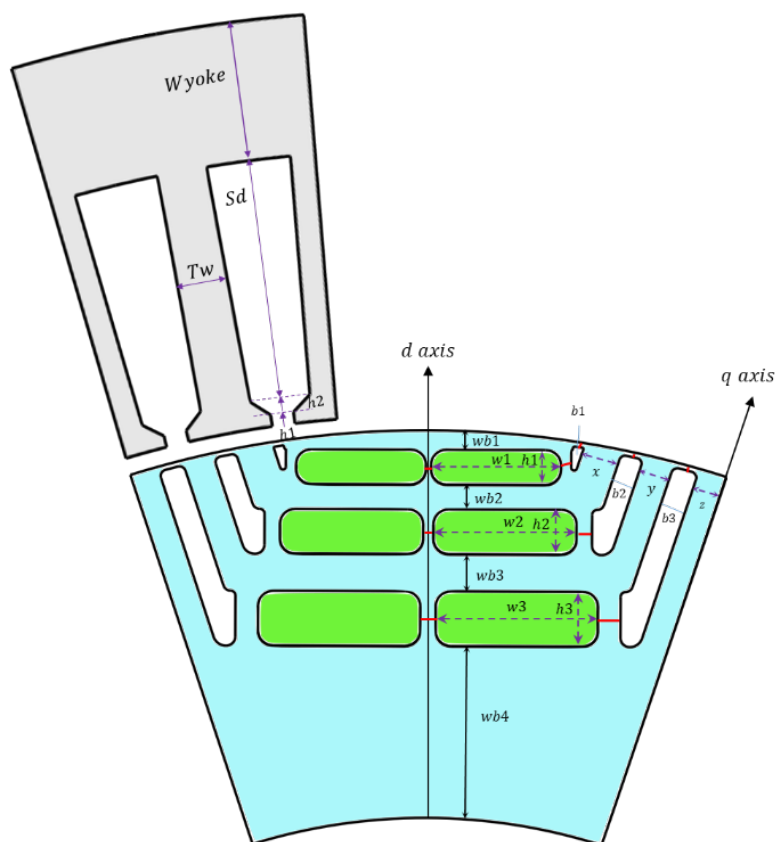


Figure 6-1 PMA-SynREL radial configuration important dimensions

The airgap is another essential design parameter in electric motors as its dimensions affect the magnetic loading. Decreasing the airgap length intensifies the magnetic loading and reduces the required current, thereby mitigating copper losses. However, a reduced airgap can also augment airgap harmonics leading to induced eddy currents. This condition could expose NdFeB magnets to higher temperatures, alongside posing mechanical issues. Therefore, in this study the airgap is standardized to 1.5mm across all combinations to prevent these potential complications.

On the other side, the stator is essential to be optimized with the rotor to ensure a uniform magnetic flux distribution. Furthermore, the sizing of the stator slots impacts the current density of the machine and hence, temperature rise. A further reduction in torque ripple and cogging torque can be achieved when optimizing the rotor and stator together.

6.4 Input variables in the optimization process

Various input geometrical parameters are considered in the optimization as shown in Table (6-2). The objective of the optimization is to minimize the active mass of the machine. Constraints are set to define the feasible region. This ensures that the solutions obtained from the optimization process are practically feasible. They represent the physical and technical limits, as all slot-pole combinations are driven by the same DC-link constraints, it must ensure that the designed machine is within the limits. Table (6-3) represents constraints that are considered in this optimization, Figure (6-2) shows the critical points of operation that are considered.

Table 6-2 Input variables in the optimization model

Input Variable	
Stator Dimensions (Figure 6-1)	Rotor Dimensions (Figure 6-1)
Tooth width (mm)	Flux barrier thickness (wb) (mm)
Stator back iron (mm)	Radial and tangential ribs (mm)
Stack Length (mm)	PM thickness (w) and height (h) (mm)
Slot open (mm)	Flux barrier outer thickness (b) (mm)
Tooth tip depth (mm)	Thickness between outer flux barriers (x,y and z)
Slot depth (mm)	

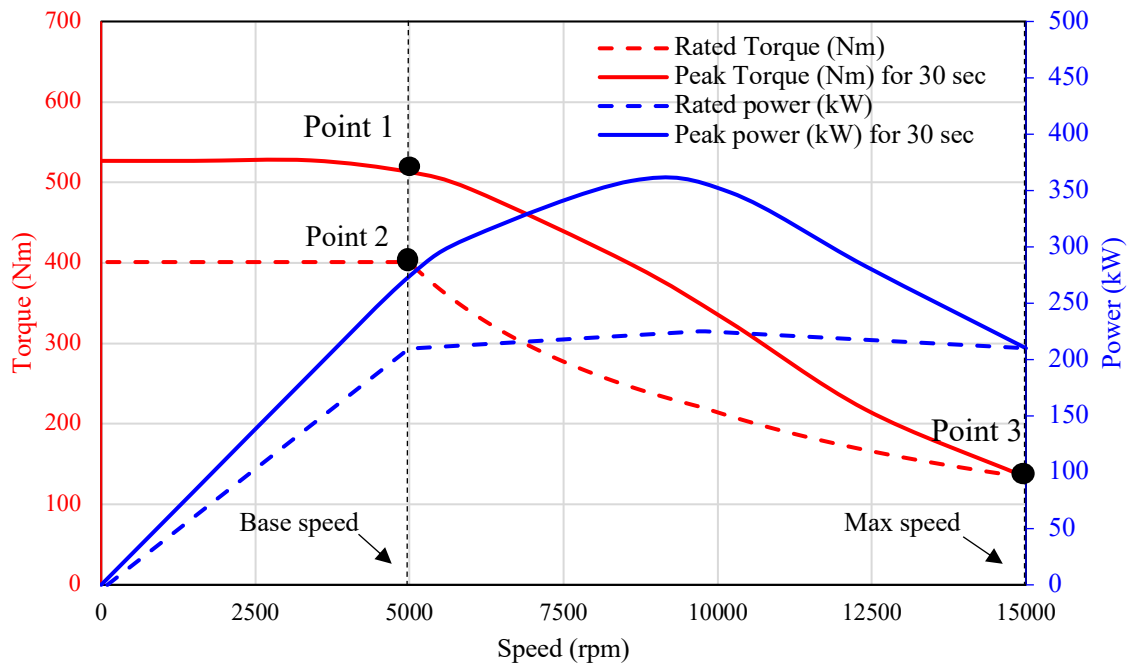


Figure 6-2 Torque Power characteristic of a heavy-duty vehicle

Table 6-3 Constraints set in the optimization model and objective

Output Variable	Constraints
Torque, Point (1)	>570 Nm
Torque, Point (2)	>399 Nm
Torque, Point (3)	>180 Nm
Torque ripple, point (3)	<30%
Voltage, point (1),(2) and (3)	<253.3 volts
Winding temperature, point (1),(2) and (3)	<180C
Magnet temperature, point (1),(2) and (3)	<150C
Rotor stresses at 16500 rpm	<720 MPa
Output variable	objective
Active Mass	Minimize less than 70kg

6.5 Design Workflow

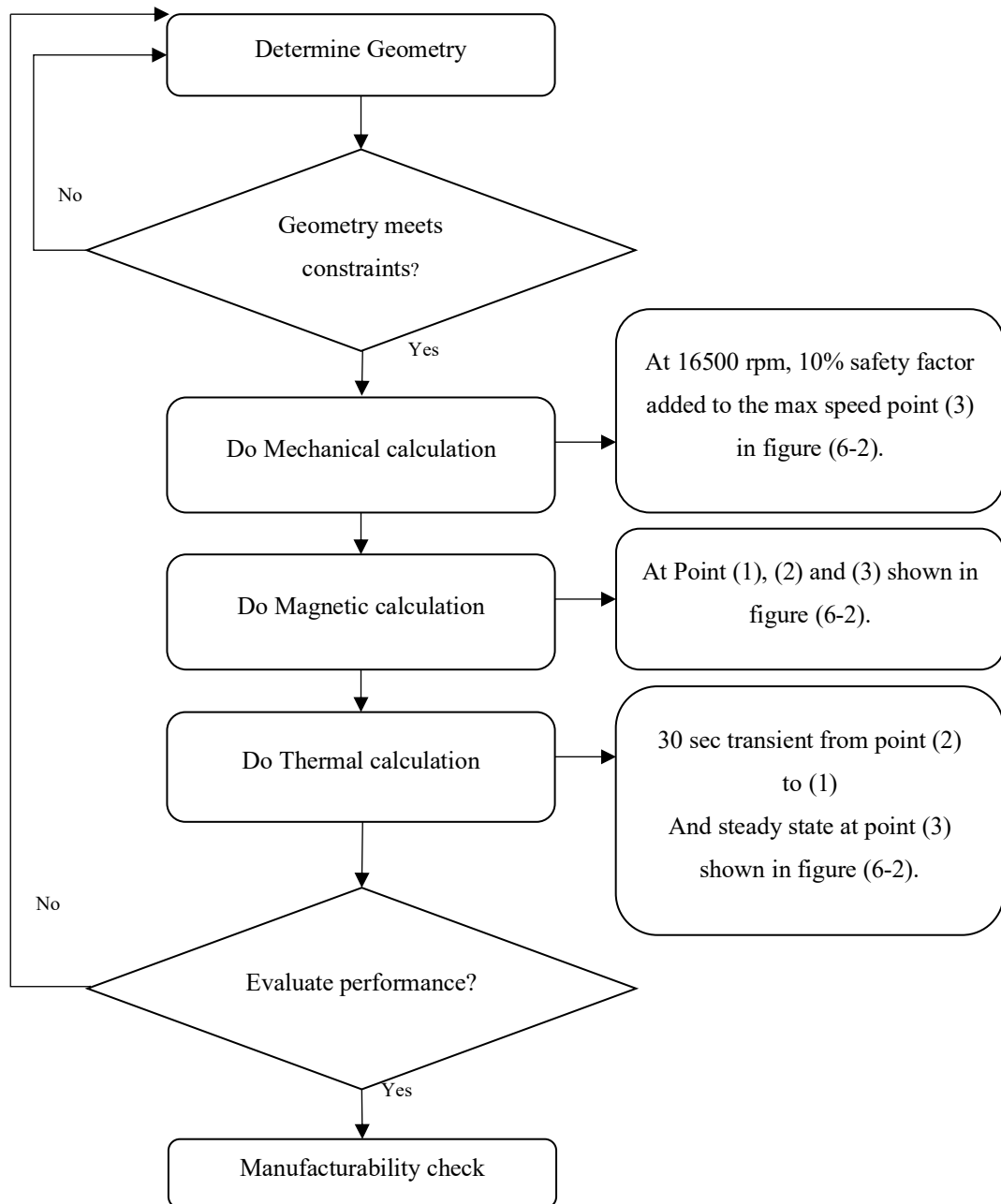


Figure 6-3 Workflow for the optimization process

The design procedure as demonstrated in Figure (6-3), involves an iterative process aimed at producing accurate and reliable results. It is paramount to define objectives and constraints accurately within this process. One of the primary goals is to optimize power density. This means adjusting components such as the stator, rotor, PMs and windings to be as lightweight as possible while still ensuring the machine can deliver the rated output power.

To ensure structural integrity and safety at high speeds, mechanical calculations are performed at 16500 rpm factoring in a 10% safety margin above the top speed. This is especially important for high-speed machines as it is crucial to ascertain that the motor operates within the maximum material stress limits right from the initial design stage. The critical role and sensitivity of the iron rib thickness in the rotor, reducing the rib thickness boosts the electromagnetic performance however, it might not be able to withstand the mechanical stress. Therefore, the mechanical aspect is checked at first to get the right balance.

Once the mechanical robustness is established the design process moves to the electromagnetic analysis stage. The focus is on ensuring that the PMA-SynREL machine meet the required performance and operates within limits. Furthermore, due to the huge field weakening the torque ripple must be checked to be within constraints.

Finally, the design process concludes with a thermal analysis. This analysis is crucial in preventing the machine from overheating, which could lead to performance loss. Because PMs are sensitive to temperature changes, maintaining an optimal operating temperature is essential for the machine's longevity and performance. This analysis ensures that the machine can dissipate heat effectively and can operate safely under various operating conditions. A transient analysis at base speed is conducted for 30 sec and at maximum speed the steady state temperature analysis is checked.

The cooling system employed in this comparison is a spiral water-jacket system. This system maintains an inlet temperature of 65°C with a fluid flow rate of 9.6 L/min. Spray cooling method which employs 12 nozzles on each side (rear-front) and utilizes ATF134 as the cooling fluid is also used. These cooling mechanisms play a crucial role in managing heat dissipation and maintaining optimal operating temperatures, thereby contributing to the machine's overall performance and lifespan.

Overall, this iterative procedure encompasses a comprehensive approach by balancing between (mechanical, electromagnetic and thermal) aspects towards achieving a feasible design.

6.6 Electromagnetic results

The machine has three operating points as described in Figure (6-2). At base speed all machines should deliver the peak torque, which is constrained to be more than 570 Nm in the optimization. Furthermore, the continuous torque at base speed should deliver a torque more than 399 Nm. At maximum speed, as described in Figure (6-2) the continuous current must achieve the torque of 180 at point 3. At maximum speed the peak torque and continuous torque are the same. The machine is driven by an inverter with a DC-link of 620 Volts and the maximum peak current is 660 Amps (rms). All machines employ three phase distributed windings with 45% fill factor, input currents and winding characteristics are shown in Table (6-4).

Table 6-4 Input currents and winding characteristics

Input	Value
Peak Current	660 Amps (rms)
Continues current	460 Amps (rms)
DC-link voltage	620 Volts
Number of turns per phase	16 turns
Winding Layout	Distributed Windings

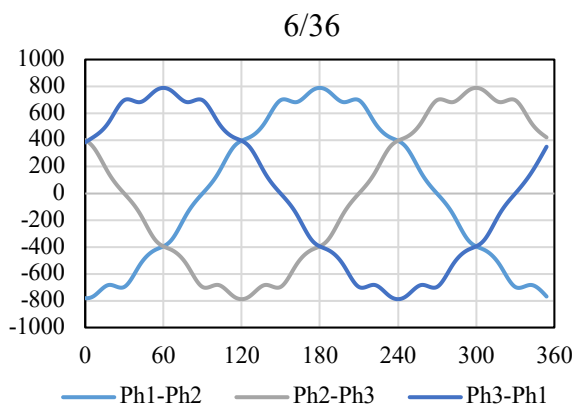
The following Table (6-5) depicts the electromagnetic results of the designed machines. It is evident that all machines have met the required performance of the machines. At maximum speed torque ripple is increased compared to the base speed torque this is due to the field weakening. High poles such as the 14 and 12 poles possess less torque ripple at maximum speed compared to low poles.

Table 6-5 Electromagnetic Optimization results

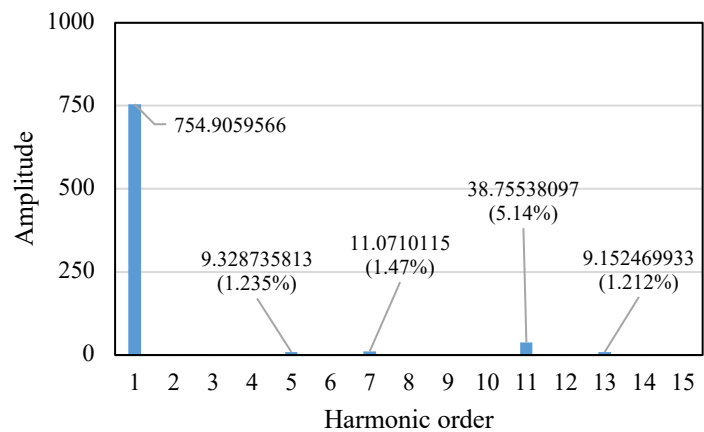
	14p/84s	12p/72s	10p/60s	8p/48s	6p/36s
Peak Torque @ base speed	573.5	572.0	572.7	572.2	572.40
Peak Torque ripple (%)	10.7	6.04	14.4	15.3	14.59
Rated Torque @ base speed	401.5	400.6	400.16	402.3	407.64
Rated Torque ripple (%)	12.4	6.61	13.4	15.52	15.26
Rated Torque @ Max Speed	210.5	207.44	200	192.77	191.21
Rated Torque ripple (%)	13.4	11.38	21.5	27.64	28.864

6.7 Open circuit test

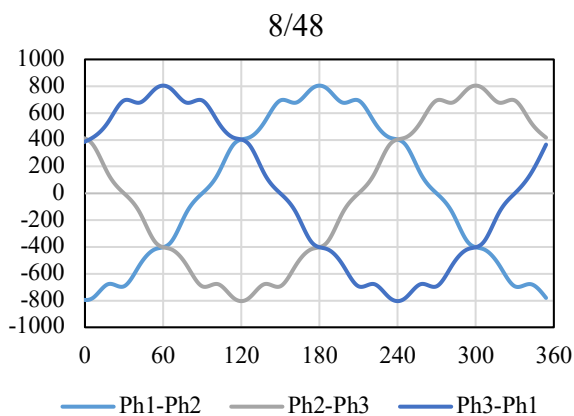
This section will operate an open circuit test on the designed machines to analyse the back-EMF voltage waveform. A critical step in the evaluation of slot-pole machines is to measure the back-EMF, which is the voltage generated in opposition to the applied voltage. By conducting this test, the distortion in the waveform is analysed.



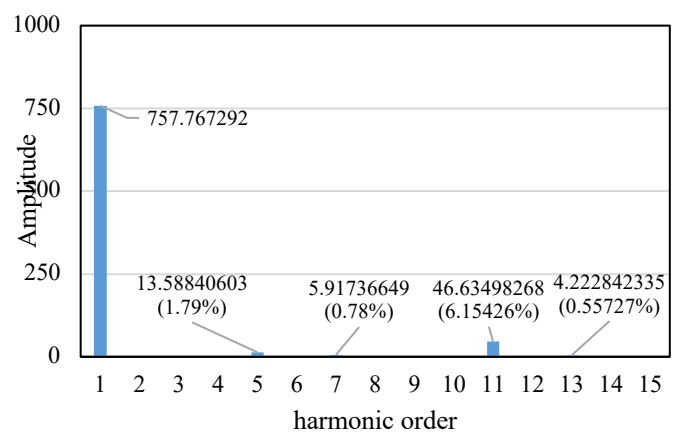
a)



b)

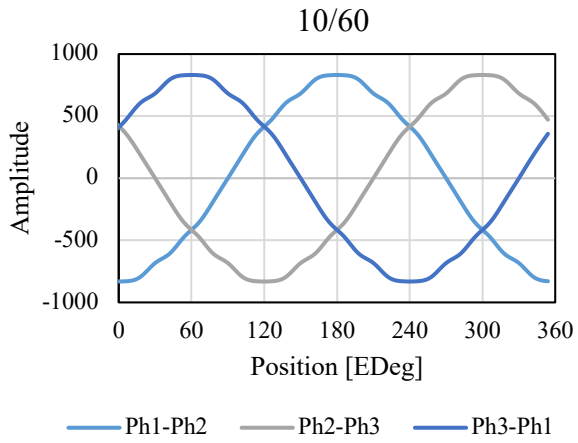


a)

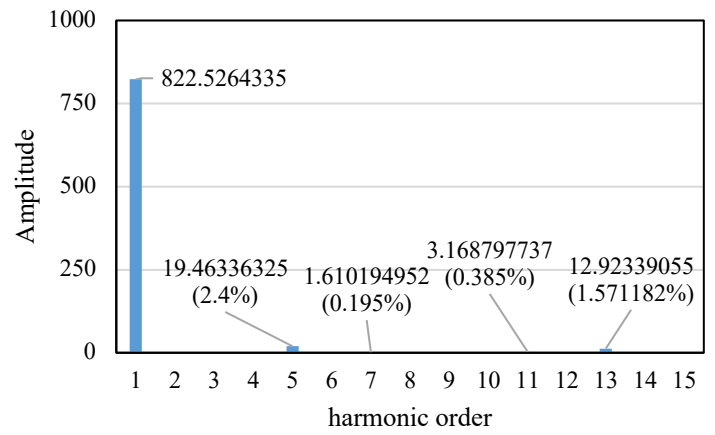


b)

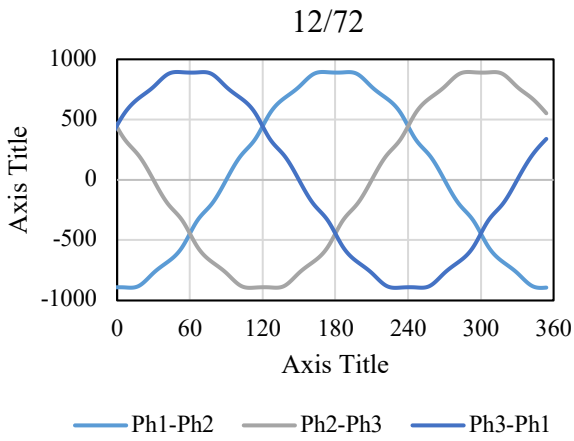
Figure 6-4 Back-EMF and FFT for 6-pole and 8-pole



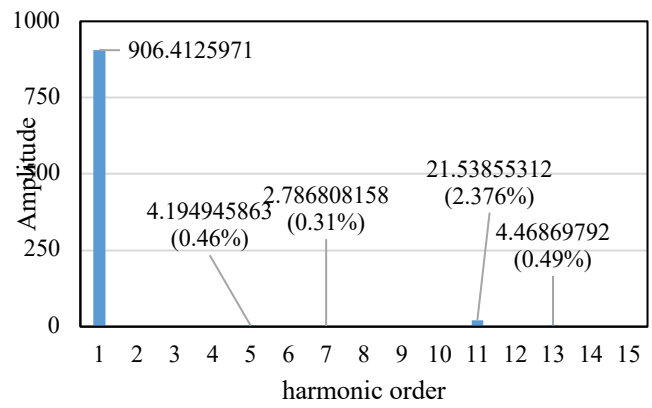
a)



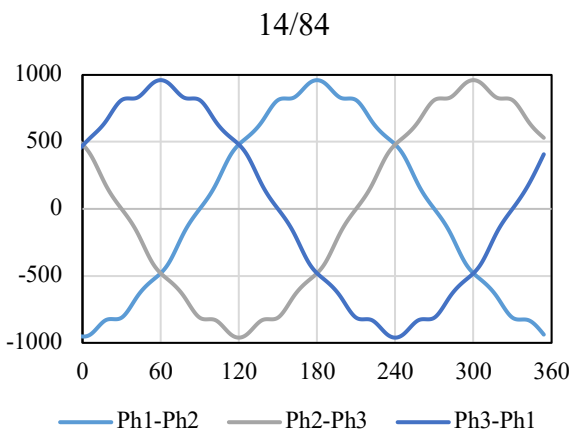
b)



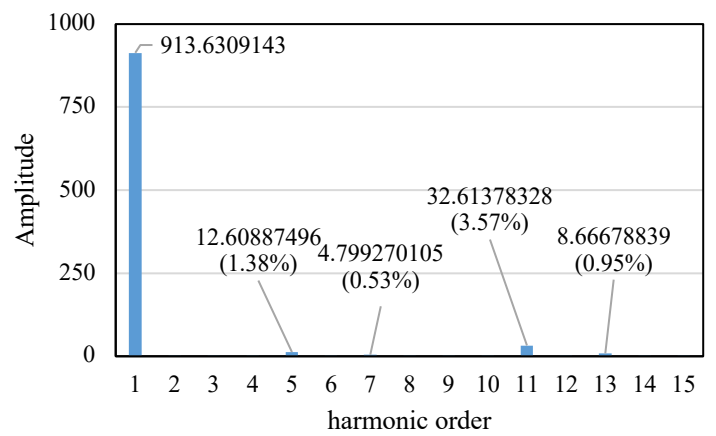
a)



b)



a)



b)

Figure 6-5 Back-EMF and its FFT for 10, 12 and 14 poles

After the back-EMF open circuit was conducted at maximum speed (15000 rpm) on the designed machines, it is shown in Figure (6-4) and (6-5), that the 14-pole 84-slot machine has the highest back-EMF this is due to the increased number of poles that increase the electric frequency of magnetic fields. The observed results are in line with the typical performance characteristics of slot-pole machines. More poles generally result in higher back EMF. This is because the back EMF in a machine is proportional to the speed and the flux per pole. Therefore, with more poles more voltage is induced resulting in higher back EMF.

As for the 12-pole 72-slot configuration exhibiting less distortion (2.49%) in the back-EMF, this could be attributed to the relationship between the number of poles and slots. Furthermore, the torque ripple of the 12-pole 72-slots at maximum speed possess the lowest torque ripple equal to (11.8%) as shown in Table (6-5). Harmonic distortion can be influenced by the slot and pole combination of the machine, which impacts the distribution and density of the magnetic field. The harmonic content of the back-EMF is primarily affected by the design of the magnetic circuit including the slot and pole arrangement.

The peak torque is required for 30 sec, so the efficiency of the continuous operation is of prime importance. From Figure (6-6), it is evident that all machines have met the target efficiency at base speed and maximum speed. However, the 6-pole 36-slot at maximum speed is around 94% due to its increased mass compared to other machines.

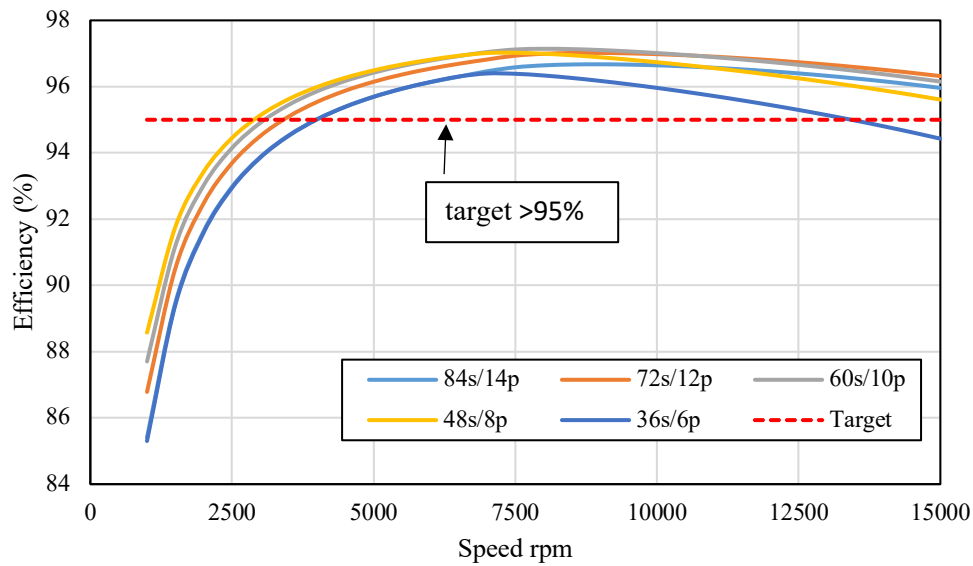


Figure 6-6 Continuous operation efficiency

The designed machines met the required performance with different machine active weight. From Figure (6-7) it's clear that by increasing the number of poles, the active weight of the motor is decreased. The electromagnetic performance for all combinations complied with the torque/speed requirements. More poles in the machine elevate the output torque, which in turn makes it possible to decrease the weight of high pole machines without compromising on the required electromagnetic performance. The 14-pole and 12-pole machines have a smaller outer diameter compared to the 10, 8, and 6-pole machines due to the reduced back iron in their stators as shown in Table (6-6). With a high pole count, PMA-SynREL machine has a thinner back iron.

As shown in Table (6-6), as the number of poles increase a reduction in the back iron is achieved. This leads to saving mass in the machine active weight as shown in Figure (6-7). Furthermore, as represented in Table (6-6) all designed machines have a machine volume which is less than 30 L of the envelop size of the application.

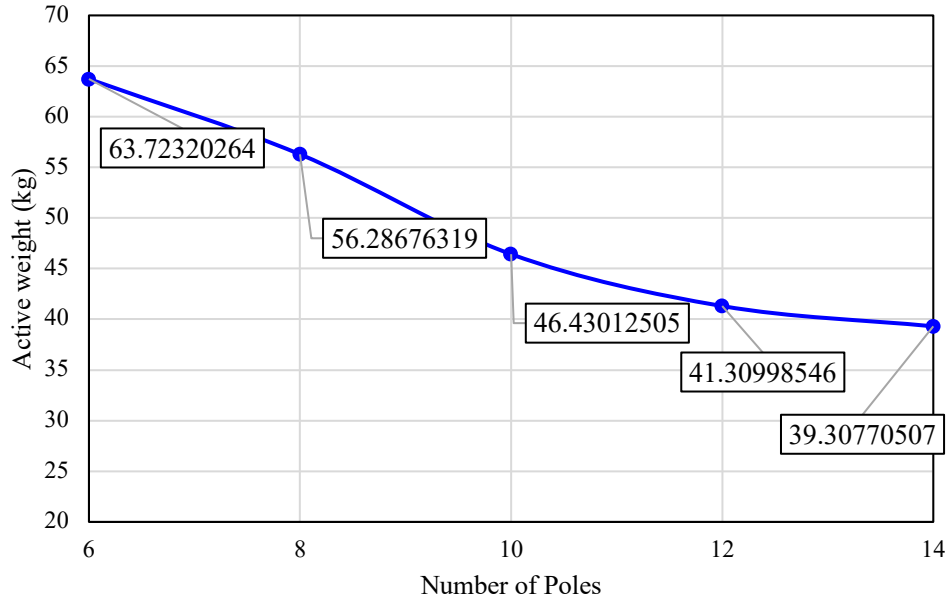


Figure 6-7 Active weight for the optimized machines

Table 6-6 Physical dimensions of the designed PMa-SynREL machines

Component	14p/84s	12p/72s	10p/60s	8p/48s	6p/36s
Stator Outer diameter (mm)	226.96	233.407	247.052	258.635	255.846
Back Iron (mm)	5.819	7.27	11.57	12.71	19.09
Rotor Outer diameter (mm)	177	177	177	177	177
Current density (continuous) (A/mm ²)	16.42	14.83	14.53	11.17	13.34
Stack Length (mm)	227.5	210	174.167	190.5	199.875
Machine Volume (L)	9.182	8.985	8.349	10.008	10.27

The incorporation of rare-earth magnets in the machine design is important to achieve the challenging performance requirement. Figure (6-8) represents the weight of PMs used in each configuration. The 8-pole 48-slot machine has the lowest amount of magnet weight, 0.4 kg less than the highest magnet usage in the 12-pole machine.

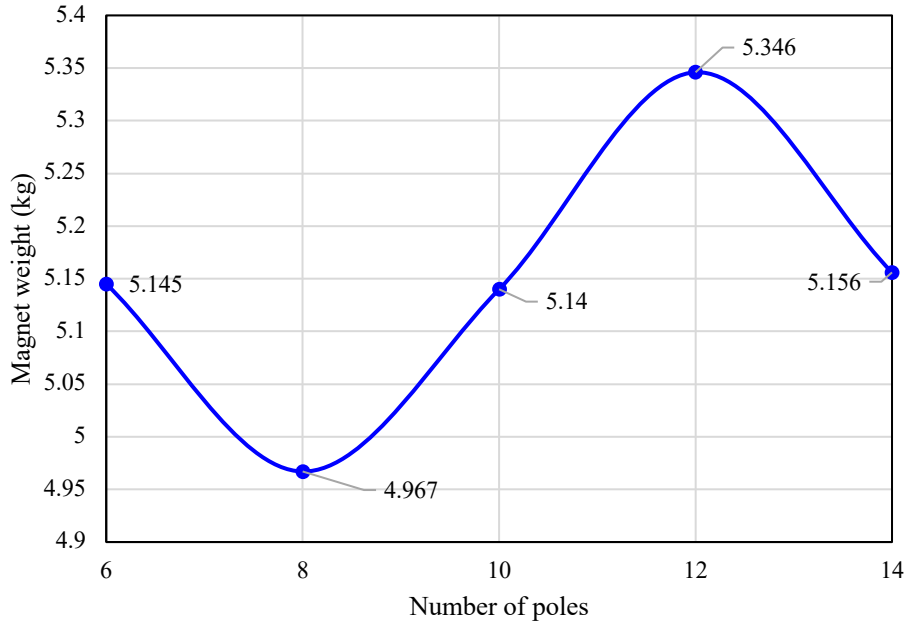


Figure 6-8 PMs weight for different poles

It is clear from Figure (6-9) that the inertia of the machine is affected by the stack length as all machines have the same rotor outer diameter. The 10-pole machine which has the lowest volume has the lowest inertia. Having a small inertia is preferred in traction machines for EVs as its responses quick to driver input and to any change which makes the driving comfort.

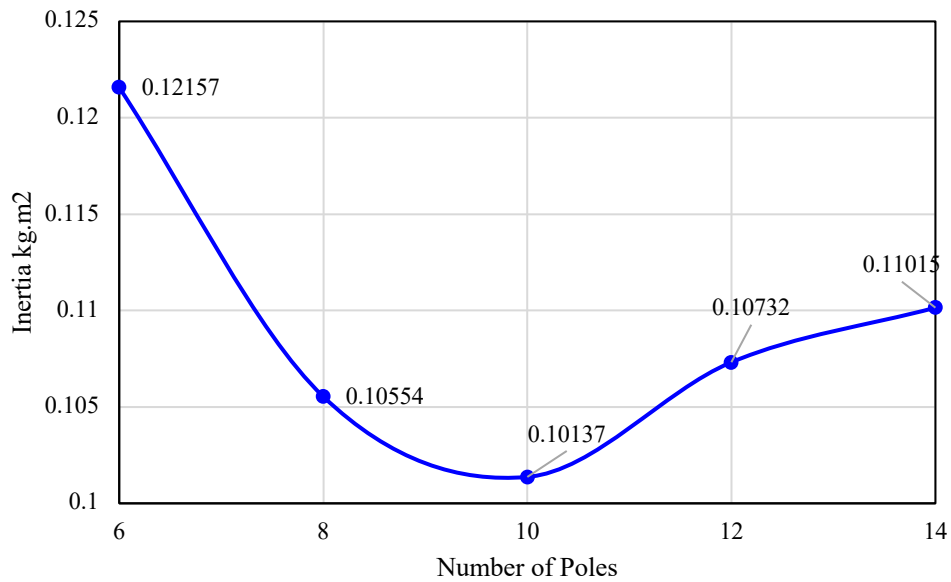


Figure 6-9 Moment of inertia for the designed machines

6.8 PM flux and field weakening

It is clear from Figure (6-10) that the slot-pole combination affects the magnetic flux produced by the magnets. In high slot-pole machines such as, the 84-slot 14-pole machine, it has more leakage hence the PM flux is reduced at no-load. Moreover, as the number of slot-poles is reduced the PM flux is increased as shown in Figure (6-10). To keep the operating voltage within the DC-voltage limit the phase advance angle must be increased at top speed hence, more negative I_d in this region is required. The amount of negative I_d is highly noticeable in the lowest slot-pole combination 36-slot 6-pole due to its increased PM flux. Therefore, the slot-pole combination has an influence on the machine performance characteristic.

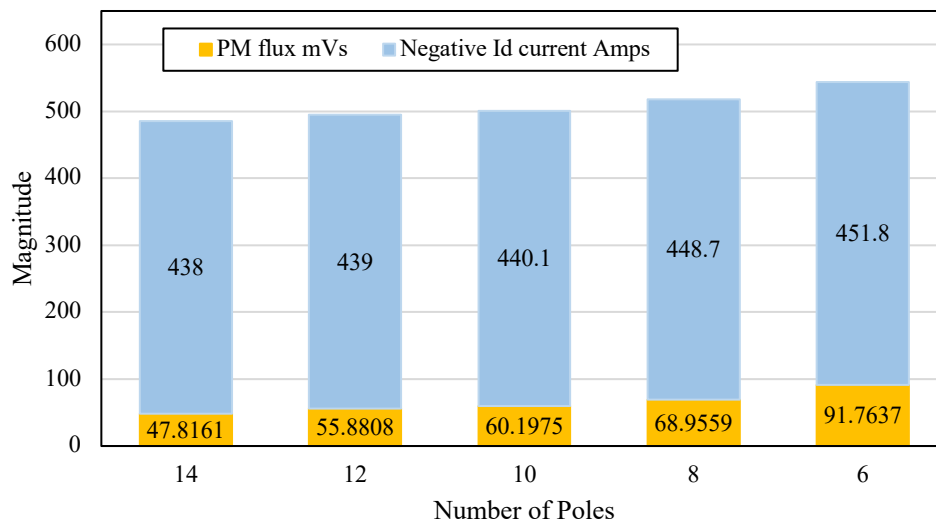


Figure 6-10 PMs flux with the required I_d for all poles

The injection of more negative I_d current is reflected on the top speed torque, it can be seen from Figure (6-11), that magnetic torque is reduced gradually with the decrease in pole count. This justifies the reason why the 8-pole and 6-pole machines have lower torque at maximum speed compared to high pole machines 14-pole, 12-pole and 10-pole.

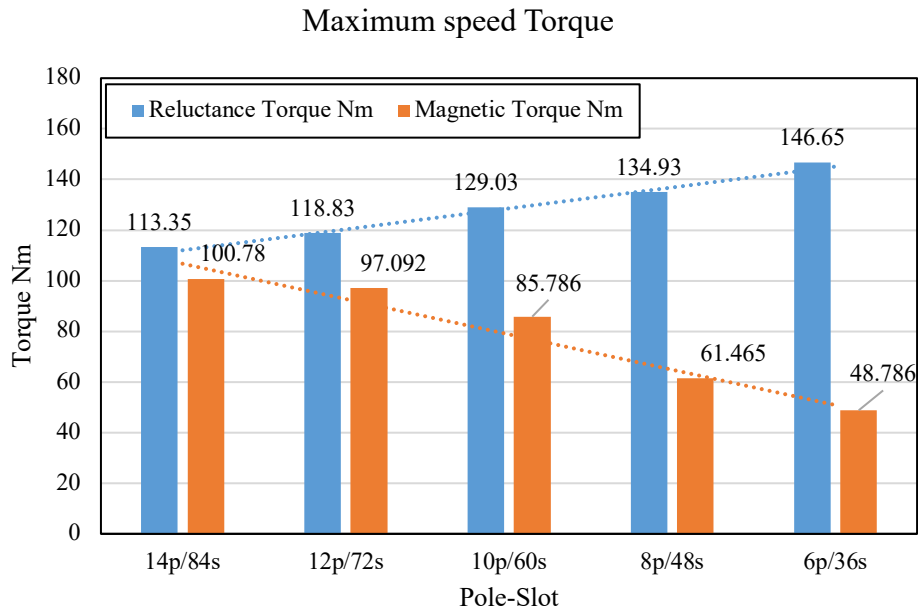


Figure 6-11 Reluctance torque and magnetic torque at top speed (15000rpm) continuous current

6.9 Mechanical integrity

The material used in all machines is 35HXT780T which is a high strength material. As all machines have the same rotor outer diameter 177mm and operate at maximum speed of 15000 rpm a 10% safety factor is added to ensure safe operation. As more poles are presented with same area of rotor, this provided a privilege for high pole machines as they were able to have reduced thickness of iron ribs and operate at the permissible stress limit. On the other side, as the number of poles reduce for the same rotor area the iron rib thickness is increased to handle the stress on the rotor this led to low number of poles like the 8-pole and 6-pole to have a high active mass weight to meet the required performance. Increasing the iron rib thickness in the rotor leads to more saturation therefore, the performance is reduced and it was certain to increase the machine volume to boost the performance. All designed machines were constrained in the optimization not to exceed the material stress. Therefore, as shown in Figure (6-12) all machines exhibit a stress lower than 720MPa.

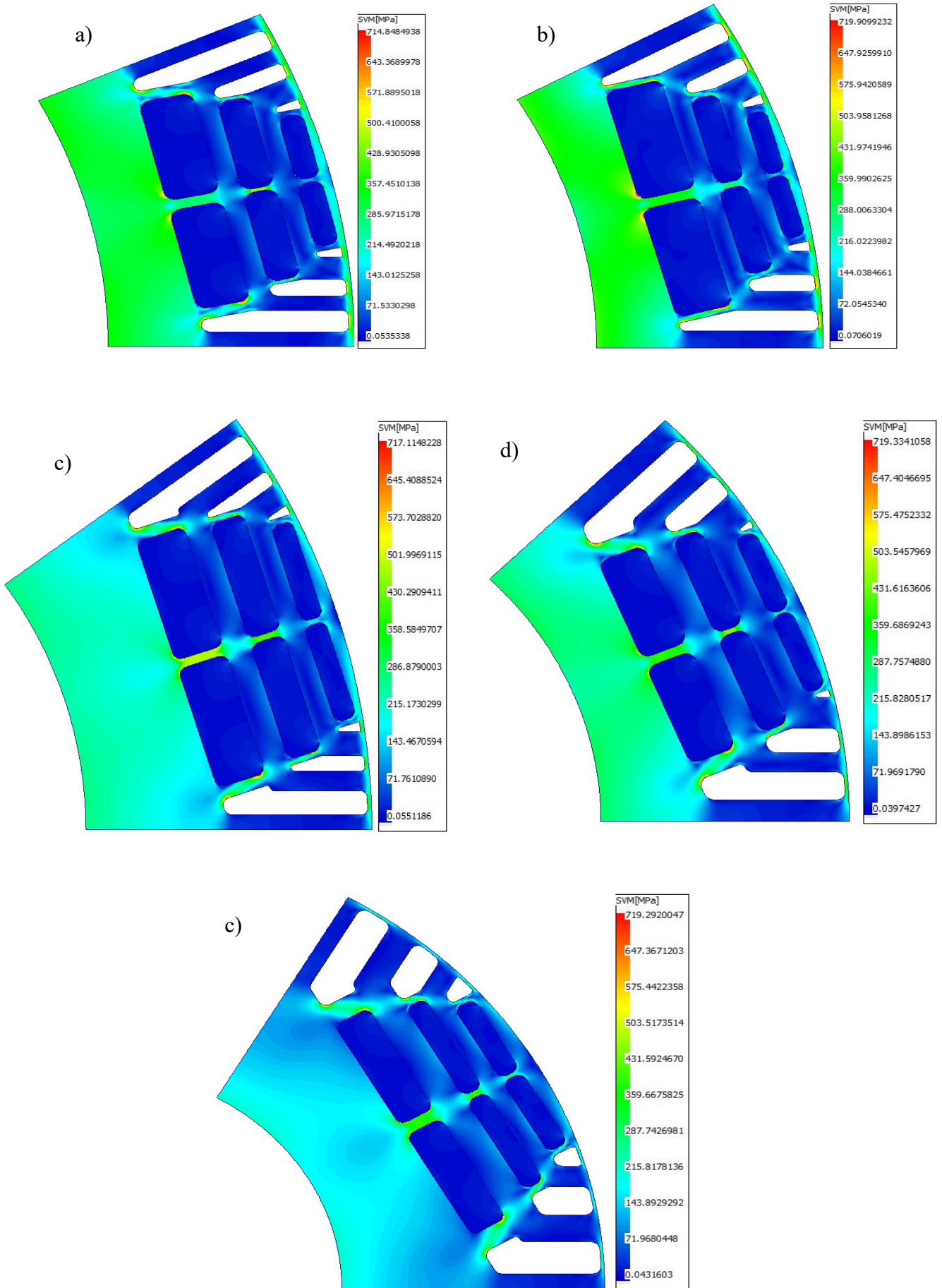


Figure 6-12 Mechanical Stresses of (a) 14p/84s (b) 12p/72s (c) 10p/60s (d) 8p/48s and (e) 6p/36s

6.10 Thermal performance

The thermal performance is an important aspect, ensuring that the designed machines are operating within the permissible temperature limit is a pivotal role in their efficiency and operation. Different slot-pole configurations can influence the dissipation of heat generated. Two cooling methods are applied in all the designed machines, a spiral water jacket and a spray cooling system. As explained previously, increasing the number of poles decreases the back iron of the machines. Hence, in this case water-jacket becomes closer to the surface. The back iron is a vital component that provides a low reluctance path for the magnetic flux. This reduction in back iron thickness has a direct effect in the machine's thermal characteristic. In the context of a spiral water-Jacket the cooling jacket becomes closer to the stator slot this positioning allows for more efficient heat transfer. Therefore, high pole machines have higher current density with a rotor geometry that has thin iron ribs these two distinctions signify the output torque. Thus, it becomes feasible to design lighter PMA-SynREL machine weight without comprising their electromagnetic performance. Table (6-7) displays the thermal results for the designed machines. At the base speed of 5000 rpm, a steady state temperature is measured under a continuous RMS current of 460 Amps. Once the steady state temperature is established at this current level, a 30 second duty cycle is applied to accommodate the peak current losses at 660 Amps RMS. At maximum speed, a steady state analysis is conducted to determine the temperature. In this case, the continuous current is sufficient to achieve the required torque, eliminating the need for transient analysis at maximum speed.

Table 6-7 Thermal results of the machine most important components

Machine components temperature at (base speed)	14p/84s	12p/72s	10p/60s	8p/48s	6p/36s
Winding Peak (°C)	179	177	173	159.5	147
Magnet Peak (°C)	66	64	58.7	65	63.2
Winding Continuous (°C)	127	128	136.4	133.8	128
Magnet Continuous (°C)	65.6	63.5	58.4	64.7	62.5
Machine components temperature at (top speed)	14p/84s	12p/72s	10p/60s	8p/48s	6p/36s
Winding Continuous (°C)	161	163	179	179	177
Magnet continuous (°C)	97.0	95.5	103	120.7	125

6.11 Summary

Every combination (slot-pole) successfully met the necessary performance criteria for the heavy-duty application. The findings suggest that increasing the number of poles decreases the back iron, situating the cooling system nearer to the heat source. This arrangement allows high pole machines to achieve higher current density and lower active weight. As illustrated in Table (6-8), the 14-pole 84-slot machine possesses the least weight equal to (39.3 kg).

The 10-pole 60-slot machine, due to its shorter stack length demonstrated reduced inertia making it the smallest in volume (8.57 L) among the machines studied. The 8-pole 48-slot machine had the lowest magnet weight (4.96 kg), a significant advantage considering the expense and availability of rare-earth magnets. With all machines sharing the same outer rotor diameter 177 mm it's evident that increasing the number of poles for the same outer diameter adds to the complexity of manufacturing, due to the additional radial and tangential ribs in the rotor's magnetic structure.

When choosing the ideal topology for the heavy-duty truck, it's crucial to select a configuration that not only meets the application's requirements but also has the lightest magnet weight, considering the cost of rare-earth magnets. Moreover, the ease of manufacture is an important factor. The operational frequency of the topology is also critical, as the design of the inverter controlling the motor must be equipped to handle this frequency.

Therefore, this chapter highlights the 8-pole 48-slot machine as the best candidate for the heavy-duty truck application. This is due to its simplified rotor-stator structure and less quantity of magnets. Its operating frequency is lower than that of high pole machines, which will influence the design of the drive system of the PMA-SynREL machine.

Table 6-8 Performance and physical comparison of all slot/pole combinations

Parameter	14p/84s	12p/72s	10p/60s	8p/48s	6p/36s
Peak Torque (Nm) @ Base speed	573.5	572.04	572.65	572.23	572.4
Peak Power (kW) @ Base speed	300.28	299.52	2.9984	2.9962	2.9971
Continuous Power (kW) @ Base speed	210.24	209.77	209.5	210.65	213.44
Continuous Torque (Nm) @ Base speed	401.52	400.63	400.11	402.31	407.65
Continuous Power (kW) @ Top speed	332.83	335.98	314.75	302.8	299.1
Continuous Torque (Nm) @ Top speed	211.89	213.89	200.38	192.77	190.41
Magnets weight (kg)	5.156	5.346	5.14	4.967	5.145
Active mass weight (kg)	39.3	41.31	46.43	56.28	63.72
Volume (L)	11.19	10.33	8.57	9.374	9.836

Chapter 7. Conclusion and Future Work

This thesis targeted two primary goals. The first was to design a high-power high-speed traction motor with a high peripheral speed for a heavy-duty truck. The second goal involved utilizing the inherent magnet (windings) in the traction motor as an inductor.

Chapter 2 provided an extensive literature review on EVs, focusing on their configurations and requirements. The discussion delved into the energy storage systems of EVs, highlighting the prominence of lithium-ion batteries due to their high-power density. Furthermore, the charging systems for EVs were considered, and the requirements for traction motors requirements in EVs were covered. The chapter emphasized the importance of high power, high speed, high efficiency and low torque ripple in a traction motor for EV applications.

In Chapter 3, an in-depth examination of traction machines was conducted. It was found that PM machines are top-tier candidates for traction machines due to their high-performance and efficiency metrics. Various topologies showcasing strong field weakening capabilities were compared, the PMa-SynREL machine identified as an outstanding topology. It balances reluctance torque and magnet torque reducing the need for rare-earth magnetic material. Additionally, the presence of reluctance torque boosts the torque at high speeds, fulfilling the requirements of heavy-duty applications.

Chapter 4 presented the power/torque profile of heavy-duty trucks. The design selection of winding layout and materials was covered. An 8-pole 48-slot combination was selected for the preliminary design to understand the PMa-SynREL machine's multi-physics better. This configuration met the application's performance requirements. The use of a dual cooling system, water jacket and spray cooling were a key enabler to maintaining high power (299 kW) and low active weight (63kg). The positioning of the flux barriers was found to be of prime importance in reducing torque ripple. This chapter illuminated the importance of rotor optimization to enhance the electromagnetic performance while maintaining rotor mechanical integrity.

Chapter 5 examined the potential for using a traction motor for dual purposes. Various layouts on a 90kW SMPM machine were investigated. This machine employs double-layer distributed windings commonly seen in many EV traction motors. The study found that the inductance of motor windings could be enhanced by specific layouts. However, an increase in inductance correlated with an increase in the number of switches needed for reconfiguration. All potential layouts yielded an average torque equal to zero due to the supply current was single-phase. The potential layouts were tested in the laboratory to detect any vibration caused by layout configuration, with the excitation current frequency component being observed in all layouts. The layout showcasing the highest inductance was examined on the PMa-SynREL machine previously designed in chapter 4. The results show that a PMa-SynREL machine can operate as an inductor. The PMa-SynREL machine has been investigated further on 3-phase charging. It's been shown that converting the 3-phase winding layout to a dual 3-phase layout gives more degrees of freedom to exploit the machine's windings in the charging circuit with no torque. The traction machine is capable of operating as a high current density inductor with safe temperature, while the machine cooling system is activated.

Chapter 6 investigated different slot-pole combinations, optimizing (14-pole 84-slot), (12-pole 72-slot), (10-pole 60-slot), (8-pole 48-slot) and (6-pole 36-slot) to meet heavy-duty vehicle performance requirements through multi-objective genetic optimization. It was found that increasing the number of poles for a fixed rotor outer diameter reduced the machine's active mass. More poles led to a narrower back iron width which allowed the cooling system to be situated closer to the slots increasing the current density. The 14-pole configuration displayed the least active weight (39.3 kg). The 10-pole 60-slot machine demonstrated the lowest volume due to a shorter stack length, while the 8-pole 48-slot machines had the least magnetic weight and a simpler rotor/stator structure compared to other topologies. Although the 8-pole 48-machine does not have the lowest active weight it offers a balance between performance, weight and manufacturing due to reduced magnetic quantity and a simpler structure.

7.1 Future research directions

- The current cooling system implemented in the heavy-duty traction motor within this thesis employs a Water-jacket and Spray cooling system. For future work, optimizing this cooling system becomes essential, particularly while maintaining the active weight of the machine. This step is critical to enhance the machine's efficiency and to reduce its overall cost.
- An examination of different flux barrier configurations for high pole machines could be beneficial. Specifically, assessing the use of either one or two flux barriers may help to lessen the manufacturing burden associated with PMA-SynREL machines, particularly for high pole topologies. Such investigation could lead to more efficient and cost-effective production processes.
- The functionality of the traction motor acting as an inductor, the thesis explored a topology with a 6-pole 36-slot configuration incorporating a samarium cobalt magnet. Future studies could probe into different magnet grades across potential layouts to scrutinize the vibration of the motor more closely. This approach would provide a more comprehensive understanding of how different magnets impact motor functionality as an inductor.
- Minimizing the number of switches required to change from the traction mode to charging mode is an issue that needs to be addressed. Facilitating the transition from both modes will increase the reliability of using a traction machine as an inductor.
- Applying the potential layouts highlighted in this thesis to machines without magnets. Such an application could significantly reduce the amplitude of vibration, potentially enhancing the longevity and reliability of the motor being used as an inductor. This approach would expand the thesis's findings to a broader range of motor types, thereby increasing its overall impact on the field.

References

- [1] D. Spratt, I. Dunlop, A. C. Barrie, and A. Retired, "Existential climate-related security risk," *A scenario approach, breakthrough*, 2019.
- [2] S. Pye, F. G. Li, J. Price, and B. Fais, "Achieving net-zero emissions through the reframing of UK national targets in the post-Paris Agreement era," *Nature energy*, vol. 2, no. 3, pp. 1-7, 2017.
- [3] *CO2 Emissions in 2022* Available: <https://iea.blob.core.windows.net/assets/3c8fa115-35c4-4474-b237-1b00424c8844/CO2Emissionsin2022.pdf>
- [4] I. Tiseo. (2023). Available: <https://www.statista.com/statistics/1185535/transport-carbon-dioxide-emissions-breakdown/>
- [5] R. Zhang and S. Fujimori, "The role of transport electrification in global climate change mitigation scenarios," *Environmental Research Letters*, vol. 15, no. 3, p. 034019, 2020.
- [6] B. Sharpe and R. Muncrief, "Literature review: real-world fuel consumption of heavy-duty vehicles in the United States, China, and the European Union," *Int Counc Clean Transp*, pp. 1-27, 2015.
- [7] M. Ehsani, K. M. Rahman, and H. A. Toliyat, "Propulsion system design of electric and hybrid vehicles," *IEEE Transactions on Industrial Electronics*, vol. 44, no. 1, pp. 19-27, 1997.
- [8] *Government takes historic step towards net-zero with end of sale of new petrol and diesel cars by 2030*. Available: <https://www.gov.uk/government/news/government-takes-historic-step-towards-net-zero-with-end-of-sale-of-new-petrol-and-diesel-cars-by-2030>
- [9] M. Ehsani, Y. Gao, and S. E. Gay, "Characterization of electric motor drives for traction applications," *IECON'03. 29th Annual Conference of the IEEE Industrial Electronics Society (IEEE Cat. No.03CH37468)*, vol. 1, pp. 891-896 vol.1, 2003.
- [10] D. Smith *et al.*, "Medium-and heavy-duty vehicle electrification: An assessment of technology and knowledge gaps," Oak Ridge National Lab.(ORNL), Oak Ridge, TN (United States); National ...2020.
- [11] *Maps and Data*. Available: https://afdc.energy.gov/data/categories/maps-data-categories?per_page=150
- [12] A. Khajepour, M. S. Fallah, and A. Goodarzi, *Electric and hybrid vehicles: technologies, modeling and control-A mechatronic approach*. John Wiley & Sons, 2014.

- [13] K. Chau, *Electric vehicle machines and drives: design, analysis and application*. John Wiley & Sons, 2015.
- [14] C. Shen, P. Shan, and T. Gao, "A comprehensive overview of hybrid electric vehicles," *International Journal of Vehicular Technology*, vol. 2011, 2011.
- [15] M. Ehsani, Y. Gao, S. Longo, and K. M. Ebrahimi, *Modern electric, hybrid electric, and fuel cell vehicles*. CRC press, 2018.
- [16] K. Chau and Y. Wong, "Overview of power management in hybrid electric vehicles," *Energy conversion and management*, vol. 43, no. 15, pp. 1953-1968, 2002.
- [17] A. Zia, "A comprehensive overview on the architecture of Hybrid Electric Vehicles (HEV)," in *2016 19th International Multi-Topic Conference (INMIC)*, 2016, pp. 1-7.
- [18] M. Kebriaei, A. H. Niasar, and B. Asaei, "Hybrid electric vehicles: An overview," in *2015 International Conference on Connected Vehicles and Expo (ICCVE)*, 2015, pp. 299-305.
- [19] S. Sharma, A. K. Panwar, and M. Tripathi, "Storage technologies for electric vehicles," *Journal of traffic and transportation engineering (english edition)*, vol. 7, no. 3, pp. 340-361, 2020.
- [20] G. Yimin, M. Ehsani, and J. M. Miller, "Hybrid Electric Vehicle: Overview and State of the Art," in *Proceedings of the IEEE International Symposium on Industrial Electronics, 2005. ISIE 2005.*, 2005, vol. 1, pp. 307-316.
- [21] C. C. Chan, "The state of the art of electric and hybrid vehicles," *Proceedings of the IEEE*, vol. 90, no. 2, pp. 247-275, 2002.
- [22] K. V. Singh, H. O. Bansal, and D. Singh, "A comprehensive review on hybrid electric vehicles: architectures and components," *Journal of Modern Transportation*, vol. 27, no. 2, pp. 77-107, 2019.
- [23] J. Y. Yong, V. K. Ramachandaramurthy, K. M. Tan, and N. Mithulananthan, "A review on the state-of-the-art technologies of electric vehicle, its impacts and prospects," *Renewable and sustainable energy reviews*, vol. 49, pp. 365-385, 2015.
- [24] O. D. Momoh and M. O. Omoigui, "An overview of hybrid electric vehicle technology," in *2009 IEEE Vehicle Power and Propulsion Conference*, 2009, pp. 1286-1292.
- [25] V. Arun *et al.*, "Review on Li-Ion Battery vs Nickel Metal Hydride Battery in EV," *Advances in Materials Science and Engineering*, vol. 2022, 2022.

- [26] J. A. Sanguesa, V. Torres-Sanz, P. Garrido, F. J. Martinez, and J. M. Marquez-Barja, "A review on electric vehicles: Technologies and challenges," *Smart Cities*, vol. 4, no. 1, pp. 372-404, 2021.
- [27] *Batteries for Electric Vehicles*. Available: https://afdc.energy.gov/vehicles/electric_batteries.html
- [28] *How does a Supercapacitor Work?* Available: <https://batteryuniversity.com/article/bu-209-how-does-a-supercapacitor-work>
- [29] M. S. Wasim, S. Habib, M. Amjad, A. R. Bhatti, E. M. Ahmed, and M. A. Qureshi, "Battery-Ultracapacitor Hybrid Energy Storage System to Increase Battery Life Under Pulse Loads," *IEEE Access*, vol. 10, pp. 62173-62182, 2022.
- [30] T. Mesbahi, P. Bartholomeüs, N. Rizoug, R. Sadoun, F. Khenfri, and P. L. Moigne, "Advanced Model of Hybrid Energy Storage System Integrating Lithium-Ion Battery and Supercapacitor for Electric Vehicle Applications," *IEEE Transactions on Industrial Electronics*, vol. 68, no. 5, pp. 3962-3972, 2021.
- [31] M. Shahjalal, T. Shams, M. N. Tasnim, M. R. Ahmed, M. Ahsan, and J. Haider, "A critical review on charging technologies of electric vehicles," *Energies*, vol. 15, no. 21, p. 8239, 2022.
- [32] *How long does it take to charge an electric car?* Available: <https://www.edfenergy.com/electric-cars/charging-points>
- [33] *A guide to electric vehicle infrastructure*. Available: <https://www.beama.org.uk/static/uploaded/5e9d2696-bec8-4179-956bedf5655a0272.pdf>
- [34] M. Al-ani, A. Walker, G. Vakil, D. Gerada, C. Gerada, and K. Paciura, "Modifications to PM-Assisted Synchronous Reluctance Machine to Achieve Rare-Earth Free Heavy-Duty Traction," *IEEE Journal of Emerging and Selected Topics in Power Electronics*, vol. 11, no. 2, pp. 2029-2038, 2023.
- [35] C. Liuchen, "Recent developments of electric vehicles and their propulsion systems," *IEEE Aerospace and Electronic Systems Magazine*, vol. 8, no. 12, pp. 3-6, 1993.
- [36] X. D. Xue, K. W. E. Cheng, and N. C. Cheung, "Selection of eLECTRIC mOTOR dRIVES for electric vehicles," in *2008 Australasian Universities Power Engineering Conference*, 2008, pp. 1-6.

- [37] C. C. Chan, K. T. Chau, J. Z. Jiang, W. Xia, M. Zhu, and R. Zhang, "Novel permanent magnet motor drives for electric vehicles," *IEEE Transactions on Industrial Electronics*, vol. 43, no. 2, pp. 331-339, 1996.
- [38] K. T. Chau, C. C. Chan, and C. Liu, "Overview of Permanent-Magnet Brushless Drives for Electric and Hybrid Electric Vehicles," *IEEE Transactions on Industrial Electronics*, vol. 55, no. 6, pp. 2246-2257, 2008.
- [39] R. Thomas, H. Husson, L. Garbuio, and L. Gerbaud, "Comparative study of the Tesla Model S and Audi e-Tron Induction Motors," in *2021 17th Conference on Electrical Machines, Drives and Power Systems (ELMA)*, 2021, pp. 1-6.
- [40] M. Zeraoulia, M. E. H. Benbouzid, and D. Diallo, "Electric Motor Drive Selection Issues for HEV Propulsion Systems: A Comparative Study," *IEEE Transactions on Vehicular Technology*, vol. 55, no. 6, pp. 1756-1764, 2006.
- [41] Z. Q. Zhu and D. Howe, "Electrical Machines and Drives for Electric, Hybrid, and Fuel Cell Vehicles," *Proceedings of the IEEE*, vol. 95, no. 4, pp. 746-765, 2007.
- [42] M. Ehsani, Y. Gao, and J. M. Miller, "Hybrid Electric Vehicles: Architecture and Motor Drives," *Proceedings of the IEEE*, vol. 95, no. 4, pp. 719-728, 2007.
- [43] J. D. Widmer, R. Martin, and M. Kimiabeigi, "Electric vehicle traction motors without rare earth magnets," *Sustainable Materials and Technologies*, vol. 3, pp. 7-13, 2015/04/01/ 2015.
- [44] Y. Lan *et al.*, "Switched reluctance motors and drive systems for electric vehicle powertrains: State of the art analysis and future trends," *Energies*, vol. 14, no. 8, p. 2079, 2021.
- [45] K. Watanabe, S. Aida, A. Komatsuzaki, and I. Miki, "Driving force characteristics of 40kW switched reluctance motor for electric vehicle," in *2007 International Conference on Electrical Machines and Systems (ICEMS)*, 2007, pp. 1894-1898.
- [46] *Switched reluctance motors power electric Land Rovers*. Available: https://drivesncontrols.com/news/fullstory.php/aid/3872/Switched_reluctance_motors_power_electric_Land_Rovers.html#:~:text=Switched%20reluctance%20motors%20deliver%20high,important%20consideration%20in%20automotive%20applications.
- [47] T. Finken, M. Felden, and K. Hameyer, "Comparison and design of different electrical machine types regarding their applicability in hybrid electrical vehicles," in *2008 18th International Conference on Electrical Machines*, 2008, pp. 1-5.

- [48] N. Zabihi and R. Gouws, "A review on switched reluctance machines for electric vehicles," in *2016 IEEE 25th International Symposium on Industrial Electronics (ISIE)*, 2016, pp. 799-804.
- [49] A. D. Gioia *et al.*, "Design of a wound field synchronous machine for electric vehicle traction with brushless capacitive field excitation," in *2016 IEEE Energy Conversion Congress and Exposition (ECCE)*, 2016, pp. 1-8.
- [50] *Renault Unveils Finalized Designs of Fluence Z.E. and Kangoo Express Z.E.; Opens Pre-Reservations.* Available: <https://www.greencarcongress.com/2010/04/renault-20100415.html>
- [51] E. M. Illiano, "Design of a highly efficient brushless current excited synchronous motor for automotive purposes," ETH Zurich, 2014.
- [52] Y. Yang *et al.*, "Design and Comparison of Interior Permanent Magnet Motor Topologies for Traction Applications," *IEEE Transactions on Transportation Electrification*, vol. 3, no. 1, pp. 86-97, 2017.
- [53] W. Xu, J. Zhu, Y. Guo, S. Wang, Y. Wang, and Z. Shi, "Survey on electrical machines in electrical vehicles," in *2009 International Conference on Applied Superconductivity and Electromagnetic Devices*, 2009, pp. 167-170.
- [54] Z. Q. Zhu and C. C. Chan, "Electrical machine topologies and technologies for electric, hybrid, and fuel cell vehicles," in *2008 IEEE Vehicle Power and Propulsion Conference*, 2008, pp. 1-6.
- [55] R. Krishnan, *Permanent magnet synchronous and brushless DC motor drives*. CRC press, 2017.
- [56] P. B. Reddy, A. El-Refaie, K. K. Huh, J. K. Tangudu, and T. M. Jahns, "Comparison of interior and surface PM machines equipped with fractional-slot concentrated windings for hybrid traction applications," in *2011 IEEE Energy Conversion Congress and Exposition*, 2011, pp. 2252-2259.
- [57] B. Sarlioglu, C. T. Morris, D. Han, and S. Li, "Benchmarking of electric and hybrid vehicle electric machines, power electronics, and batteries," in *2015 Intl Aegean Conference on Electrical Machines & Power Electronics (ACEMP), 2015 Intl Conference on Optimization of Electrical & Electronic Equipment (OPTIM) & 2015 Intl Symposium on Advanced Electromechanical Motion Systems (ELECTROMOTION)*, 2015, pp. 519-526: IEEE.

- [58] T. Burress, "Benchmarking state-of-the-art technologies," in *Oak Ridge National Laboratory (ORNL), 2013 US DOE Hydrogen and Fuel Cells Program and Vehicle Technologies Program Annual Merit Review and Peer Evaluation Meeting*, 2013.
- [59] T. A. Burress *et al.*, "Evaluation of the 2010 Toyota Prius hybrid synergy drive system," Oak Ridge National Lab.(ORNL), Oak Ridge, TN (United States). Power ...2011.
- [60] T. Burress, "Electrical performance, reliability analysis, and characterization," *DoE VTO Annual Merit Review*, 2017.
- [61] L. Yuefeng, L. Feng, and T. A. Lipo, "A novel permanent magnet motor with doubly salient structure," *IEEE Transactions on Industry Applications*, vol. 31, no. 5, pp. 1069-1078, 1995.
- [62] W. Hua, Z. Q. Zhu, M. Cheng, Y. Pang, and D. Howe, "Comparison of flux-switching and doubly-salient permanent magnet brushless machines," in *2005 International Conference on Electrical Machines and Systems*, 2005, vol. 1, pp. 165-170 Vol. 1.
- [63] C. Wang, S. A. Nasar, and I. Boldea, "Three-phase flux reversal machine (FRM)," *IEE Proceedings - Electric Power Applications*, vol. 146, no. 2, pp. 139-146, 1999.
- [64] R. P. Deodhar, S. Andersson, I. Boldea, and T. J. E. Miller, "The flux-reversal machine: a new brushless doubly-salient permanent-magnet machine," *IEEE Transactions on Industry Applications*, vol. 33, no. 4, pp. 925-934, 1997.
- [65] Z. Q. Zhu, Y. Pang, D. Howe, S. Iwasaki, R. Deodhar, and A. Pride, "Analysis of electromagnetic performance of flux-switching permanent-magnet Machines by nonlinear adaptive lumped parameter magnetic circuit model," *IEEE Transactions on Magnetics*, vol. 41, no. 11, pp. 4277-4287, 2005.
- [66] L. Tom *et al.*, "Comparative Analysis of Synchronous Reluctance Machine against Conventional Induction Machine for Railway Traction," in *2022 International Conference on Electrical Machines (ICEM)*, 2022, pp. 69-75.
- [67] M. Ferrari, N. Bianchi, A. Doria, and E. Fornasiero, "Design of synchronous reluctance motor for hybrid electric vehicles," in *2013 International Electric Machines & Drives Conference*, 2013, pp. 1058-1065.
- [68] S. Taghavi and P. Pillay, "A Sizing Methodology of the Synchronous Reluctance Motor for Traction Applications," *IEEE Journal of Emerging and Selected Topics in Power Electronics*, vol. 2, no. 2, pp. 329-340, 2014.
- [69] A. P. Goncalves, S. M. A. Cruz, F. J. T. E. Ferreira, A. M. S. Mendes, and A. T. D. Almeida, "Synchronous Reluctance Motor Drive for Electric Vehicles Including Cross-

- Magnetic Saturation," in *2014 IEEE Vehicle Power and Propulsion Conference (VPPC)*, 2014, pp. 1-6.
- [70] P. Ramesh and N. C. Lenin, "High Power Density Electrical Machines for Electric Vehicles—Comprehensive Review Based on Material Technology," *IEEE Transactions on Magnetics*, vol. 55, no. 11, pp. 1-21, 2019.
- [71] H. Cai, B. Guan, and L. Xu, "Low-Cost Ferrite PM-Assisted Synchronous Reluctance Machine for Electric Vehicles," *IEEE Transactions on Industrial Electronics*, vol. 61, no. 10, pp. 5741-5748, 2014.
- [72] S. Morimoto, S. Ooi, Y. Inoue, and M. Sanada, "Experimental Evaluation of a Rare-Earth-Free PMASynRM With Ferrite Magnets for Automotive Applications," *IEEE Transactions on Industrial Electronics*, vol. 61, no. 10, pp. 5749-5756, 2014.
- [73] B. D. Varaticeanu, P. Minciunescu, and S. Matei, "Design of Permanent Magnet Assisted Synchronous Reluctance Motor for light urban electric vehicle," in *2014 International Symposium on Fundamentals of Electrical Engineering (ISFEE)*, 2014, pp. 1-6.
- [74] N. Bianchi, E. Fornasiero, E. Carraro, S. Bolognani, and M. Castiello, "Electric vehicle traction based on a PM assisted synchronous reluctance motor," in *2014 IEEE International Electric Vehicle Conference (IEVC)*, 2014, pp. 1-6.
- [75] T. Arakawa *et al.*, "Examination of an Interior Permanent Magnet Type Axial Gap Motor for the Hybrid Electric Vehicle," *IEEE Transactions on Magnetics*, vol. 47, no. 10, pp. 3602-3605, 2011.
- [76] F. Profumo, Z. Zheng, and A. Tenconi, "Axial flux machines drives: a new viable solution for electric cars," in *Proceedings of the 1996 IEEE IECON. 22nd International Conference on Industrial Electronics, Control, and Instrumentation*, 1996, vol. 1, pp. 34-40 vol.1.
- [77] M. Gärtner, P. Seibold, and N. Parspour, "Laminated circumferential transverse flux machines - lamination concept and applicability to electrical vehicles," in *2011 IEEE International Electric Machines & Drives Conference (IEMDC)*, 2011, pp. 831-837.
- [78] B. Kaiser and N. Parspour, "Transverse Flux Machine—A Review," *IEEE Access*, vol. 10, pp. 18395-18419, 2022.
- [79] G. Kastinger, "Design of a novel transverse flux machine," in *proc. ICEM*, 2002.

- [80] E. Padurariu, L. E. Somesan, I. A. Viorel, and L. Szabo, "Large power permanent magnet transverse flux motor, steady-state and dynamic behavior," in *2012 ELEKTRO*, 2012, pp. 221-224.
- [81] W. Zhao, A. Ahmed, I. Husain, and E. Muljadi, "A novel transverse flux machine for vehicle traction applications," in *2015 IEEE Power & Energy Society General Meeting*, 2015, pp. 1-5.
- [82] Z. Rahman, "Evaluating radial, axial and transverse flux topologies for 'in-wheel' motor," in *Power Electronics in Transportation (IEEE Cat. No.04TH8756)*, 2004, pp. 75-81.
- [83] D. G. Dorrell, A. M. Knight, M. Popescu, L. Evans, and D. A. Staton, "Comparison of different motor design drives for hybrid electric vehicles," in *2010 IEEE Energy Conversion Congress and Exposition*, 2010, pp. 3352-3359.
- [84] I. Subotic, N. Bodo, E. Levi, B. Dumnic, D. Milicevic, and V. Katic, "Overview of fast on-board integrated battery chargers for electric vehicles based on multiphase machines and power electronics," *IET Electric Power Applications*, vol. 10, no. 3, pp. 217-229, 2016.
- [85] M. Yilmaz and P. T. Krein, "Review of Battery Charger Topologies, Charging Power Levels, and Infrastructure for Plug-In Electric and Hybrid Vehicles," *IEEE Transactions on Power Electronics*, vol. 28, no. 5, pp. 2151-2169, 2013.
- [86] T. Na, X. Yuan, J. Tang, and Q. Zhang, "A review of on-board integrated electric vehicles charger and a new single-phase integrated charger," *CPSS Transactions on Power Electronics and Applications*, vol. 4, no. 4, pp. 288-298, 2019.
- [87] S. Haghbin, S. Lundmark, M. Alakula, and O. Carlson, "Grid-Connected Integrated Battery Chargers in Vehicle Applications: Review and New Solution," *IEEE Transactions on Industrial Electronics*, vol. 60, no. 2, pp. 459-473, 2013.
- [88] A. Khaligh and S. Dusmez, "Comprehensive Topological Analysis of Conductive and Inductive Charging Solutions for Plug-In Electric Vehicles," *IEEE Transactions on Vehicular Technology*, vol. 61, no. 8, pp. 3475-3489, 2012.
- [89] S. Q. Ali, D. Mascarella, G. Joos, and L. Tan, "Torque Cancellation of Integrated Battery Charger Based on Six-Phase Permanent Magnet Synchronous Motor Drives for Electric Vehicles," *IEEE Transactions on Transportation Electrification*, vol. 4, no. 2, pp. 344-354, 2018.

- [90] I. Subotic, N. Bodo, and E. Levi, "Single-Phase On-Board Integrated Battery Chargers for EVs Based on Multiphase Machines," *IEEE Transactions on Power Electronics*, vol. 31, no. 9, pp. 6511-6523, 2016.
- [91] M. Y. Metwly, M. S. Abdel-Majeed, A. S. Abdel-Khalik, R. A. Hamdy, M. S. Hamad, and S. Ahmed, "A Review of Integrated On-Board EV Battery Chargers: Advanced Topologies, Recent Developments and Optimal Selection of FSCW Slot/Pole Combination," *IEEE Access*, vol. 8, pp. 85216-85242, 2020.
- [92] W. E. Rippel and A. G. Cocconi, "Integrated motor drive and recharge system," ed: Google Patents, 1992.
- [93] A. G. Cocconi, "Combined motor drive and battery recharge system," ed: Google Patents, 1994.
- [94] S. Seung-Ki and L. Sang-Joon, "An integral battery charger for four-wheel drive electric vehicle," *IEEE Transactions on Industry Applications*, vol. 31, no. 5, pp. 1096-1099, 1995.
- [95] L. Solero, "Nonconventional on-board charger for electric vehicle propulsion batteries," *IEEE Transactions on Vehicular Technology*, vol. 50, no. 1, pp. 144-149, 2001.
- [96] H. Chang and C. Liaw, "An Integrated Driving/Charging Switched Reluctance Motor Drive Using Three-Phase Power Module," *IEEE Transactions on Industrial Electronics*, vol. 58, no. 5, pp. 1763-1775, 2011.
- [97] I. Subotic, N. Bodo, and E. Levi, "An EV Drive-Train With Integrated Fast Charging Capability," *IEEE Transactions on Power Electronics*, vol. 31, no. 2, pp. 1461-1471, 2016.
- [98] I. Subotic, N. Bodo, E. Levi, M. Jones, and V. Levi, "Isolated Chargers for EVs Incorporating Six-Phase Machines," *IEEE Transactions on Industrial Electronics*, vol. 63, no. 1, pp. 653-664, 2016.
- [99] I. Subotic, N. Bodo, E. Levi, and M. Jones, "Onboard Integrated Battery Charger for EVs Using an Asymmetrical Nine-Phase Machine," *IEEE Transactions on Industrial Electronics*, vol. 62, no. 5, pp. 3285-3295, 2015.
- [100] H. S. Song and K. Y. Jang, "System for recharging plug-in hybrid vehicle by controlling pre-charge of a DC link," ed: Google Patents, 2014.

- [101] L. D. Sousa, B. Silvestre, and B. Bouchez, "A combined multiphase electric drive and fast battery charger for Electric Vehicles," in *2010 IEEE Vehicle Power and Propulsion Conference*, 2010, pp. 1-6.
- [102] S. Haghbin, S. Lundmark, M. Alakula, and O. Carlson, "An Isolated High-Power Integrated Charger in Electrified-Vehicle Applications," *IEEE Transactions on Vehicular Technology*, vol. 60, no. 9, pp. 4115-4126, 2011.
- [103] A. S. Abdel-Khalik, A. Massoud, and S. Ahmed, "Interior permanent magnet motor-based isolated on-board integrated battery charger for electric vehicles," *IET Electric Power Applications*, vol. 12, no. 1, pp. 124-134, 2018.
- [104] A. S. Abdel-Khalik, S. Ahmed, and A. M. Massoud, "Performance Evaluation of an On-Board Integrated Battery Charger System Using a 12-Slot/10-Pole Surface-Mounted PM Propulsion Motor," in *2017 9th IEEE-GCC Conference and Exhibition (GCCCE)*, 2017, pp. 1-9.
- [105] M. S. Diab, A. A. Elserougi, A. S. Abdel-Khalik, A. M. Massoud, and S. Ahmed, "A Nine-Switch-Converter-Based Integrated Motor Drive and Battery Charger System for EVs Using Symmetrical Six-Phase Machines," *IEEE Transactions on Industrial Electronics*, vol. 63, no. 9, pp. 5326-5335, 2016.
- [106] I. Subotic, E. Levi, and N. Bodo, "A Fast On-Board Integrated Battery Charger for EVs Using an Asymmetrical Six-Phase Machine," in *2014 IEEE Vehicle Power and Propulsion Conference (VPPC)*, 2014, pp. 1-6.
- [107] C. Viana, M. Pathmanathan, and P. W. Lehn, "Dual-Inverter-Integrated Three-Phase EV Charger Based on Split-Phase Machine," *IEEE Transactions on Power Electronics*, vol. 37, no. 12, pp. 15175-15185, 2022.
- [108] C. Shi, Y. Tang, and A. Khaligh, "A Three-Phase Integrated Onboard Charger for Plug-In Electric Vehicles," *IEEE Transactions on Power Electronics*, vol. 33, no. 6, pp. 4716-4725, 2018.
- [109] S. Loudot, B. Briane, O. Ploix, and A. Villeneuve, "Fast charging device for an electric vehicle," ed: Google Patents, 2014.
- [110] G. Pellegrino, T. M. Jahns, N. Bianchi, W. L. Soong, and F. Cupertino, *The rediscovery of synchronous reluctance and ferrite permanent magnet motors: tutorial course notes*. Springer, 2016.
- [111] H. Dogan, F. Wurtz, A. Foggia, and L. Garbuio, "Analysis of slot-pole combination of fractional-slots PMSM for embedded applications," in *International Aegean*

- Conference on Electrical Machines and Power Electronics and Electromotion, Joint Conference*, 2011, pp. 611-615.
- [112] A. M. E.-. Refaie, "Fractional-Slot Concentrated-Windings Synchronous Permanent Magnet Machines: Opportunities and Challenges," *IEEE Transactions on Industrial Electronics*, vol. 57, no. 1, pp. 107-121, 2010.
- [113] S. Kwon, S. Kim, P. Zhang, and J. Hong, "Performance comparison of IPMSM with distributed and concentrated windings," in *Conference Record of the 2006 IEEE Industry Applications Conference Forty-First IAS Annual Meeting*, 2006, vol. 4, pp. 1984-1988.
- [114] J. Goss, D. Staton, R. Wrobel, and P. Mellor, "Brushless AC interior-permanent magnet motor design: Comparison of slot/pole combinations and distributed vs. concentrated windings," in *2013 IEEE Energy Conversion Congress and Exposition*, 2013, pp. 1213-1219.
- [115] M. C. Kulan, N. J. Baker, K. A. Liogas, O. Davis, J. Taylor, and A. M. Korsunsky, "Empirical Implementation of the Steinmetz Equation to Compute Eddy Current Loss in Soft Magnetic Composite Components," *IEEE Access*, vol. 10, pp. 14610-14623, 2022.
- [116] A. Krings, A. Boglietti, A. Cavagnino, and S. Sprague, "Soft Magnetic Material Status and Trends in Electric Machines," *IEEE Transactions on Industrial Electronics*, vol. 64, no. 3, pp. 2405-2414, 2017.
- [117] D. Gerada, A. Mebarki, N. L. Brown, C. Gerada, A. Cavagnino, and A. Boglietti, "High-Speed Electrical Machines: Technologies, Trends, and Developments," *IEEE Transactions on Industrial Electronics*, vol. 61, no. 6, pp. 2946-2959, 2014.
- [118] S. Panda and R. K. Keshri, "Evaluation of Permanent Magnet Assisted Synchronous Reluctance Motor for Light Electric Vehicle Applications," in *2020 IEEE International Conference on Power Electronics, Smart Grid and Renewable Energy (PESGRE2020)*, 2020, pp. 1-6.
- [119] *NEODYMIUM VS. SMCO MAGNETS FOR HYBRID ELECTRIC VEHICLES PERMANENT MAGNETS DOMINATE EV.* Available: <https://www.arnoldmagnetics.com/blog/neodymium-vs-smco-magnets-for-hybrid-electric-vehicles/?ssp=1&setlang=en-GB&safesearch=moderate>
- [120] J. Seok-Myeong, C. Jang-Young, K. Kyoung-Jin, K. Il-Jung, and S. Ho-Kyung, "Performance analysis of permanent magnet machines considering magnetic losses

- based on analytical parameter estimation," in *2008 International Conference on Electrical Machines and Systems*, 2008, pp. 3152-3157.
- [121] A. Hebala, S. Nuzzo, P. H. Connor, G. Volpe, C. Gerada, and M. Galea, "Analysis and Mitigation of AC Losses in High Performance Propulsion Motors," *Machines*, vol. 10, no. 9, p. 780, 2022.
- [122] A. Bardalai, D. Gerada, T. Zou, M. Degano, C. Zhang, and C. Gerada, "Comparison of AC Losses in the Winding of Electrical Machines with Fixed Strands Positions, Fixed Conductor Shapes and Random Winding," *Energies*, vol. 15, no. 15, p. 5701, 2022.
- [123] G. Bertotti, "General properties of power losses in soft ferromagnetic materials," *IEEE Transactions on Magnetics*, vol. 24, no. 1, pp. 621-630, 1988.
- [124] X. Yang, A. Fatemi, T. Nehl, L. Hao, W. Zeng, and S. Parrish, "Comparative Study of Three Stator Cooling Jackets for Electric Machine of Mild Hybrid Vehicle," in *2019 IEEE International Electric Machines & Drives Conference (IEMDC)*, 2019, pp. 1202-1209.
- [125] P. S. Ghahfarokhi, A. Podgornovs, A. Kallaste, A. J. M. Cardoso, A. Belahcen, and T. Vaimann, "The Oil Spray Cooling System of Automotive Traction Motors: The State of the Art," *IEEE Transactions on Transportation Electrification*, vol. 9, no. 1, pp. 428-451, 2023.
- [126] J. Pyrhonen, T. Jokinen, and V. Hrabovcova, *Design of rotating electrical machines*. John Wiley & Sons, 2013.
- [127] D.-K. Lee and J.-S. Ro, "Analysis and design of a high-performance traction motor for heavy-duty vehicles," *Energies*, vol. 13, no. 12, p. 3150, 2020.
- [128] A. M. TECHNOLOGIES. *N42UH*. Available: <https://www.arnoldmagnetics.com/wp-content/uploads/2017/11/N42UH-151021.pdf>

Appendix A Technical skills

The software used for the electric machine design in this thesis are:

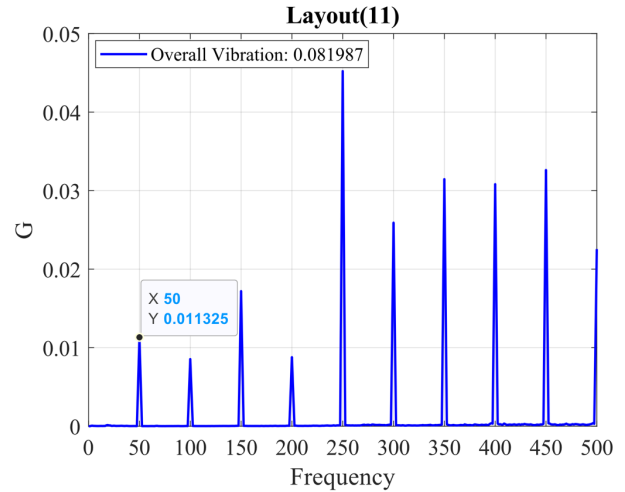
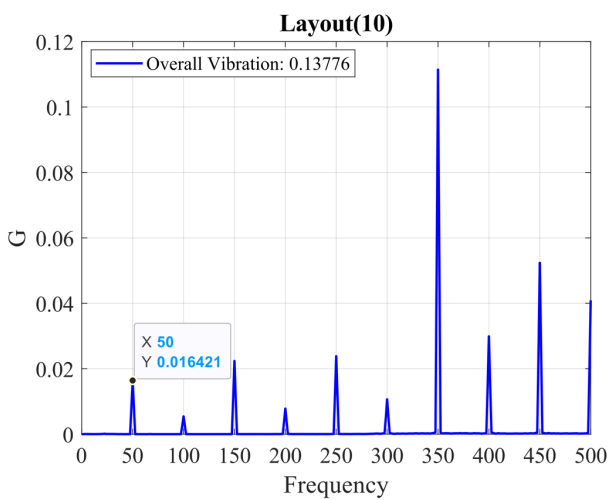
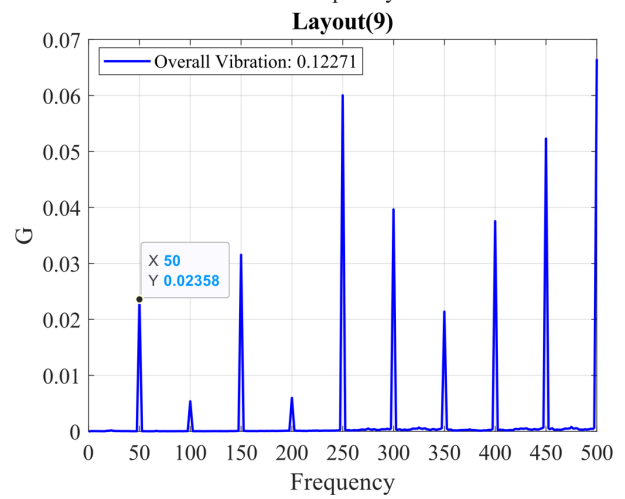
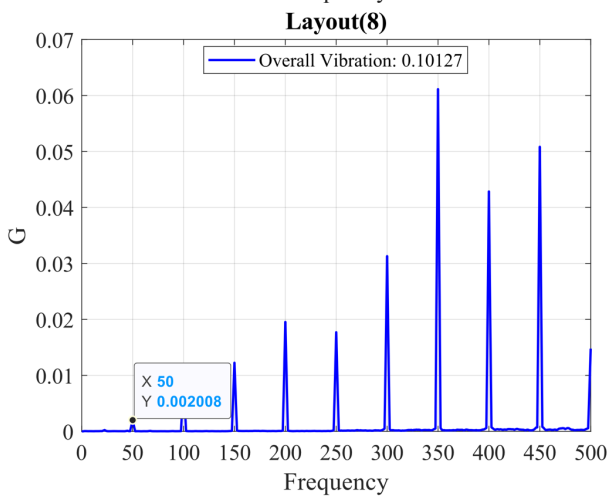
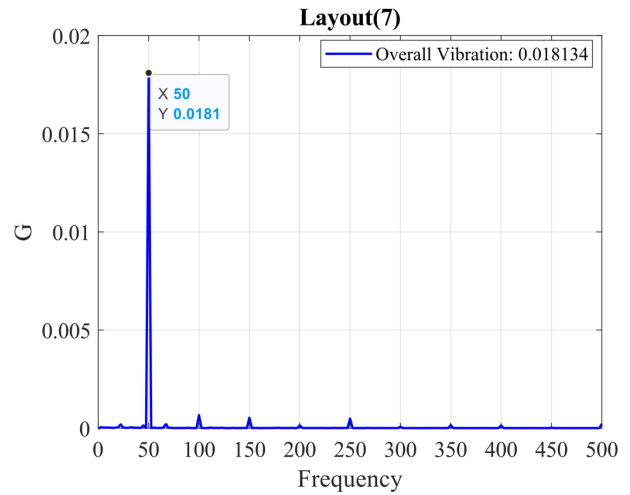
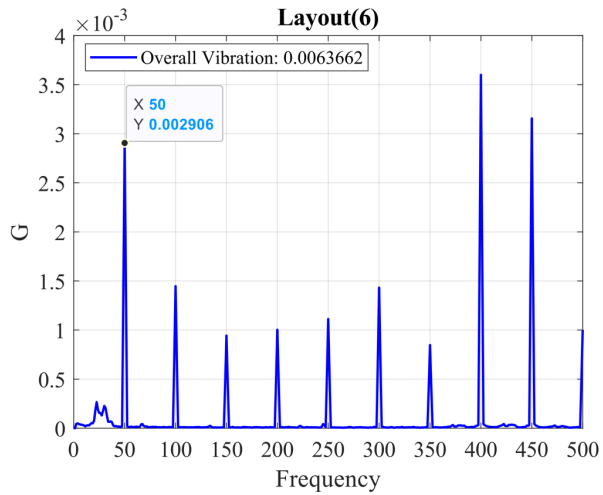
- a) MATLAB
- b) Motor-CAD
- c) modeFRONTIER
- d) ANSYS Electronics Desktop

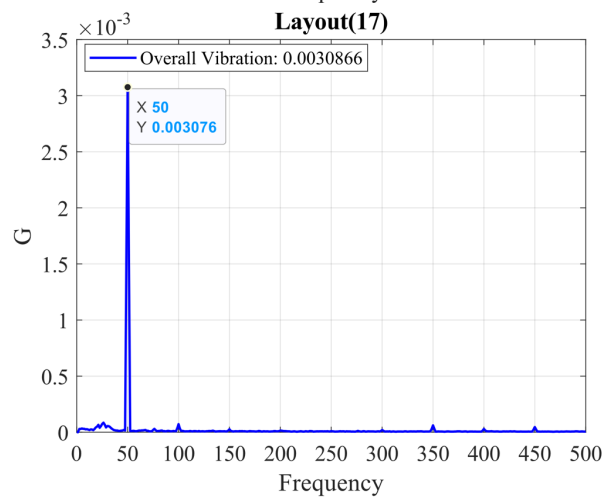
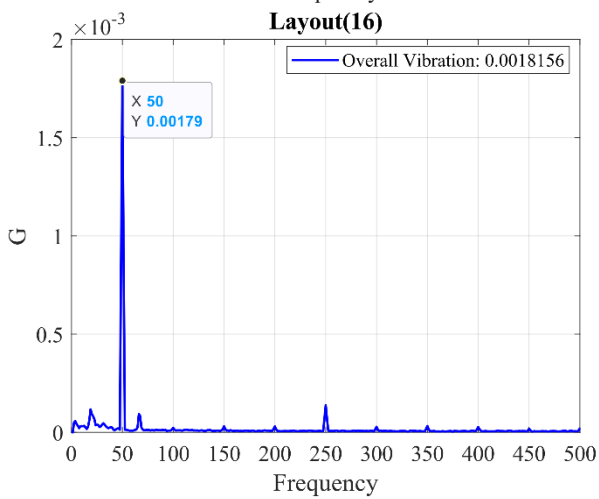
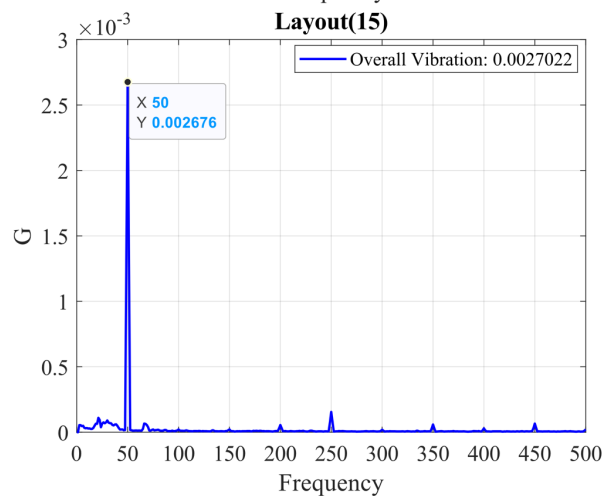
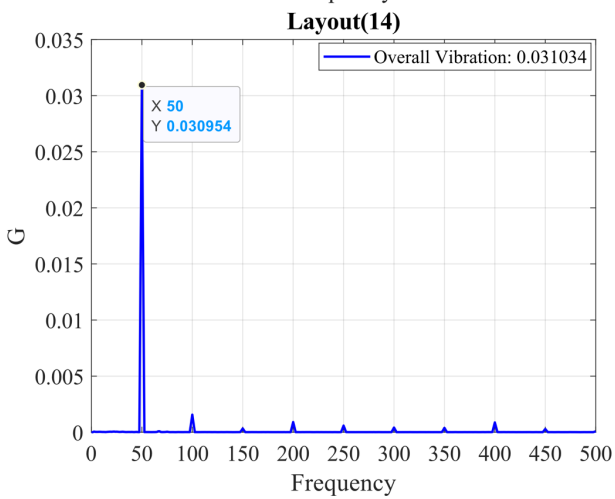
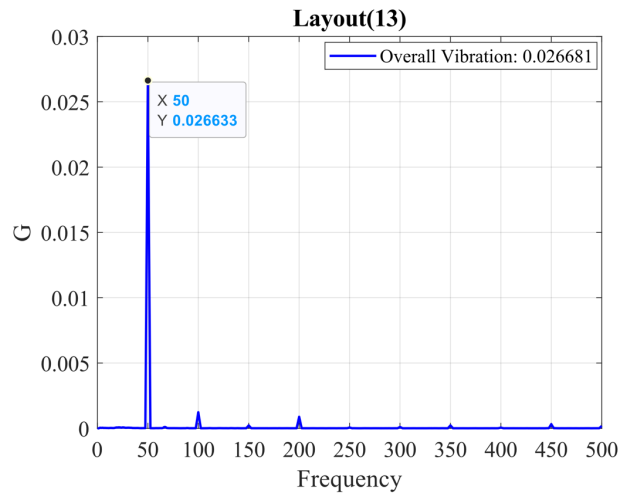
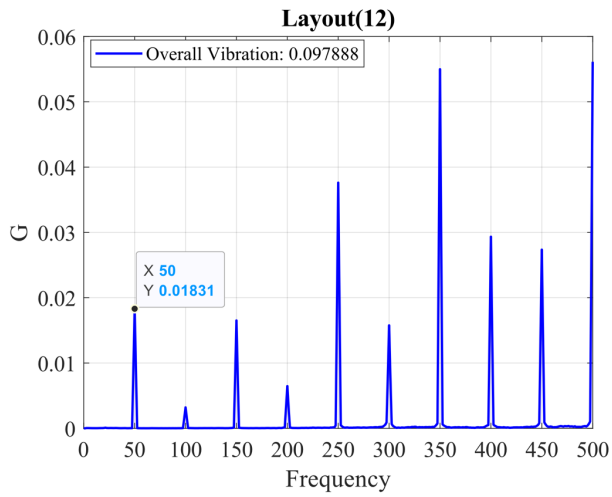
MATLAB a robust high-level language extensively used across various scientific and engineering disciplines is employed to form analytical equations and set the input variables associated with machine geometries. These crucial parameters encapsulate the design specifications and performance criteria for the motor. Once these are configured within MATLAB, they are transferred smoothly into Motor-CAD, a software designed explicitly for motor optimization. Motor-CAD leverages these parameters to perform a comprehensive analysis that considers the motor's electromagnetic, thermal and mechanical aspects leading to a highly efficient and integrated workflow.

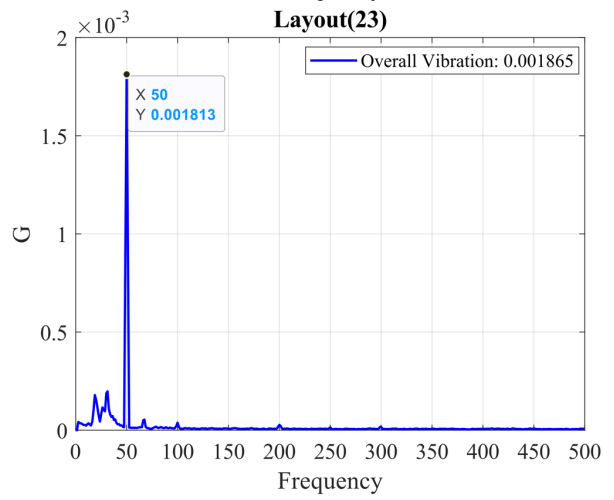
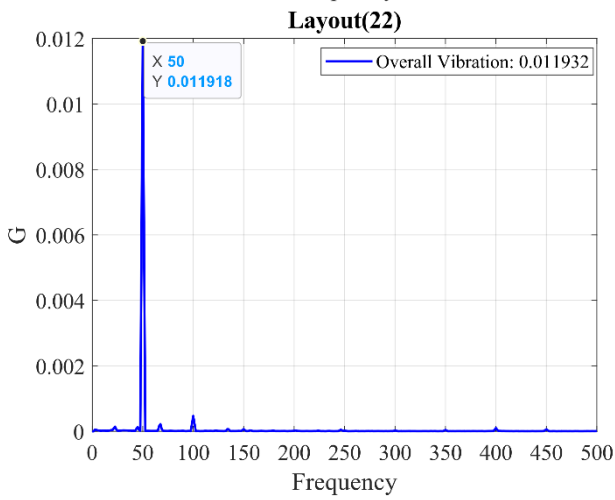
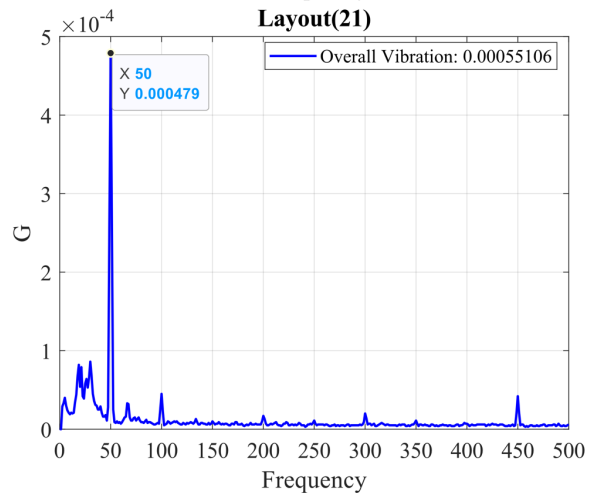
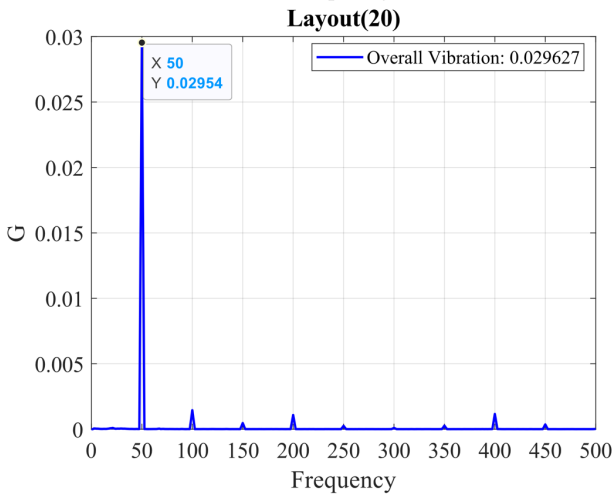
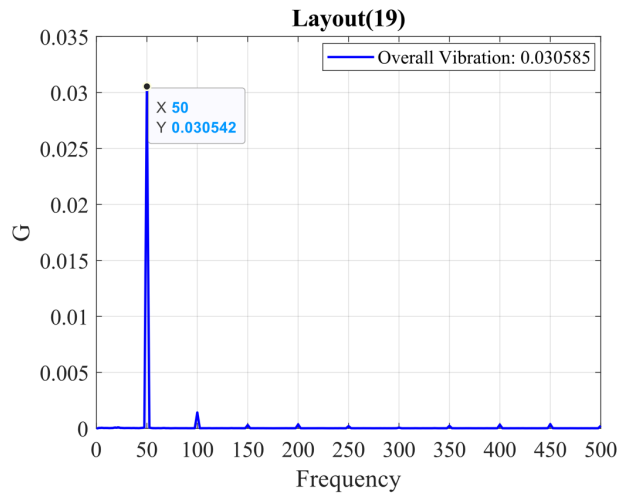
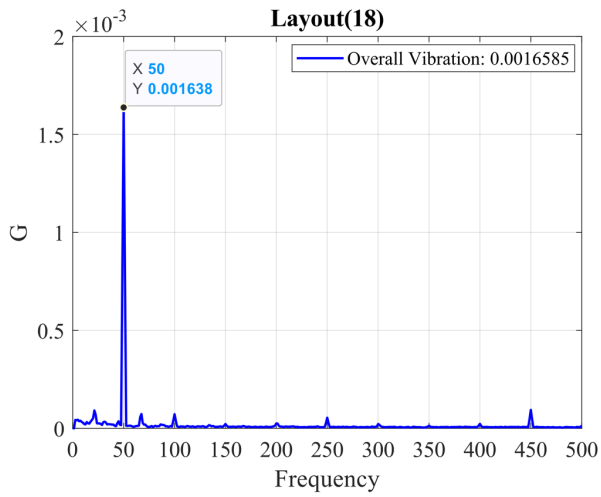
Moreover, modeFRONTIER can also interface directly with Motor-CAD via MATLAB. In modeFRONTIER, design inputs, outputs, constraints, and multi-objective criteria are established to facilitate a comprehensive multi-physic analysis, including electromagnetic, thermal and mechanical simulations. This process is iterative with the results from Motor-CAD feeding back into modeFRONTIER. This feedback mechanism enables continuous refinement of design parameters driving the process towards an optimal solution that balances the multiple design objectives.

The second aim of the thesis, which involves utilizing the machine as an inductor necessitates the use of software that offers extensive electromagnetic modelling capabilities. ANSYS Electronics Desktop is a comprehensive software package that provides solutions for electromagnetic field simulations. One of its features is its ability to freely model and manipulate the windings of the motor, providing the flexibility needed to explore various winding configurations. This is important as the winding configuration plays a crucial role in the machine's operation as an inductor. It affects several aspects, such as magnetic flux linkage, electrical losses and inductance.

Appendix B Vibration meter results







Appendix C SKF vibration meter sensor positioning

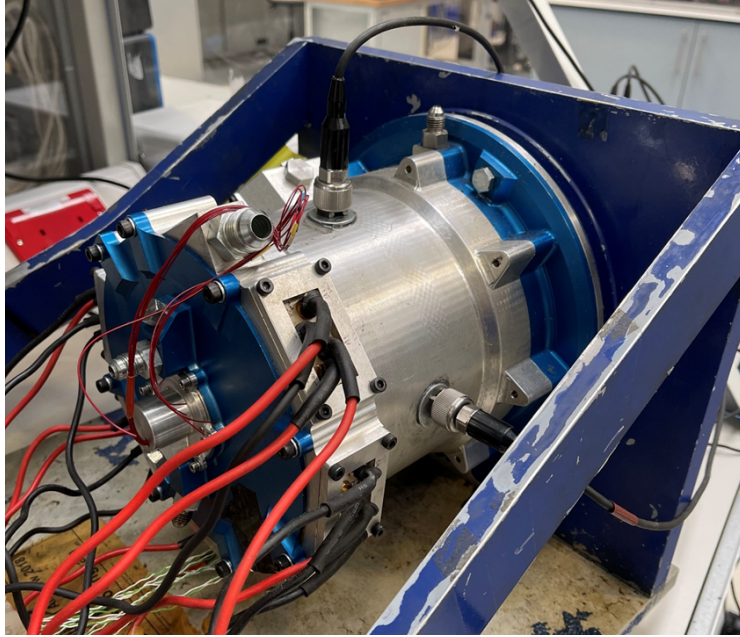


Figure C-1 SMPM machine with SKF meter sensor positioned 90 degrees



Figure C-2 Rotor aligned to d-axis

Appendix D Inductance measurement

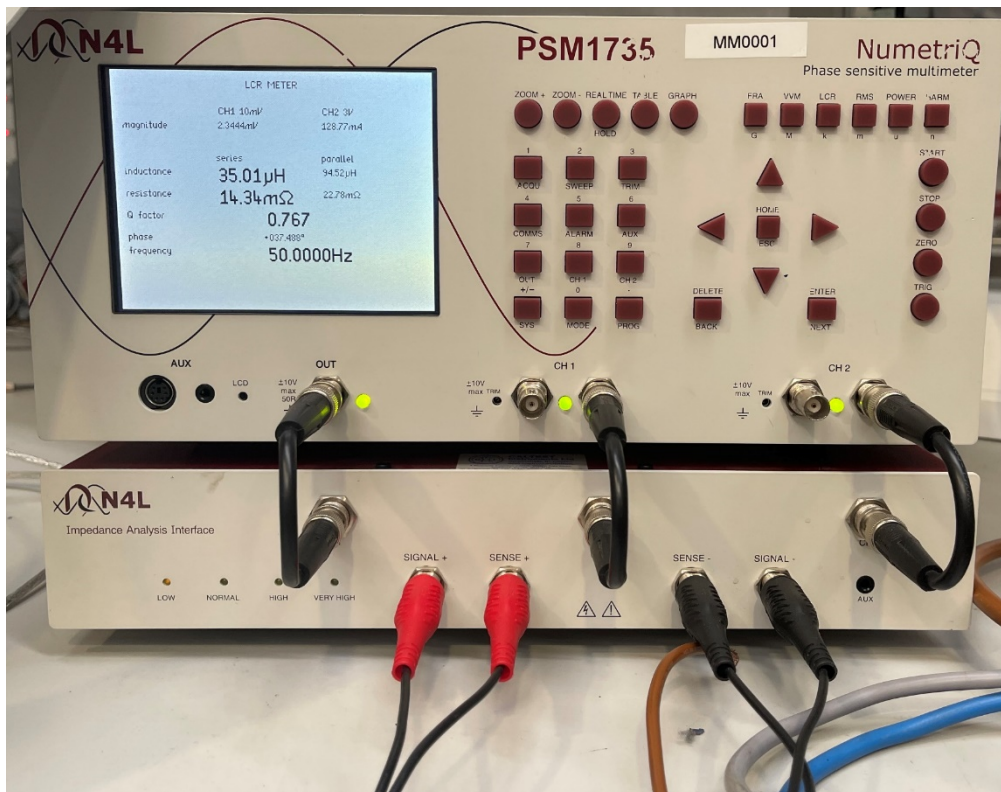


Figure D-1 Inductance measurement for phase A SMPM machine

Appendix E Rig supply and load

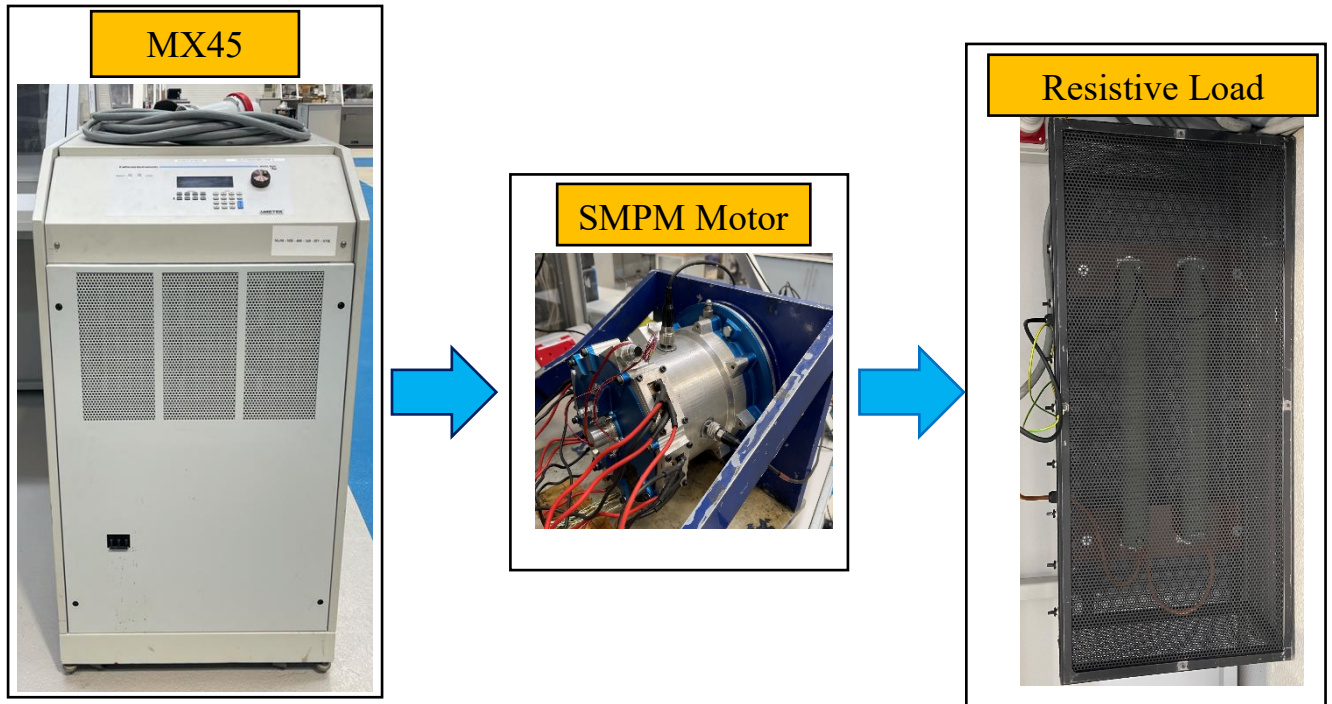


Figure E-1 Machine as inductor circuit